



*nanomaterials*

# Nanostructured Solar Cells

---

Edited by  
Guanying Chen, Zhijun Ning and Hans Agren  
Printed Edition of the Special Issue Published in *Nanomaterials*

# Nanostructured Solar Cells

## Special Issue Editors

Guanying Chen

Zhijun Ning

Hans Agren

MDPI • Basel • Beijing • Wuhan • Barcelona • Belgrade





*Special Issue Editors*

Guanying Chen  
Harbin Institute of Technology  
China

Zhijun Ning  
ShanghaiTech University  
China

Hans Agren  
Royal Institute of Technology  
Sweden

*Editorial Office*

MDPI AG  
St. Alban-Anlage 66  
Basel, Switzerland

This edition is a reprint of the Special Issue published online in the open access journal *Nanomaterials* (ISSN 2079-4991) from 2015–2017 (available at: [http://www.mdpi.com/journal/nanomaterials/special\\_issues/nano\\_solar\\_cell](http://www.mdpi.com/journal/nanomaterials/special_issues/nano_solar_cell)).

For citation purposes, cite each article independently as indicated on the article page online and as indicated below:

Author 1; Author 2. Article title. <i>Journal Name</i> <b>Year</b> , Article number, page range.
--

**First Edition 2017**

**ISBN 978-3-03842-532-8 (Pbk)**

**ISBN 978-3-03842-533-5 (PDF)**

Articles in this volume are Open Access and distributed under the Creative Commons Attribution license (CC BY), which allows users to download, copy and build upon published articles even for commercial purposes, as long as the author and publisher are properly credited, which ensures maximum dissemination and a wider impact of our publications. The book taken as a whole is © 2017 MDPI, Basel, Switzerland, distributed under the terms and conditions of the Creative Commons license CC BY-NC-ND (<http://creativecommons.org/licenses/by-nc-nd/4.0/>).

# Table of Contents

About the Special Issue Editors .....	v
Preface to “Nanostructured Solar Cells” .....	vii
<b>Prathap Pathi, Akshith Peer and Rana Biswas</b> Nano-Photonic Structures for Light Trapping in Ultra-Thin Crystalline Silicon Solar Cells Reprinted from: <i>Nanomaterials</i> <b>2017</b> , 7(1), 17; doi: 10.3390/nano7010017 .....	1
<b>Yinan Zhang, Boyuan Cai and Baohua Jia</b> Ultraviolet Plasmonic Aluminium Nanoparticles for Highly Efficient Light Incoupling on Silicon Solar Cells Reprinted from: <i>Nanomaterials</i> <b>2016</b> , 6(6), 95; doi: 10.3390/nano6060095 .....	17
<b>Tom Grace, LePing Yu, Christopher Gibson, Daniel Tune, Huda Alturaif, Zeid Al Othman and Joseph Shapter</b> Investigating the Effect of Carbon Nanotube Diameter and Wall Number in Carbon Nanotube/Silicon Heterojunction Solar Cells Reprinted from: <i>Nanomaterials</i> <b>2016</b> , 6(3), 52; doi: 10.3390/nano6030052 .....	28
<b>Won-Yeop Rho, Myeung-Hwan Chun, Ho-Sub Kim, Hyung-Mo Kim, Jung Sang Suh and Bong-Hyun Jun</b> Ag Nanoparticle-Functionalized Open-Ended Freestanding TiO <sub>2</sub> Nanotube Arrays with a Scattering Layer for Improved Energy Conversion Efficiency in Dye-Sensitized Solar Cells Reprinted from: <i>Nanomaterials</i> <b>2016</b> , 6(6), 117; doi: 10.3390/nano6060117 .....	42
<b>Jin Wang, Kosti Tapio, Aurélie Habert, Sebastien Sorgues, Christophe Colbeau-Justin, Bernard Ratier, Monica Scarisoreanu, Jussi Toppari, Nathalie Herlin-Boime and Johann Bouclé</b> Influence of Nitrogen Doping on Device Operation for TiO <sub>2</sub> -Based Solid-State Dye-Sensitized Solar Cells: Photo-Physics from Materials to Devices Reprinted from: <i>Nanomaterials</i> <b>2016</b> , 6(3), 35; doi: 10.3390/nano6030035 .....	53
<b>Chunze Yuan, Lin Li, Jing Huang, Zhijun Ning, Licheng Sun and Hans Ågren</b> Improving the Photocurrent in Quantum-Dot-Sensitized Solar Cells by Employing Alloy PbxCd1-xS Quantum Dots as Photosensitizers Reprinted from: <i>Nanomaterials</i> <b>2016</b> , 6(6), 97; doi: 10.3390/nano6060097 .....	72
<b>Jue Wei, Qiuyang Xiong, Seyed Milad Mahpeykar and Xihua Wang</b> Numerical Study of Complementary Nanostructures for Light Trapping in Colloidal Quantum Dot Solar Cells Reprinted from: <i>Nanomaterials</i> <b>2016</b> , 6(4), 55; doi: 10.3390/nano6040055 .....	85
<b>Michael Eck and Michael Krueger</b> Correlation between CdSe QD Synthesis, Post-Synthetic Treatment, and BHJ Hybrid Solar Cell Performance Reprinted from: <i>Nanomaterials</i> <b>2016</b> , 6(6), 115; doi: 10.3390/nano6060115 .....	94

<b>Sofia Paulo, Emilio Palomares and Eugenia Martinez-Ferrero</b> Graphene and Carbon Quantum Dot-Based Materials in Photovoltaic Devices: From Synthesis to Applications Reprinted from: <i>Nanomaterials</i> <b>2016</b> , 6(9), 157; doi: 10.3390/nano6090157 .....	106
<b>Zhen Lu, Wen Liu, Jingjing Li, Tao Fang, Wanning Li, Jicheng Zhang, Feng Feng and Wenhua Li</b> The Influence of Fluorination on Nano-Scale Phase Separation and Photovoltaic Performance of Small Molecular/PC71BM Blends Reprinted from: <i>Nanomaterials</i> <b>2016</b> , 6(4), 80; doi: 10.3390/nano6040080 .....	127
<b>Il Ku Kim, Jun Hyung Jo and Jung-Ho Yun</b> Morphology-Controlled High-Efficiency Small Molecule Organic Solar Cells without Additive Solvent Treatment Reprinted from: <i>Nanomaterials</i> <b>2016</b> , 6(4), 64; doi: 10.3390/nano6040064 .....	139
<b>Yiming Bai, Lingling Yan, Jun Wang, Lin Su, Zhigang Yin, Nuofu Chen and Yuanyuan Liu</b> Enhancing the Photocurrent of Top-Cell by Ellipsoidal Silver Nanoparticles: Towards Current- Matched GaInP/GaInAs/Ge Triple-Junction Solar Cells Reprinted from: <i>Nanomaterials</i> <b>2016</b> , 6(6), 98; doi: 10.3390/nano6060098 .....	146
<b>Yunfei Shang, Shuwei Hao, Chunhui Yang and Guanying Chen</b> Enhancing Solar Cell Efficiency Using Photon Upconversion Materials Reprinted from: <i>Nanomaterials</i> <b>2015</b> , 5(4), 1782–1809; doi: 10.3390/nano5041782 .....	154

## About the Special Issue Editors

**Guanying Chen** received his BS degree in applied physics in 2004 and PhD degree in optics in 2009, respectively, from Harbin Institute of Technology, China. After that, he became an assistant professor at School of Chemistry and Chemical Engineering, Harbin Institute of Technology in 2009, and then promoted to associate and full professor in 2013, and 2014, respectively. He did his postdoctoral fellow (2010–2011) at University at Buffalo, State University of New York, and then hold a joint position as an adjunct research faculty there. He received the Top-Notch National Young Investigator Award of China in 2015, and served as editorial board member for several peer-reviewed journals, such as *Scientific Reports* and *Nanomaterials*. His current interests include lanthanide-doped nanomaterials, nanostructured solar cells, and nanoparticles-based diagnostics and therapeutics.

**Zhijun Ning** received his PhD degree from Department of Applied Chemistry, East China University of Science and Technology. From 2009 to 2011, he was a postdoctoral Scholar at Royal Institute of Technology, Sweden. From 2011 to 2014, he was a Postdoctoral Scholar in the Department of Electrical and Computer Engineering, University of Toronto. Since December 2014, he holds a faculty position at School of Physical Science and Technology, ShanghaiTech University. He received the Chinese Young 1000 program award in 2015. His publications have been cited over 4500 times. His current research interest focuses on solution processed optoelectronic materials, especially leveraging chemistry method to address interface and surface management in nanomaterials.

**Hans Agren**, professor, graduated with a PhD in 1979 in experimental atomic and molecular physics at the University of Uppsala, Sweden, under the supervision of Nobel laureate Kai Siegbahn. After a couple of Post Doc years in USA he became in 1981 an assistant professor in Quantum Chemistry at Lund University. He became the first holder of the chairs in Computational Physics at Linköping University in 1991 and in Theoretical Chemistry at the Royal Institute of Technology (KTH), Stockholm, in 1998. He heads the Department of Theoretical Chemistry and Biology at KTH which houses ca. 20 scientists and 40 PhD students, with research activities in theoretical modeling primarily in the areas of molecular/nano/biophotonics and electronics, in catalysis and in X-ray science. The research is a mix of method development and problem oriented applications in collaboration with experimentalists. Hans Ågren participates in several national and international networks in his research areas. He has received the Swedish Bjurzon and Roos' awards.



# Preface to “Nanostructured Solar Cells”

With the growth of global economy, the ever-increasing demand of energy resource has become one of the biggest challenges for human being. Solar energy, due to its tremendous reserves, and environmental friendly character, is generally regarded as one of the most important renewable energy resources.

Tremendous progress has been made for the commercialization of solar cells in the past decade under the support of government subsidy. However, the large scale replacement of fossil fuel by solar cells requires the further decrease of cost. High energy output efficiency and low cost are two criteria in order to reach this purpose. Nanostructured solar cells provided an effective strategy to address both issues simultaneously. Firstly, nanostructure can be explored to enhance light harvesting capability, and increase the efficiency. Secondly, nanostructure allow the use of less materials for device fabrication, which can further decrease the cost.

Significant efforts have been made to explore nanostructure to improve the performance of solar cells. For example, the use of nanostructure significantly decreases the silicon materials consumption, favoring the commercialization of silicon solar cells. Moreover, aside traditional solar cells, nanostructures are actively applied for emerging solar cells such as dye sensitized solar cells, perovskite solar cells, quantum dots sensitized solar cells, polymer solar cells, inorganic-organic hybrid solar cells, and multi-junction solar cells. This entails enhanced light trapping capability of the device, more efficient separation of charge carriers, and more effective utilization of solar spectrum without altering the device configuration.

This book aims to integrate the most recent study of nanostructured solar cells, allowing readers to quickly follow the recent development in this area.

**Guanying Chen, Zhijun Ning and Hans Agren**

*Special Issue Editors*





Article

# Nano-Photonic Structures for Light Trapping in Ultra-Thin Crystalline Silicon Solar Cells

Prathap Pathi <sup>1,2</sup>, Akshit Peer <sup>3</sup> and Rana Biswas <sup>4,\*</sup>

<sup>1</sup> Ames Laboratory, Microelectronics Research Center, Iowa State University, Ames, IA 50011, USA; prathap@nplindia.org

<sup>2</sup> Silicon Solar Cell Division, CSIR-National Physical Laboratory, Dr. K.S. Krishnan Road, New Delhi-110012, India

<sup>3</sup> Ames Laboratory, Microelectronics Research Center, Department of Electrical and Computer Engineering, Iowa State University, Ames, IA 50011, USA; apeer@iastate.edu

<sup>4</sup> Ames Laboratory, Microelectronics Research Center, Department of Physics and Astronomy, Department of Electrical and Computer Engineering, Iowa State University, Ames, IA 50011, USA

\* Correspondence: biswasr@iastate.edu; Tel.: +1-515-294-6987

Academic Editors: Guanying Chen, Zhijun Ning and Hans Agren

Received: 2 August 2016; Accepted: 30 December 2016; Published: 13 January 2017

**Abstract:** Thick wafer-silicon is the dominant solar cell technology. It is of great interest to develop ultra-thin solar cells that can reduce materials usage, but still achieve acceptable performance and high solar absorption. Accordingly, we developed a highly absorbing ultra-thin crystalline Si based solar cell architecture using periodically patterned front and rear dielectric nanocone arrays which provide enhanced light trapping. The rear nanocones are embedded in a silver back reflector. In contrast to previous approaches, we utilize dielectric photonic crystals with a completely flat silicon absorber layer, providing expected high electronic quality and low carrier recombination. This architecture creates a dense mesh of wave-guided modes at near-infrared wavelengths in the absorber layer, generating enhanced absorption. For thin silicon (<2  $\mu\text{m}$ ) and 750 nm pitch arrays, scattering matrix simulations predict enhancements exceeding 90%. Absorption approaches the Lambertian limit at small thicknesses (<10  $\mu\text{m}$ ) and is slightly lower (by ~5%) at wafer-scale thicknesses. Parasitic losses are ~25% for ultra-thin (2  $\mu\text{m}$ ) silicon and just 1%–2% for thicker (>100  $\mu\text{m}$ ) cells. There is potential for 20  $\mu\text{m}$  thick cells to provide 30 mA/cm<sup>2</sup> photo-current and >20% efficiency. This architecture has great promise for ultra-thin silicon solar panels with reduced material utilization and enhanced light-trapping.

**Keywords:** nano-photonics; solar cell; light-trapping; scattering

## 1. Introduction

Crystalline silicon solar cells are the dominant technology for solar panels, accounting for nearly 90% of the present market share. Crystalline silicon solar cells have achieved ~25% power conversion efficiency (PCE) in small area laboratory cells [1,2] and up to 22% in larger area panels. A very attractive feature of crystalline silicon (c-Si) technology is its high stability over several years, with a degradation rate typically less than 0.5% per year.

The silicon wafers utilized in solar panels are typically 180  $\mu\text{m}$  thick. Hence, the material costs associated with thick silicon wafers are a considerable component of the system costs. It is of great interest to thin the c-Si wafers considerably, and employ recently developed light-trapping techniques [3] to absorb solar photons in thin layers. Moreover, thin silicon solar cells may be flexible and adapted to curved surfaces, increasing tremendously their range of application. Thus, the development of ultra-thin c-Si cells will be an important new technology direction that may have many significant technological impacts.

A major technical hurdle is that the absorption length ( $l_d(\lambda) = 4\pi \text{Im}(n(\lambda))/\lambda$ ) of photons (Figure 1) rapidly increases at wavelengths near the band edge (1100 nm or 1.12 eV), where  $n(\lambda)$  is the complex refractive index of Si [4]. At the near-infrared wavelength,  $\lambda = 900$  nm and  $l_d(\lambda)$  is 10  $\mu\text{m}$  for Si and grows exponentially for longer wavelengths, exceeding the thickness of the absorbing layer in thin cells. Such photons cannot be effectively absorbed in thin Si layers. It is necessary to employ light trapping techniques to increase the path length of long wavelength red and near-infra-red (IR) photons. A very attractive solar cell architecture for thin amorphous silicon (a-Si:H) and nano-crystalline Si (nc-Si) solar cells [5–12] is to utilize a periodically corrugated back-reflector and grow a conformal solar cell on top of this structure such that all layers have the periodic corrugation. This architecture traps light through (i) strong diffraction leading to a dense mesh of wave-guided modes propagating in the plane of the structure and (ii) propagating surface plasmon modes at the semiconductor-metal interface where the light intensity is considerably enhanced. These effects have resulted in measured enhancement of short circuit current ( $J_{SC}$ ) exceeding 30% in periodically corrugated nc-Si cells.

A similar diffractive structure has been proposed for thin c-Si solar cells [13–15] consisting of a periodic array of silicon nanocones both on the front and back of the structure combined with a perfect electrical conductor serving as a back reflector. Such thin c-Si cells, with a thickness of just  $\sim 2$   $\mu\text{m}$ , are predicted to have absorption and photo-current near the Lambertian limit [16,17]. However, preliminary experimental solar cells with this architecture [14] have considerably lower PCE (8%), much lower than predicted [13]. The reason for this is that the photonic crystal is composed of corrugated Si surfaces, where the corrugation leads to a large surface area and surface recombination of photo-excited carriers. The increased recombination losses outweigh the advantages of optical absorption enhancements. A triangular array of dielectric nanospheres on a flat Ag layer has been alternatively proposed [18,19] to be a high performing back reflector, which preserves the flatness of the c-Si layers and is also amenable to fabrication.

Thus, an effective solar light-trapping architecture is to utilize diffractive photonic crystal surfaces that involve flat silicon layers, that minimize carrier recombination losses, and use periodic arrays of insulating materials for diffractive effects. In this paper, we develop and design a practical light-trapping architecture utilizing photonic crystals of insulating materials that preserves electronic quality of the interfaces. There are analogies with the proposed architecture of Ingenito et al. [20] where a front surface was composed of textured "black-silicon" combined with the back surface having a random pyramidal silicon texture and a distributed Bragg reflector (DBR), with predicted absorption near the Lambertian limit. We design an alternative architecture based on periodic nanostructured arrays (rather than random features) and use a simpler metallic back reflector rather than the DBR. The present architecture avoids the alkaline texturization process, which is performed for absorption enhancement of c-Si solar cells. Enhancement of long wavelength absorption in thin Si through rear surface plasmons has been demonstrated for planar Si absorbing layers with Ag nanoparticles on a detached back surface reflector [21,22], an architecture that preserves high electronic quality of interfaces.

Light trapping has also been applied to crystallized silicon on glass (CSG) cells by texturing of the glass substrate [23] leading to  $J_{SC}$  of 29  $\text{mA}/\text{cm}^2$ –29.5  $\text{mA}/\text{cm}^2$  for up to 3.5  $\mu\text{m}$  thick poly-Si absorber layers. This is slightly lower than the Lambertian limit (34  $\text{mA}/\text{cm}^2$ ). Front texturing of the glass increases light path through randomization but may not approach the full randomization of light within the absorber layer as suggested by the Lambertian limit. We have theoretically [24] and experimentally [25] studied periodic texturing of the glass in solar cells and found gains that were significantly lower than those possible from texturing the absorber layer itself. As described by Varlamov et al., light trapping in CSG cells has also been implemented via etch-back texturing of the poly-Si itself and does extremely well at long wavelengths ( $>600$  nm) but not in the broad band spectrum, resulting in  $J_{SC}$  of 29.5  $\text{mA}/\text{cm}^2$  for a 3.6  $\mu\text{m}$  cell.

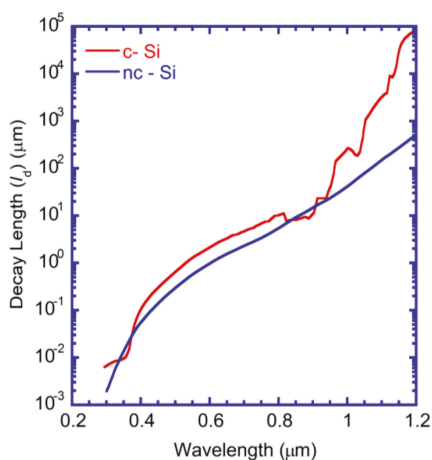


**Figure 1.** Photon absorption length as a function of wavelength for crystalline silicon (c-Si) and nano-crystalline silicon (nc-Si) (using the complex refractive index ( $n, k$ ) parameters of Reference [26]).

## 2. Results

### 2.1. Approach and Structure

We design a practical light trapping architecture where all silicon interfaces are planar and demonstrate a high degree of light trapping, close to the Lambertian limit, that is achieved by photonic crystals of non-absorbing insulating materials. This architecture is concurrently expected to have superior electronic properties, comparable to conventional high-efficiency silicon solar cells. Our solar architecture differs from the previous work of Wang et al. [13] where the silicon was part of the photonic crystal leading to much higher surface recombination of photo-excited carriers.

Our proposed solar cell architecture (Figure 2) consists of (1) an upper photonic crystal array of dielectric titania nano-cones arranged in a triangular lattice, with height  $d_0$  and pitch  $a$ ; on (2) a passivating layer of titania (thickness  $d_1$ ); (3) the flat silicon absorber layer (thickness  $d_2$ ); (4) another passivating layer of titania (thickness  $d_3$ ); followed by (5) a lower photonic crystal array of titania nanocones with height  $d_4$  and pitch  $a$ ; that is coated with (6) a metallic (Ag) reflecting layer. The upper photonic crystal has two functions. It diffracts incoming light into the thin absorber layer and realizes a gradual transition from air to the dielectric, thereby reducing impedance mismatch and reflection loss of incoming light back to air. The lower photonic crystal is effective in diffraction of long wavelength light that reaches the back of the cell, but has a much smaller effect on shorter wavelengths that are absorbed within the upper portion of the absorber layer. Without the metallic back-reflector, the long wavelength photons can transmit and escape through the back of the cell. For computational convenience, the front and lower photonic crystal arrays have the same pitch. As required in the high efficiency silicon solar cells, both interfaces of silicon are passivated with thin titanium dioxide ( $\text{TiO}_2$ ) layers. The passivating layers are flat minimizing interfacial recombination. These unique structures have great promise for the fabrication of high efficiency thin c-Si solar cells using PERC (passivated emitter rear contact), PERL (passivated emitter with rear locally diffused), or PERT (passivated emitter, rear totally diffused) configurations.

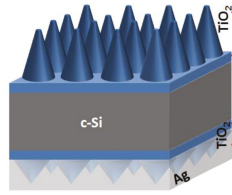


**Figure 2.** Proposed solar architecture consists of thin flat spacer titanium dioxide (TiO<sub>2</sub>) layers on the front and rear surfaces of silicon, nanocone gratings on both sides with optimized pitch and height, and rear cones are surrounded by Ag metal reflector.

It is necessary to systematically design the solar cell structure for optimal performance. We first design optimum photonic crystal based silicon solar architectures with rigorous vectorial simulations using the scattering matrix method, where Maxwell’s equations are solved in a plane wave basis, i.e., in Fourier space, for both polarizations of the incident wave. Maxwell’s equations in real space are converted to equations for each frequency  $\omega$ , in Fourier space:

$$\begin{aligned} \nabla \times E &= i\omega H \\ \nabla \times H &= i\omega \epsilon(r)E \end{aligned} \quad (1)$$

In Fourier space, the solutions of Maxwell’s equations are independent for each incoming frequency ( $\omega$ ) or incoming wavelength  $\lambda$ .

Experimentally measured wavelength-dependent complex dielectric functions  $\epsilon(\lambda)$  for Si, Ag, and TiO<sub>2</sub> are utilized. The solar cell is divided into layers in the  $z$  direction. Within each layer of the structure (Figure 2), the dielectric function  $\epsilon(x, y)$  is a function of the spatial coordinates  $(x, y)$  but not of  $z$ . This allows the dielectric function in each layer to be expanded in a two-dimensional basis of reciprocal lattice vectors  $G$ , providing the Fourier components of the dielectric function  $\epsilon(G)$ . Similarly, the electric fields and magnetic fields ( $E(G), H(G)$ ) are expanded in Bloch waves. Within each layer, Maxwell’s equations are solved in Fourier space in an eigenvalue expansion [27,28] to obtain the electric and magnetic fields in each layer. A transfer matrix is used to relate the  $E$  and  $H$  fields within each layer. Maxwell’s equations are integrated with the continuity boundary conditions throughout the unit cell to obtain the scattering matrices of each layer and the entire structure. From the scattering matrix we find the total reflectance  $R$  (including diffracted beams) and transmission  $T$  (which is 0) at each incident wavelength. The absorption at each wavelength is then  $A = 1 - R - T$ . Details have been covered in previous publications [29]. We characterize solar cell architectures by their weighted absorption  $\langle A_w \rangle$ ,

$$\langle A_w \rangle = \int_{\lambda_1}^{\lambda_2} A(\lambda) \frac{dI}{d\lambda} d\lambda, \quad (2)$$

and short circuit current  $J_{SC}$ ,

$$J_{SC} = \frac{e}{hc} \int_{\lambda_1}^{\lambda_2} \lambda A(\lambda) \frac{dI}{d\lambda} d\lambda \quad (3)$$

Here,  $dI/d\lambda$  is the incident solar spectrum. We assume ideal internal quantum efficiency, i.e., absorption of each incoming photon generates an electron-hole pair. We have been very successful in designing optimized thin silicon periodic nano-photonic structures with this rigorous approach [5,29].

## 2.2. Design of Light Trapping Architecture Methods and Structure

It is of much interest to harvest photons in thin Si-layers/foils over a broad-band of wavelengths below the Si band edge (1.12  $\mu\text{m}$ ). The large index mismatch between silicon and air causes significant

reflection losses for flat structures. This can be reduced using ergonomic tapered nanostructures which grade the refractive index from Si to the air value. Furthermore, the nanostructures diffract in-coming light and increase the photon path length within the absorber layer.

We performed a systematic set of optimizations for all parameters in this architecture (Figure 3). To conceptually understand the enhancement mechanism, it has been convenient to perform optimization by disassembling some of the components and starting with the simpler structure of two TiO<sub>2</sub> layers passivating silicon. The optimal passivating layer thicknesses was found to be 60 nm and 50 nm on the front and rear Si-surfaces, respectively, close to the expected quarter-wavelength for red light ( $\lambda \approx 600$  nm).

After this step the front nano-cones were added and their structure was optimized. Finally, the back cones were added followed by the metallic back reflector. All structural parameters were optimized to achieve maximum anti-reflection and light trapping over the broad-band solar spectrum (300 nm–1100 nm) of interest for a silicon cell. We chose TiO<sub>2</sub> for the dielectric layers due to its dual characteristic of passivating p-type and n-type silicon surfaces and ability to transport electrons.

### 2.2.1. Front Nanocone Array

Light trapping in the Si absorber layer is achieved through the generation of wave-guided modes propagating parallel to the interface [30,31]. In order to achieve the maximum light absorption, ensuring anti-reflection and light trapping, the structural requirements (pitch, aspect ratio) of the front and rear cone morphology were studied individually, and then combined. The front cone height was first optimized to achieve maximum absorption in silicon. The structure simulated consists of a front texture comprised of flat silicon (1  $\mu\text{m}$  thickness), front spacer layer, front cones, and rear spacer layer without cones (Figure 3a). The optimum cone height was studied for different array pitch values ranging from 0.25  $\mu\text{m}$  to 1.5  $\mu\text{m}$  in steps of 0.25  $\mu\text{m}$ . As shown in Figure 3b,c, the weighted absorption  $\langle A_w \rangle$  and photo-current  $J_{SC}$  have a strong inter-dependence of the pitch and cone height. The absorption and  $J_{SC}$  are low at small pitch values (below 0.5  $\mu\text{m}$ ) irrespective of the cone height. There is a region of high absorption where  $\langle A_w \rangle \approx 0.61$  (in the orange region Figure 3a), where the cone height ranges from 0.6 to 1.2  $\mu\text{m}$ , for pitch values of 0.75 to 1.5  $\mu\text{m}$ , with the optimized cone height increasing with the pitch.  $J_{SC}$  shows similar trends with a correspondingly wider region of high  $J_{SC} \approx 20.7$  mA/cm<sup>2</sup> (Figure 3c), where the optimized cone height increases from 0.6 to 1.4  $\mu\text{m}$  as the pitch increases from 0.75 to 1.5  $\mu\text{m}$ . As expected from mode coupling studies [31], the optimum pitch values are of the same order as the range of wavelengths that need to be absorbed. The simulation reveals it is advantageous to use a pitch larger than 0.75  $\mu\text{m}$ , since optimum height has a tolerance of  $>\pm 100$  nm and does not demand high precision processing equipment, an advantage for manufacturing. For example, a pitch of 1.25  $\mu\text{m}$  is coupled with a cone height of 700 nm–900 nm.

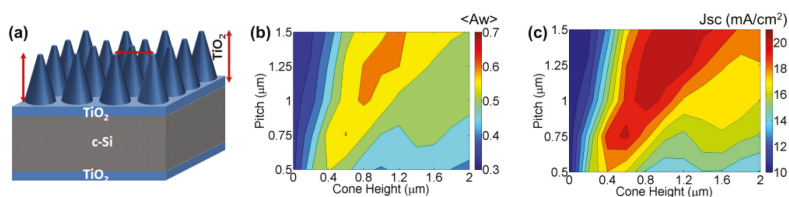


**Figure 3.** (a) Cell structure used for optimization of texture parameter using simulations. The structure consists of thin flat TiO<sub>2</sub> layers on the front and rear surfaces of flat silicon (1  $\mu\text{m}$ ). The cones are only on the front surface without rear cones and Ag metal reflector; (b) Weighted absorption,  $\langle A_w \rangle$  and (c) Short-circuit current density,  $J_{SC}$ , as a function of cone height for different pitch values. Figure shows optimum pitch  $>750$  nm and cone height  $>500$  nm with an increasing trend of tolerance of optimum cone height at larger pitch.

In the next optimization sequence, we kept the front cone geometry fixed (with pitch 750 nm and height 600 nm), introduced back cones, and varied the height of the back cones. For computational convenience, we chose the same pitch for the front and back photonic crystals. The height of the back cone was optimized and found to be  $\sim 200$  nm.

Even with the back cones there is significant transmission through the structure. To completely eliminate this transmission, the back cones were embedded in the silver back reflector; this eliminated transmission and provided a rear mirror to enhance absorption and photo-current.

### 2.2.2. Absorption Enhancement

A sequence of light-trapping photonic crystal structures (Figure 4), that were systematically built-up on a flat silicon surface, were analyzed to understand the enhancement contributions from the different components. The four sequential configurations (Figure 4) are the (a) Grating-free cell; (b) Front-grating cell; (c) Rear-grating cell, and (d) Dual-grating cell with a metallic back-reflector.

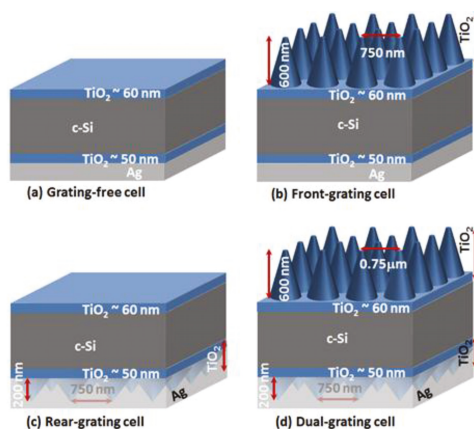


**Figure 4.** Sequence of light trapping structures on flat silicon. (a) Grating-free cell with thin layers of 60 and 50 nm on front and rear surface, respectively, and flat Ag back-reflector; (b) Front-grating cell with only front cones of height of 600 nm and a pitch of 750 nm and flat Ag back-reflector; (c) Rear-grating cell with only rear cones of height of 200 nm and a pitch of 750 nm and corrugated Ag back-reflector; (d) Dual-grating cell with a combination of front and rear cones with optimized parameters used in 'b' and 'c' with corrugated Ag back-reflector.

Scattering matrix simulations were performed for each solar architecture (Figure 4) with a flat c-Si absorber layer of 2  $\mu\text{m}$ . The optimized value for the photonic crystal arrays were obtained, and the wavelength-dependent absorbance of each architecture (Figure 5a–d) was compared with the Lambertian ( $4n^2$ ) limit, in which the light is completely randomized [32] within the absorber layer.

The starting flat solar cell (Figure 4a) with a flat back reflector (Figure 5a) displays poor absorbance at short wavelengths ( $\lambda < 550$  nm), wave-guiding modes in the red and near-IR (between 600 nm and 900 nm), absorbance considerably below the Lambertian limit, and a photo-current of 15  $\text{mA}/\text{cm}^2$  (Figure 5e,f). The addition of the front photonic crystal (Figure 4b) reduces the reflectance loss, coupling light more effectively into the cell, and increases the absorbance at shorter wavelengths ( $\lambda < 550$  nm) to near the Lambertian limit (Figure 5b). The overall absorbance at longer wavelengths ( $\lambda > 800$  nm) is still low, indicating inadequate light trapping.

Alternatively, when the back photonic crystal is added to the flat solar cell (Figure 4c), the near-IR absorbance ( $\lambda > 800$  nm) is considerably improved, approaching the Lambertian limit due to the dense mesh of waveguided modes (Figure 5c). However, the absorbance at short wavelengths ( $\lambda < 550$  nm)

is still low, similar to the flat cell, since these blue-green photons are reflected away from the solar cell. This emphasizes that the front grating is particularly beneficial in reducing reflectance loss and coupling short  $\lambda$  photons into the solar cell. The rear photonic crystal affects only longer-wavelength near-IR photons that reach the back reflector without being absorbed in the absorber layer and generates enhanced absorption at the Lambertian limit ( $\lambda > 800$  nm).

The optimized front- and rear-photonic crystals were combined (Figure 4d) to generate a high absorbance over the entire wavelength range (Figure 5d). The absorbance and photo-current (Figure 5e,f) are very close to the Lambertian limit. As observed in previous studies [5,13] the absorbance exceeds the Lambertian limit at the specific wavelengths where wave-guiding in the plane of the structure occurs [33,34].

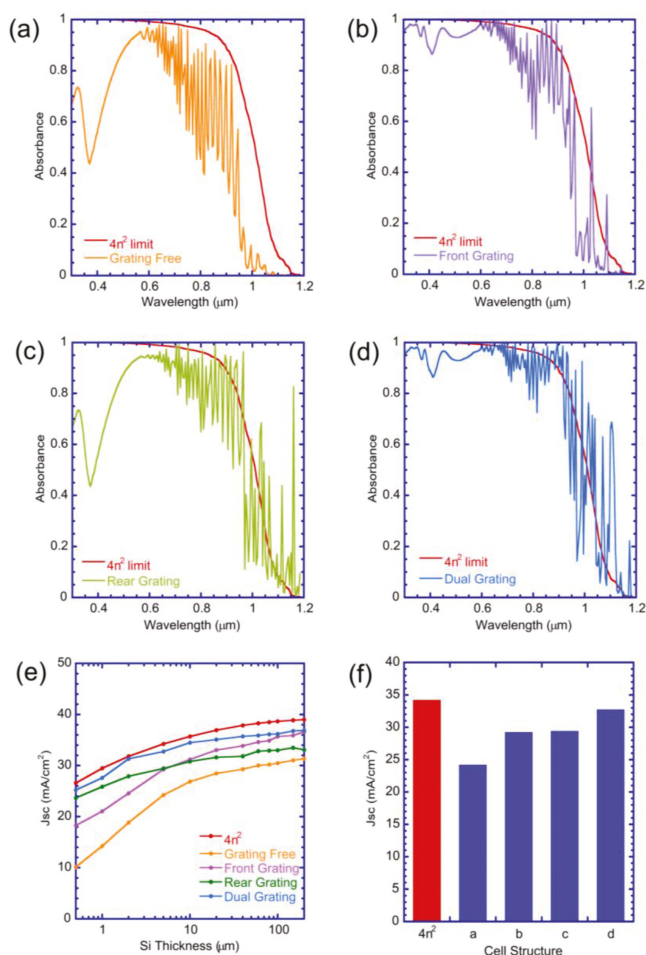


**Figure 5.** Comparison of absorption spectra of planar silicon with  $4n^2$  absorption limit for different light trapping configurations shown in Figure 2 such as (a) *grating-free cell*, (b) *front-grating cell*, (c) *rear-grating cell*, and (d) *dual-grating cell* using the optimized grating parameter for 2  $\mu\text{m}$  silicon; (e) Comparison of  $J_{SC}$  of planar cell for different light trapping configurations shown in Figure 2 with respect to silicon thickness using optimized grating parameters for 2  $\mu\text{m}$  silicon; (f)  $J_{SC}$  of the cell for a particular thickness of 2  $\mu\text{m}$  for four different configurations.



The dense mesh of wave-guiding modes generates absorption maxima from the diffraction resonances which are observed when the phase difference between modes reflected from the front and rear surfaces are multiples of  $2\pi$  or  $k_z = m\pi/d$ ,  $k_z$  is the z-component of the wave-vector [5]. For a triangular lattice, any reciprocal lattice vector  $G$  has components  $i(2\pi/a)$  and  $(2j - i)(2\pi/a)/\sqrt{3}$ , respectively, where  $i$  and  $j$  are integers. Incident light with wave-vector  $k_{||}$  is diffracted according to  $k_{||}' = k_{||} + G$ , since  $k_z = m\pi/d$ ,  $k_z^2 + k_{||}^2 = n(\lambda)^2(\omega/c)^2$  and wave-guiding occurs at resonant wavelengths given by:

$$\lambda(i, j, m) = \frac{2\pi n(\lambda)}{\left[ \left( i^2 + \frac{1}{3}(2j - i)^2 \right) \left( \frac{2\pi}{a} \right)^2 + \left( \frac{m\pi}{d} \right)^2 \right]^{1/2}} \quad (4)$$

where  $i$ ,  $j$  and  $m$  are integers. A dense mesh of wave-guided modes occurs in the long  $\lambda$  region (Figure 5), for our choice of parameters, where the wavelength inside silicon  $\lambda/n(\lambda)$  is smaller than the pitch ( $a$ ) of the cones, resulting in large values of  $i$ ,  $j$  and  $m$ . The phase coherence of waves is assumed at each interface. Accordingly, the resonant wavelength at which waveguide mode occurs is given by Equation (3).

The diffraction resonances result in propagation of wave-guided modes in the plane of the absorber layer that increases the path length and results in significant enhancement in the absorption at the wavelengths (Figure 5b–d) and enhanced  $J_{SC}$ .

It is of interest to study the enhancement and photo-current  $J_{SC}$  as a function of silicon thickness (Figure 5e) for the different solar cell architectures. The front cones are more effective at higher c-Si thicknesses ( $>40 \mu\text{m}$ ), providing a substantial increase from the grating-free flat solar cell. The rear cones are more beneficial at lower thickness ( $<10 \mu\text{m}$ ) in increasing the computed  $J_{SC}$  (Figure 5e) from the flat case, but their benefit levels off at larger thicknesses. At the smaller thicknesses, diffraction induced by the rear cones improved the photon absorption at longer wavelengths. As discussed by Bermel et al. [35], the modes diffracted by the rear cones improves the coupling of electromagnetic field with diffraction modes as c-Si thickness is reduced.

The highest performing architecture is the dual-grating cell (Figure 4d) for all Si-thicknesses. The relative enhancement in  $J_{SC}$  of the dual-photon crystal cell with respect to the flat cell is 94% for the cell thickness of  $1 \mu\text{m}$  as compared to 11% for a  $200 \mu\text{m}$  thick cell. Figure 5f, shows the progression of  $J_{SC}$  for a silicon thickness of  $2 \mu\text{m}$  for different dielectric photonic crystal arrays. The flat solar cell has  $J_{SC} = 18.9 \text{ mA/cm}^2$ . The front-grating improved the absorption and  $J_{SC}$  to  $24.6 \text{ mA/cm}^2$ , while the rear-grating alone improved it further to  $J_{SC}$  of  $27.9 \text{ mA/cm}^2$ . The dual-grating cell resulted in the  $J_{SC}$  of  $31.3 \text{ mA/cm}^2$ , which is very close to the  $4n^2$  limit of  $31.8 \text{ mA/cm}^2$ . The enhancement in  $\langle A_w \rangle$  and  $J_{SC}$  are found to be 69% and 66%, respectively, in comparison to the grating-free cell. The  $J_{SC}$  difference between Lambertian and the dual PC enhanced cell increases with thickness while the enhancement factors decrease with thickness. The dual nanocone arrays offer great promise to trap light in ultra-thin c-Si ( $<2 \mu\text{m}$ ) and collect suitable currents.

We varied the aspect ratio of the front and rear nano-cones by varying their base radii,  $R$ , for a different pitch,  $a$ . We found that  $R/a \approx 0.4$  provides the best absorption, consistent with previous results for photonic crystal enhanced absorption [24,36]. With this geometry, there is a small flat section of the titania surface in between neighboring nano-cones.

### 2.2.3. Variation with Angle of Incidence

Strong light absorption over a wide range of incident angles is crucial for the optimum performance of a solar cell during the entire daytime operating hours. Omni-directional absorbance is highly beneficial in capturing diffuse sunlight. The cell response was simulated for the optimized dual photonic crystal (PC) light-trapping architecture as a function of angle of incidence (AoI) ( $\theta$ ) for both incident polarizations. Figure 6a shows the contour plot of angle-dependent absorption of the  $2 \mu\text{m}$  thick c-Si substrate with optimized surface nanostructures for different incident angles (in

the azimuthal  $x$ - $z$  plane) over the entire wavelength range of the solar spectrum. The absorbance exceeds 0.9 at an angle  $\theta$  of  $10^\circ$  and is nearly constant above 0.8 until  $\theta \approx 70^\circ$ , above which the absorption decreases. Figure 6b shows the predicted photo-current for both p- and s-polarizations over a wide range of  $\theta$ .  $J_{SC}$  is similar for both polarizations at large  $\theta$ . Interestingly, the photo-current  $J_{SC}$  has a maximum at  $\theta \approx 30^\circ$  for p-polarization, while it has a maximum for  $10^\circ$  for s-polarization, so that these photonic crystal arrays perform better when the angle of incidence is somewhat away from the normal direction, and the incident light is nearly parallel to the surface of the nano-cones. This is advantageous for solar collection with fixed (non-tracking) solar panels, where the sun sweeps across the sky. The average  $J_{SC}$  for both polarizations has a maximum of about  $33.7 \text{ mA/cm}^2$  at  $\theta \approx 10^\circ$  and is over  $30 \text{ mA/cm}^2$  for  $\theta > 70^\circ$ . A similar trend was observed for the 1D or 2D silicon grating structures [37] and nano-photonic conformal nc-Si solar architectures [5]. For the grating-free cell,  $J_{SC}$  for the p-polarization peaks at an  $\theta \approx 60^\circ$  as a result of the Brewster angle, which reduces reflectance to zero at the front surface (inset of Figure 6b). Averaging both polarizations results in a constant  $J_{SC}$  until  $\theta \approx 60^\circ$ , after which the absorption and photo-current suffer sharply. The substantial increase of  $J_{SC}$  for the nanocones over wide range of  $\theta$  is due to the improved in-coupling of light by the PC array as discussed by Heine and Morf [37] for silicon gratings with respect to the incident angle of light.

The wide-angle light trapping and polarization independent characteristics of the nanocone arrays are due to their smooth graded-index profile and their gradual variation of optical density coupling which is better with incident light. The grating structures outperform the biomimetic silicon nanostructures [38] or silicon gratings with low-aspect ratio [39].

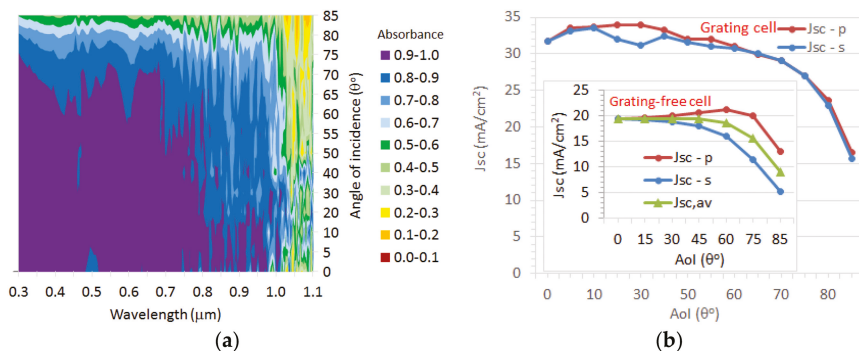


**Figure 6.** (a) Absorption spectra of the dual-grating cell (c-Si thickness =  $2 \mu\text{m}$ ) and (b) corresponding  $J_{SC}$  of the cell as a function of angle of incidence (AoI) in the range  $0^\circ$ – $85^\circ$  in steps of  $5^\circ$  (inset shows the  $J_{SC}$  of grating-free cell for p- and s-polarization and its average). The average absorption is more than 80% over a wide wavelength band.  $J_{SC}$  is independent of polarization and is less influenced until the AoI reaches  $70^\circ$ , showing the omni-directionality of the nanocone grating structures.

## 2.2.4. Field Distribution

The photonic crystal structures are effective in exciting wave-guided modes at wavelengths in the order of, or slightly larger than, the pitch of the arrays, according to the wave-guiding condition of the round-trip phase difference from the top and bottom being a multiple of  $2\pi$  (Equation (3)). The transverse electric (TE) ( $x$ -polarized) modes in the c-Si of a thickness of  $2 \mu\text{m}$  are simulated in a cross section of the solar architecture. The field distribution of the mode (Figure 7) shows the electric field intensity  $|E|^2$  at an incident wavelength of  $500 \text{ nm}$  (Figure 7a) and  $700 \text{ nm}$  (Figure 7b) (typical for the long  $\lambda$  regime) for the dual-photonic crystal cell with the optimized light trapping architecture. At  $\lambda = 500 \text{ nm}$ , the incident photons are effectively absorbed at the top of the cell (Figure 6a) and do not interact with the rear nanostructure. Since the absorption length ( $l_d$ ) of light at  $750 \text{ nm}$  exceeds the

thickness of the cell, the incident photons reach the rear photonic crystal array and both front and rear arrays are effective in diffraction. Standing waves are produced in the silicon layer by the nanocone arrays (Figure 7b). The separation between the maxima of the standing waves in the  $z$ -direction is the expected value  $\lambda/2n$ , which is close to 100 nm. This separation between maxima increases as the incident wavelength increases. In the case of nanocone array architecture (Figure 7b), there are regions of high field concentration at the top of the layer, where the field intensity is enhanced by a factor of  $\sim 7$ , which is one order more than that of its grating-free counterpart.

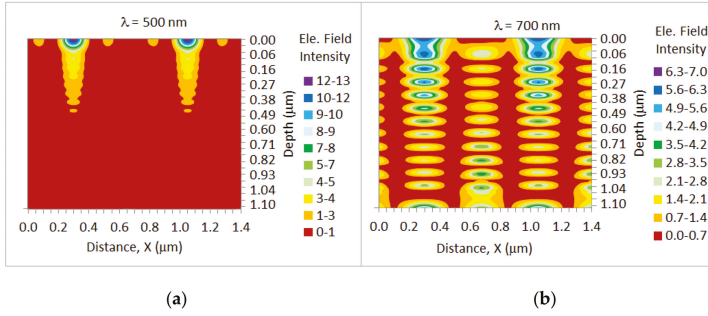


**Figure 7.** Electric field intensity distribution across the silicon absorber layer at an incident wavelength of (a) 500 nm and (b) 700 nm for the dual-grating cell with optimized parameters for the front and rear nano-cone arrays. The incident electric field intensity is normalized to 1.

The guided mode in the dual photonic crystal structure propagates in the  $x$ -direction planar to the silicon layer, with a wavelength controlled by the pitch ( $a \approx 750$  nm) of the structure. For the flat cell, the guided modes cannot be excited by plane wave illumination from air, since the light line lies above the light line for the dielectric.

### 2.2.5. Parasitic Losses

One of the critical questions is the magnitude of the parasitic losses within the metal electrode at the back of the cell, especially at long wavelengths, and the predicted enhancements when all parasitic losses are accounted for. Since the Ag electrode has  $n_2 = Im(n) > 0$ , there are losses in the silver at longer wavelengths. Qualitatively, these losses are expected to be more severe for thinner cells where more light reaches the back-reflector. In the previous sections, the calculated wavelength dependent absorption,  $A(\lambda)$  included contributions from the Ag [5,24]. To de-convolute the contribution of the absorption from only the Si layer, it was necessary to extract the electric fields  $E(r)$  and magnetic fields  $H(r)$  in real space by transformation of the computed fields in Fourier space [24]. The absorption rate  $R$  per unit volume at the position  $r$  is:

$$R = \frac{1}{8\pi} \omega Im(\epsilon(\omega)) |E(r)|^2 \tag{5}$$

The absorption  $A$  is obtained by integrating over the volume  $V$  of the absorber layer:

$$A = \frac{1}{V} \int \frac{4\pi n_1 n_2}{\lambda} |E(x, y, z)|^2 dx dy dz \tag{6}$$

Such a procedure is computationally laborious and not well suited for the present scattering matrix method where Maxwell’s equations are solved in Fourier space rather than real space. In fact, such procedures are more amenable to real space solvers such as the finite difference time domain (FDTD) method. The use of Fourier space has great advantages for parallelization and computational efficiency at the expense of not directly calculating the real space fields and separating the losses.

Nonetheless, we have implemented this procedure of extracting the real space fields and we separately calculate the losses only in the silicon. More than 1000 CPU hours are needed in a multi-processor environment utilizing 64 processors.

We simulated the absorption and  $J_{SC}$  (Figure 8) with this real-space method as a function of the Si-absorber layer thickness and compared it with the previous Fourier space simulation that includes the absorption in the metal. The absorption and  $J_{SC}$  is lower with the real-space method due to parasitic absorption in Ag. The difference between the real space and Fourier space is largest for the thinner absorber layers, but nearly negligible for thicker Si absorber layers (Figure 8). The difference between the photo-current by the real-space and Fourier space methods is the parasitic absorption, which varies from 1% for 200  $\mu\text{m}$  Si to 15% for 10  $\mu\text{m}$  and 33% for the thinnest 1  $\mu\text{m}$  Si absorber.  $J_{SC}$  reaches  $\sim 24 \text{ mA/cm}^2$  for the 2  $\mu\text{m}$  Si after accounting for parasitic losses. In comparison,  $\langle A_w \rangle$  is 0.5% to 25% lower as the Si thickness is decreased from 200  $\mu\text{m}$  to 1  $\mu\text{m}$ , respectively. This trend is to be expected since the red and near-IR wavelengths are absorbed in thicker cells and do not reach the back reflector, which consequently has negligible effect on parasitic absorption. A large fraction of the incident light reaches the back reflector in thin cells, increasing the parasitic absorption. Parasitic losses are due to ohmic losses in the structured Ag-dielectric interface. In principle, the parasitic absorption may be reduced by the use of a conductive distributed back reflector (DBR) [20,29] with flat interfaces, but the wavelength bandwidth of high reflectance may be smaller.

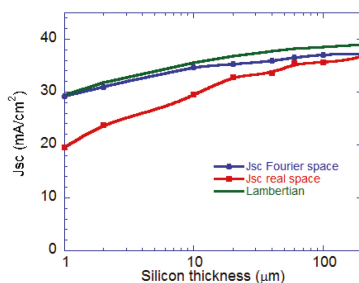


**Figure 8.** Comparison of the simulated short-circuit photo-current  $J_{SC}$  as a function of the thickness of the Si absorber layer in the real-space method utilizing only the absorption in the Si layer, compared to the Fourier space method which includes the absorption in all layers. The difference between the real-space and Fourier space results is the parasitic absorption. The Lambertian limit is shown for comparison.

### 3. Discussion

Flat interfaces of silicon with passivating titania are expected to have a minimum density of surface defects with a high degree of passivation and electronic quality in comparison to that of the textured or patterned silicon surfaces. The photonic crystal arrays reside within the titania that control light trapping and can be easily fabricated by spraying titania gels on silicon and nano-imprinting the gel in a roll-to-roll method, viable for large scale production. Micro-transfer molding techniques using polydimethylsiloxane (PDMS) templates are suitable for small area laboratory cells. Additionally, the titania layers could be cured during the metallization step, where the metal top contacts are fabricated to the silicon layer. This reduces the additional substrate heating during the deposition step of the antireflection/passivation layer. The spacer layer thickness can be controlled by the processing parameters of pressure, temperature, etc., during imprinting. Our study demonstrates a large tolerance of the optimum design to grating parameters, which does not impose stringent conditions over the processing parameters. The grating structure allows for the use of thinner silicon substrates and avoids the physical or chemical etching or patterning processes that are used for light management in the standard silicon solar cell fabrication. The imprint process is proved to be attractive on plastic substrates for mass production [40].

After accounting for parasitic losses in the thin cells (Figure 8) we obtain predicted short circuit currents  $J_{SC}$  of  $\sim 30$  mA/cm<sup>2</sup> (24 mA/cm<sup>2</sup>) for 20  $\mu$ m (2  $\mu$ m) thick cells. Utilizing the highest reported cell parameters of  $V_{oc} = 0.74$  V and fill factor (FF) of 0.827 for the Panasonic c-Si cell [2,41], we predict the efficiency to be  $\sim 20.2\%$  (14.7%) for a 20  $\mu$ m (2  $\mu$ m) thick cell, which reduces Si material utilization by  $\sim 15$  (compared to a 300  $\mu$ m cell). This suggests that a  $\sim 20$  cell  $\mu$ m may yield acceptable efficiency at significantly lower cost.

This work is significantly different from our previous dual photonic crystal solar architecture [24] which used (i) an organic absorber layer; (ii) a polymer lens array on glass for focusing; and (iii) a nanostructured organic layer, none of which are present here.

An alternative to the periodically structured photonic crystals is the use of a random texture on both the front and back surface [20] that randomizes light distribution in the material, a feature that has been extensively utilized in thin amorphous silicon cells.

An issue of much practical importance is that solar panels are subjected to harsh environmental conditions. To protect such panels with nanocone arrays we anticipate using a front glass protective sheet that is commonly employed in most solar panels. Thus, the nanocones are not in direct contact with the outside environment and are expected to have high stability. We have performed simulations with a protective glass sheet that shows the enhancements are similar to those in this paper.

This work mainly targets the state-of-the-art crystalline silicon cell structures (i.e., PERC/PERL/PERT) in the industrial environment irrespective of silicon thickness. These advanced structures require efficient passivation on both surfaces. Rear surface/back surface field (BSF) is contacted through via-holes, which are generally made using screen printer/laser ablation followed by metal filling. Therefore, the charge collection is ensured through via-holes filled with metal, and not through the TiO<sub>2</sub> layer.

#### *Proof of Concept Demonstration of TiO<sub>2</sub> Nanocone Array Fabrication*

We have developed a nano-imprinting procedure to demonstrate the feasibility of fabricating nano-cone arrays of titania on silicon substrates, and we illustrate a pathway for experimental fabrication of the simulated light-trapping structures. Briefly, the process started with a polycarbonate master pattern having nanocone gratings in triangular lattice with a period of  $\sim 750$  nm and height  $\sim 150$  nm. The master pattern was used to replicate the inverse of the nanocone array on a polydimethylsiloxane (PDMS) mold using soft lithography, using a procedure described in our previous publication [42]. The resulting PDMS mold with the inverse nanocup array was then used to imprint the TiO<sub>2</sub> film. We adopted the process in Chen et al. [43] with slight modifications to fabricate the TiO<sub>2</sub> film. We spin-coated 0.45 M titanium diisopropoxide bis(acetylacetonate) on a clean silicon wafer at 3000 rpm for 30 s. The film was then imprinted under elevated temperature and pressure with the PDMS mold using the process illustrated schematically in Figure 9 with more details in the following Section 4.

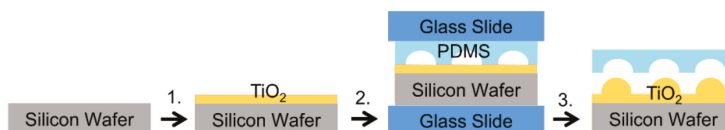


**Figure 9.** Schematic of the TiO<sub>2</sub> nanoimprinting process. (1) TiO<sub>2</sub> film is spin-coated on silicon substrate using a precursor titanium diisopropoxide bis(acetylacetonate); (2) The polydimethylsiloxane (PDMS) stamp having nanocup is placed on the spin-coated film with patterned side facing the film. The whole assembly is sandwiched between two glass slides and held together with binder clips (not shown here); (3) After keeping at  $\sim 170$  °C for 15 min, the binder clips are released to reveal the inverse of PDMS nanocup on the TiO<sub>2</sub> film.

Figure 10a shows the atomic force microscopy image of the nanoimprinted TiO<sub>2</sub> film fabricated using soft lithography. The atomic force microscopy (AFM) line scan and three-dimensional view (Figure 10b) shows the well-replicated regular array of nanocones on TiO<sub>2</sub> with a period of ~750 nm and average height of ~35 nm. It is to be noted that the feature height can be varied easily using the initial PDMS stamp of different nanocup depth. Since the TiO<sub>2</sub> material is inherently hard and compact, the shallower stamp has difficulty in penetrating deeper into the film. However, the PDMS nanocup of much higher depths of the order of ~1 micron will yield nanocone gratings with height >500 nm–600 nm which is of interest to solar cell fabrication for efficient light trapping based on simulation results. The similar imprinting procedure has been successfully implemented by our group in nanoimprinting various polymer films such as polystyrene [40] and poly(L-lactic acid) [44].

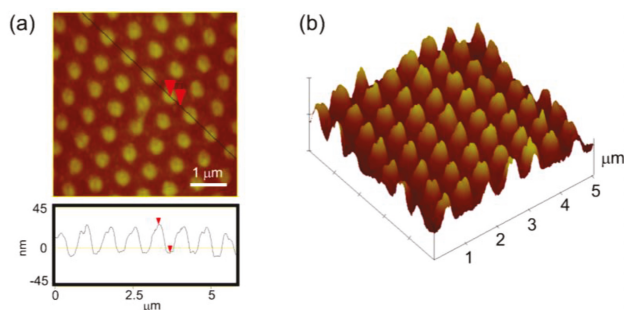


**Figure 10.** (a) Atomic force microscopy (AFM) image of the periodic array of nanocones imprinted on TiO<sub>2</sub> film. The AFM line scan shows the periodicity at ~750 nm and the average height of nanocones at ~35 nm; (b) Three-dimensional view of the structure showing titania nanocone arrays.

#### 4. Materials and Methods

The solar cell is divided into layers in the  $z$  direction. Within each layer of the structure (Figure 2), the dielectric function  $\epsilon(x, y)$  is a function of the spatial coordinates  $(x, y)$  but not of  $z$ . This allows the dielectric function in each layer to be expanded in a two-dimensional basis of reciprocal lattice vectors  $G$ , providing the Fourier components of the dielectric function  $\epsilon(G)$ . Similarly, the electric fields and magnetic fields ( $E(G), H(G)$ ) are expanded in Bloch waves. Within each layer, Maxwell's equations are solved in Fourier space in an eigenvalue expansion. A transfer matrix is used to relate the  $E$  and  $H$  fields within each layer. Maxwell's equations are integrated with the continuity boundary conditions throughout the unit cell to obtain the scattering matrices of each layer and the entire structure. From the scattering matrix we find the total reflectance  $R$  (including diffracted beams) and transmission  $T$  (which is 0) at each incident wavelength. The absorption at each wavelength is then  $A = 1 - R - T$ . This computational algorithm is executed on massively parallel computing clusters (using 192 to 256 processors) with each wavelength/frequency sent to a different processor, which considerably speeds the design time. The advantage of this scattering matrix approach is that a real-space grid is not needed, avoiding complications of large memory requirements for substrates.

Experimentally, the nanocones are fabricated using nanoimprint lithography (NIL) of sol-gel derived TiO<sub>2</sub> layers. The PDMS mold was generated from the polycarbonate master. The precursor solution 0.45 M titanium diisopropoxide bis(acetylacetonate) was spin-coated on a clean silicon wafer at 3000 rpm for 30 s. The PDMS mold was placed such that the patterned side faced the spin-coated titania film and the whole assembly was sandwiched together in two glass slides using binder clips, which served to apply adequate pressure for nanoimprinting. After keeping the assembly at 170 °C for 15 min, the binder clips were released and the PDMS stamp was subsequently lifted to reveal the nanoimprinted film. The sample was then sintered in a furnace at 550 °C for 15 min. The nanoimprinted substrate was then immersed in 50 mM TiCl<sub>4</sub> solution for 30 min at 70 °C and washed with deionized



(DI) water, followed by annealing at 550 °C for 30 min. The purpose of annealing is to harden the nanoimprinted TiO<sub>2</sub> film.

The imprinting process is more industrial friendly for roll-to-roll (R2R) or large area fabrication. The evolution of R2R or roll-to-plate (R2P) makes the NIL process cheaper and compatible with the existing fabrication lines in the photovoltaic (PV) industry [45].

## 5. Conclusions

We have designed a highly absorbing thin film crystalline Si based solar architecture, using periodically patterned front and rear photonic crystals. In contrast to previous approaches, we utilize dielectric photonic crystals, ensuring that the c-Si absorber layer has completely flat interfaces, which is expected to result in high electronic quality and low carrier recombination. The mechanism for enhanced absorption is the generation of a dense mesh of wave-guided modes at near IR wavelengths, propagating in the Si absorbing layer. An optimized structure consists of a triangular lattice of front nanocones of titania with a height of 600 nm and pitch of 750 nm, although other ranges of height/pitch combinations can provide similar results, such as a 1000 nm pitch with a nanocone height of 800 ± 100 nm. The nanocone height and pitch are strongly inter-related. The back reflector consists of another periodic array of nanocones of titania with similar pitch as the front array, embedded with a silver back reflector. For thin c-Si absorber layers (<2 μm), we achieve an absorption and photo-current enhancement exceeding 100%. For thick c-Si absorber layers, the enhancement is up to 20%. The absorption has approached the Lambertian limit at small thicknesses (<10 μm) and is only slightly lower by (~5%) at larger thickness of 200 μm. Although the absorption at any particular wavelength can exceed the Lambertian limit, the absorption averaged over all wavelengths and the photo-current is below the Lambertian value. The limiting Lambertian value, when averaged over all wavelengths, is an aspect for fundamental studies.

Parasitic losses are significant (>25%) for ultra-thin Si layers below 2 μm thickness, but decrease rapidly as the thickness of the Si absorber layer increases, and are just ~1%–2% for thick (>100 μm) cells. Electric field distributions demonstrate waveguiding modes and high intensity focusing regions within the absorber layer. The strong enhancements predicted by simulation should be tested by fabrication of such nano-photonic structured solar cells. The proposed structure is very promising for high performance flexible, ultra-thin Si solar cells, providing a pathway for low cost high performing silicon solar modules which should be valuable to researchers in this area.

**Acknowledgments:** This work was supported (in part, Rana Biswas, Akshit Peer) by the U.S. Department of Energy (DOE), Office of Science, Basic Energy Sciences, Materials Science and Engineering Division. The research was performed at Ames Laboratory, which is operated for the U.S. DOE by Iowa State University under contract # DE-AC02-07CH11358. This work was also supported (in part, Prathap Pathi) by the IUSSTF (Indo-US Science and Technology Forum) and DST (Department of Science & Technology), Govt. of India, under the BASE (Bhaskara Advanced Solar Energy) Fellowship program (Award No. 2014/F-3/Prathap Pathi). The research used resources at the National Energy Research Scientific Computing Center (NERSC), which is supported by the Office of Science of the U.S. DOE under Contract No. DE-AC02-05CH11231.

**Author Contributions:** Rana Biswas and Prathap Pathi conceived the study, performed the simulations, and analyzed the data; Akshit Peer performed experimental studies; Rana Biswas, Prathap Pathi, and Akshit Peer wrote the manuscript.

**Conflicts of Interest:** The authors declare no conflict of interest. The funding sponsors had no role in the design of the study; in the collection, analyses, or interpretation of data; in the writing of the manuscript, and in the decision to publish the results.

## References

1. National Renewable Energy Laboratory (NREL). National Center for Photovoltaics Solar Efficiency Chart. Available online: [http://www.nrel.gov/pv/assets/images/efficiency\\_chart.jpg](http://www.nrel.gov/pv/assets/images/efficiency_chart.jpg) (accessed on 30 December 2016).
2. Green, M.A.; Emery, K.; Hishikawa, Y.; Warta, W.; Dunlop, E.D. Solar Efficiency Tables (version 47). *Prog. Photovolt.* **2016**, *24*, 3–11. [CrossRef]
3. Atwater, H.; Polman, A. Plasmonics for improved photonic devices. *Nat. Photonics* **2010**, *9*, 9–16.



4. Palik, E. *Handbook of the Optical constants of Solids*; Academic Press: San Diego, CA, USA, 1998.
5. Biswas, R.; Xu, C. Nano-crystalline silicon solar cell architecture with absorption at the classical  $4n^2$  limit. *Opt. Exp.* **2011**, *19*, A672. [CrossRef] [PubMed]
6. Bhattacharya, J.; Chakravarty, N.; Pattnaik, S.; Slafer, W.D.; Biswas, R.; Dalal, V. A Novel photonic-plasmonic Structure for Enhancing Light Absorption in Thin Film Solar Cells. *Appl. Phys. Lett.* **2011**, *99*, 131114. [CrossRef]
7. Ferry, V.E.; Verschuur, M.A.; Li, H.B.T.; Schropp, R.E.I.; Atwater, H.A.; Polman, A. Improved red-response in thin film a-Si:H solar cells with soft-imprinted plasmonic back reflectors. *Appl. Phys. Lett.* **2009**, *95*, 183503. [CrossRef]
8. Sai, H.; Saito, K.; Hozuki, N.; Kondo, M. Relationship between the cell thickness and the optimum period of textured back reflectors in thin-film microcrystalline silicon solar cells. *Appl. Phys. Lett.* **2013**, *102*, 053509.
9. Han, S.E.; Chen, G. Toward the Lambertian limit of light trapping in thin nanostructured silicon solar cells. *Nano Lett.* **2010**, *10*, 4692–4696. [CrossRef] [PubMed]
10. Zhao, H.; Ozturk, B.; Schiff, E.A.; Sivec, L.; Yan, B.; Yang, J.; Guha, S. Back reflector morphology effects and thermodynamic light-trapping in thin-film silicon solar cells. *Sol. Energy Mater. Sol. Cells* **2014**, *129*, 104–114. [CrossRef]
11. Battaglia, C.; Escarre, J.; Soderstrom, K.; Charriere, M.; Despeisse, M.; Haug, F.-J.; Ballif, C. Nanomoulding of transparent zinc oxide electrodes for efficient light trapping in solar cells. *Nat. Photonics* **2011**, *5*, 535–538. [CrossRef]
12. Soderstrom, T.; Haug, F.J.; Daudrix, V.T.; Ballif, C. Flexible micromorph tandem a-Si/ $\mu$ c-Si solar cells. *J. Appl. Phys.* **2010**, *107*, 014507. [CrossRef]
13. Wang, K.X.; Yu, Z.; Liu, V.; Cui, Y.; Fan, S. Absorption enhancement in ultrathin crystalline silicon solar cells with antireflection and light-trapping nanocone gratings. *Nano Lett.* **2012**, *2012*, 1616–1619. [CrossRef] [PubMed]
14. Wang, S.; Weil, B.D.; Li, Y.; Wang, K.X.; Garnett, E.; Fan, S.; Cui, Y. Large-area free-standing ultrathin single-crystal silicon as processable materials. *Nano Lett.* **2013**, *13*, 4393–4398. [CrossRef] [PubMed]
15. Zhang, R.; Shao, B.; Dong, J.R.; Zhang, J.C.; Yang, H. Absorption enhancement analysis of crystalline Si thin film solar cells based on broadband antireflection nanocone grating. *J. Appl. Phys.* **2011**, *110*, 113105.
16. Yablonovitch, E. Statistical ray optics. *J. Opt. Soc. Am.* **1982**, *72*, 899–907. [CrossRef]
17. Tiedje, T.; Yablonovitch, E.; Cody, G.D.; Brooks, B. Limiting efficiency of silicon solar cells. *IEEE Trans. Electron Devices* **1984**, *31*, 711–716. [CrossRef]
18. Xu, Q.; Johnson, C.; Disney, C.; Pillai, S. Enhanced broadband light trapping in c-Si solar cells using Nanosphere-Embedded Metallic Grating Structure. *IEEE J. Photovolt.* **2016**, *6*, 61–67. [CrossRef]
19. Eisenlohr, J.; Benick, J.; Peters, M.; Bläsi, B.; Goldschmidt, J.C.; Hermle, M. Hexagonal sphere gratings for enhanced light trapping in crystalline silicon solar cells. *Opt. Exp.* **2014**, *22*, A111–A119. [CrossRef] [PubMed]
20. Ingenito, A.; Isabella, O.; Zeman, M. Experimental demonstration of  $4n^2$  classical absorption limit in nanotextured ultrathin solar cells with dielectric omnidirectional back reflector. *ACS Photonics* **2014**, *1*, 270–278. [CrossRef]
21. Ouyang, Z.; Pillai, S.; Beck, F.; Kunz, O.; Varlamov, S.; Catchpole, K.R.; Campbell, P.; Green, M.A. Effective light trapping in polycrystalline silicon thin film solar cells with localized surface plasmons. *Appl. Phys. Lett.* **2010**, *96*, 261109. [CrossRef]
22. Pillai, S.; Catchpole, K.R.; Trupke, T.; Green, M.A. Surface plasmon enhanced solar cells. *J. Appl. Phys.* **2007**, *101*, 093107. [CrossRef]
23. Varlamov, S.; Dore, J.; Evans, R.; Ong, D.; Eggleston, B.; Kunz, O.; Schubert, H.; Young, T.; Huang, J.; Soderstrom, T.; et al. Polycrystalline silicon on glass thin film solar cells: A transition from solid-phase to liquid-phase crystallized silicon. *Sol. Energy Mater. Sol. Cells* **2013**, *119*, 246–255. [CrossRef]
24. Peer, A.; Biswas, R. Nano-photonic Organic Solar Cell Architecture for Advanced Light Trapping with Dual Photonic Crystals. *ACS Photonics* **2014**, *1*, 840–847. [CrossRef]
25. Chen, Y.; Elshobaki, M.; Gebhardt, R.; Bergeson, S.; Noack, M.; Park, J.-M.; Hillier, A.C.; Ho, K.-M.; Biswas, R.; Chaudhary, S. Reducing optical losses in organic solar cells using microlens arrays: Theoretical-experimental investigation of microlens dimensions. *Phys. Chem. Chem. Phys.* **2015**, *17*, 3723–3730. [CrossRef] [PubMed]
26. Shah, A.V.; Schade, H.; Vanecek, M.; Meier, J.; Vallat-Sauvain, E.; Wyrsh, N.; Kroll, U.; Droz, C.; Bailat, J. Thin-film silicon solar cell technology. *Prog. Photovolt.* **2004**, *12*, 113–142. [CrossRef]

27. Li, Z.Y.; Lin, L.L. Photonic band structures solved by a plane-wave based transfer matrix method. *Phys. Rev. E* **2003**, *67*, 046607. [CrossRef] [PubMed]
28. Biswas, R.; Neginhal, S.; Ding, C.G.; Puscasu, I.; Johnson, E. Mechanisms underlying extraordinary transmission in sub-wavelength hole arrays. *J. Opt. Soc. Am. B* **2007**, *24*, 2489–2495. [CrossRef]
29. Zhou, D.Y.; Biswas, R. Photonic crystal enhanced light-trapping in thin film solar cells. *J. Appl. Phys.* **2008**, *103*, 093102. [CrossRef]
30. Yu, Z.; Raman, A.; Fan, S. Fundamental limit of light trapping in grating structures. *Opt. Exp.* **2010**, *18*, A366–A380. [CrossRef] [PubMed]
31. Yu, Z.; Raman, A.; Fan, S. Fundamental limit of nanophotonic light trapping in solar cells. *Proc. Natl. Acad. Sci. USA* **2010**, *107*, 17491–17496. [CrossRef] [PubMed]
32. Schiff, E.A. Thermodynamic limit to photonic-plasmonic light trapping in thin films on metals. *J. Appl. Phys.* **2011**, *110*, 104501. [CrossRef]
33. Van Lare, M.; Lenzenmann, F.; Verschuuren, M.A.; Polman, A. Mode coupling by plasmonic surface scatterers in thin-film silicon solar cell. *Appl. Phys. Lett.* **2012**, *101*, 221110. [CrossRef]
34. Ferry, V.E.; Munday, J.N.; Atwater, H.A. The design considerations for plasmonic photovoltaics. *Adv. Mater.* **2010**, *22*, 4794–4808. [CrossRef] [PubMed]
35. Bernel, P.; Luo, C.; Zeng, L.; Kimerling, L.C.; Joannopoulos, J.D. Improving thin-film crystalline silicon solar cell efficiencies with photonic crystals. *Opt. Exp.* **2007**, *15*, 16986–17000. [CrossRef]
36. Zanotto, S.; Liscidini, M.; Andreani, L.C. Light trapping regimes in thin film silicon cells with a photonic pattern. *Opt. Exp.* **2010**, *18*, 4260–4274. [CrossRef] [PubMed]
37. Heine, C.; Morf, R.H. Sub-micrometer gratings for solar energy applications. *Appl. Opt.* **1995**, *34*, 2476–2482. [CrossRef] [PubMed]
38. Huang, Y.; Chattopadhyay, S.; Jen, Y.; Peng, C.; Liu, T.; Hsu, Y.; Pan, C.; Lo, H.; Hsu, C.; Chang, Y.; et al. Improved broadband and quasi-omnidirectional anti-reflection properties with biomimetic silicon nanostructures. *Nat. Nanotechnol.* **2007**, *2*, 770–774. [CrossRef] [PubMed]
39. Li, J.; Yu, H.; Li, Y.; Wang, F.; Yang, M.; Wong, S.M. Low aspect-ratio hemispherical nanopit surface texturing for enhancing light absorption in crystalline Si thin film-based solar cells. *Appl. Phys. Lett.* **2011**, *98*, 021905. [CrossRef]
40. Ok, J.G.; Youn, H.S.; Kwak, M.K.; Lee, K.; Shin, Y.J.; Guo, L.J.; Greenwald, A.; Liu, Y. Continuous and scalable fabrication of flexible metamaterial films via roll-to-roll nanoimprint process for broadband plasmonic infrared filters. *Appl. Phys. Lett.* **2012**, *101*, 223102. [CrossRef]
41. Masuko, K.; Shigematsu, M.; Hashiguchi, T.; Fujishima, D.; Kai, M.; Yoshimura, N.; Yamaguchi, T.; Ichihashi, Y.; Yamanishi, T.; Takahama, T.; et al. Achievement of more than 25% conversion efficiency with crystalline silicon heterojunction solar cell. *IEEE J. Photovolt.* **2014**, *4*, 1433–1435. [CrossRef]
42. Peer, A.; Biswas, R. Extraordinary optical transmission in nanopatterned ultrathin metal films without holes. *Nanoscale* **2016**, *8*, 4657–4666. [CrossRef] [PubMed]
43. Chen, Q.; Zhou, H.; Hong, Z.; Luo, S.; Duan, H.S.; Wang, H.H.; Liu, Y.; Li, G.; Yang, Y. Planar heterojunction perovskite solar cells via vapor-assisted solution process. *J. Am. Chem. Soc.* **2013**, *136*, 622–625. [CrossRef] [PubMed]
44. Peer, A.; Dhakal, R.; Biswas, R.; Kim, J. Nanoscale patterning of biopolymers for functional biosurfaces and controlled drug release. *Nanoscale* **2016**, *8*, 18654–18664. [CrossRef] [PubMed]
45. Kooy, N.; Mohamme, K.; Pin, L.T.; Guan, O.S. A review of roll-to-roll nanoimprint lithography. *Nanoscale Res. Lett.* **2014**, *9*, 320. [CrossRef] [PubMed]



© 2017 by the authors. Licensee MDPI, Basel, Switzerland. This article is an open access article distributed under the terms and conditions of the Creative Commons Attribution (CC BY) license (<http://creativecommons.org/licenses/by/4.0/>).

Article

# Ultraviolet Plasmonic Aluminium Nanoparticles for Highly Efficient Light Incoupling on Silicon Solar Cells

Yinan Zhang <sup>1,\*</sup>, Boyuan Cai <sup>2</sup> and Baohua Jia <sup>1,\*</sup>

<sup>1</sup> Centre for Micro-Photonics, Faculty of Science, Engineering and Technology, Swinburne University of Technology, Hawthorn, Victoria 3122, Australia

<sup>2</sup> Institute of Photonics Technology, Jinan University, Guangzhou 510632, China; caiboyuan@jnu.edu.cn

\* Correspondence: yinanzhang@swin.edu.au (Y.Z.); bjia@swin.edu.au.com (B.J.); Tel.: +61-3-9214-8879 (Y.Z.); +61-3-9214-4819 (B.J.)

Academic Editors: Guanying Chen, Zhijun Ning and Hans Agren

Received: 31 March 2016; Accepted: 18 May 2016; Published: 24 May 2016

**Abstract:** Plasmonic metal nanoparticles supporting localized surface plasmon resonances have attracted a great deal of interest in boosting the light absorption in solar cells. Among the various plasmonic materials, the aluminium nanoparticles recently have become a rising star due to their unique ultraviolet plasmonic resonances, low cost, earth-abundance and high compatibility with the complementary metal-oxide semiconductor (CMOS) manufacturing process. Here, we report some key factors that determine the light incoupling of aluminium nanoparticles located on the front side of silicon solar cells. We first numerically study the scattering and absorption properties of the aluminium nanoparticles and the influence of the nanoparticle shape, size, surface coverage and the spacing layer on the light incoupling using the finite difference time domain method. Then, we experimentally integrate 100-nm aluminium nanoparticles on the front side of silicon solar cells with varying silicon nitride thicknesses. This study provides the fundamental insights for designing aluminium nanoparticle-based light trapping on solar cells.

**Keywords:** ultraviolet plasmonics; aluminium nanoparticles; light incoupling; light trapping; solar cells

## 1. Introduction

Light management is of critical importance for constructing high efficiency solar cells. Conventionally, micro-scale textured surfaces, such as pyramid structure, have been widely employed to improve the light absorption in Si solar cells. Textured surfaces not only reduce the surface reflection by increasing the chance of the reflected light bounced back to the Si layer but also enhance the light trapping through the redirection of the incident light. Although they have been well demonstrated and applied on the commercial solar cells, they induce a few drawbacks as well. Firstly, textured surfaces increase the surface area of the solar cells, leading to an increase of the surface recombination and thus the reduction of the solar cell performance. Secondly, they increase the total volume of the depletion junction region. Thirdly, they are not suitable for the light management in ultra-thin solar cells, which have been identified as one of the most effective strategies for the cost reduction of the solar cells.

Recently, nano-scale light management strategies, particularly the plasmonic nanoparticles (NPs) and nanostructures have emerged and attracted a great deal of interest [1–3]. Metal NPs, supporting localized surface plasmons, exhibit both far-field scattering and near-field light concentration due to the collective oscillation of the free electrons in the metal [4,5]. Both effects can contribute to the light absorption enhancement of solar cells. By tuning the geometry parameters

of the NPs, the strength of light scattering/concentration and the resonance wavelength can be adjusted accordingly. Nanoparticles with a size smaller than 20 nm show strong near-field light concentration in their immediate vicinity, which can potentially enhance the light absorption in this region. However, so far, all of the thicknesses of the active layers of the solar cells are a few times larger than the near-field light concentration regions of the NPs. Therefore, the near-field light concentration is hardly able to increase the absorption of the solar cells. On the other hand, the scattering of the particles has been the main mechanism used for light absorption enhancement. Nanoparticles larger than 100 nm show strong scattering strength. Once they are placed on the surface of the solar cells, light will be preferentially scattered into the high-index substrates. This increases the photon absorption in solar cells in at least two ways. Firstly, the preferential scattering reduces the light reflection due to the optical impedance matching, leading to an enhanced light incoupling into the solar cell. Secondly, light is redistributed inside the solar cells as a result of the scattering, leading to an increased light path length, which is particularly useful for the weakly absorbed near-bandgap energy.

At the early stage of the plasmonic solar cell research, the noble metal Ag and Au NPs were widely studied and demonstrated to be effective in trapping the near bandgap energy due to higher radiative efficiency [6–25]. However, a transmission reduction is always found at the short wavelength of the usable solar spectrum (300–1200 nm) due to the Fano effect, *i.e.*, the destructive interference between the incident light and the scattered modes at the wavelengths below the surface plasmon resonances (SPRs) [26]. Furthermore, the noble metal Ag and Au are expensive, limiting their real-life applications. Al NPs, with their SPRs spanning from visible to ultraviolet region, can potentially blueshift this reduction away from the usable solar spectrum, thereby leading to a broadband light incoupling [27–30]. Together with the low cost, earth-abundance, and their high compatibility with the complementary metal-oxide semiconductor (CMOS) manufacturing process, Al NPs hold great promises for the next-generation plasmonic solar cells. It should be mentioned here that embedding the NPs in a thin dielectric layer can also avoid this detrimental Fano effect, providing another way to mitigate this light incoupling reduction at the short wavelengths [31].

So far, Al NPs have been applied to many types of solar cells, such as Si wafer solar cells [32], thin-film GaAs solar cells [33], thin-film Si solar cells [34,35], GaInP/GaInAs/Ge triple junction solar cells [36], dye-sensitized solar cells [37], and organic solar cells [38], making them a rising star in this field. However, there is no systemic study on the critical parameters of the Al NP array, which is of importance in designing and optimizing their light incoupling. Here, in this paper, we report some key factors that determine the light incoupling by the Al NPs located on the front side of Si solar cells. Figure 1 schematically shows the structure of the solar cells, consisting of the Al NPs, the  $\text{SiN}_x$  spacing layer, and the Si layer. We first numerically study the scattering and absorption properties of the Al NPs and the influence of the NP shape, size, surface coverage, and the spacing layer on the light incoupling using the finite difference time domain (FDTD) method. Followed this, we experimentally integrate 100-nm Al NPs on the front side of Si solar cells with varying  $\text{SiN}_x$  spacing layer thicknesses.

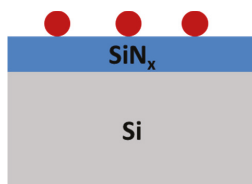


**Figure 1.** Schematic diagram of the investigated solar cell structure, consisting of the Al nanoparticles (NPs), the  $\text{SiN}_x$  spacing layer, and the Si layer with the red spheres representing the metal NPs.

## 2. Results and Discussion

### 2.1. Broadband Light Incoupling by Al NPs

To investigate the light incoupling properties, it is important to understand the scattering and absorption properties of the Al NPs in comparison to other widely used metal NPs, including Ag and Au. Figure 2a,b illustrate the normalized scattering and absorption cross sections of the three types of metal NPs (100-nm diameter) on top of a Si layer, with the arrows indicating their dipole resonance wavelengths. Clearly, the SPRs of the Ag and Au NPs both lie in the visible ranges at around 400 nm and 550 nm, respectively, whereas the Al NP shows an ultraviolet resonance at around 300 nm. The absorption cross sections of the NPs (Figure 2b) demonstrate an associated absorption loss, particularly at the resonance region. It should be noted that the slightly large absorption at around 800 nm for Al NPs is introduced by the interband transition.

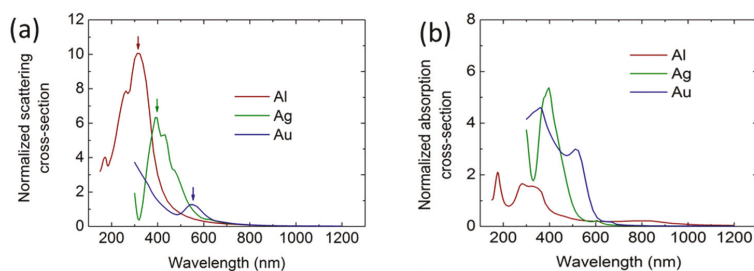


**Figure 2.** Calculated normalized scattering (a) and absorption (b) cross sections of the Al NPs with a 100-nm diameter on top of a Si layer, in comparison with Ag and Au NPs.

To demonstrate the superiority of the Al NPs in light incoupling, we simulated the light transmittance into the solar cells integrated with an ordered periodic NP array with a 100-nm diameter and 10% surface coverage (280-nm pitch) for all the three materials: Al, Ag, and Au. In an ordered array, far-field diffraction occurs, leading to a redistribution of the scattered light and change of the light incoupling spectra, whereas the total scattering and incoupling of the NPs in a random array is generally the sum of that for each NP, provided that the surface coverage is low enough [23]. Figure 3a shows the normalized transmittance of the solar cell integrated with NPs. As can be seen, the light transmittance into Si has been increased at wavelengths above the SPRs for Ag and Au NPs, with the largest enhancement up to 43% at 510 nm and 26% at 600 nm, respectively. However, at short wavelengths, the light transmittance has been largely reduced. For Al NPs, the light transmittance has been increased among the entire wavelengths from 300 to 1200 nm without any reduction, demonstrating a broadband light incoupling enhancement. Figure 3b shows that Al NPs also perform better in terms of loss control at the wavelengths below 600 nm, except at around 800 nm with a minor absorption.

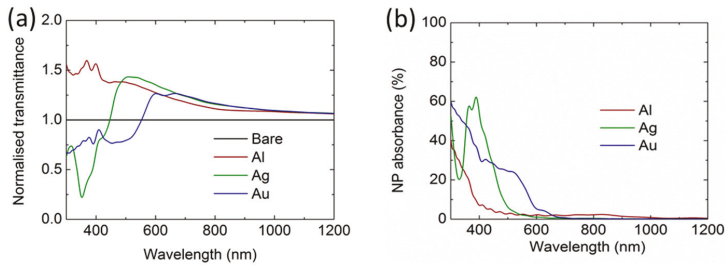


**Figure 3.** (a) Calculated normalized light transmittance of Si solar cells integrated with an array of Al NPs (100-nm diameter and 10% surface coverage), compared with the Si solar cells integrated with Ag and Au NPs. (b) Calculated absorption losses in the NP arrays.

### 2.2. Shape Study of the Al NPs

We have demonstrated that the Al NPs show broadband light incoupling, compared with Ag and Au NPs. In this section, we study the influence of the shape of the Al NPs on the light incoupling in the Si wafer solar cells. We simulated the light transmittance of a Si wafer with an ordered hemispherical (100-nm diameter) and cubic (100-nm width) Al NP array with 10% surface coverage, with the results shown in Figure 4. It is remarkable and interesting that the transmittance of the Si wafer with the hemispherical and cubic Al NPs reduces at the longer wavelengths (Figure 4a), compared with that of the bare Si wafer, which is attributed to the redshifts of the Fano resonance for the dipole scattering modes. To understand this, we calculated the scattering cross sections of the hemispherical and cubic Al NP on top of a Si layer, as shown in Figure 4b. Clearly, the dipole resonance shifts to around 1050 nm and 960 nm for the hemispherical and cubic NPs due to the large contact area between the NPs and the high index Si substrate. Therefore, the light incoupling reduction shifts to the long wavelengths. This is distinct from the broadband light incoupling of the 100-nm spherical Al NPs with only a point contact with the Si layers.

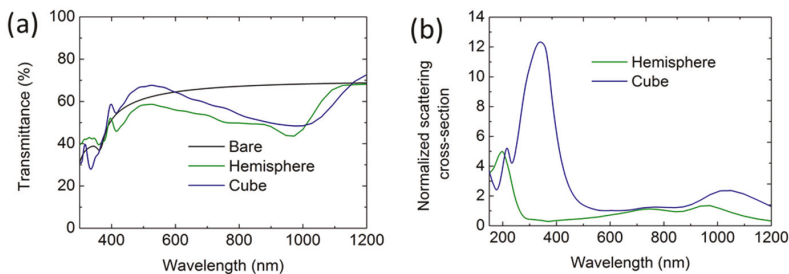


**Figure 4.** (a) Calculated transmittance of the Si solar cells with an array of hemispherical and cubic Al NPs (100-nm diameter/width and 10% surface coverage), referenced to that of a bare Si layer. (b) Calculated normalized scattering cross sections of the corresponding Al NPs on top of the Si layer.

### 2.3. Size and Surface Coverage Effect

Since spherical Al NPs have been demonstrated to be more effective in light incoupling than the other shapes, this section studies the two key parameters in optimizing the spherical Al NP array, *i.e.*, the diameter and the surface coverage. Before investigating their influence on the light incoupling, we calculated the scattering and absorption of the Al NPs with different sizes. Figure 5a,b give the normalized scattering and absorption cross sections of the spherical Al NPs with varying diameters. As can be seen, the dipole resonance scattering (indicated with arrows) redshifts and broadens when the

particle size increases. At the same time, higher order resonances are excited at the short wavelengths and also redshift. For the absorption, it is found that the interband absorption peaks at around 200 nm do not shift, but the strength reduces when the particle size increases. However, the absorption at around 800 nm increases when the particle size increases, which is distinct from the phenomena observed in the widely used Ag and Au NPs. This is possibly due to the fact that the dipole resonances shift to this region, leading to a resonance-related near-field light confinement, which overlays onto the interband absorption of the Al NPs.

Figure 6a,b present the light transmittance of the Si solar cells integrated with an array of Al NPs under the configurations of varying diameter at 10% surface coverage and increasing surface coverage from 10% to 70% for a 100-nm particle size. Compared with 100-nm Al NPs, 200-nm and 300-nm Al NPs induce a transmission reduction region at short wavelengths due to the redshifts of the dipole scattering-related Fano resonance (Figure 5a). However, the transmission becomes larger at the longer wavelengths owing to the increased scattering cross section when the particle size increases. With the surface coverage increasing, the transmission increases at first and then decreases, reaching a maximum value (>90%) at 600 nm for 40% surface coverage. When the surface coverage increases beyond 40%, the particle interplay becomes severe, leading to redshifts of the dipole scattering modes; therefore, the Fano resonance-related transmission reduction occurs. The optimization of the size and the surface coverage would be a result of the spectra shifts matching the peak intensity of the standard AM1.5G solar photon fluxes. The optimized enhancement could be around 28.7% for the Al NPs under the configuration of a 150-nm diameter and 30% surface coverage. By further tuning the particle height and width, the enhancement can be as high as 30%. This is far higher than that induced by the optimized Ag (27.2%) and Au (14.5%) NPs.

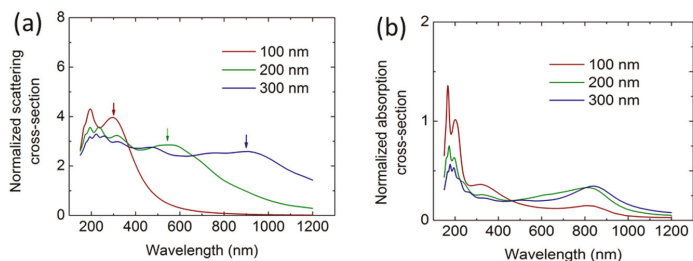


**Figure 5.** Calculated normalized scattering (a) and absorption (b) cross sections of the Al NPs in the air with 100-nm, 200-nm and 300-nm diameters, respectively.

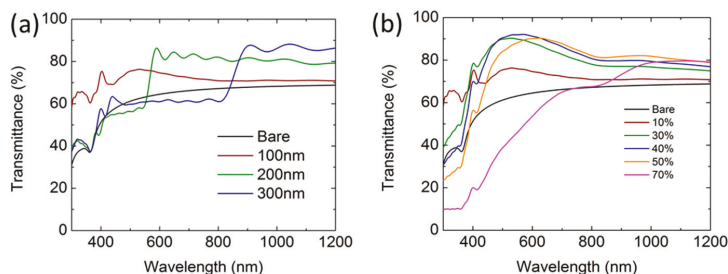


**Figure 6.** Calculated light transmittance into the Si wafer under the configurations of (a) varying diameter at 10% surface coverage and (b) increasing surface coverage from 10% to 70% for a 100-nm particle size.



#### 2.4. Study on the Thickness of SiN<sub>x</sub> Spacing Layer

The spacing layer between the Al NPs and the Si layer plays an important role in determining the incoupling efficiency induced by the Al NPs since it affects the distance between the excited dipole moment in the NPs and the underlying substrate. This section gives some study on the influence of the spacing layer thickness on the Al NPs incoupling, using the SiN<sub>x</sub> spacing layer as an example. The light transmittance into the Si layer by the Al NP array, using an example configuration of a 100-nm diameter and 10% surface coverage, was calculated with varying thicknesses of the SiN<sub>x</sub> layer from 20 nm to 120 nm. Figure 7a shows the transmittance spectra of the Si wafer integrated with the Al NPs on top of 20-nm SiN<sub>x</sub>. As shown, the 20-nm SiN<sub>x</sub> boosts the transmittance across the entire wavelength band from 300 nm to 1200 nm. It acts as an antireflection layer, making use of the destructive interference between the reflected light from the air/SiN<sub>x</sub> and SiN<sub>x</sub>/Si interfaces. By adding the Al NPs, the transmittance is further increased, with an enhancement up to 25% at the wavelength around 400 nm compared with that of the solar cells with 20-nm SiN<sub>x</sub> solely. Figure 7b gives the integrated transmittance at different thicknesses of SiN<sub>x</sub> layer by weighting the transmittance to the AM1.5G solar photon fluxes. Clearly, as the SiN<sub>x</sub> thickness increases from 20 nm to 120 nm, the integrated transmittance firstly increases and then reduces, reaching a maximum transmittance at 80-nm SiN<sub>x</sub> for both the cells with and without NPs. However, the enhancement (the ratio of the integrated transmittance of the solar cells with NPs to that without NPs) reduces from around 12% to 2%, as shown in the inset of Figure 7b, demonstrating that thicker spacing layer reduces the light incoupling efficiency.

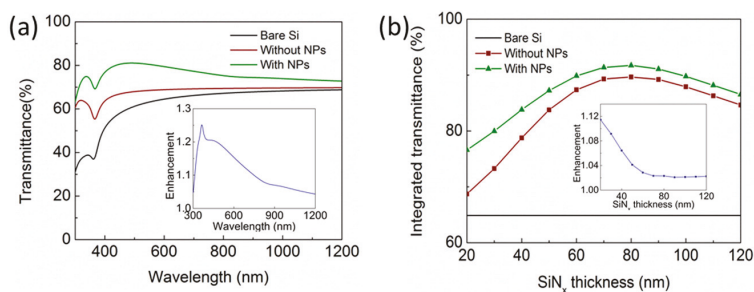


**Figure 7.** (a) Calculated light transmittance spectra of the Si wafer integrated with the Al NP array (100-nm diameter and 10% surface coverage) on top of the 20-nm SiN<sub>x</sub>, referenced to that without Al NPs and the bare Si. (b) Calculated integrated light transmittance of the Si wafer with the Al NPs as a function of the SiN<sub>x</sub> spacing layer thickness. The inset figures show the relative enhancement.

#### 2.5. Experimental Demonstration

As a demonstration, we experimentally fabricated the Al and Ag NPs with a 100-nm average size and integrated them on the front side of the bare Si solar cells by the spray-coating method. Before the integration, we measured their morphologies and optical properties. Figure 8a,b present the scanning electron images (SEMs) of the prepared Al and Ag NPs, with their extinction spectra shown in Figure 8c,d, respectively. As shown, the particles are randomly distributed on the surface of the Si and aggregate in some regions, which slightly affects the particle resonances and the light incoupling. The SPRs for Al and Ag NPs lie in below 300 nm and around 400 nm, respectively, which agree well with the above-mentioned simulation.

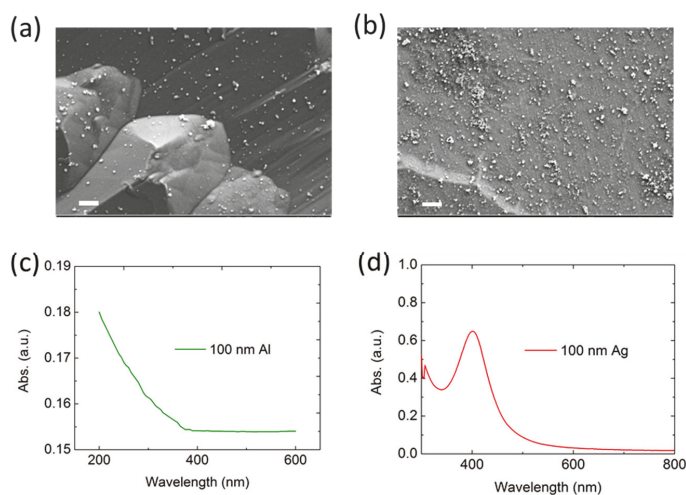


**Figure 8.** Scanning electron images (SEM) of the fabricated Al (a) and Ag (b) NPs (Scale bar: 1 μm). The UV-VIS-NIR spectra of the Al (c) and Ag (d) NPs in deionized water solution.

Figure 9a,b show the reflectance and the normalized external quantum efficiency (EQE) of the solar cells integrated with Al and Ag NPs without the SiN<sub>x</sub> layer, respectively. It is noted that the reflectance for both solar cells reduces among the entire wavelength region. However, the EQE enhancement for the Al NPs is broadband over the entire spectrum with an enhancement up to 40% at the short wavelengths, whereas that for the Ag NPs is found to reduce at the short wavelengths below 400 nm. This agrees well with the simulated light transmittance shown in Figure 3a. Then, the Al NPs were integrated on the front surface of the solar cells with various SiN<sub>x</sub> thicknesses at 20 nm, 40 nm, 60 nm, and 80 nm, respectively. The EQE results and the corresponding photocurrent density are shown in Figure 10a,b, respectively. As can be seen, the EQE is increased among the entire wavelengths from 300 nm to 1200 nm, even with a 20-nm-thick SiN<sub>x</sub> layer, agreeing well with the light transmittance shown in Figure 7a. Accordingly, the photocurrent was increased from 26.2 mA/cm<sup>2</sup> to 28.3 mA/cm<sup>2</sup>, representing an enhancement of 8%. In Figure 10b, the photocurrents of the solar cells integrated with and without Al NPs both increase when the SiN<sub>x</sub> thickness increases from 20 nm to 80 nm. However, the enhancement induced by the Al NPs shown in the inset figure shows a saturated trend due to a reduced light coupling. The largest photocurrent achieved is 36 mA/cm<sup>2</sup> with Al NPs on top of the 80-nm-thick SiN<sub>x</sub> layer.

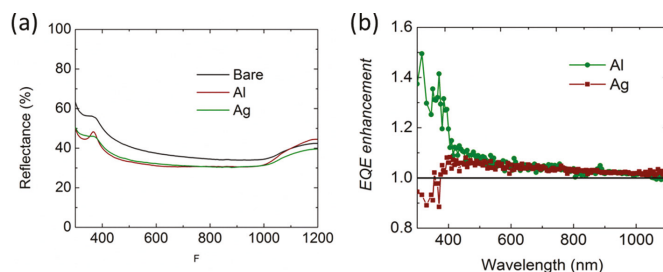


**Figure 9.** (a) Measured reflectance of the Si solar cells integrated with Al and Ag NPs. (b) Measured external quantum efficiency (EQE) enhancement of the solar cells integrated with Al and Ag NPs, relative to that without NPs.

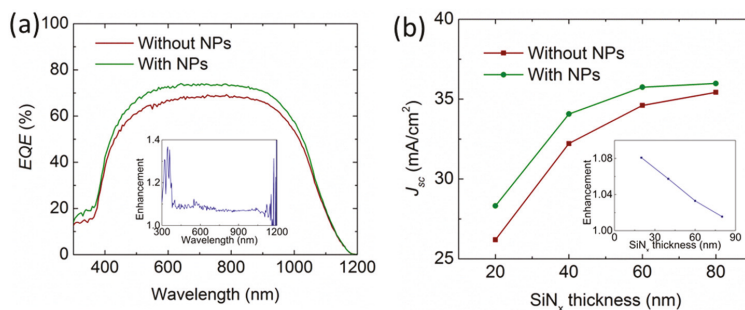


**Figure 10.** (a) Measured EQE of the solar cells with the Al NPs on top of a 20-nm SiN<sub>x</sub> spacing layer, compared with that without Al NPs. (b) The corresponding photocurrent density as a function of the SiN<sub>x</sub> layer thickness. The inset figures are the relative enhancement.

### 3. Materials and Methods

#### 3.1. Numerical Simulations

Lumerical FDTD solutions (Lumerical Solutions, Inc., Vancouver, Canada) was employed to perform the optical simulation. For the scattering/absorption cross-section calculation, a 3-D total-field scattered-field (TFSF) source from 300 nm to 1200 nm was used to surround a NP. Two analysis groups, comprising 6 transmission monitors for each group in 3-D, were placed inside and outside the light source box, respectively. The inside and outside groups obtain the absorption power and the scattering power, respectively. The boundary conditions were set as the perfect matcher layers (PMLs) to prevent the scattering light bouncing back to the NPs from the boundaries, leading to an interference effect. For the light incoupling calculation, a spherical NP was placed on the surface of a planar Si slab with and without a SiN<sub>x</sub> spacing layer and illuminated under a 300–1200-nm plane wave source weighted against the AM1.5G solar spectrum. PML boundary conditions were used in the incident direction to prevent an interference effect, and periodic boundary conditions (PBCs) were used in the lateral direction to simulate an ordered array of NPs.

#### 3.2. NP Fabrication and Characterization

Due to the strong activeness of the Al NPs, which can be easily oxidized, it is challenging to synthesize Al NPs using the conventional chemical reduction method. To overcome this challenge, we developed a novel fabrication process based on the conventional thermal evaporation and annealing process. An ultra-thin Al film, with a few nanometers in thickness, was evaporated on the NaCl powder substrate, followed by a high temperature annealing process. Then, the powder was dissolved in the deionized water, and the Al NPs were separated from the water solution by centrifugation. The particle size can be adjusted by tuning the thickness of the Al film and the annealing condition. In this paper, 10-nm Al film was evaporated and annealed in a nitrogen atmosphere at 400 °C to form the Al NPs with the desired size (around 100 nm in diameter). As a remark, the Al itself is easy to be oxidized, leading to a thin layer of alumina on the surface of the Al NPs, preventing it from being further oxidized. This thin layer of alumina is only a few nanometers, as shown in [29], and would not affect the optical properties of the Al NPs much. For the purpose of comparison, we also synthesized 100-nm Ag NPs by the NaBH<sub>4</sub> reduction of silver nitrate solution [39]. A 5-mL deionized water solution with 5 mM AgNO<sub>3</sub> and 5 mM sodium citrate were prepared. Next, the suspension was subjected to the sonication. A 0.6-mL portion of 50 mM freshly prepared NaBH<sub>4</sub> was injected quickly at room temperature, followed by 30 s of sonication. Then, the solution was centrifuged at 5000 rpm for 10 min, and the supernatant was removed and the precipitate, containing the Ag NPs was redispersed in deionized

water. The UV-VIS-IR spectrum of the NPs in the solution was measured by the spectrophotometer (Lambda 1050, PerkinElmer, Waltham, MA, USA).

### 3.3. Solar Cell Fabrication and Characterization

The planar Si solar cells were fabricated by the following processes. 200- $\mu\text{m}$  thick Si wafers with resistivities around 1–3  $\Omega\cdot\text{cm}$  were used. Firstly, the saw-damaged surface of the wafer with around 20  $\mu\text{m}$  were etched off by dipping the wafers into the  $\text{HNO}_3/\text{HF}$  solution. After the standard RCA cleaning (as developed at Radio Corporation of America) process, the  $n^+$  emitters were formed by a phosphorus diffusion process using the  $\text{POCl}_3$  source at the temperature around 850  $^\circ\text{C}$ . The phosphosilicate glass introduced by the diffusion process was removed by the HF solution. Then, Al paste was screen printed on the rear surface and fired at a temperature around 800  $^\circ\text{C}$  for a few seconds to form the back surface field (BSF) and the back contact. An Al front contact grid was formed by the photolithography. After that, the  $\text{SiN}_x$  ARC was deposited by the plasmon-enhanced chemical vapour deposition (PECVD) system at 350  $^\circ\text{C}$ . The EQE of the solar cells was measured across 300–1200 nm using PV Measurements QEX10 (PV Measurements, Boulder, CO, USA). The photocurrent density was calculated by integrating the EQE to the AM1.5G solar photon fluxes.

## 4. Conclusions

In conclusion, we have demonstrated highly efficient light incoupling by Al NPs and have revealed the key factors that determine the incoupling efficiency, including the shape, size, surface coverage, and the spacing layer through numerical simulation. Furthermore, we experimentally compared the performance of the Si solar cells integrated with and without the Al NPs on top of the  $\text{SiN}_x$  spacing layer at varying thicknesses.

**Acknowledgments:** Baohua Jia thanks the Australia Research Council for its support (DP150102972).

**Author Contributions:** Y.Z. and B.J. conceived and designed the simulations and experiments; Y.Z. performed the simulations and experiments; Y.Z., B.C. and B.J. analyzed the data; Y.Z. wrote the paper, B.C. and B.J. revised the paper.

**Conflicts of Interest:** The authors declare no conflict of interest.

## References

1. Atwater, H.A.; Polman, A. Plasmonics for improved photovoltaic devices. *Nat. Mater.* **2010**, *9*, 205–213. [CrossRef] [PubMed]
2. Green, M.A.; Pillai, S. Harnessing plasmonics for solar cells. *Nat. Photonics* **2012**, *6*, 130–132. [CrossRef]
3. Pillai, S.; Green, M.A. Plasmonics for photovoltaic applications. *Sol. Energy Mater. Sol. Cells* **2010**, *94*, 1481–1486. [CrossRef]
4. Kelly, K.L.; Coronado, E.; Zhao, L.L.; Schatz, G.C. The Optical Properties of Metal Nanoparticles: The Influence of Size, Shape, and Dielectric Environment. *J. Phys. Chem. B* **2003**, *107*, 668–677. [CrossRef]
5. Maier, S.A.; Atwater, H.A. Plasmonics: Localization and guiding of electromagnetic energy in metal/dielectric structures. *J. Appl. Phys.* **2005**, *98*, 11101–11110. [CrossRef]
6. Catchpole, K.R.; Polman, A. Plasmonic solar cells. *Opt. Express* **2008**, *16*, 21793–21800. [CrossRef] [PubMed]
7. Catchpole, K.R.; Polman, A. Design principles for particle plasmon enhanced solar cells. *Appl. Phys. Lett.* **2008**, *93*, 191113–191113. [CrossRef]
8. Akimov, Y.A.; Koh, W.S.; Ostrikov, K. Enhancement of optical absorption in thin-film solar cells through the excitation of higher-order nanoparticle plasmon modes. *Opt. Express* **2009**, *17*, 10195–10205. [CrossRef] [PubMed]
9. Beck, F.J.; Polman, A.; Catchpole, K.R. Tunable light trapping for solar cells using localized surface plasmons. *J. Appl. Phys.* **2009**, *105*. [CrossRef]
10. Mokkaapati, S.; Beck, F.J.; Polman, A.; Catchpole, K.R. Designing periodic arrays of metal nanoparticles for light-trapping applications in solar cells. *Appl. Phys. Lett.* **2009**, *95*. [CrossRef]

11. Beck, F.J.; Mokkaapati, S.; Catchpole, K.R. Plasmonic light-trapping for Si solar cells using self-assembled, Ag nanoparticles. *Prog. Photovolt. Res. Appl.* **2010**, *18*, 500–504. [CrossRef]
12. Haggglund, C.; Zach, M.; Petersson, G.; Kasemo, B. Electromagnetic coupling of light into a silicon solar cell by nanodisk plasmons. *Appl. Phys. Lett.* **2008**, *92*. [CrossRef]
13. Moulin, E.; Sukmanowski, J.; Luo, P.; Carius, R.; Royer, F.X.; Stiebig, H. Improved light absorption in thin-film silicon solar cells by integration of silver nanoparticles. *J. Non-Cryst. Solids* **2008**, *354*, 2488–2491. [CrossRef]
14. Moulin, E.; Sukmanowski, J.; Schulte, M.; Gordijn, A.; Royer, F.X.; Stiebig, H. Thin-film silicon solar cells with integrated silver nanoparticles. *Thin Solid Films* **2008**, *516*, 6813–6817. [CrossRef]
15. Henson, J.; DiMaria, J.; Paiella, R. Influence of nanoparticle height on plasmonic resonance wavelength and electromagnetic field enhancement in two-dimensional arrays. *J. Appl. Phys.* **2009**, *106*, 93111–93116. [CrossRef]
16. Eminian, C.; Haug, F.J.; Cubero, O.; Niquille, X.; Ballif, C. Photocurrent enhancement in thin film amorphous silicon solar cells with silver nanoparticles. *Prog. Photovolt. Res. Appl.* **2011**, *19*, 260–265. [CrossRef]
17. Qu, D.; Liu, F.; Yu, J.; Xie, W.; Xu, Q.; Li, X.; Huang, Y. Plasmonic core-shell gold nanoparticle enhanced optical absorption in photovoltaic devices. *Appl. Phys. Lett.* **2011**, *98*, 113119–113113. [CrossRef]
18. Spinelli, P.; Hebbink, M.; de Waele, R.; Black, L.; Lenzmann, F.; Polman, A. Optical Impedance Matching Using Coupled Plasmonic Nanoparticle Arrays. *Nano Lett.* **2011**, *11*, 1760–1765. [CrossRef] [PubMed]
19. Ho, W.; Su, S.; Lee, Y.; Syu, H.; Lin, C. Performance-Enhanced Textured Silicon Solar Cells Based on Plasmonic Light Scattering Using Silver and Indium Nanoparticles. *Materials* **2015**, *8*, 6668–6676. [CrossRef]
20. Lare, M.; Lenzmann, F.; Verschuuren, M.; Polman, A. Mode coupling by plasmonic surface scatters in thin-film silicon solar cells. *Appl. Phys. Lett.* **2012**, *101*, 221110. [CrossRef]
21. Dao, V.; Choi, H. Highly-Efficient Plasmon-Enhanced Dye-Sensitized Solar Cells Created by Means of Dry Plasma Reduction. *Nanomaterials* **2016**, *6*. [CrossRef]
22. Yu, J.; Shao, W.; Zhou, Y.; Wang, H.; Liu, X.; Xu, X. Nano Ag-enhanced energy conversion efficiency in standard commercial pc-Si solar cells and numerical simulations with finite difference time domain method. *Appl. Phys. Lett.* **2013**, *103*. [CrossRef]
23. Temple, T.; Bagnall, D. Broadband scattering of the solar spectrum by spherical metal nanoparticles. *Prog. Photovolt. Res. Appl.* **2012**, *21*, 600–611. [CrossRef]
24. Temple, T.; Bagnall, D. Optical properties of gold and aluminium nanoparticles for silicon solar cell applications. *J. Appl. Phys.* **2011**, *109*. [CrossRef]
25. Cai, B.; Li, X.; Zhang, Y.; Jia, B. Significant light absorption enhancement in silicon thin film tandem solar cells with metallic nanoparticles. *Nanotechnology* **2016**, *27*. [CrossRef] [PubMed]
26. Lukyanchuk, B.; Zheludev, N.I.; Maier, S.A.; Halas, N.J.; Nordlander, P.; Giessen, H.; Chong, C.T. The Fano resonance in plasmonic nanostructures and metamaterials. *Nat. Mater.* **2010**, *9*, 707–715. [CrossRef] [PubMed]
27. Ekinci, Y.; Solak, H.H.; Löffler, J.F. Plasmon resonances of aluminum nanoparticles and nanorods. *J. Appl. Phys.* **2008**, *104*. [CrossRef]
28. Knight, M.W.; King, N.S.; Liu, L.; Everitt, H.O.; Nordlander, P.; Halas, N.J. Aluminum for Plasmonics. *ACS Nano* **2014**, *8*, 834–840. [CrossRef] [PubMed]
29. Langhammer, C.; Schwind, M.; Kasemo, B.; Zorić, I. Localized Surface Plasmon Resonances in Aluminum Nanodisks. *Nano Lett.* **2008**, *8*, 1461–1471. [CrossRef] [PubMed]
30. Maidecchi, G.; Gonella, G.; Zaccaria, R.P.; Moroni, R.; Anghinolfi, L.; Giglia, A.; Nannarone, S.; Mattered, L.; Dai, H.-L.; Canepa, M.; *et al.* Deep Ultraviolet Plasmon Resonance in Aluminum Nanoparticle Arrays. *ACS Nano* **2013**, *7*, 5834–5841. [CrossRef] [PubMed]
31. Powell, A.; Wincott, M.; Watt, A.; Assender, H.; Smith, J. Controlling the optical scattering of plasmonic nanoparticles using a thin dielectric layer. *J. Appl. Phys.* **2013**, *113*, 184311. [CrossRef]
32. Villesen, T.; Uhrenfeldt, C.; Johansen, B.; Larsen, A. Self-assembled Al nanoparticles on Si and fused silica, and their application for Si solar cells. *Nanotechnology* **2013**, *24*. [CrossRef] [PubMed]
33. Hylton, N.P.; Li, X.F.; Giannini, V.; Lee, K.-H.; Ekins-Daukes, N.J.; Loo, J.; Vercrucysse, D.; van Dorpe, P.; Sodabanlu, H.; Sugiyama, M.; *et al.* Loss mitigation in plasmonic solar cells: Aluminium nanoparticles for broadband photocurrent enhancements in GaAs photodiodes. *Sci. Rep.* **2013**, *3*. [CrossRef] [PubMed]
34. Akimov, Y.; Koh, W. Design of Plasmonic Nanoparticles for Efficient Subwavelength Light Trapping in Thin-Film Solar Cells. *Plasmonics* **2011**, *6*, 155–161. [CrossRef]

35. Akimov, Y.; Koh, W. Resonant and nonresonant plasmonic nanoparticle enhancement for thin-film silicon solar cells. *Nanotechnology* **2010**, *21*. [CrossRef] [PubMed]
36. Yang, L.; Pillai, S.; Green, M.A. Can plasmonic Al nanoparticles improve absorption in triple junction solar cells? *Sci. Rep.* **2015**, *5*, 11852. [CrossRef] [PubMed]
37. Xu, Q.; Liu, F.; Liu, Y.; Meng, W.; Cui, K.; Feng, X.; Zhang, W.; Huang, Y. Aluminum plasmonic nanoparticles enhanced dye sensitized solar cells. *Opt. Express* **2014**, *22*, A301–A310. [CrossRef] [PubMed]
38. Kochergin, V.; Neely, L.; Jao, C.-Y.; Robinson, H.D. Aluminum plasmonic nanostructures for improved absorption in organic photovoltaic devices. *Appl. Phys. Lett.* **2011**, *98*. [CrossRef]
39. Orbaek, A.W.; McHale, M.M.; Barron, A.R. Synthesis and Characterization of Silver Nanoparticles for an Undergraduate Laboratory. *J. Chem. Educ.* **2015**, *92*, 339–344. [CrossRef]



© 2016 by the authors. Licensee MDPI, Basel, Switzerland. This article is an open access article distributed under the terms and conditions of the Creative Commons Attribution (CC BY) license (<http://creativecommons.org/licenses/by/4.0/>).



Article

# Investigating the Effect of Carbon Nanotube Diameter and Wall Number in Carbon Nanotube/Silicon Heterojunction Solar Cells

Tom Grace <sup>1</sup>, LePing Yu <sup>1</sup>, Christopher Gibson <sup>1</sup>, Daniel Tune <sup>1,2</sup>, Huda Alturaif <sup>3</sup>, Zeid Al Othman <sup>3</sup> and Joseph Shapter <sup>1,\*</sup>

<sup>1</sup> Centre for Nanoscale Science & Technology (CNST), Flinders University of South Australia, South Australia 5042, Australia; tom.grace@flinders.edu.au (T.G.); leping.yu@flinders.edu.au (L.Y.); christopher.gibson@flinders.edu.au (C.G.); daniel.tune@flinders.edu.au (D.T.)

<sup>2</sup> Institute of Nanotechnology, Karlsruhe Institute of Technology, 76021 Karlsruhe, Germany

<sup>3</sup> Advanced Material Research Chair, Chemistry Department, College of Science, King Saud University, Riyadh 11451, Saudi Arabia; h.a.alturaif@hotmail.com (H.A.); zaothman@ksu.edu.sa (Z.A.O.)

\* Correspondence: joe.shapter@flinders.edu.au; Tel.: +61-8-8201-2005

Academic Editors: Guanying Chen, Zhijun Ning and Hans Agren

Received: 14 February 2016; Accepted: 11 March 2016; Published: 22 March 2016

**Abstract:** Suspensions of single-walled, double-walled and multi-walled carbon nanotubes (CNTs) were generated in the same solvent at similar concentrations. Films were fabricated from these suspensions and used in carbon nanotube/silicon heterojunction solar cells and their properties were compared with reference to the number of walls in the nanotube samples. It was found that single-walled nanotubes generally produced more favorable results; however, the double and multi-walled nanotube films used in this study yielded cells with higher open circuit voltages. It was also determined that post fabrication treatments applied to the nanotube films have a lesser effect on multi-walled nanotubes than on the other two types.

**Keywords:** carbon nanotubes; solar cells; carbon nanotube (CNT)/Si heterojunction solar cells; double-walled carbon nanotube (DWCNT); multi-walled carbon nanotubes (MWCNT)

## 1. Introduction

The search for efficient, low-cost renewable energy sources is one of great importance in the modern world. As the conventional fossil fuel sources of electricity become scarcer, and are discovered to cause severe problems for our planet's climate, it becomes all the more imperative to seek out new and innovative ways of exploiting sustainable resources.

Solar energy is the quintessential sustainable resource, however there are some significant disadvantages of current commercial solar cells. Firstly, silicon solar panels have a high manufacturing cost due to the need for high purity, processed silicon to produce high efficiency solar panels. While other semiconducting materials may be used in photovoltaic (PV) devices, they will generally consist of alloys of rare and/or toxic elements such as arsenic, cadmium, indium, gallium, germanium and ruthenium [1]. Innovations in PV technologies are making solar cells more and more competitive. Some methods of improving the economic viability of solar capture technology involve investigating solar cells containing organic molecules, quantum dots, or dye-sensitized solar cells [2]. However, this paper investigates a cell design that combines the already established good solar properties of silicon with an inexpensive material, namely carbon nanotubes (CNTs). Carbon nanotubes are considered to be an exciting prospect for solar cell integration due to a wide range of unique and interesting properties, such as; high charge carrier mobilities, ballistic transport properties,



high optical transmittance, low light reflectance [3–5], and photoelectrochemical effects under light irradiation [3,5–9]. In addition, there are many different types of nanotubes to choose from with a wide array of possible bandgaps, thus the bandgap can be “tuned” for the situation. CNTs are also highly resistant to damage, whether it be mechanical, chemical or radiation induced [7]. Coupled with their potential low cost due to the abundance of carbon [4] and the miniscule quantities of material required in applications, it is clear why they are an exciting material for research. Solar cells consisting of a heterogeneous junction (heterojunction) between a (generally n-doped) silicon substrate and a CNT film have been shown to be an appealing prospect for the future of solar energy capture technologies.

In 2007, Wei *et al.* designed a new kind of cell in which CNTs function not only as transport charge carriers, but also assist in exciton separation [10–13], using double-walled CNTs (DWCNTs) deposited via water expansion and aqueous film transfer of an as grown chemical vapor deposition (CVD) film [11,12]. While these cells had a power conversion efficiency of only 1.3% (compared to commercial silicon cells at generally 13%–25%) [14,15] many improvements have since been made to the cell design and doping methods, with 15% efficiencies reported in 2012 [2] and 17% efficiencies reported in 2015 [6,16]. Although, for the most part, these efficiencies could only be achieved via the use of an anti-reflection coating on the surface of the solar cell, with the 15% value achieved by depositing a TiO<sub>2</sub> layer over a solar cell which previously achieve efficiencies of around 8% and the 17% efficiency was achieved through the use of a molybdenum oxide layer on a solar cell design with an intrinsic efficiency of 11.1%. In terms of solar cell intrinsic efficiencies, without an anti-reflection layer, the highest in 2013 was 11.5% [17], which was improved to a record high intrinsic efficiency of 13.85% in 2015 [18]. Thus, in less than a decade the cell efficiency has been improved by a factor of 10. This rapid improvement is one of the reasons for much excitement around this solar cell design. In addition, these cells are interesting for future research as their manufacturing process is both simple and scalable [10]. The typical architecture for these solar cells is much like that of a single junction crystalline silicon solar cell with the emitter layer replaced by a film of p-doped CNTs [11]. While Wei's initial design used DWCNTs, most studies have since used single-walled carbon nanotubes (SWCNTs), and multi-walled carbon nanotubes (MWCNTs) may also be used [10,19]. In all of these cases, the CNT film acts as a component of the heterojunction to enable charge separation, as a highly conductive network for charge transport and as a transparent electrode to allow good light illumination and charge collection [10].

Li *et al.* [20] found that post-fabrication treatment of a SWCNT layer with the *p*-type dopant thionyl chloride (SOCl<sub>2</sub>) increased the power conversion efficiency of the cells by over 45% by lowering the sheet resistance, and increasing the short circuit current density ( $J_{SC}$ ) and open circuit voltage. Hall Effect measurements showed that the SOCl<sub>2</sub> treatment led to an increase of carrier density from  $3.1 \times 10^{15}$  to  $4.6 \times 10^{17}$  cm<sup>-2</sup> and an improvement from 0.23 to 1.02 cm<sup>2</sup> V<sup>-1</sup> s<sup>-1</sup> of the effective mobilities [11,20]. In addition, it was found that SOCl<sub>2</sub> treatment adjusted the Fermi level and shifted the major conduction mechanism in the SWCNT layer from hopping towards tunneling [21,22].

Jia *et al.* [23] performed the first comparison between SWCNTs, DWCNTs and MWCNTs for use in CNT/Si cells in terms of area density of the films. It was found that SWCNTs are superior to MWCNTs at low densities and that the density (and thus optical transmittance) is vitally important in the performance of these cells. Increasing film transparency (lowering CNT density) increases the efficiency of the cells by allowing more light to reach the silicon, while decreasing the transparency (increasing the CNT density) increases the efficiency by lowering the sheet resistance across the film [11,23]. Thus, some optimal thickness must exist to achieve maximum efficiency. This research team also found their DWCNT cells to be significantly superior to both the SWCNT and MWCNT cells. However, their DWCNT films were produced using a different method to the SWCNT and MWCNT films [23] and were significantly longer and more pristine. This makes it difficult to draw a good comparison, as the nanotube film properties are highly dependent on film morphology [11] and fabrication route.



The aim of the research reported in this paper was to provide a more reliable comparison by creating suspensions of single, double and multi-walled carbon nanotubes under the same solvent conditions and examining the differences in solar cell properties between the different types. This study further improves on previous nanotube comparisons by using nanotubes that were specifically chosen to be of similar length and the films were all produced using the exact same procedure.

## 2. Results

Films were produced for each nanotube sample and were deposited on silicon substrates and imaged with scanning electron microscopy (SEM) to determine the film morphology. The images are shown in Figure 1. It is immediately noticeable that the DWCNT-2 suspension did not form a homogeneous film as the SEM image shows that the nanotubes clump together rather than spread across the membrane during film formation. The poor film morphology is due to issues dispersing DWCNTs in suspension. There are several possible reasons for this poor dispersion including tube length, contaminants and the surface properties of the nanotubes in the sample. Due to the poor film morphologies and coverage obtained for the DWCNT-2 sample, further work with this sample proved unfruitful and thus it will not be discussed in the rest of this study. The DWCNT-1 sample also did not form a fully homogenous surface covering film, however the film coverage was much closer to the SWCNT and MWCNT samples than DWCNT-2. Due to difficulties faced in suspending the DWCNTs, those suspensions were more dilute than the SWCNT or MWCNT suspensions, despite the addition of the same volume of dry nanotubes. It may be that the DWCNTs tend to remain bundled together more in suspension than the other nanotube types and thus form less homogeneous, more clustered films. There does not appear to be a large difference in the film morphology between the SWCNTs and MWCNTs: all three of these samples appear to form good, homogeneous coverings. There are noticeable holes in the SWCNT-1 films, which were formed during the vacuum filtration process when the vacuum was allowed to run for a time after all liquid has passed through. These are likely more prominent in this example as the film formed was thicker than the others. Overall, the SEM images show that all the types of nanotubes form suspensions well enough to produce homogenous films on a substrate and are thus usable for PV solar cell projects.

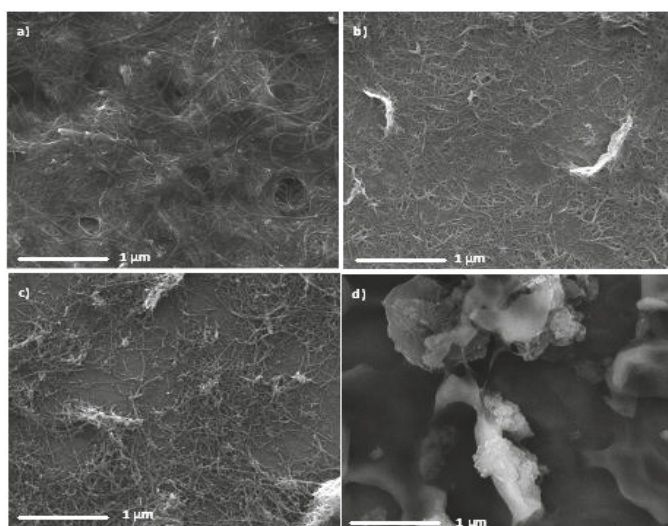
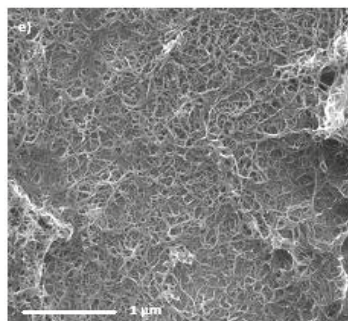


Figure 1. Cont.



**Figure 1.** Scanning electron microscopy (SEM) images of various types of carbon nanotube (CNT) samples on Si: (a) single-walled carbon nanotube sample 1 (SWCNT-1); (b) single-walled carbon nanotube sample 2 (SWCNT-2); (c) double-walled carbon nanotube sample 1 (DWCNT-1); (d) DWCNT-2; and (e) multi-walled carbon nanotube (MWCNT).

Optical absorption spectroscopy was performed on the nanotube films to determine the thickness and was also performed on the nanotube solutions to help confirm the nanotube types. It is expected that the ultra-violet/visible (UV/Vis) spectrum for MWCNT and DWCNT nanotubes will be featureless with an increase in absorption as the light wavelength decreases. A different spectrum is expected for SWCNT nanotubes, for which the van Hove singularities present in the SWCNT density of states lead to characteristic peaks in the optical spectra.

It can be observed from Figure 2 that the SWCNT spectra display peaks in the regions of 600–800 nm due to the  $S_{11}$  transition and 350–500 nm regions due to the  $M_{11}$  transition, and thus show the presence of SWCNTs in these solutions. This is the expected shape for UV/Vis spectra of single-walled nanotubes, due to their unique density of states allowing electronic transitions in the UV/Vis range. The differences in peak position in the two SWCNT samples are likely caused by species of different chirality being present in each sample. It is also noticeable that the SWCNT-1 sample had much less distinct peaks than the SWCNT-2 sample. This is likely due to the presence of a range of closely related nanotube chiralities in sample SWCNT-1. The spectra of the DWCNT and MWCNT samples are relatively featureless with an increase in absorbance at the lower wavelength end of the spectra as expected.

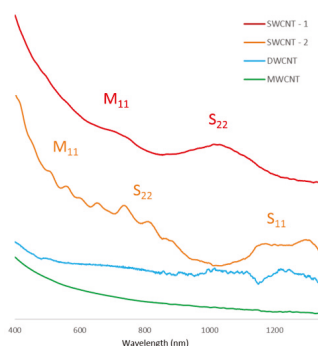


**Figure 2.** Ultra-violet/visible (UV/Vis) absorption spectra for all as prepared CNT suspensions. The absorbance values have been offset to allow easier viewing. Included in the figure are reference labels for semiconducting tube Van Hove singularity transitions  $S_{11}$  and  $S_{22}$  and metallic tube Van Hove singularity transition  $M_{11}$ .

In Raman spectroscopy, carbon nanotubes display characteristic peaks at around  $1580\text{ cm}^{-1}$  and at around  $1350\text{ cm}^{-1}$  known as the G and D bands, respectively. The G band is characteristic of highly ordered carbon species such as graphite or CNTs while the D band is characteristic of disordered carbon species. Thus the intensity of the G band relative to that of the D band is a strong indicator of crystallinity [24]. A radial breathing mode (RBM) between  $100$  and  $500\text{ cm}^{-1}$  can also be uniquely observed in Raman spectra of carbon nanotubes and is seen as direct evidence for the presence of SWCNTs [25] or DWCNTs [24] in the sample. An overtone of the D mode, known as the  $G'$  band (an overtone of the D band) is from a two-phonon, second-order Raman scattering process and expected to be seen at around  $2700\text{ cm}^{-1}$  while a signal at  $1550\text{ cm}^{-1}$  is known as a Breit-Wigner-Fano (BWF) band and is attributed to metallic carbons (metallic nanotubes in this case) [25]. Figure 3 displays the spectra obtained for each nanotube sample. As well as the characteristic D and G bands for CNTs the spectra also display the  $G'$  band at  $2700\text{ cm}^{-1}$  and while no RBM can be observed in the MWCNT sample. Peaks between  $100$  and  $500\text{ cm}^{-1}$  can be observed in all other samples in Figure 3a. The ratio of the intensities of the D and G bands (D/G ratio) is often used to measure the disorder in carbon nanotube samples. The D/G ratio in the MWCNT sample is significantly different than that of the other four samples, as expected for MWCNTs [24]. The D/G peak height ratios for all nanotube types are shown in Table 1. It can be seen from the values in Table 1 that the SWCNT-1 and DWCNT-1 nanotubes exhibit the lowest ratios, and are thus the most highly ordered nanotube or purest species in this study. The SWCNT-2 sample exhibited a higher D/G ratio, indicating a higher level of disorder or impurity, whereas the MWCNT sample gave a ratio above 1, due to the D peak being higher than the G peak, which is expected for MWCNTs [24,25]. The amount of CNT disorder is important to investigate as chemical reactions with nanotubes are more likely to occur at disordered regions than ordered regions.

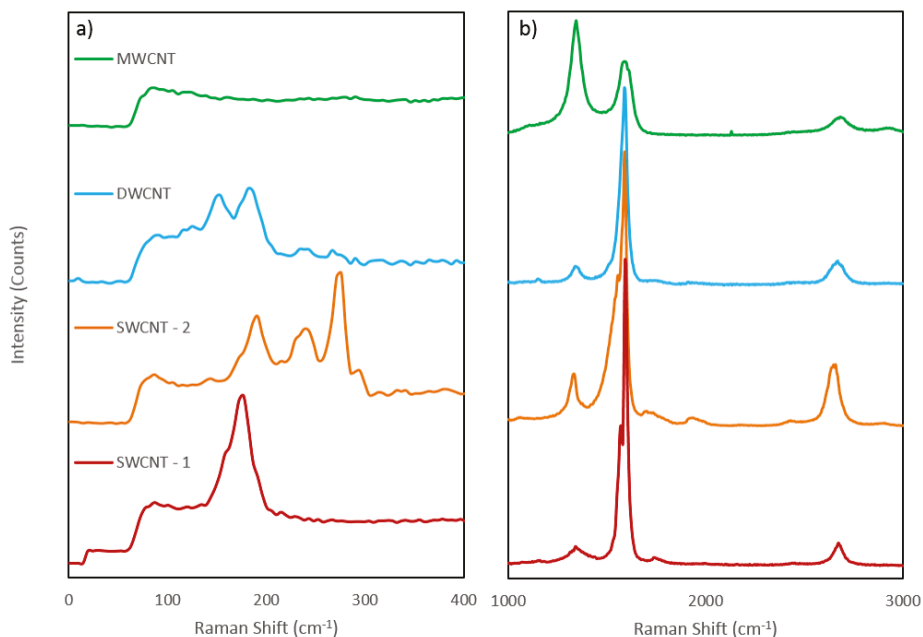


**Figure 3.** (a) Low wavenumber region of the Raman spectra for all CNT samples showing the D, G,  $G'$  and Breit-Wigner-Fano (BWF) bands, the intensity values have been offset to allow for easier viewing. (b) High wavenumber region of the Raman spectra for all CNT samples, showing the radial breathing mode (RBM) region. The intensity values have been offset to allow for easier viewing.

**Table 1.** D band to G band ratios for each nanotube type (two single-walled carbon nanotube samples (SWCNT-1 and SWCNT-2), one double-walled carbon nanotube sample (DWCNT) and one multi-walled carbon nanotube sample (MWCNT)).

Nanotube Sample	SWCNT-1	SWCNT-2	DWCNT	MWCNT
D/G Ratio	0.049	0.171	0.078	1.55

The Raman shift at which the RBM occurs can be used to calculate the nanotube diameter for SWCNTs as the RBM frequency is inversely proportional to the diameter of the tubes [26]. The equation relating the RBM shift to the diameter is:  $\text{RBM shift (cm}^{-1}\text{)} = \frac{A}{d_t \text{ (nm)}} + B$  where A has an approximate value of  $234 \text{ nm} \cdot \text{cm}^{-1}$  as determined from first principles (*ab initio*) calculations and B is approximately  $10 \text{ cm}^{-1}$ , which corrects the intertube interaction frequencies in SWCNT bundles [26,27]. This equation is applied to the RBM data shown in Figure 3a to give a calculated diameter for the SWCNT-1, SWCNT-2 and DWCNT nanotube samples and is compared with the manufacturer supplied diameters in Table 2 (note that the value of B was 0 in the DWCNT case as B is a correction for SWCNT bundles). Firstly, the calculation shows a very good agreement with the manufacturer supplied diameters for both of the SWCNT samples, with the calculated value(s) falling within the range given by the manufacturers. The DWCNT calculation does not agree, with the large peaks giving diameters around 0.75 nm smaller than the lowest diameter given by the manufacturer. This discrepancy can be explained by assigning the visible RBM peaks to the inner tubes of the DWCNTs since the interwall difference is known to be around 0.33–0.41 nm [28,29]. To achieve a diameter of  $>2 \text{ nm}$  the RBM peak for the outer tube would have to be at or below  $117 \text{ cm}^{-1}$ . The two small peaks to the left of the larger peaks on the DWCNT spectrum are closer to this range, with the left most peak occurring at around the expected  $117 \text{ cm}^{-1}$  and thus these smaller peaks could be due to the outer tubes.

**Table 2.** Calculation of nanotube diameter from radial breathing mode (RBM) Raman shift.

Nanotube Sample	RBM Raman Shift ( $\text{cm}^{-1}$ )	Calculated Diameter (nm)	Supplied Diameter (nm)
SWCNT-1	177	1.40	1.4–1.5
SWCNT-2	191, 239, 276	1.29, 1.02, 0.88	0.8–1.2
DWCNT Small Peaks	115, 125	2.03, 1.87	2–4
DWCNT Large Peaks	154, 186	1.52, 1.25	2–4

A series of films of different transparencies were prepared to determine suspension volume required to give similar transmittances. The data from these experiments are provided in Table S1. Films of each nanotube sample were produced at approximately the same transmittance for use in the solar cells. All samples displayed good transmittance values between 58% and 65%.

The sheet resistances of the nanotube films at each stage of treatment are shown in Table 3. The data show that the SWCNT films had a lower sheet resistance than the DWCNT and MWCNT films. Since the amount of material in the films was the same, as indicated by the optical measurements, this suggests improved charge carrier transport in the SWCNT films. The changes in sheet resistance with treatment are expected and are due to carrier doping and reductions in tube-tube contact resistance.

**Table 3.** Average sheet resistance for each carbon nanotube (CNT) sample with treatment ( $\Omega\cdot\text{sq}^{-1}$ ).

Film Type with Transmittance Percentage	As Prepared ( $\Omega\cdot\text{sq}^{-1}$ )	HCl Treatment 1 ( $\Omega\cdot\text{sq}^{-1}$ )	Thionyl Chloride Treatment ( $\Omega\cdot\text{sq}^{-1}$ )	HCl Treatment 2 ( $\Omega\cdot\text{sq}^{-1}$ )
SWCNT-1 60%	1440 $\pm$ 8.2%	951 $\pm$ 1.9%	693 $\pm$ 42%	543 $\pm$ 2.9%
SWCNT-2 65%	4070 $\pm$ 7.0%	3650 $\pm$ 2.6%	1880 $\pm$ 4.0%	2410 $\pm$ 12%
DWCNT 58%	138,000 $\pm$ 84%	4190 $\pm$ 39%	19,600 $\pm$ 138%	2550 $\pm$ 38%
MWCNT 60%	3340 $\pm$ 6.0%	3520 $\pm$ 6.0%	3020 $\pm$ 23%	2890 $\pm$ 27%

### 2.1. Solar Cell Performance

Films of all nanotube samples were deposited on the standard solar cell substrates described in the experimental details and their solar cell performance was measured four times: once directly after fabrication and then once after each treatment (HF etch,  $\text{SOCl}_2$  treatment, and 2nd HF etch).

Figure 4 shows the current-voltage characteristics of the best performing cells for each nanotube type after the complete treatment sequence, and the corresponding dark curves are shown in Figure S1. Both SWCNT samples show similar behavior under illumination, the only difference being a higher short-circuit current density ( $J_{\text{SC}}$ ) for SWCNT-1 and a slightly higher open circuit voltage ( $V_{\text{OC}}$ ) for SWCNT-2. Both the DWCNT and MWCNT samples display lower  $J_{\text{SC}}$  values. However, it can be seen that the DWCNT and the MWCNT cells produced a significantly higher  $V_{\text{OC}}$  than all the other cells. This is unexpected as the  $V_{\text{OC}}$  is determined by the energy levels of the system and should not be greatly affected by a change in nanotube type in this regard. It is likely, however, that this higher  $V_{\text{OC}}$  is caused by a lower rate of recombination in these nanotube types.

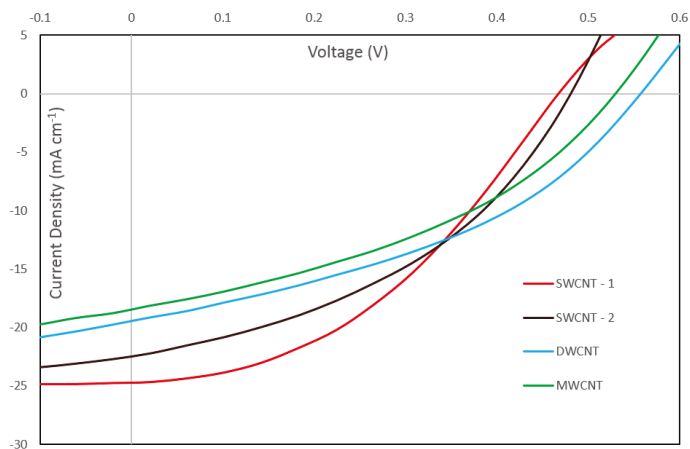


**Figure 4.** Current density vs voltage ( $J/V$ ) curves for best performing cells for each CNT sample after the second HF etch. Curves for two single-walled carbon nanotube samples (SWCNT-1 and SWCNT-2), one double-walled carbon nanotube sample (DWCNT) and one multi-walled carbon nanotube sample (MWCNT) are shown.

Figure 5 shows how the power conversion efficiency (PCE) of the best performing cell of each nanotube type varies with treatment. By the second HF etch the best cell PCEs ranged from 3.78% for the MWCNT sample to 4.79% for the SWCNT-1 sample. This difference of 1% absolute, or over 25% relative (based on the MWCNT device), between the two nanotube types is quite significant considering the care taken to control other differences between devices and the fact that the average relative error was around 15%. The ratio of the direct current (DC) electrical to optical conductivity,  $\sigma_{\text{DC}}/\sigma_{\text{OP}}$  for all films is very similar (see Table S1). The value is slightly higher for the SWCNT-1 film,

which likely explains its higher PCE value. The origin of the large increase in performance of the DWCNT devices after the 2nd HF treatment is unknown. It is not consistent with a model in which the  $\text{SOCl}_2$  is the *p*-type dopant increasing conductivity and lowering Fermi energy relative to the silicon, and thus improving device performance, as this effect should be observed after the  $\text{SOCl}_2$  treatment. It could possibly be due to acid digestion of the non-nanotube carbonaceous impurities (up to 40% by weight in the starting material) by the sequence of aggressive chemical treatments, resulting in better contact between the (purer) nanotube film and the underlying silicon, but further investigations are required to shed light on this.

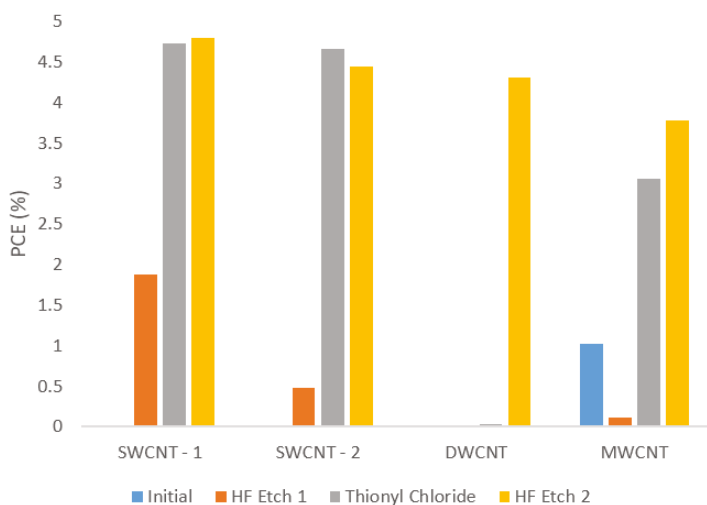


**Figure 5.** Solar cell efficiencies (%) for all nanotube types with treatment. PCE: power conversion efficiency.

Cells containing MWCNTs generally performed better at the initial stage of testing, but did not improve to the same extent as the SWCNT and DWCNT cells with doping. This can be explained by considering the surface area to volume ratio of MWCNTs compared to SWCNTs and DWCNT. Multi-walled nanotubes have a larger bulk than the other types for the same surface area, and thus surface acting treatments such as HF and  $\text{SOCl}_2$  will not have the same effect on bulk MWCNT films. Additionally, unlike SWCNTs, the large diameter and complex mixing of wall types and energy states in MWCNTs means they only have metallic character and therefore there are no tube-tube energy barriers to be lowered by doping. Thus, the MWCNTs are less affected by the acid and the thionyl chloride treatments used in this study.

### 3. Discussion

Table 4 shows a breakdown of the solar cell data. It can be seen that the highest  $J_{SC}$  was achieved by the cell that gives the highest efficiency. This is expected, as the efficiency is proportional to the current density. The efficiency is also proportional to the open circuit voltage ( $V_{OC}$ ) and the fill factor (FF). Thus the fact that the SWCNT-1 sample also achieved the equal highest fill factor is expected. It is surprising that the open circuit voltage is lower for both SWCNT samples than for the DWCNT and MWCNT samples. The higher voltages for these samples can be attributed to the smaller saturation current ( $J_{SAT}$ ) values for these cells. A smaller  $J_{SAT}$  indicates less current flowing in the undesired direction in the cell. The relation between  $J_{SAT}$  and  $V_{OC}$  for the best performing cells for each sample can be seen in Figure S2. The huge error values attached to the  $J_{SAT}$  measurements are due to the order of magnitude differences between the  $J_{SAT}$  values in each cell for each sample. The improved

efficiencies seen in the SWCNT samples over the DWCNT and MWCNT samples can be partially understood by observing the difference between the estimated shunt resistance ( $R_{shunt}$ ) and series resistance ( $R_{series}$ ). The series resistance value represents the amount of resistance opposing current flow in the desired direction and thus the ideal situation for a solar cell is to have a low  $R_{series}$ . Conversely, the shunt resistance value represents the amount of resistance opposing current flow over “short-cuts” in the cell circuit, thus the ideal value for  $R_{shunt}$  is high. Table 4 shows that the difference between  $R_{shunt}$  and  $R_{series}$  is an order of magnitude in the SWCNT cases, but is less than this in the DWCNT and MWCNT cases. This is a likely explanation for the slightly improved PCE for the SWCNT samples. The SWCNT-1 sample produced a higher diode ideality than the other three samples, given that the ideal value is 1 it is apparent that this cell was not as ideal as the other samples. This is likely indicative of a poorer contact with the silicon substrate in the solar cell, when compared with the other samples.

**Table 4.** Solar cell properties for best performing cells for each CNT sample in bold text, average properties and error values for sets of three (two for the Carbon Allotropes DWCNT) cells in regular text.  $J_{SC}$ : Short circuit current density.  $V_{OC}$ : Open circuit voltage. PCE: Power conversion efficiency. FF: fill factor.

	SWCNT-1	SWCNT-2	DWCNT	MWCNT
$J_{SC}$ (mA cm <sup>-2</sup> )	<b>24.7;</b>	<b>22.5;</b>	<b>19.5;</b>	<b>18.4;</b>
	24 ± 4.3%	22.2 ± 1.5%	18.9 ± 4.5%	18.1 ± 2.5%
$V_{OC}$ (V)	<b>0.468;</b>	<b>0.483;</b>	<b>0.58;</b>	<b>0.533;</b>
	0.427 ± 9.17%	0.449 ± 7.8%	0.553 ± 1.3%	0.465 ± 17.6%
FF	<b>0.41;</b>	<b>0.41;</b>	<b>0.40;</b>	<b>0.38;</b>
	0.41 ± 8.64%	0.39 ± 5.13%	0.40 ± 0.0%	0.35 ± 8.7%
PCE%	<b>4.79;</b>	<b>4.45;</b>	<b>4.31;</b>	<b>3.78;</b>
	4.21 ± 18.74%	3.90 ± 13.8%	4.14 ± 6.0%	3.03 ± 28.2%
$R_{shunt}$ (Ohm)	<b>6.42 × 10<sup>3</sup>;</b>	<b>1.06 × 10<sup>3</sup>;</b>	<b>8.42 × 10<sup>2</sup>;</b>	<b>8.07 × 10<sup>2</sup>;</b>
	2.81 × 10 <sup>3</sup> ± 112%	7.91 × 10 <sup>2</sup> ± 30.2%	9.61 × 10 <sup>2</sup> ± 17.5%	6.65 × 10 <sup>2</sup> ± 24.8%
$R_{series}$ (Ohm)	<b>1.21 × 10<sup>2</sup>;</b>	<b>1.11 × 10<sup>2</sup>;</b>	<b>1.44 × 10<sup>2</sup>;</b>	<b>1.64 × 10<sup>2</sup>;</b>
	1.08 × 10 <sup>2</sup> ± 16.3%	1.12 × 10 <sup>2</sup> ± 9.4%	1.57 × 10 <sup>2</sup> ± 11.3%	1.68 × 10 <sup>2</sup> ± 2.1%
Diode Ideality	<b>2.37;</b>	<b>1.98;</b>	<b>1.67;</b>	<b>1.94;</b>
	3.27 ± 23.96%	1.95 ± 16.4%	1.93 ± 19.3%	2.75 ± 33.2%
$J_{SAT}$ (mA cm <sup>-2</sup> )	<b>2.20 × 10<sup>-3</sup>;</b>	<b>4.64 × 10<sup>-4</sup>;</b>	<b>1.35 × 10<sup>-5</sup>;</b>	<b>1.31 × 10<sup>-4</sup>;</b>
	2.45 × 10 <sup>-1</sup> ± 106%	1.81 × 10 <sup>-3</sup> ± 145%	1.26 × 10 <sup>-4</sup> ± 126%	1.39 × 10 <sup>-1</sup> ± 171%
Film Transmittance (%)	60	65	58	60
Final Sheet Resistance of Film (Ω·sq <sup>-1</sup> )	543 ± 2.9%	2410 ± 12%	2550 ± 38%	2890 ± 27%

Overall the SWCNT samples performed better than the other nanotube types. This is expected from the sheet resistance measurements, as the SWCNT samples exhibited lower resistance after the final treatment. This improved resistance is likely due to the better morphology of the SWCNT films compared to the DWCNT films. There has been some work to suggest that DWCNTs should conduct charge better [30]. The fact that the DWCNT sample produces a poorer film is likely traceable to the fact that the suspension is more difficult to make and the lower purity of most DWCNT samples. The MWCNT sample showed a good film morphology and overall good sheet resistance. However the resistance of these films did not decrease with treatment at the same rate as for the SWCNT films.

#### 4. Materials and Methods

Five nanotube samples were used in this study, as shown in Table 5.

**Table 5.** Types of nanotube samples used.

Type	Company	Diameter (nm)	Length (nm)	Purity (%)
SWCNT-1	Carbon Solutions (Riverside, CA, USA)	1.4–1.5	500–1500	90
SWCNT-2	NanoIntegris (Boisbriand, QC, Canada)	0.8–1.2	100–1000	95
DWCNT-1	Carbon Allotropes ((Kensington, NSW, Australia)	2–4	<1500	>>60
DWCNT-2	Sigma-Aldrich (St Louis, MI, USA)	3.5	3000	90
MWCNT	Sigma-Aldrich	9.5	1500	95



Each nanotube suspension was produced in the same manner. The nanotubes (95 mg) were added to an aqueous TritonX-100 solution (1% *v/v*, 50 mL) (Sigma-Aldrich, St. Louis, MI, USA) and bath sonicated ( $\approx 50 W_{RMS}$  (root mean squared Watts),  $3 \times 20$  min intervals, Elmasonic S 30H (Singen, Germany)). In between each sonication the sonicating bath water was changed to prevent the suspension heating too much during sonication. The resulting sonicated suspension was centrifuged (1 h, 17,500 g, Beckmann-Coulter Allegra X-22 (Brea, CA, USA)) then the upper two thirds of the liquid in each tube was carefully extracted, combined, and centrifuged again with the same parameters. The upper two thirds of the liquid in each tube was carefully extracted and combined. The remaining third contained black lumps of unsuspended carbon and was discarded.

The photovoltaic cell substrates were produced by cutting silicon pieces of approximately  $1.5 \text{ cm}^2$  from a wafer of n-doped (phosphorous) silicon with a 100 nm oxide layer on one side. Each piece was patterned using a positive photoresist (Methoxypropyl acetate) applied via spin coating (30 s, 3000 rpm) and soft baked ( $100 \text{ }^\circ\text{C}$ , 1 min). The resist was exposed to UV light through a mask and the exposed resist was dissolved in a developer solution (trimethyl ammonium hydroxide) to leave an active area of  $0.079 \text{ cm}^2$  still covered. The substrate was sputter coated with a 5 nm layer of chromium and a 145 nm layer of gold. The thickness is controlled by a quartz crystal microbalance. The gold coated substrates were submerged in acetone (30 min) before sonicating briefly to dissolve the unexposed resist. One drop of buffered oxide etch (BOE, 6:1 ratio of 40%  $\text{NH}_4\text{F}$  and 49% hydrofluoric acid (HF)) was placed on the active area for 90 s in order to remove the 100 nm thermal oxide and allow the nanotubes to contact the silicon [31]. A schematic of the photovoltaic cell substrate is shown in Figure 6.

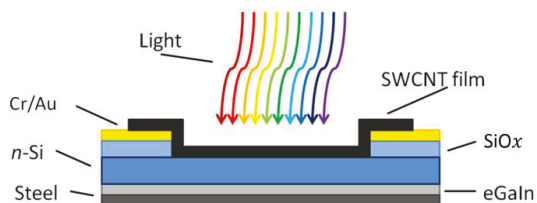


**Figure 6.** Simple schematic of the cells used in this experiment (Not to scale). Gallium indium eutectic (eGaln).

The nanotube films were produced via vacuum filtration. This was accomplished by first mixing the required amount of nanotube suspension (dependent on the concentration of the suspension in question, can vary from tens of microliters to up to 15 mL) with MilliQ water (Kansas City, MO, USA) to produce a solution of 250 mL. This solution was filtered using a vacuum produced with a water aspirator through a series of two microporous filter papers. The bottom filter paper (VSWP, Millipore (Billerica, MA, USA),  $0.025 \mu\text{m}$  pore size) was patterned with holes the size of the desired nanotube films ( $0.5 \text{ cm}^2$  in this case), while the top filter paper (HAWP, Millipore (Billerica, MA, USA),  $0.45 \mu\text{m}$  pore size) was unpatterned. The difference in flow rate through the filter papers causes the solution to pass preferentially through the top film where the bottom film is patterned. The nanotubes are thus caught by the top film in the same shape as the template film. The solution that had passed through both films was passed through the filtration apparatus two more times, to ensure enough nanotubes were retained on the top film. Pure MilliQ water was then passed through to wash out Triton X-100 surfactant remaining in the nanotube film. In most cases in these experiments the template used in each filtration produced four  $0.5 \text{ cm}^2$  films, one for attachment to glass to measure the optical transmittance, sheet resistance and Raman spectra and the other three for attachment to solar cells.

Nanotube films were attached to either glass (prewashed in ethanol) or the silicon substrate in the same manner. The films were cut from the filter paper and placed nanotube side down on the substrate. They were wetted with a small drop of water and sandwiched with a piece of Teflon and



a glass piece and clamped together. The clamped substrate was heated at around 80 °C for 15 min then left to cool in the dark for 1 h. The substrates were washed in acetone (first wash 30 min, second and third wash 30 min with stirring) to remove the attached filter paper. To complete cell preparation, the reverse side of each piece of silicon was manually scratched to remove the oxide layer. A gallium indium eutectic (eGaIn) was applied to the scratched surface and then a piece of stainless steel was attached as the back contact.

The cells were tested after the steel attachment and then a further 3 times after different post fabrication treatment steps. Firstly a drop of 2% HF was applied to the active area to etch silicon oxide formed between the silicon and the nanotube film produced during the film attachment step. Secondly, the nanotube film was treated with a few drops of thionyl chloride (SOCl<sub>2</sub>) and left until it evaporated, the residue was washed with ethanol prior to testing. The last step was another 2% HF treatment, which is observed to significantly improve performance, though the mechanism for this is still unclear [32].

At each stage of treatment the solar cells were tested by applying contacts to the back and front electrodes and reading the current density as the voltage is ramped from 1 V to −1 V. This is performed both in the absence of light and under illumination provided by a solar spectrum simulator at 100 mW·cm<sup>−1</sup> to measure both a “dark” and “light” curve the light is filtered through an AM1.5G filter (Irvine, CA, USA). The irradiance at the sample was kept constant by measuring with a silicon reference cell (PV Measurements, National Institute of Standards and Technology (NIST)-traceable calibration). The information was collected using a Keithley 2400 SourceMeter (Solon, OH, USA) attached to a PC running a program written in LabView (Austin, TX, USA).

The amount of light that passes through the CNT film to reach the CNT/Si junction directly affects the amount of energy that the cell can produce. Thus, it was important to perform nanotube type comparisons between films that allowed a similar amount of light to pass through. A series of films were produced from each sample using different amounts of nanotube suspension. The average light transmittance over a wavelength range of 300–1100 nm was determined for each sample and samples with the same or similar percentage transmittances were used on solar cells for comparative experiments.

Sheet resistance measurements were performed on nanotube films using a four point probe attached to Keithlink software (Solon, OH, USA), three sets of five measurements were performed on each film at different orientations and the results were averaged. The resistance was measured at each stage of the solar cell treatment process. However, as HF etches glass, a 2% HCl treatment was performed for 10 s as per the HF treatment. Scanning electron microscopy (SEM) was performed using an FEI Inspect F50 (Hillsboro, OR, USA) on nanotube films mounted on silicon wafers.

Raman spectra of the various nanotube types were obtained using a Witec Alpha R confocal Raman microscope (Ulm, Germany). The laser used was a Nd:YAG 532 nm (2.33 eV) laser and the power used at the sample was less than 10 mW. A 40× magnification objective with a Numerical Aperture (NA) of 0.6 was used. The data collected were single spectra with 10 spectra collected per sample at 5 different locations on each sample. The integration time was between 5 and 10 s with 3 accumulations per spectrum.

## 5. Conclusions

Suspensions of each nanotube type were produced under the exact same solvent conditions and procedures. This allowed an unambiguous comparison to be made between different nanotube types in a silicon/CNT heterojunction solar cell in which the suspension and film preparation were identical.

It was observed that although one SWCNT sample produced a higher efficiency than the other samples, both single-walled samples and the double-walled sample produced similar power conversion efficiencies as each other, with a difference of less than 0.5% between the three samples. Single-walled films produced better short circuit current densities, whereas double-walled and multi-walled carbon nanotube films displayed higher open circuit voltages. Fill factors were found

to be similar across the board, with SWCNT films producing better  $R_{\text{Shunt}}$  to  $R_{\text{Series}}$  ratios. It was discovered that cells made with MWCNT films improve to a lesser extent with doping treatment. Overall, the results of this study indicate that when variables other than nanotube type are controlled, large diameter single-walled carbon nanotube films provide the best performance in silicon/CNT solar cells. This conclusion differs from some previous work in which other variables were not well controlled, and will inform future research and development in this field.

**Supplementary Materials:** The following are available online at <http://www.mdpi.com/2079-4991/6/3/52/s1>, Figure S1: Dark J/V curves for cells for each type of sample after the second HF etch: (a) SWCNT-1; (b) SWCNT-2; (c) DWCNT; and (d) Sigma Aldrich MWCNT. Figure S2: A plot of the relation between  $J_{\text{SAT}}$  and  $V_{\text{OC}}$  for the best performing cells for each sample. Table S1: Sheet resistance as a function of thickness. The values marked with an asterisk were the volumes used to produce films for solar cells in this study.

**Acknowledgments:** This work is supported by the Australian Microscopy and Microanalysis Research Facility (AMMRF), and The Flinders University Centre for Nanoscale Science & Technology (CNST) and was financially supported by Vice Deanship of Research Chairs, King Saud University.

**Author Contributions:** Daniel Tune and Joseph Shapter conceived and designed the experiments; Tom Grace, LePing Yu, Christopher Gibson and Huda Alturaif performed the experiments; Tom Grace, Christopher Gibson, Zeid Al Othman and Daniel Tune analyzed the data; Joseph Shapter and Zeid Al Othman contributed reagents/materials/analysis tools; and Tom Grace wrote the paper.

**Conflicts of Interest:** The authors declare no conflict of interest.

## Abbreviations

The following abbreviations are used in this manuscript:

SWCNT:	Single-walled Carbon Nanotube
DWCNT:	Double-walled Carbon Nanotube
MWCNT:	Multi-walled Carbon Nanotube
CNT:	Carbon Nanotube
PCE:	power conversion efficiency
CVD:	chemical vapor deposition
PV:	photovoltaics
RBM:	radial breathing mode

## References

- Colinge, J.-P.C.; Cynthia, A. *Physics of Semiconductor Devices*; Kluwer Academic: Norwell, MA, USA, 2002; p. 436.
- Shi, E.; Zhang, L.; Li, Z.; Li, P.; Shang, Y.; Jia, Y.; Wei, J.; Wang, K.; Zhu, H.; Wu, D. TiO<sub>2</sub>-coated carbon nanotube-silicon solar cells with efficiency of 15%. *Sci. Rep.* **2012**, *2*. [CrossRef] [PubMed]
- Durkop, T.G.; Cobas, S.A.; Fuhrer, M.S. Extraordinary mobility in semiconducting carbon nanotubes. *Nano Lett.* **2004**, *4*, 35–39. [CrossRef]
- Barnes, T.M.; Blackburn, J.L.; van de Lagemaat, J.; Coutts, T.J.; Heben, M.J. Reversibility, dopand desorption, and tunneling in the temperature-dependent conductivity of type-separated, conductive carbon nanotube networks. *ACS Nano* **2008**, *2*, 1968–1976. [CrossRef] [PubMed]
- Baughman, R.H.; Zakhidov, A.A.; de Heer, W.A. Carbon nanotubes—The route toward applications. *Science* **2002**, *297*, 787–792. [CrossRef] [PubMed]
- Wang, F.; Kozawa, D.; Miyauchi, Y.; Hiraoka, K.; Mouri, S.; Ohno, Y.; Matsuda, K. Considerably improved photovoltaic performance of carbon nanotube-based solar cells using metal oxide layers. *Nat. Commun.* **2015**, *6*. [CrossRef] [PubMed]
- Tzolov, M.B.; Kuo, T.-F.; Straus, D.A.; Yin, A.; Xu, J. Carbon nanotube-silicon heterojunction arrays and infrared photocurrent responses. *J. Phys. Chem. C* **2007**, *111*, 5800–5804. [CrossRef]
- Javey, A.; Guo, J.; Farmer, D.B.; Wang, Q.; Yenilmez, E.; Gordon, R.G.; Lundstrom, M.; Dai, H. Self-aligned ballistic molecular transistors and electrically parallel nanotube arrays. *Nano Lett.* **2004**, *4*, 1319–1322. [CrossRef]
- Kongkanand, A.; Domínguez, R.M.; Kamat, P.V. Single wall carbon nanotube scaffolds for photoelectrochemical solar cells. Capture and transport of photogenerated electrons. *Nano Lett.* **2007**, *7*, 676–680. [CrossRef] [PubMed]

10. Jia, Y.; Wei, J.; Wang, K.; Cao, A.; Shu, Q.; Gui, X.; Zhu, Y.; Zhuang, D.; Zhang, G.; Ma, B. Nanotube-silicon heterojunction solar cells. *Adv. Mater.* **2008**, *20*, 4594–4598. [CrossRef]
11. Tune, D.D.; Flavel, B.S.; Krupke, R.; Shapter, J.G. Carbon nanotube-silicon solar cells. *Adv. Energy Mater.* **2012**, *2*, 1043–1055. [CrossRef]
12. Wei, J.; Jia, Y.; Shu, Q.; Gu, Z.; Wang, K.; Zhuang, D.; Zhang, G.; Wang, Z.; Luo, J.; Cao, A. Double-walled carbon nanotube solar cells. *Nano Lett.* **2007**, *7*, 2317–2321. [CrossRef] [PubMed]
13. Castrucci, P. Carbon nanotube/silicon hybrid heterojunctions for photovoltaic devices. *Adv. Nano Res.* **2014**, *2*, 23–56. [CrossRef]
14. Honsberg, C.; Bowden, S. PVCDROM. Available online: <http://www.pveducation.org/pvcdrom> (accessed on 22 September 2014).
15. Green, M.A.; Emery, K.; Hishikawa, Y.; Warta, W.; Dunlop, E.D. Solar cell efficiency tables (Version 45). *Prog. Photovolt. Res. Appl.* **2015**, *23*, 1–9. [CrossRef]
16. Yu, L.; Tune, D.D.; Shearer, C.J.; Shapter, J.G. Implementation of antireflection layers for improved efficiency of carbon nanotube–silicon heterojunction solar cells. *Sol. Energy* **2015**, *118*, 592–599. [CrossRef]
17. Jung, Y.; Li, X.; Rajan, N.K.; Taylor, A.D.; Reed, M.A. Record high efficiency single-walled carbon nanotube/silicon p–n junction solar cells. *Nano Lett.* **2012**, *13*, 95–99. [CrossRef] [PubMed]
18. Harris, J.M.; Semler, M.; May, S.; Fagan, J.A.; Hobbie, E.K. Nature of record efficiency fluid-processed nanotube–silicon heterojunctions. *J. Phys. Chem. C* **2015**, *119*, 10295–10303. [CrossRef]
19. Castrucci, P.; Scilletta, C.; Del Gobbo, S.; Scarselli, M.; Camilli, L.; Simeoni, M.; Delley, B.; Continenza, A.; De Crescenzi, M. Light harvesting with multiwall carbon nanotube/silicon heterojunctions. *Nanotechnology* **2011**, *22*. [CrossRef] [PubMed]
20. Li, Z.; Kunets, V.P.; Saini, V.; Xu, Y.; Dervishi, E.; Salamo, G.J.; Biris, A.R.; Biris, A.S. SOCl<sub>2</sub> enhanced photovoltaic conversion of single wall carbon nanotube/n-silicon heterojunctions. *Appl. Phys. Lett.* **2008**, *93*. [CrossRef]
21. Li, Z.; Kunets, V.P.; Saini, V.; Xu, Y.; Dervishi, E.; Salamo, G.J.; Biris, A.R.; Biris, A.S. Light-harvesting using high density p-type single wall carbon nanotube/n-type silicon heterojunctions. *ACS Nano* **2009**, *3*, 1407–1414. [CrossRef] [PubMed]
22. Tune, D.D.; Blanch, A.J.; Krupke, R.; Flavel, B.S.; Shapter, J.G. Nanotube film metallicity and its effect on the performance of carbon nanotube–silicon solar cells. *Phys. Status Solidi* **2014**, *211*, 1479–1487. [CrossRef]
23. Jia, Y.; Li, P.; Wei, J.; Cao, A.; Wang, K.; Li, C.; Zhuang, D.; Zhu, H.; Wu, D. Carbon nanotube films by filtration for nanotube-silicon heterojunction solar cells. *Mater. Res. Bull.* **2010**, *45*, 1401–1405. [CrossRef]
24. Liu, L.; Kong, L.B.; Yin, W.Y.; Chen, Y.; Matisine, S. Carbon Nanotubes. In *Chapter 5—Microwave Dielectric Properties of Carbon Nanotube Composites*; Marulanda, J.M., Ed.; Intech: Vukovar, Croatia, 2010.
25. Dresselhaus, M.S.; Dresselhaus, G.; Saito, R.; Jorio, A. Raman spectroscopy of carbon nanotubes. *Phys. Rep.* **2005**, *409*, 47–99. [CrossRef]
26. Arvanitidis, J.; Christofilos, D.; Papagelis, K.; Andrikopoulos, K.; Takenobu, T.; Iwasa, Y.; Kataura, H.; Ves, S.; Kourouklis, G. Pressure screening in the interior of primary shells in double-wall carbon nanotubes. *Phys. Rev. B* **2005**, *71*. [CrossRef]
27. Pfeiffer, R.; Kuzmany, H.; Kramberger, C.; Schaman, C.; Pichler, T.; Kataura, H.; Achiba, Y.; Kürti, J.; Zólyomi, V. Unusual high degree of unperturbed environment in the interior of single-wall carbon nanotubes. *Phys. Rev. Lett.* **2003**, *90*. [CrossRef] [PubMed]
28. Dresselhaus, M.; Dresselhaus, G.; Saito, R. Physics of carbon nanotubes. *Carbon* **1995**, *33*, 883–891. [CrossRef]
29. Ren, W.; Li, F.; Chen, J.; Bai, S.; Cheng, H.-M. Morphology, diameter distribution and Raman scattering measurements of double-walled carbon nanotubes synthesized by catalytic decomposition of methane. *Chem. Phys. Lett.* **2002**, *359*, 196–202. [CrossRef]
30. Moore, K.E.; Flavel, B.S.; Ellis, A.V.; Shapter, J.G. Comparison of double-walled with single-walled carbon nanotube electrodes by electrochemistry. *Carbon* **2011**, *49*, 2639–2647. [CrossRef]

31. Tune, D.D.; Flavel, B.S.; Quinton, J.S.; Ellis, A.V.; Shapter, J.G. Single-walled carbon nanotube/polyaniline/n-silicon solar cells: Fabrication, characterization, and performance measurements. *ChemSusChem* **2013**, *6*, 320–327. [CrossRef] [PubMed]
32. Li, X.; Hung, J.-S.; Nejeti, S.; McMillon, L.; Huang, S.; Osuji, C.O.; Hazari, N.; Taylor, A.D. The role of HF in oxygen removal from carbon nanotubes: Implications for high performance carbon electronics. *Nano Lett.* **2014**, *14*, 6179–6184. [CrossRef] [PubMed]



© 2016 by the authors. Licensee MDPI, Basel, Switzerland. This article is an open access article distributed under the terms and conditions of the Creative Commons Attribution (CC BY) license (<http://creativecommons.org/licenses/by/4.0/>).

Communication

# Ag Nanoparticle–Functionalized Open-Ended Freestanding TiO<sub>2</sub> Nanotube Arrays with a Scattering Layer for Improved Energy Conversion Efficiency in Dye-Sensitized Solar Cells

Won-Yeop Rho <sup>1,2,†</sup>, Myeung-Hwan Chun <sup>2,†</sup>, Ho-Sub Kim <sup>2</sup>, Hyung-Mo Kim <sup>1</sup>, Jung Sang Suh <sup>2</sup> and Bong-Hyun Jun <sup>1,\*</sup>

<sup>1</sup> Department of Bioscience and Biotechnology, Konkuk University, Seoul 143-701, Korea; rho72@snu.ac.kr (W.-Y.R.); hmkim0109@konkuk.ac.kr (H.-M.K.)

<sup>2</sup> Department of Chemistry, Seoul National University, Seoul 151-747, Korea; hwanmc@hanmail.net (M.-H.C.); hosub@snu.ac.kr (H.-S.K.); jssuh@snu.ac.kr (J.S.S.)

\* Correspondence: bjun@konkuk.ac.kr; Tel.: +82-2-450-0521

† These authors contribute equally to this work.

Academic Editors: Guanying Chen, Zhijun Ning and Hans Agren

Received: 30 March 2016; Accepted: 6 June 2016; Published: 15 June 2016

**Abstract:** Dye-sensitized solar cells (DSSCs) were fabricated using open-ended freestanding TiO<sub>2</sub> nanotube arrays functionalized with Ag nanoparticles (NPs) in the channel to create a plasmonic effect, and then coated with large TiO<sub>2</sub> NPs to create a scattering effect in order to improve energy conversion efficiency. Compared to closed-ended freestanding TiO<sub>2</sub> nanotube array–based DSSCs without Ag or large TiO<sub>2</sub> NPs, the energy conversion efficiency of closed-ended DSSCs improved by 9.21% (actual efficiency, from 5.86% to 6.40%) with Ag NPs, 6.48% (actual efficiency, from 5.86% to 6.24%) with TiO<sub>2</sub> NPs, and 14.50% (actual efficiency, from 5.86% to 6.71%) with both Ag NPs and TiO<sub>2</sub> NPs. By introducing Ag NPs and/or large TiO<sub>2</sub> NPs to open-ended freestanding TiO<sub>2</sub> nanotube array–based DSSCs, the energy conversion efficiency was improved by 9.15% (actual efficiency, from 6.12% to 6.68%) with Ag NPs and 8.17% (actual efficiency, from 6.12% to 6.62%) with TiO<sub>2</sub> NPs, and by 15.20% (actual efficiency, from 6.12% to 7.05%) with both Ag NPs and TiO<sub>2</sub> NPs. Moreover, compared to closed-ended freestanding TiO<sub>2</sub> nanotube arrays, the energy conversion efficiency of open-ended freestanding TiO<sub>2</sub> nanotube arrays increased from 6.71% to 7.05%. We demonstrate that each component—Ag NPs, TiO<sub>2</sub> NPs, and open-ended freestanding TiO<sub>2</sub> nanotube arrays—enhanced the energy conversion efficiency, and the use of a combination of all components in DSSCs resulted in the highest energy conversion efficiency.

**Keywords:** open-ended freestanding TiO<sub>2</sub> nanotube arrays; dye-sensitized solar cells; plasmonic; scattering; anodization

## 1. Introduction

Since the original work by O'Regan and Grätzel in 1991 [1], dye-sensitized solar cells (DSSCs) have been investigated extensively because of their high energy conversion efficiency and low cost [2–9]. Generally, mesoporous TiO<sub>2</sub> nanoparticle (NP) films and ruthenium sensitizers are used for DSSCs [2–4,10–16]. However, the efficiency of mesoporous TiO<sub>2</sub> NP film–based DSSCs is limited by grain boundaries, defects, and numerous trapping sites. Moreover, mesoporous TiO<sub>2</sub> NP films can cause charge recombination and mobility [17,18].

TiO<sub>2</sub> nanotubes, which enhance electron transport and charge separation by creating direct pathways and accelerating charge transfer between interfaces, have great potential to overcome the

problems of mesoporous TiO<sub>2</sub> NP films [19–22]. TiO<sub>2</sub> nanotubes can be prepared by a hydrothermal method [23] or an electrochemical method [24], known as anodization. TiO<sub>2</sub> nanotube arrays prepared by anodization have a well-ordered and vertically oriented tubular structure that facilitates a high degree of electron transport and less charge recombination than mesoporous TiO<sub>2</sub> NP films [25–27]. There is much room for improvement in the energy conversion efficiency of current DSSCs based on TiO<sub>2</sub> nanotube arrays compared to the relatively extensively researched mesoporous TiO<sub>2</sub> NP film-based DSSCs [28].

To date, several approaches for improving the energy conversion efficiency of TiO<sub>2</sub> nanotube array-based DSSCs have been reported. Metal NPs, which can harvest light via surface plasmon resonance (SPR), have been used to enhance the energy conversion efficiency of DSSCs by introducing Au or Ag NPs into TiO<sub>2</sub> nanotube arrays [29–32]. Barrier layers remove TiO<sub>2</sub> nanotube arrays, so open-ended TiO<sub>2</sub> nanotube arrays, which can also be classified as arrays of columnar nanopores, have been used for DSSCs to provide increased energy conversion efficiency [33]. Moreover, the energy conversion efficiency of TiO<sub>2</sub> nanotube array-based DSSCs can be further increased by introducing a scattering layer to the active layer [34].

So far, TiO<sub>2</sub> nanotubes that make use of a scattering layer [34] or plasmonic materials [14] have been reported, but a scattering layer with plasmonic materials has not been used in TiO<sub>2</sub> nanotube-based DSSCs. In this study, we report the development of freestanding TiO<sub>2</sub> nanotube arrays filled with Ag NPs and large TiO<sub>2</sub> NPs, which improve the energy conversion efficiency of DSSCs. Furthermore, we compare the effects of Ag NPs and large TiO<sub>2</sub> NPs in open- and closed-ended freestanding TiO<sub>2</sub> nanotube arrays in DSSCs. The energy conversion efficiencies of the following eight types of DSSCs were compared: closed-ended freestanding TiO<sub>2</sub> nanotube arrays with/without Ag NPs and/or a TiO<sub>2</sub> scattering layer and open-ended freestanding TiO<sub>2</sub> nanotube arrays with/without Ag NPs and/or a TiO<sub>2</sub> scattering layer.

## 2. Results and Discussion

### 2.1. Structure of DSSCs with Freestanding TiO<sub>2</sub> Nanotube Arrays with Channels Containing Ag NPs

Figure 1 illustrates the fabrication of DSSCs with Ag NPs and large TiO<sub>2</sub> NPs to enable plasmonic and scattering effects in open-ended freestanding TiO<sub>2</sub> nanotube array-based DSSCs. Ti plates were anodized and then annealed at 500 °C for 1 h to prepare anatase TiO<sub>2</sub> nanotube arrays. After carrying out secondary anodization, the TiO<sub>2</sub> nanotube arrays were easily detached from the Ti plates. TiO<sub>2</sub> nanotube arrays, once separated from the Ti plates, are termed “closed-ended freestanding TiO<sub>2</sub> nanotube arrays”. Freestanding TiO<sub>2</sub> nanotube arrays have a barrier layer at the bottom that disturbs electron transport and electrolyte diffusion. This barrier layer was removed using the ion-milling method with several minutes of Ar<sup>+</sup> bombardment to yield “open-ended freestanding TiO<sub>2</sub> nanotube arrays”. The closed- and open-ended freestanding TiO<sub>2</sub> nanotube arrays were transferred to fluorine-doped tin oxide (FTO) glass using TiO<sub>2</sub> paste and annealed to enhance the adhesion between the closed- and open-ended freestanding TiO<sub>2</sub> nanotube arrays and the fluorine-doped tin oxide (FTO) glass. To improve the energy conversion efficiency by the plasmonic effect, Ag NPs were embedded in the channel of freestanding TiO<sub>2</sub> nanotube arrays using 254 nm ultraviolet (UV) irradiation with aqueous silver nitrate. To further enhance the energy conversion efficiency, large TiO<sub>2</sub> NPs (400 nm) as a scattering layer were coated onto the active layer by the doctor blade method. This substrate was sandwiched with the counter electrode and filled with electrolyte. The active area of the DSSCs was ~0.25 cm<sup>2</sup>.

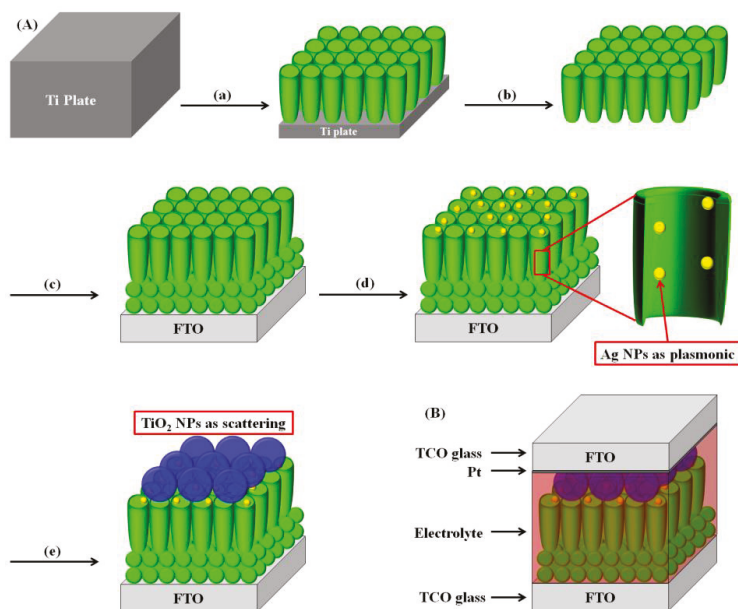


**Figure 1.** Overall scheme of dye-sensitized solar cells (DSSCs) with open-ended freestanding TiO<sub>2</sub> nanotube arrays with Ag nanoparticles (NPs) and large TiO<sub>2</sub> NPs. (A) (a) Ti anodization for TiO<sub>2</sub> nanotube arrays; (b) freestanding TiO<sub>2</sub> nanotube arrays and etching by ion milling; (c) transference of open-ended freestanding TiO<sub>2</sub> nanotube arrays onto fluorine-doped tin oxide (FTO) glass; (d) formation of Ag NPs by ultraviolet (UV) irradiation; and (e) introduction of large TiO<sub>2</sub> NPs. (B) Structure of a DSSC with freestanding TiO<sub>2</sub> nanotube arrays and large TiO<sub>2</sub> NPs.

## 2.2. Characterization of Freestanding TiO<sub>2</sub> Nanotube Arrays with Channels Containing Ag NPs

Field emission scanning electron microscope (FE-SEM) images of freestanding TiO<sub>2</sub> nanotube (TNT) arrays are shown in Figure 2. The top side of the freestanding TiO<sub>2</sub> nanotube arrays had 100-nm-diameter pores, as shown in Figure 2a. The bottom layer of closed-ended freestanding TiO<sub>2</sub> nanotube arrays before ion milling lacked pores, as shown in Figure 2b. However, after ion milling, 20-nm-diameter pores were evident on the bottom layer of open-ended freestanding TiO<sub>2</sub> nanotube arrays, as shown in Figure 2c. Open-ended TNT arrays can be prepared by chemical etching [35] or physical etching [33,36]. In the chemical etching method, the bottom layers of TNT arrays were easily removed by the etchant. However, the surface morphology and length of TNT arrays were also dissolved in etchant and TNT arrays are fragile when they are attached to a substrate because of their amorphous crystallinity. In the physical etching method, the bottom layer of TNT arrays was removed by the plasma or ion milling process, which is not simple. However, the surface morphology and length of TNT arrays are not damaged in the process and they are very stable when they are attached to a substrate because TNT arrays have the ability to change crystallinity from the amorphous to the anatase phase. After UV irradiation using a silver source, ~30 nm Ag NPs were seen in the channels of freestanding TiO<sub>2</sub> nanotubes in high-angle annular dark-field (HAADF) images, as shown in Figure 2d. The length of the TiO<sub>2</sub> nanotubes was ~22 μm and the length of the scattering layer, which consisted of 400 nm TiO<sub>2</sub> NPs, was ~10 μm.



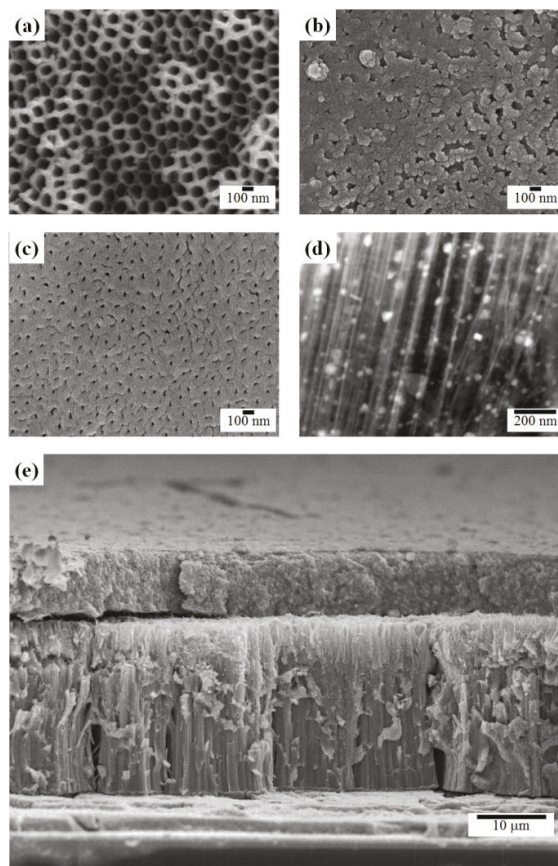


**Figure 2.** Field emission scanning electron microscope (FE-SEM) images of the (a) top, (b) bottom, and (c) bottom of post-ion milling freestanding TiO<sub>2</sub> nanotube arrays; (d) a high-angle annular dark-field (HAADF) image of Ag NPs in the channel of TiO<sub>2</sub> nanotube arrays; and (e) a side view of the active layer with freestanding TiO<sub>2</sub> nanotube arrays and a scattering layer.

The ultraviolet-visible (UV-vis) spectrum of Ag NPs in the channels of freestanding TiO<sub>2</sub> nanotubes is shown in Figure 3. A broad absorption peak centered at 402 nm was observed. The value is different from what it would be in the general solution phase, which is a 420 nm UV absorbance from 30 nm Ag NPs. This discrepancy may stem from different synthesis and measurement conditions used in this study [37–39]; the Ag NPs were synthesized by UV irradiation (at 254 nm) without adding a stabilizer and the Ag NPs were measured under dry conditions. The absorption band of Ag NPs is matched with the dye, *cis*-diisothiocyanato-bis(2,2'-bipyridyl-4,4'-dicarboxylato) ruthenium(II) bis(tetrabutylammonium) (N719) has two visible absorption bands, 390 nm and 531 nm, [40] that were affected by the plasmon band. Moreover, the shell of Ag NPs was prepared with TiCl<sub>4</sub> to prevent the trapping of electrons by Ag NPs and to enable better electron transport in the channel of the TiO<sub>2</sub> nanotube arrays.



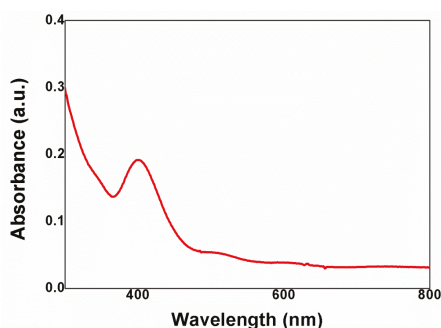


Figure 3. Ultraviolet-visible (UV-vis) spectrum of Ag NP-functionalized TiO<sub>2</sub> nanotubes.

### 2.3. DSSCs with Closed-Ended Freestanding TiO<sub>2</sub> Nanotube Arrays with Channels Containing Ag NPs and Large TiO<sub>2</sub> NPs

The photocurrent-voltage curves of DSSCs fabricated using closed-ended freestanding TiO<sub>2</sub> nanotube arrays measured under air mass 1.5 illumination (100 mW/cm<sup>2</sup>) are shown in Figure 4 and Table 1. Four types of closed-ended freestanding TiO<sub>2</sub> nanotube array-based DSSCs were fabricated in order to assess the effect of each component on the energy conversion efficiency: closed-ended freestanding TiO<sub>2</sub> nanotube array-based DSSCs without Ag or large TiO<sub>2</sub> NPs (a), with Ag NPs (b), with large TiO<sub>2</sub> NPs (c), and with both Ag NPs and large TiO<sub>2</sub> NPs (d). The open-circuit voltage ( $V_{oc}$ ), short-circuit current ( $J_{sc}$ ), fill factor ( $ff$ ), and energy conversion efficiency ( $\eta$ ) values are shown in Table 1. The energy conversion efficiency of DSSCs based on closed-ended freestanding TiO<sub>2</sub> nanotube arrays lacking NPs was 5.86%. The energy conversion efficiencies of DSSCs based on closed-ended freestanding TiO<sub>2</sub> nanotube arrays with Ag NPs, with large TiO<sub>2</sub> NPs, and with both Ag NPs and large TiO<sub>2</sub> NPs were 6.40%, 6.24%, and 6.71%, respectively. The introduction of Ag NPs increased the energy conversion efficiency significantly, by 9.21% (actual efficiency change, from 5.86% to 6.40%) compared to closed-ended freestanding TiO<sub>2</sub> nanotube array-based DSSCs without Ag and large TiO<sub>2</sub> NPs, because of increased light harvesting by the plasmonic effect. The introduction of large TiO<sub>2</sub> NPs also increased the energy conversion efficiency significantly, by 6.48% (actual efficiency, from 5.86% to 6.24%), owing to increased light harvesting by the scattering effect. Moreover, the introduction of both Ag NPs and large TiO<sub>2</sub> NPs increased the energy conversion efficiency significantly, by 14.50% (actual efficiency, from 5.86% to 6.71%), because of increased light harvesting resulting from both the plasmonic and scattering effects.

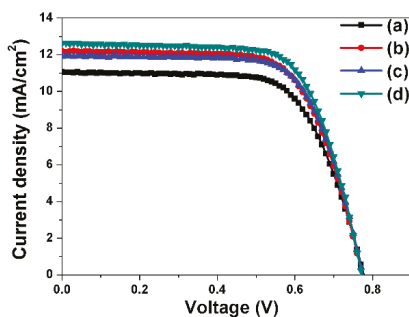


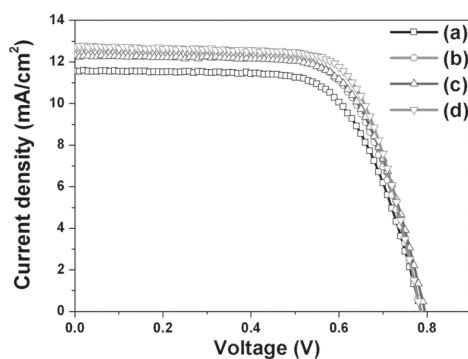
Figure 4. I-V curves of DSSC-based closed-ended freestanding TiO<sub>2</sub> nanotube arrays fabricated without NPs (a), with Ag NPs (b), with large TiO<sub>2</sub> NPs (c), and with Ag NPs and large TiO<sub>2</sub> NPs (d).

**Table 1.** Photovoltaic properties of dye-sensitized solar cells (DSSCs) based on closed-ended freestanding TiO<sub>2</sub> nanotube arrays.

DSSCs	$J_{sc}$ (mA/cm <sup>2</sup> )	$V_{oc}$ (V)	$ff$	$\eta$ (%)
(a) Closed-ended freestanding TiO <sub>2</sub> nanotube arrays without any NPs	11.05	0.78	0.68	5.86
(b) Closed-ended freestanding TiO <sub>2</sub> nanotube arrays with Ag NPs	12.22	0.77	0.68	6.40
(c) Closed-ended freestanding TiO <sub>2</sub> nanotube arrays with large TiO <sub>2</sub> NPs	11.90	0.76	0.69	6.24
(d) Closed-ended freestanding TiO <sub>2</sub> nanotube arrays with Ag NPs and large TiO <sub>2</sub> NPs	12.63	0.77	0.69	6.71

#### 2.4. DSSCs with Open-Ended Freestanding TiO<sub>2</sub> Nanotube Arrays with Channels Containing Ag NPs and Large TiO<sub>2</sub> NPs

The photocurrent-voltage curves of DSSCs fabricated using open-ended freestanding TiO<sub>2</sub> nanotube arrays are shown in Figure 5 and Table 2; they are useful in assessing the effect of each component on the energy conversion efficiency. Four types of DSSCs based on open-ended freestanding TiO<sub>2</sub> nanotube arrays were fabricated: open-ended freestanding TiO<sub>2</sub> nanotube array-based DSSCs without Ag or large TiO<sub>2</sub> NPs (a), with Ag NPs (b), with large TiO<sub>2</sub> NPs (c), and with both Ag NPs and large TiO<sub>2</sub> NPs (d). The  $V_{oc}$ ,  $J_{sc}$ ,  $ff$ , and  $\eta$  values are summarized in Table 2. The energy conversion efficiency of DSSCs based on open-ended freestanding TiO<sub>2</sub> nanotube arrays lacking NPs was 6.12%. The energy conversion efficiencies of DSSCs based on open-ended freestanding TiO<sub>2</sub> nanotube arrays with Ag NPs, with large TiO<sub>2</sub> NPs, and with both Ag NPs and large TiO<sub>2</sub> NPs were 6.68%, 6.62%, and 7.05%, respectively. The introduction of Ag NPs, large TiO<sub>2</sub> NPs, and both increased the energy conversion efficiency by 9.15%, 8.17%, and 15.20%, respectively. Compared to closed-ended freestanding TiO<sub>2</sub> nanotube arrays, the energy conversion efficiency of DSSCs based on open-ended freestanding TiO<sub>2</sub> nanotube arrays was 5.07% (6.71%–7.05%) higher due to enhanced electron transport and electrolyte diffusion [33].

**Figure 5.** I–V curves of DSSCs based on open-ended freestanding TiO<sub>2</sub> nanotube arrays fabricated without NPs (a), with Ag NPs (b), with large TiO<sub>2</sub> NPs (c), and with both Ag NPs and large TiO<sub>2</sub> NPs (d).

**Table 2.** Photovoltaic properties of DSSCs based on open-ended freestanding TiO<sub>2</sub> nanotube arrays.

ADSSCs	$J_{sc}$ (mA/cm <sup>2</sup> )	$V_{oc}$ (V)	$ff$	$\eta$ (%)
(a) Open-ended freestanding TiO <sub>2</sub> nanotube arrays without any NPs	11.56	0.79	0.67	6.12
(b) Open-ended freestanding TiO <sub>2</sub> nanotube arrays with Ag NPs	12.45	0.79	0.68	6.68
(c) Open-ended freestanding TiO <sub>2</sub> nanotube arrays with large TiO <sub>2</sub> NPs	12.33	0.79	0.68	6.62
(d) Open-ended freestanding TiO <sub>2</sub> nanotube arrays with Ag NPs and large TiO <sub>2</sub> NPs	12.74	0.78	0.71	7.05

Although TiO<sub>2</sub> nanotube array-based DSSCs have great potential, as far as we know, the theoretical maximum improvement by Ag NPs or a TiO<sub>2</sub> scattering layer of TiO<sub>2</sub> nanotube-based DSSCs has not yet been reported. However, the open-ended TiO<sub>2</sub> nanotube-based devices exhibited an increase in one-sun efficiency from 5.3% to 9.1%, corresponding to a 70% increase, which is a much higher increase than we achieved [35]. We believe that there is ample room to improve efficiency by combining each parameter in an optimal condition based on theoretical studies.

### 3. Materials and Methods

#### 3.1. Materials

Titanium plates (99.7% purity, 0.25 mm thickness, Alfa Aesar, Ward Hill, MA, USA), ammonium fluoride (NH<sub>4</sub>F, Showa Chemical Industry Co., Beijing, China, 97.0%), ethylene glycol (Daejung Chemical, Siheung, Korea, 99%), hydrogen peroxide (H<sub>2</sub>O<sub>2</sub>, Daejung Chemical, Siheung, Korea, 30%), fluorine-doped tin oxide (FTO) glass (Pilkington, St. Helens, UK, TEC-A7), titanium diisopropoxide bis(acetylacetonate) solution (Aldrich, St. Louis, MS, USA, 75 wt % in isopropanol), n-butanol (Daejung Chemical, Siheung, Korea, 99%), TiO<sub>2</sub> paste (Ti-Nanoxide T/SP, Solaronix, Aubonne, Switzerland), scattering TiO<sub>2</sub> paste (18NR-AO, Dyesol, Queanbeyan, Australia), silver nitrate (AgNO<sub>3</sub>, Aldrich, St. Louis, MS, USA, 99%), titanium chloride (TiCl<sub>4</sub>, Aldrich, St. Louis, MS, USA, 0.09 M in 20% HCl), dye (cis-diisothiocyanato-bis(2,2'-bipyridyl-4,4'-dicarboxylato) ruthenium(II) bis(tetrabutylammonium) (N719, Solaronix, Aubonne, Switzerland), chloroplatinic acid hexahydrate (H<sub>2</sub>PtCl<sub>6</sub>·6H<sub>2</sub>O, Aldrich, St. Louis, MS, USA), 1-butyl-3-methyl-imidazolium iodide (BMII, Aldrich, St. Louis, MS, USA, 99%), iodine (I<sub>2</sub>, Aldrich, St. Louis, MS, USA, 99%), guanidium thiocyanate (GSCN, Aldrich, St. Louis, MS, USA, 99%), 4-tertbutylpyridine (TBP, Aldrich, St. Louis, MS, USA, 96%), acetonitrile (CH<sub>3</sub>CN, Aldrich, St. Louis, MS, USA, 99.8%), and valeronitrile (CH<sub>3</sub>(CH<sub>2</sub>)<sub>3</sub>CN, Aldrich, St. Louis, MS, USA, 99.5%) were obtained from commercial manufacturers.

#### 3.2. Preparation of Freestanding TiO<sub>2</sub> Nanotube Arrays

TiO<sub>2</sub> nanotube arrays were prepared by anodization of thin Ti plates. Ti anodization was carried out in an electrolyte composed of 0.8 wt % NH<sub>4</sub>F and 2 vol % H<sub>2</sub>O in ethylene glycol at 25 °C and at a constant voltage of 60 V direct current (DC) for 2 h. After being anodized, the Ti plates were annealed at 500 °C for 1 h under ambient conditions to improve the crystallinity of the TiO<sub>2</sub> nanotube arrays, and then a secondary anodization was conducted at a constant voltage of 30 V DC for 10 min. The Ti plates were immersed in 10% H<sub>2</sub>O<sub>2</sub> solution for several hours in order to detach the TiO<sub>2</sub> nanotube arrays from the Ti plates and produce freestanding TiO<sub>2</sub> nanotube arrays. The bottom of the TiO<sub>2</sub> nanotube arrays was removed by ion milling with Ar<sup>+</sup> bombardment for several minutes in order to produce open-ended freestanding TiO<sub>2</sub> nanotube arrays.

### 3.3. Preparation of Ag NPs in the Channel of Freestanding TiO<sub>2</sub> Nanotube Arrays

A TiO<sub>2</sub> blocking layer was formed on FTO glass by spin-coating with 5 wt % titanium di-isopropoxide bis(acetylacetonate) in butanol, followed by annealing at 500 °C for 1 h under ambient conditions to induce crystallinity. A TiO<sub>2</sub> paste was coated onto the TiO<sub>2</sub> blocking/FTO glass using the doctor blade method, and closed- and open-ended freestanding TiO<sub>2</sub> nanotube arrays were then introduced onto the TiO<sub>2</sub> paste. The substrate was annealed at 500 °C for 1 h under ambient conditions to enhance the adhesion between the TiO<sub>2</sub> NPs and freestanding TiO<sub>2</sub> nanotube arrays. The substrate was dipped in 0.3 mM AgNO<sub>3</sub> aqueous solution and exposed to 254 nm UV irradiation. The substrate was treated with 10 mM TiCl<sub>4</sub> solution at 50 °C for 30 min and then annealed at 500 °C for 1 h.

### 3.4. Fabrication of DSSCs with Freestanding TiO<sub>2</sub> Nanotube Arrays with Channels Containing Ag NPs

A substrate that consisted of freestanding TiO<sub>2</sub> nanotube arrays with channels containing Ag NPs was coated with ~400 nm TiO<sub>2</sub> NPs for scattering and then annealed at 500 °C for 1 h under ambient conditions to induce crystallinity and adhesion. The substrate was immersed in a dye solution at 50 °C for 8 h to function as a working electrode. The working electrode was sandwiched with a counter electrode, Pt on FTO glass, by a 60- $\mu$ m-thick hot-melt sheet and filled with electrolyte solution composed of 0.7 M 1-butyl-3-methyl-imidazolium iodide (BMII), 0.03 M I<sub>2</sub>, 0.1 M guanidium thiocyanate (GSCN), and 0.5 M 4-tertbutylpyridine (TBP) in a mixture of acetonitrile and valeronitrile (85:15, *v/v*).

### 3.5. Instruments

The morphology, thickness, size, and presence of Ag NPs in the channels of freestanding TiO<sub>2</sub> nanotube arrays were confirmed using a field emission scanning electron microscope (FE-SEM, JSM-6330F, JEOL Inc., Tokyo, Japan) and the high angular annular dark field (HAADF) technique with a scanning transmission electron microscope (TEM, JEM-2200FS, JEOL Inc., Tokyo, Japan). The current density–voltage (*J–V*) characteristics and the incident photon-to-current conversion efficiency (IPCE) of the DSSCs were measured using an electrometer (Keithley 2400, Keithley Instruments, Inc., Cleveland, OH, USA) under AM 1.5 illumination (100 mW/cm<sup>2</sup>) provided by a solar simulator (1 kW xenon with AM 1.5 filter, PEC-L01, Peccell Technologies, Inc., Yokohama, Kanagawa, Japan), or using a solar cell IPCE measurement System (K3100, McScience Inc., Suwon, Korea) with reference to the calibrated diode.

## 4. Conclusions

In this study, we compared the natural consequences of altering three parameters, the plasmonic effect, the scattering effect, and open- *vs.* closed-ended freestanding TiO<sub>2</sub> nanotubes, as a basic means of exploring improvements in efficiency. We demonstrated that the plasmonic and scattering effects enhanced the energy conversion efficiency of freestanding TiO<sub>2</sub> nanotube arrays in DSSCs. Ag NPs were added to the channels of TiO<sub>2</sub> nanotube arrays by UV irradiation to induce a plasmonic effect, and large TiO<sub>2</sub> NPs were introduced to TiO<sub>2</sub> nanotube arrays to induce a scattering effect. The energy conversion efficiency of DSSCs with both Ag NPs and large TiO<sub>2</sub> NPs was higher than that of DSSCs without Ag NPs owing to the plasmonic effect, and it was higher than that of DSSCs without large TiO<sub>2</sub> NPs owing to the scattering effect. Compared to closed-ended freestanding TiO<sub>2</sub> nanotube arrays, open-ended freestanding TiO<sub>2</sub> nanotube arrays [40] exhibited enhanced energy conversion efficiency. We demonstrate that Ag NPs, TiO<sub>2</sub> NPs, and open-ended freestanding TiO<sub>2</sub> nanotube arrays enhanced the energy conversion efficiency; furthermore, the combination of all components exhibited the highest energy conversion efficiency. Our research suggests that the energy conversion efficiency of DSSCs is improved by both the plasmonic and scattering effects. This knowledge has applications in organic solar cells, hybrid solar cells, and perovskite solar cells.

**Author Contributions:** Won-Yeop Rho, Myeung-Hwan Chun, Jung Sang Suh and Bong-Hyun Jun designed the research and wrote the manuscript. Won-Yeop Rho, Ho-Sub Kim and Hyung-Mo Kim carried out experiments. All authors discussed the results and commented on the manuscript. Won-Yeop Rho and Bong-Hyun Jun guided all aspects of the work.

**Conflicts of Interest:** The authors declare no conflict of interest.

## References

- Oregan, B.; Gratzel, M. A low-cost, high-efficiency solar-cell based on dye-sensitized colloidal TiO<sub>2</sub> films. *Nature* **1991**, *353*, 737–740. [CrossRef]
- Lim, J.; Kim, H.A.; Kim, B.H.; Han, C.H.; Jun, Y. Reversely fabricated dye-sensitized solar cells. *RSC Adv.* **2014**, *4*, 243–247. [CrossRef]
- Jo, Y.; Yun, Y.J.; Khan, M.A.; Jun, Y. Densely packed setose ZnO nanorod arrays for dye sensitized solar cells. *Synth. Met.* **2014**, *198*, 137–141. [CrossRef]
- Kim, J.; Lim, J.; Kim, M.; Lee, H.S.; Jun, Y.; Kim, D. Fabrication of carbon-coated silicon nanowires and their application in dye-sensitized solar cells. *ACS Appl. Mater. Interfaces* **2014**, *6*, 18788–18794. [CrossRef] [PubMed]
- Ko, K.W.; Lee, M.; Sekhon, S.; Balasingam, S.K.; Han, C.H.; Jun, Y. Efficiency enhancement of dye-sensitized solar cells by the addition of an oxidizing agent to the TiO<sub>2</sub> paste. *Chem. Sus. Chem.* **2013**, *6*, 2117–2123. [CrossRef] [PubMed]
- Balasingam, S.K.; Kang, M.G.; Jun, Y. Metal substrate based electrodes for flexible dye-sensitized solar cells: Fabrication methods, progress and challenges. *Chem. Commun.* **2013**, *49*, 11457–11475. [CrossRef] [PubMed]
- Jung, C.-L.; Lim, J.; Park, J.-H.; Kim, K.-H.; Han, C.-H.; Jun, Y. High performance dye sensitized solar cells by adding titanate co-adsorbant. *RSC Adv.* **2013**, *3*, 20488–20491. [CrossRef]
- Nath, N.C.D.; Ahammad, A.; Sarker, S.; Rahman, M.; Lim, S.-S.; Choi, W.-Y.; Lee, J.-J. Carbon nanotubes on fluorine-doped tin oxide for fabrication of dye-sensitized solar cells at low temperature condition. *J. Nanosci. Nanotechnol.* **2012**, *12*, 5373–5380. [CrossRef] [PubMed]
- Deb Nath, N.C.; Lee, H.J.; Choi, W.-Y.; Lee, J.-J. Effects of phenylalkanoic acids as co-adsorbents on the performance of dye-sensitized solar cells. *J. Nanosci. Nanotechnol.* **2013**, *13*, 7880–7885. [CrossRef]
- Grätzel, M. Dye-sensitized solar cells. *J. Photochem. Photobiol. C* **2003**, *4*, 145–153. [CrossRef]
- Du, L.C.; Furube, A.; Hara, K.; Katoh, R.; Tachiya, M. Mechanism of particle size effect on electron injection efficiency in ruthenium dye-sensitized TiO<sub>2</sub> nanoparticle films. *J. Phys. Chem. C* **2010**, *114*, 8135–8143. [CrossRef]
- Ahn, J.; Lee, K.C.; Kim, D.; Lee, C.; Lee, S.; Cho, D.W.; Kyung, S.; Im, C. Synthesis of novel ruthenium dyes with thiophene or thienothiophene substituted terpyridyl ligands and their characterization. *Mol. Cryst. Liquid Cryst.* **2013**, *581*, 45–51. [CrossRef]
- Kwon, T.H.; Kim, K.; Park, S.H.; Annamalai, A.; Lee, M.J. Effect of seed particle size and ammonia concentration on the growth of ZnO nanowire arrays and their photoconversion efficiency. *Int. J. Nanotechnol.* **2013**, *10*, 681–691. [CrossRef]
- Rho, W.-Y.; Kim, H.-S.; Lee, S.H.; Jung, S.; Suh, J.S.; Hahn, Y.-B.; Jun, B.-H. Front-illuminated dye-sensitized solar cells with Ag nanoparticle-functionalized freestanding TiO<sub>2</sub> nanotube arrays. *Chem. Phys. Lett.* **2014**, *614*, 78–81. [CrossRef]
- Hwang, K.-J.; Cho, D.W.; Lee, J.-W.; Im, C. Preparation of nanoporous TiO<sub>2</sub> electrodes using different mesostructured silica templates and improvement of the photovoltaic properties of DSSCs. *New J. Chem.* **2012**, *36*, 2094–2100. [CrossRef]
- Nath, N.C.D.; Kim, J.C.; Kim, K.P.; Yim, S.; Lee, J.-J. Deprotonation of N<sub>3</sub> adsorbed on TiO<sub>2</sub> for high-performance dye-sensitized solar cells (DSSCs). *J. Mater. Chem. A* **2013**, *1*, 13439–13442. [CrossRef]
- Nakade, S.; Saito, Y.; Kubo, W.; Kitamura, T.; Wada, Y.; Yanagida, S. Influence of TiO<sub>2</sub> nanoparticle size on electron diffusion and recombination in dye-sensitized TiO<sub>2</sub> solar cells. *J. Phys. Chem. B* **2003**, *107*, 8607–8611. [CrossRef]
- Zhu, K.; Kopydakis, N.; Neale, N.R.; van de Lagemaat, J.; Frank, A.J. Influence of surface area on charge transport and recombination in dye-sensitized TiO<sub>2</sub> solar cells. *J. Phys. Chem. B* **2006**, *110*, 25174–25180. [CrossRef] [PubMed]

19. Chung, K.-H.; Rahman, M.M.; Son, H.-S.; Lee, J.-J. Development of well-aligned TiO<sub>2</sub> nanotube arrays to improve electron transport in dye-sensitized solar cells. *Int. J. Photoenergy* **2012**, *2012*. [CrossRef]
20. Lee, G.I.; Nath, N.C.D.; Sarker, S.; Shin, W.H.; Ahammad, A.S.; Kang, J.K.; Lee, J.-J. Fermi energy level tuning for high performance dye sensitized solar cells using sp<sup>2</sup> selective nitrogen-doped carbon nanotube channels. *Phys. Chem. Chem. Phys.* **2012**, *14*, 5255–5259. [CrossRef] [PubMed]
21. Nath, N.C.D.; Sarker, S.; Ahammad, A.S.; Lee, J.-J. Spatial arrangement of carbon nanotubes in TiO<sub>2</sub> photoelectrodes to enhance the efficiency of dye-sensitized solar cells. *Phys. Chem. Chem. Phys.* **2012**, *14*, 4333–4338. [CrossRef] [PubMed]
22. Yadav, S.K.; Madeshwaran, S.R.; Cho, J.W. Synthesis of a hybrid assembly composed of titanium dioxide nanoparticles and thin multi-walled carbon nanotubes using “click chemistry”. *J. Colloid Interface Sci.* **2011**, *358*, 471–476. [CrossRef] [PubMed]
23. Bavykin, D.V.; Parmon, V.N.; Lapkin, A.A.; Walsh, F.C. The effect of hydrothermal conditions on the mesoporous structure of TiO<sub>2</sub> nanotubes. *J. Mater. Chem.* **2004**, *14*, 3370–3377. [CrossRef]
24. Macak, J.M.; Tsuchiya, H.; Schmuki, P. High-aspect-ratio TiO<sub>2</sub> nanotubes by anodization of titanium. *Angew. Chem. Int. Ed. Engl.* **2005**, *44*, 2100–2102. [CrossRef] [PubMed]
25. Law, M.; Greene, L.E.; Johnson, J.C.; Saykally, R.; Yang, P. Nanowire dye-sensitized solar cells. *Nat. Mater.* **2005**, *4*, 455–459. [CrossRef] [PubMed]
26. Mor, G.K.; Varghese, O.K.; Paulose, M.; Shankar, K.; Grimes, C.A. A review on highly ordered, vertically oriented TiO<sub>2</sub> nanotube arrays: Fabrication, material properties, and solar energy applications. *Sol. Energy Mater. Sol. Cells* **2006**, *90*, 2011–2075. [CrossRef]
27. Jennings, J.R.; Ghicov, A.; Peter, L.M.; Schmuki, P.; Walker, A.B. Dye-sensitized solar cells based on oriented TiO<sub>2</sub> nanotube arrays: Transport, trapping, and transfer of electrons. *J. Am. Chem. Soc.* **2008**, *130*, 13364–13372. [CrossRef] [PubMed]
28. Rho, W.-Y.; Jeon, H.; Kim, H.-S.; Chung, W.-J.; Suh, J.S.; Jun, B.-H. Recent progress in dye-sensitized solar cells for improving efficiency: TiO<sub>2</sub> nanotube arrays in active layer. *J. Nanomater.* **2015**, *2015*. [CrossRef]
29. Atwater, H.A.; Polman, A. Plasmonics for improved photovoltaic devices. *Nat. Mater.* **2010**, *9*, 865–865. [CrossRef]
30. Standridge, S.D.; Schatz, G.C.; Hupp, J.T. Distance dependence of plasmon-enhanced photocurrent in dye-sensitized solar cells. *J. Am. Chem. Soc.* **2009**, *131*, 8407–8409. [CrossRef] [PubMed]
31. Brown, M.D.; Suteewong, T.; Kumar, R.S.S.; D’Innocenzo, V.; Petrozza, A.; Lee, M.M.; Wiesner, U.; Snaith, H.J. Plasmonic dye-sensitized solar cells using core-shell metal-insulator nanoparticles. *Nano Lett.* **2011**, *11*, 438–445. [CrossRef] [PubMed]
32. Qi, J.F.; Dang, X.N.; Hammond, P.T.; Belcher, A.M. Highly efficient plasmon-enhanced dye-sensitized solar cells through metal@oxide core-shell nanostructure. *ACS Nano* **2011**, *5*, 7108–7116. [CrossRef] [PubMed]
33. Rho, C.; Min, J.H.; Suh, J.S. Barrier layer effect on the electron transport of the dye-sensitized solar cells based on TiO<sub>2</sub> nanotube arrays. *J. Phys. Chem. C* **2012**, *116*, 7213–7218. [CrossRef]
34. Rho, W.-Y.; Chun, M.-H.; Kim, H.-S.; Hahn, Y.-B.; Suh, J.S.; Jun, B.-H. Improved energy conversion efficiency of dye-sensitized solar cells fabricated using open-ended TiO<sub>2</sub> nanotube arrays with scattering layer. *Bull. Korean Chem. Soc.* **2014**, *35*. [CrossRef]
35. Lin, C.-J.; Yu, W.-Y.; Chien, S.-H. Transparent electrodes of ordered opened-end TiO<sub>2</sub>-nanotube arrays for highly efficient dye-sensitized solar cells. *J. Mater. Chem.* **2010**, *20*, 1073–1077. [CrossRef]
36. Li, L.-L.; Chen, Y.-J.; Wu, H.-P.; Wang, N.S.; Diau, E.W.-G. Detachment and transfer of ordered TiO<sub>2</sub> nanotube arrays for front-illuminated dye-sensitized solar cells. *Energy Environ. Sci.* **2011**, *4*, 3420–3425. [CrossRef]
37. Hahn, E.; Jeong, D.; Cha, M.G.; Choi, J.M.; Pham, X.-H.; Kim, H.-M.; Kim, H.; Lee, Y.-S.; Jeong, D.H.; Jung, S. β-CD dimer-immobilized Ag assembly embedded silica nanoparticles for sensitive detection of polycyclic aromatic hydrocarbons. *Sci. Rep.* **2016**, *6*. [CrossRef] [PubMed]
38. Arockia Jency, D.; Umadevi, M.; Sathe, G. Sers detection of polychlorinated biphenyls using β-cyclodextrin functionalized gold nanoparticles on agriculture land soil. *J. Raman Spectrosc.* **2015**, *46*, 377–383. [CrossRef]

39. Xie, Y.; Wang, X.; Han, X.; Xue, X.; Ji, W.; Qi, Z.; Liu, J.; Zhao, B.; Ozaki, Y. Sensing of polycyclic aromatic hydrocarbons with cyclodextrin inclusion complexes on silver nanoparticles by surface-enhanced Raman scattering. *Analyst* **2010**, *135*, 1389–1394. [CrossRef] [PubMed]
40. Kim, H.-Y.; Rho, W.-Y.; Lee, H.Y.; Park, Y.S.; Suh, J.S. Aggregation effect of silver nanoparticles on the energy conversion efficiency of the surface plasmon-enhanced dye-sensitized solar cells. *Sol. Energy* **2014**, *109*, 61–69. [CrossRef]



© 2016 by the authors. Licensee MDPI, Basel, Switzerland. This article is an open access article distributed under the terms and conditions of the Creative Commons Attribution (CC BY) license (<http://creativecommons.org/licenses/by/4.0/>).



Article

# Influence of Nitrogen Doping on Device Operation for TiO<sub>2</sub>-Based Solid-State Dye-Sensitized Solar Cells: Photo-Physics from Materials to Devices

Jin Wang <sup>1</sup>, Kosti Tapio <sup>2</sup>, Aurélie Habert <sup>1</sup>, Sebastien Sorgues <sup>3</sup>, Christophe Colbeau-Justin <sup>3</sup>, Bernard Ratier <sup>4</sup>, Monica Scarisoreanu <sup>5</sup>, Jussi Toppari <sup>2</sup>, Nathalie Herlin-Boime <sup>1,\*</sup> and Johann Bouclé <sup>4,\*</sup>

<sup>1</sup> IRAMIS/NIMBE/LEDNA, UMR 3685, CEA Saclay, 91191 Gif sur Yvette, France; 516208050@qq.com (J.W.); aurelie.habert@cea.fr (A.H.)

<sup>2</sup> Nanoscience Center, Department of Physics, University of Jyväskylä, P.O. Box 35, 40014 Jyväskylä, Finland; kosti.t.o.tapio@jyu.fi (K.T.); j.jussi.toppari@jyu.fi (J.T.)

<sup>3</sup> Laboratoire de Chimie Physique, UMR8000, Université Paris-Sud, 91405 Orsay, France; sebastien.sorgues@u-psud.fr (S.S.); christophe.colbeau-justin@u-psud.fr (C.C.-J.)

<sup>4</sup> XLIM UMR 7252, Université de Limoges/CNRS, 87060 Limoges Cedex, France; bernard.ratier@unilim.fr

<sup>5</sup> National Institute for Lasers Plasma and Radiation Physics, P.O. Box MG 36, R-077125 Bucharest, Romania; monica.scarisoreanu@inflpr.ro

\* Correspondence: nathalie.herlin@cea.fr (N.H.); johann.boucle@unilim.fr (J.B.); Tel.: +33-1-6908-3684 (N.H.); +33-5-8750-6762 (J.B.)

Academic Editors: Guanying Chen, Zhijun Ning and Hans Agren

Received: 19 December 2015; Accepted: 13 February 2016; Published: 23 February 2016

**Abstract:** Solid-state dye-sensitized solar cells (ssDSSC) constitute a major approach to photovoltaic energy conversion with efficiencies over 8% reported thanks to the rational design of efficient porous metal oxide electrodes, organic chromophores, and hole transporters. Among the various strategies used to push the performance ahead, doping of the nanocrystalline titanium dioxide (TiO<sub>2</sub>) electrode is regularly proposed to extend the photo-activity of the materials into the visible range. However, although various beneficial effects for device performance have been observed in the literature, they remain strongly dependent on the method used for the production of the metal oxide, and the influence of nitrogen atoms on charge kinetics remains unclear. To shed light on this open question, we synthesized a set of N-doped TiO<sub>2</sub> nanopowders with various nitrogen contents, and exploited them for the fabrication of ssDSSC. Particularly, we carefully analyzed the localization of the dopants using X-ray photo-electron spectroscopy (XPS) and monitored their influence on the photo-induced charge kinetics probed both at the material and device levels. We demonstrate a strong correlation between the kinetics of photo-induced charge carriers probed both at the level of the nanopowders and at the level of working solar cells, illustrating a direct transposition of the photo-physic properties from materials to devices.

**Keywords:** solid-state dye-sensitized solar cells; TiO<sub>2</sub>; nitrogen doping; photo-physics; photo-response; spiro-OMeTAD

## 1. Introduction

Since the pioneering work of Bach *et al.* in 1998 [1], solid-state dye-sensitized solar cells (ssDSSC) based on the organic molecular glass 2',7,7'-Tetrakis-(*N,N*-di-4-methoxy phenylamino)-9,9'-spirobifluorene (spiro-OMeTAD) as p-type solid-state electrolyte have demonstrated constant performance improvement, thanks to the rational engineering of organic sensitizers and doping



strategies. In particular, doping of hole-transporting materials (HTM) by cobalt complexes [2] or organic compounds such as 1,1,2,2-tetrachloroethan (TeCA) [3] have led to power conversion efficiencies over 7% under standard illumination conditions, illustrating the relevance of hybrid solid-state approaches for solar energy conversion. Improved spectral coverage of the solar spectrum as well as enhanced light harvesting efficiencies are now achieved by exploiting various metal-free organic dyes [4], such as porphyrin [5] or arylamine derivatives [6]. More recently, and apart from perovskite solar cells [7,8], which are not the primary topic of this article, ssDSSC based on TiO<sub>2</sub> porous electrodes have received additional benefits from the intensive developments made on HTMs [9–11]. Consequently, efficiencies over 8% were demonstrated using p-type perovskite materials [12,13] or Copper phenanthroline complexes [14] such as HTM.

In a typical device, the TiO<sub>2</sub> porous electrode acts simultaneously as a high specific area substrate for dye adsorption, and as the electron transporting material [15,16]. The metal oxide photo-electrode is therefore crucial for both light absorption and current generation. Several approaches have been proposed to improve the charge generation and collection efficiencies of nanostructured metal oxide electrodes using alternative electrode morphologies, such as nanorods or hierarchical structures [17]; substitution of TiO<sub>2</sub> by other metal oxides such as ZnO or SnO<sub>2</sub> [18]; deposition of insulating oxide shell on TiO<sub>2</sub> [19,20]; insertion of metallic (Au, Ag, . . .) [21,22] or non-metallic (S, N, *etc.*) [23–26] elements. Among all of these strategies, the doping of TiO<sub>2</sub> materials by nitrogen can exploit several effects, which can positively affect device performance. Asahi *et al.* reported in 2001 that, compared to pure TiO<sub>2</sub>, N-doped TiO<sub>2</sub> exhibits a broader absorption range that extends into the visible up to 500 nm [27]. Since then, some attention has been paid to the origin of this additional absorption feature [28]. In a theoretical approach [29,30], Di Valentin *et al.* pointed out that if N atoms are in substitutional positions, N2p states can lie 0.13 eV above the top of the valence band of TiO<sub>2</sub>. Moreover, if N is found in interstitial positions or at the surface of the nanoparticles, NO species can be formed and introduce  $\pi^*$ -NO-states into the band gap (0.73 eV above the top of the valence band). Asahi *et al.* investigated the effects of different nitrification conditions, and found out that substitutional N can be chemically more stable in the presence of oxygen vacancies [31]. Therefore, benefits induced by the N-doping rapidly raised the interest of researchers in the fields of photo-catalysis and photovoltaics.

In the field of hybrid solar cells, Ma *et al.* demonstrated an N-TiO<sub>2</sub> based liquid DSSC presenting an improved efficiency and stability than that prepared from a pristine TiO<sub>2</sub> electrode [24]. An enhancement of the incident photon to charge carrier efficiency (IPCE) was observed within the 380–520 nm range, related to the contribution of nitrogen to the absorption of N-TiO<sub>2</sub> powders. Tian *et al.* analyzed the electron lifetime in the sol-gel synthesized N-TiO<sub>2</sub> solar cells and found that the formation of O-Ti-N in the TiO<sub>2</sub> lattice could retard charge recombination reactions at the TiO<sub>2</sub> electrode/electrolyte interface [32]. In addition, the insertion of N atoms can alter the Fermi level of electrons in the oxide [33], potentially leading to a slight increase of the open-circuit voltage of the cell, as well as of the overall device efficiency. However, most of the studies reported on N-doping were carried out on liquid DSSC. In our previous study [34], we reported on solid-state DSSCs based on N-doped TiO<sub>2</sub> electrodes processed from nanocrystals synthesized by laser pyrolysis. We provided evidence of a significant contribution from the N-doped electrode to the generation of charge carriers, as a secondary current generation pathway. Although recent studies based on quasi-solid state DSSC devices demonstrated similar trends [35], no clear correlation between material properties and device performance were drawn.

In this work, we systematically report on the influence of nitrogen doping on ssDSSC device operation and photo-physics properties. To this end, we synthesized a set of TiO<sub>2</sub> nano-particles doped with different levels of nitrogen. Using complementary characterization techniques, both at the material and device levels, we focus on the impact of the presence of N atoms on the photo-generated charges in the metal oxide, and discuss its implications on the photovoltaic performance of the cells. X-ray photoelectron spectroscopy (XPS) is exploited to monitor the exact location of N atoms in the TiO<sub>2</sub> crystalline sites, while time-resolved microwave conductivity (TRMC) is used to assess its

impact on photo-generated charge dynamics. Photo-conductivity measurements performed on test devices based on un-doped and N-doped porous TiO<sub>2</sub> electrodes are finally discussed with regard to charge recombination kinetics measured on full devices using transient photo-voltage. Considering the different treatments applied to the powders for the preparation of porous electrodes suitable for device testing, such methodology is particularly relevant to reveal the influence of the nitrogen doping both in the starting powders and in the final solar cells.

## 2. Results

### 2.1. Properties of the Starting Powders

Laser pyrolysis was used to synthesize a set of N-doped TiO<sub>2</sub> nanopowders [36]. This technique is an efficient method for the production of well-controlled nanocrystals with tunable properties, well-adapted for the photovoltaic application [37,38]. Here, the precursor mixture included ammonia as the source of N atoms. More details on the experimental conditions used for the synthesis of the powders can be found in Supplementary materials (Table S1), which also summarizes the chemical composition of the samples. In all cases, the as-synthesized nanopowders contain free carbon phases easily removed by thermal annealing under air. This treatment, which does not alter the main physical properties of the samples [36], was therefore applied to all powders considered in the following parts of this article. Figure 1 presents the transmission electron microscopy (TEM) image of a typical TiO<sub>2</sub> powders (doped with nitrogen in this case).

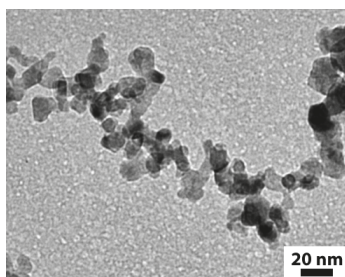


**Figure 1.** Transmission electron microscopy (TEM) image of a typical N-doped TiO<sub>2</sub> powder (after annealing treatment in air). The nitrogen content is 0.2 wt % in this case.

We observed a typical “chain-like” morphology of nano-scaled grains (mean diameter within 10 to 20 nm), typical of gas phase synthesis methods.

Table 1 summarizes the main physical parameters of the powders synthesized in this work, including nitrogen content, crystalline phase and crystallite diameter extracted from X-ray diffraction (XRD), as well as specific area and mean particle diameter estimated from the BET (Brunauer, Emmett, and Teller) method. The Spurr and Scherrer equations were used on the XRD patterns (Supplementary materials, Figure S1) to extract the Anatase to rutile crystalline fraction and the mean crystal diameter [39,40].

**Table 1.** Main physico-chemical properties of the TiO<sub>2</sub> and N-doped TiO<sub>2</sub> powders including N content determined by elemental analysis, anatase crystalline fraction and mean crystal diameter obtained by X-ray diffraction (XRD), as well as Brunauer, Emmett, and Teller (BET) specific area and mean grain diameter.

Sample	N content (wt %)	Data extracted from XRD		BET analysis	
		Fraction of anatase (%)	Mean crystal diameter (nm)	Specific area (m <sup>2</sup> g <sup>-1</sup> )	Mean grain diameter (nm)
TiO <sub>2</sub>	<<0.1	94	15.6	77	20
N-TiO <sub>2</sub> -0.1	0.1	80	12.0	86	18
N-TiO <sub>2</sub> -0.2	0.2	90	11.4	86	18
N-TiO <sub>2</sub> -0.3	0.3	94	12.4	90	17
N-TiO <sub>2</sub> -0.6	0.6	94	15.0	96	16

The N content in the final powders is directly driven by the level of ammonia in the precursor mixture (see Supplementary materials Table S1). The sizes estimated by BET are slightly larger than those extracted from the XRD analysis, revealing the presence of amorphous regions in the powders, or a slight particle agglomeration [36]. Both the crystalline phase and particle diameter are only slightly dependent on the doping level, leading to five powders with rather comparable morphologic features.

Regarding their optical properties, N-doped TiO<sub>2</sub> powders exhibit a dominant yellow color (see inset of Figure 2), indicating a shift in their absorption threshold towards the visible range. Figure 2 shows the Kubelka–Munk function of the powders calculated from diffused reflectance measurements. Comparing to pure titania, N-doped TiO<sub>2</sub> powders exhibit an additional absorption band between 370 and 550 nm. This optical feature, which was discussed in previous reports [24,34], can be assigned to the influence of nitrogen on the energetic level of TiO<sub>2</sub>, through a mixing of N and O 2p states [27]. We observe that the intensity of this additional absorption band increases with the N doping level.

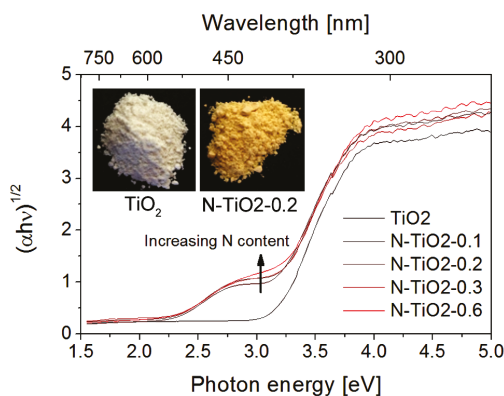


**Figure 2.** Optical data extracted from diffuse reflectance measurements on the TiO<sub>2</sub> and N-doped TiO<sub>2</sub> powders. The inset presents pictures of the N-TiO<sub>2</sub>-0.2 sample (N content of 0.2 wt %) compared to the TiO<sub>2</sub> reference sample.

A more detailed picture of the local environment of nitrogen atoms in the metal oxide structure is drawn from X-ray photoelectron spectroscopy (XPS) applied on the powders. Data associated with annealed powders are presented in Figure 3, together with their deconvolution, while data associated with as-prepared samples are presented in Supplementary materials (Figures S2 and S3, respectively).

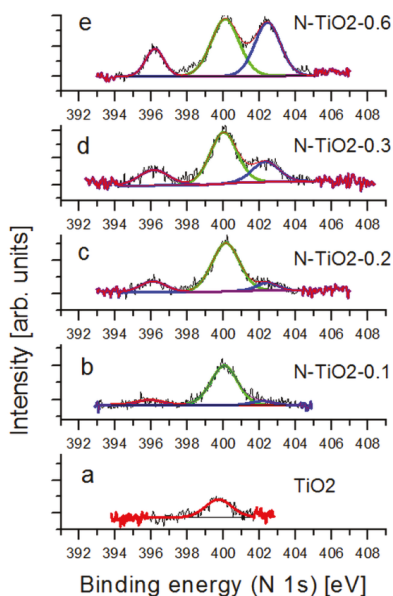


**Figure 3.** XPS spectra (N 1s) of the undoped and N-doped TiO<sub>2</sub> powders as a function of N content (from 0 to 0.6 wt %).

Concerning the pure TiO<sub>2</sub> sample, the only peak appearing at 399.7 eV in the spectra, both before and after annealing (see Supplementary materials), can be attributed to N<sub>2</sub> species chemically adsorbed on the TiO<sub>2</sub> surface, which is a feature being often observed in the literature [41]. The situation is more complex in the case of the N-doped powders. Three main contributions centered at 396.2 eV, 399.9 eV, and 402.2 eV are observed, and their exact assignment is still under debate in the literature [27,32,41,42]. The peak at 396.2 eV is usually attributed to Ti-N bonds and it thus implies that N atoms are situated at substitutional sites in the TiO<sub>2</sub> lattice [24]. In most of the cases, the peak at 399.9 eV is assigned to O-Ti-N bonds—in other words, to interstitial nitrogen atoms [29,32,43,44]. This assignment is consistent with the high electronegativity of oxygen, which reduces the electron density on nitrogen compared to Ti-N. As a result, the binding energy of O-Ti-N is slightly larger than that of Ti-N. However, several groups associate this peak with NO in interstitial sites or NO<sub>2</sub> in substitutional sites [31]. We reckon that part of this peak can also result from chemically adsorbed N<sub>2</sub> species on the TiO<sub>2</sub> surface, like in undoped TiO<sub>2</sub>. However, comparing the absolute intensities of the signals, we can safely conclude that the peak at 399.9 eV in our N-TiO<sub>2</sub> samples can be assigned to interstitial nitrogen. The last peak at 402.2 eV is often observed in the literature [24]. Asahi *et al.* [27], as well as Tian *et al.* [32], assigned it to atomically adsorbed N species. Therefore, we associate this peak as the signature of nitrogen present at the surface of the TiO<sub>2</sub> particles. These surface N atoms should however be quite different than the adsorbed N<sub>2</sub> species observed on the surface of the pure TiO<sub>2</sub> samples (Figure 3a), as the associated binding energies are quite dispersed on all N-doped spectra (Figure 3b–e). Considering the nature of our samples, this third feature is likely to be associated to NO or NO<sub>2</sub> groups on the particle surface. Table 2 summarizes the relative contributions of the three features associated to nitrogen in the doped samples (see the Supplementary materials for data associated with non-annealed samples, Table S2).

**Table 2.** Relative contributions of the X-ray photoelectron spectroscopy (XPS) peaks observed for samples doped by nitrogen at various contents. The table is presenting data for annealed powders (see Supplementary materials for data associated with as-prepared samples).

Sample	Relative contributions of XPS features		
	Substitutional N (peak at 396 eV)	Interstitial N (peak at 400 eV)	Surface N (peak at 402 eV)
N-TiO <sub>2</sub> -0.1	11%	89%	Not measurable
N-TiO <sub>2</sub> -0.2	16%	74%	9%
N-TiO <sub>2</sub> -0.3	19%	58%	23%
N-TiO <sub>2</sub> -0.6	15%	46%	39%

Comparing the relative contributions of the different peaks in the as-prepared and annealed powders, we observe a significant decrease of the intensity of the 396.2 eV peak with annealing (Table S2 and Table 2), which indicates a significant oxidation of substitutional Nitrogen. DFT calculations performed by Di Valentin *et al.* [40] show that the transition from substitutional to interstitial N is an exothermic process. Under oxygen-poor conditions, substitutional N position is favored. This is typically our case during particle growth, as powders are synthesized under inert or reducing conditions. In the opposite case, the annealing treatment performed at 400 °C in the presence of oxygen results in the rapid oxidation of substitutional nitrogen atoms. Thus, for low nitrogen content, most of the N atoms are located in interstitial positions for annealed powders (about 89% of all nitrogen atoms for sample doped at 0.1 wt %). However, for higher doping levels, not only the percentage of substitutional N increases, but a strong increase of the contribution of surface nitrogen is also observed. For comparison, Wang *et al.* reported that most of the N atoms were located only in interstitial sites for TiO<sub>2</sub> doped with 1.53 atom % of nitrogen [44]. In our case, because substitutional N atoms are always present in as-prepared samples, these types of N atoms are already present at low doping levels. In particular, our analysis suggests that the thermal treatment leads to an overall decrease of the substitutional N present in as-prepared samples (due to the oxygen-free synthesis conditions) and to a migration of the N atoms to the surface of the particles, especially at high doping levels. This feature is an important drawback of nitrogen doping, as free charge generation and current collection is drastically limited by surface states in DSSC and ssDSSC.

## 2.2. Photovoltaic Performance of ssDSSC Based on N-Doped TiO<sub>2</sub> Electrodes

Several independent sets of solid-state dye-sensitized solar cells (ssDSSC) were prepared from the un-doped and doped metal oxide nanopowders following procedures already described [34,37]. Briefly, a metal oxide paste is initially formulated and used to deposit the electrode on FTO/compact TiO<sub>2</sub> substrates. After sintering, porous electrodes of around two microns thick are obtained, which are further sensitized by the D102 indoline dye and infiltrated by the reference spiro-OMeTAD molecular glass acting as HTM. The conventional dopants (lithium salt and *tert*-butylpyridine) are used in our case. SEM cross sections of the infiltrated D102-sensitized electrodes are presented in Supplementary materials for the undoped and N-doped electrodes (Figure S4). In all cases, the solid-state electrolyte is clearly visible down to the bottom of the electrode. This observation is consistent with the morphologies of the starting nanopowders. Rather similar particle morphologies result in similar porous electrode morphology and, keeping all other parameters equal (nature of the dye, HTM concentration, and infiltration parameters), lead to comparable pore filling fractions. The absorption coefficient of the dye-sensitized electrodes, before HTM infiltration (Supplementary materials, Figure S5), does not clearly reveal any additional band associated to N-doping. However, a slight increase in absorption with increasing N content is observed over the entire wavelength range, with a more pronounced effect in the the 400–550 nm region. This region covers both the absorption band related to nitrogen doping in TiO<sub>2</sub> and the absorption band of the D102 dye, usually centered at 480 nm. It is thus reasonable to suggest that nitrogen doping is likely to slightly contribute to this increase of absorption.

However, we believe that the main effect of doping is related to a better sensitization of the electrodes, as previously reported [24,34]. A better dye grafting may also result from a change in surface potential induced by doping [45]. The electrical characteristics of the solar cells under illumination (AM1.5G,  $100 \text{ mW} \cdot \text{cm}^{-2}$ ) are presented in Figure 4, while Table 3 summarizes the corresponding photovoltaic parameters (the electrical characteristics in the dark are presented in Figure S6).

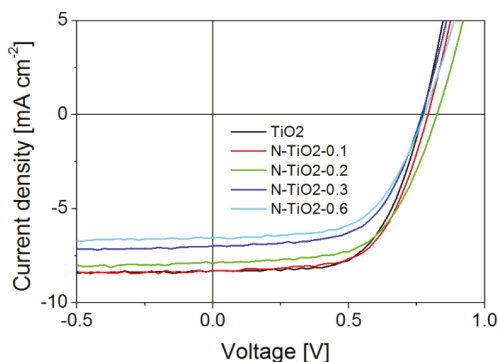


**Figure 4.** Current density/voltage characteristics of ssDSSC solar cells under standard illumination conditions (AM1.5G,  $100 \text{ mW} \cdot \text{cm}^{-2}$ ) for the different N contents.

**Table 3.** Photovoltaic parameters of solar cells based on N-doped  $\text{TiO}_2$  electrodes as a function of Nitrogen content.

Nature of porous electrode	$V_{OC}$ (V)	$J_{SC}$ ( $\text{mA} \cdot \text{cm}^{-2}$ )	FF	$\eta$ (%)
$\text{TiO}_2$	0.77	8.31	0.62	4.0
N-TiO <sub>2</sub> -0.1	0.79	8.31	0.62	4.1
N-TiO <sub>2</sub> -0.2	0.82	7.86	0.60	3.9
N-TiO <sub>2</sub> -0.3	0.77	7.00	0.61	3.3
N-TiO <sub>2</sub> -0.6	0.78	6.55	0.60	3.0

Let us note here that our reference device based on pure  $\text{TiO}_2$  shows state-of-the-art performance considering the material used [37,46]. A slight improvement of solar cell efficiency is evident for low nitrogen content (up to 0.1 wt %) compared to the pure  $\text{TiO}_2$  electrode, before a drastic decrease in performance at higher doping levels. Although the beneficial influence of nitrogen at low doping levels on the overall power conversion efficiency seems not so clear, the trend is unambiguously confirmed through several independent set of devices (not shown here), and is consistent with our preliminary report [34]. The incident photon to charge carrier efficiency (IPCE, or external quantum efficiency EQE) spectra of the cells (Figure S7, Supplementary materials) still especially exhibit an increase of photocurrent generation in the 400–500 nm region that can be related to nitrogen doping. We also note a significant decrease of IPCE as a function of doping level in the 550–650 nm region. This drop in photocurrent generation efficiency is related to the existence of surface-related electronic features, as revealed by photoluminescence spectroscopy on the nanopowders (Figure S8, Supplementary materials). A typical emission at 2.03 eV, associated with radiative recombination of self-trapped excitons at the particle surface, is observed for all powders [38]. This emission is found more pronounced in the presence of N atoms (especially when they are located at the particle surface), and results in a rapid recombination of photo-generated excitons following excitation in this spectral range. This decrease of IPCE in the 550–600 nm region is in fact counterbalancing the relative increase around 450 nm, leading to lower photocurrent as the doping level increases.

Going back to device performance, when the doping level reaches 0.2 to 0.3 wt %, device performance starts to significantly drop. Xie *et al.* also reported this trend, although no threshold was clearly pointed out [47]. For liquid cells, Guo *et al.* observed an optimal doping level of about 0.4 atom % [45], which is consistent with our data if we consider that our best performing device is associated with a nitrogen content of 0.1 wt %.

If we carefully check the photovoltaic parameters of the cells, the open circuit voltage of the N-doped devices is slightly improved compared to pure TiO<sub>2</sub>, as usually observed in the literature [24,48]. This increase is likely to be due to a slight shift of the quasi-Fermi level of electrons in N-TiO<sub>2</sub> [29], especially if we consider that nitrogen is more concentrated at the particle surface. The short-circuit current density is at the maximum for both the un-doped device and for the one based on the lowest Nitrogen content (N-TiO<sub>2</sub>-0.1), before decreasing for a higher doping level. In most of the cases, larger currents are evident for N-doped devices when the doping level is near this optimum concentration. This improved photocurrent, also observed in our preliminary study [34], was attributed to a beneficial contribution of nitrogen on the optical absorption of the electrode in the visible range [28,49]. Moreover, in the studies reporting significant increases in photocurrents and efficiency with doping, N atoms were mainly detected in substitutional or interstitial positions [48,50]. Smaller currents for N-doped electrodes compared to un-doped reference cells have also been reported in some cases [32]. The next sections of this article will focus on the elucidation of the relation between charge kinetics and nitrogen location going from materials to devices using techniques adapted to each scale.

### 2.3. Charge Kinetics Probed by Transient Photo-Voltage at the Device Level

To get a better insight into the exact influence of nitrogen on charge kinetics in ssDSSC devices, we performed transient photo-voltage measurements under working conditions, as a function of the incident light intensities. Under open circuit conditions, the transient photo-generated charges can decay only through recombination at the TiO<sub>2</sub>-dye-HTM interface, as no carrier can be extracted in the external circuit. Figure 5 presents the corresponding recombination time for ssDSSC based on pure and N-doped TiO<sub>2</sub> electrodes.

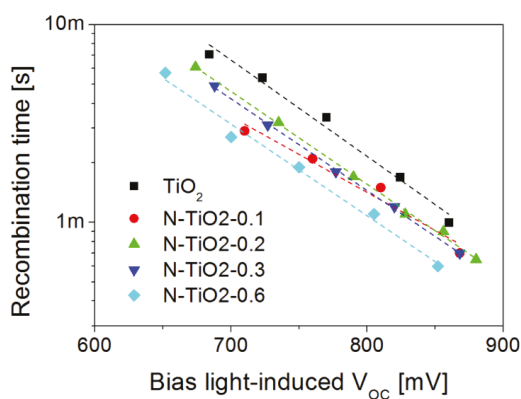


**Figure 5.** Recombination kinetics of ssDSSC probed by transient photo-voltage decay measurements, as a function of doping level.

Clearly, the charge lifetime decreases in all N-doped devices. Furthermore, recombination seems to become faster as the nitrogen content increases, especially under high light intensities (when the bias-light induced open-circuit voltage of the cells exceeds 800 mV). This initial observation indicates that N-doping is responsible for accelerated charge recombination in the devices, especially under



standard illumination conditions. Our observation is opposite to that of Tian *et al.* who reported that N-doped TiO<sub>2</sub> can retard charge recombination due to the presence of O-Ti-N bonds [32]. However, faster recombination has been observed for N-doped electrodes elaborated from particles with large diameters (>20 nm) [49,51,52]. Such a phenomenon being unlikely in our case (see Table 1), this decrease in charge lifetime seems to be a direct consequence of the presence of N dopants in our TiO<sub>2</sub> materials. In particular, the preferential location of nitrogen atoms at the particle surface for high doping levels is consistent with shorter charge carrier lifetimes and lower performance. However, charge kinetics probed at the level of working devices is potentially strongly affected by the various processing steps used for cell fabrication, including sintering steps at high temperature which may significantly alter the nitrogen distribution. Therefore, the next section focuses on the characterization of charge dynamics at the material level.

#### 2.4. Charge Kinetics Probed by Transient Techniques at the Material Level

In order to understand the role played by nitrogen atoms on charge generation, time-resolved microwave conductivity (TRMC) measurements were performed on the starting TiO<sub>2</sub> and N-TiO<sub>2</sub> powders. This technique, briefly described in Supplementary materials, is not a common tool of photo-physicists and photo-chemists. It was however successfully used to analyze charge kinetics of metal oxide materials for photo-catalysis [53–55] and photovoltaics [56–58]. It appears particularly well suited to investigate the influence of doping on the photo-conductivity properties of TiO<sub>2</sub> in the context of this study [59]. Figure 6 presents the absolute and normalized TRMC signals for the pure and N-doped TiO<sub>2</sub> before and after light excitation at 355 nm. In order to remove the effect of the number of photons, all the TRMC signals presented in this work are divided by the number of photons in nanoEinstein (nein), corresponding to the number of nanomoles of photons.

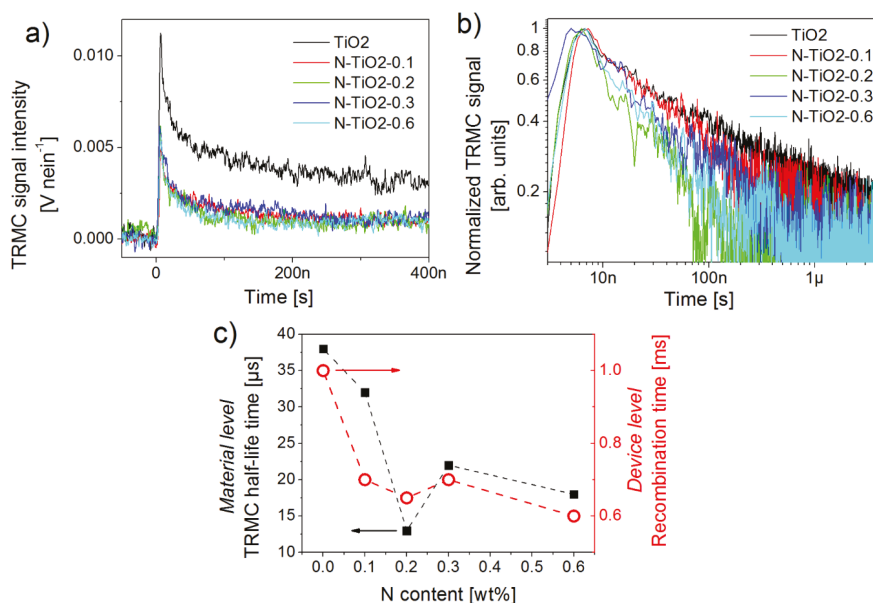


**Figure 6.** (a) absolute and (b) normalized time-resolved microwave conductivity (TRMC) signals of pure and N-doped TiO<sub>2</sub> powders with light excitation at 355 nm for the different N-doping levels; (c) TRMC decay half-times (black squares) measured at the material level on the TiO<sub>2</sub> and N-TiO<sub>2</sub> powders, and compared to recombination times extracted from transient photo-voltage at the device level.



The maximum intensity of the TRMC signal depends on three factors: the absorption coefficient of the material at the excitation wavelength; the interaction between the microwave electronic field and the materials, *i.e.*, the dielectric constant of the material; the recombination rate of electrons and holes during the laser pulse. Considering that the absorption coefficient at 355 nm of both un-doped and doped TiO<sub>2</sub> is mainly driven by transitions from O 2p to Ti 3d orbitals, we safely assume a similar absorption coefficient for all samples. We also assume a rather similar dielectric constant for the powders, as they present comparable crystalline structure and morphology (see Table 1), assuming low doping levels (always below 1 wt %). In these conditions, the strong decrease of TRMC signal with doping is consistent with additional recombination of free charge carriers during the laser pulse. Such observation is consistent with a previous report on N-doped titania materials [59], as well as with our transient photo-voltage analysis performed at the level of working devices (Figure 5). Accordingly, faster TRMC decay rates are observed with increasing N content in the nanopowders compared to the reference (Figure 6b). In addition, and except for sample N-TiO<sub>2</sub>-0.2, the decay rate is faster for large nitrogen content (Figure 6c). This is quite expected as when N atoms are inserted into the TiO<sub>2</sub> lattice, additional defects, such as oxygen vacancies, are spontaneously generated to ensure the global electric neutrality of the system. The photo-generated electrons are therefore more likely to be trapped in such defects, with a probability following in principle the nitrogen content. In our previous work, DFT calculations confirmed the occurrence of oxygen vacancies induced by the presence of nitrogen dopants [34]. Such processes have also been reported by other groups [59]. Finally, the extracted TRMC half-life time shows a strong correlation with the recombination kinetics measured on devices by transient photo-voltage decays (Figure 6c). This correlation, which was also confirmed through charge kinetics extracted from impedance spectroscopy applied on the same devices (not shown here), shows, in this particular case, the relevance for a multi-scale photo-physical approach from materials to devices. Our observations suggest that the features introduced by nitrogen doping are preserved during device fabrication, and that the dynamics of photo-generated charge carriers probed in the TiO<sub>2</sub> nanopowders still mainly drives device performance under simulated sunlight.

Considering the photo-activity of the N-doped samples in the visible region, we now give a better look at the influence of nitrogen on charge kinetics probed by TRMC using an excitation in the visible range. First, no TRMC signal is evidenced for the un-doped TiO<sub>2</sub> powder, in accordance with a flat absorption in this region. However, significant TRMC signals are recorded for the N-doped nanopowders, which is consistent with their optical absorption (Figure 2). No significant differences in the TRMC decay profiles of doped samples are, however, observed by exciting them either at 355, 420, 450, or 480 nm (see Supplementary materials, Figure S9 corresponding to sample N-TiO<sub>2</sub>-0.6). Similar reports were made in the literature [59], which are associated with the fact that both the O 2p to Ti 3d and the N 2p to Ti 3d transitions, induced through UV and visible excitation, respectively, show a similar final state. By fixing the excitation to 450 nm, the amplitudes of the TRMC signals increase with the nitrogen content up to 0.6 wt % in the powder (Figure 7), indicating that the photo-conductivity of the samples increases with the nitrogen content during the first 100 ns. This observation is consistent with the creation of a larger amount of electron-hole pairs for high doping levels. Considering our previous conclusions, this result suggests that a competition between charge transport and recombination is occurring in doped samples. In order to better interpret these effects, we finally analyze more carefully the electrical photo-conductivity of porous TiO<sub>2</sub> electrodes processed from the doped and un-doped nanopowders, *i.e.*, an intermediate elaboration level between the powder and the device.

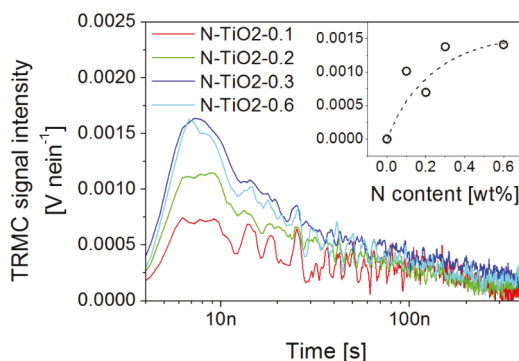


**Figure 7.** TRMC signals associated with an excitation at 450 nm, for N-doped powder samples. The inset shows the maximum TRMC signal amplitude (recorded after 9 ns in all cases) as a function of N content in the nanopowders.

### 2.5. Photo-Conductivity Measurements on Porous Electrodes

As the conductivity of semiconductors depends directly on the charge carrier density, it can be temporarily influenced by photo-generated electron-hole pairs into the material (*i.e.*, transitions of electrons from the valence band or donor levels to the conduction band). The technique is briefly presented in Supplementary materials. Considering the bandgap of anatase TiO<sub>2</sub> [60,61], photo-excitation by wavelengths above 400 nm mainly involves electrons from the donor band while UV excitation mainly involves electrons initially in the valence band. Figure 8 presents the current change ( $\Delta I$ ), defined as the difference between the current level in the dark and the saturation value under illumination, as a function of UV light intensity (excitation in the 330–380 nm range, see the Experimental section) for the un-doped and N-doped porous electrodes deposited from the nanopowders. It is worth noting that a sintering procedure similar to that used for device fabrication was also carried out in this case.

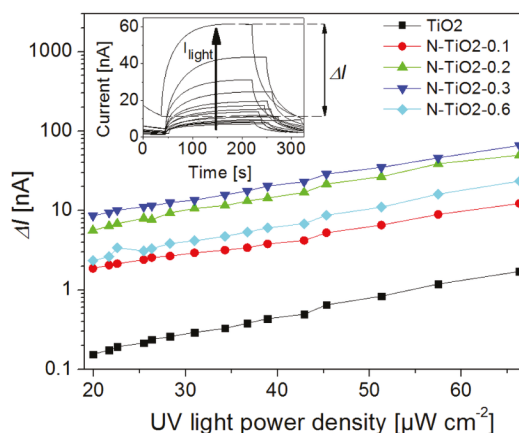


**Figure 8.** Photo-current response  $\Delta I(t)$  under UV excitation of porous TiO<sub>2</sub> electrodes as a function of incident light intensity and for various nitrogen doping levels. The inset presents characteristic photo-response curves for various illumination intensities from 20 to 66  $\mu\text{W}\cdot\text{cm}^{-2}$ , for the sample N-TiO<sub>2</sub>-0.2. The current jump  $\Delta I$  can be calculated from this data by subtracting the dark current from the saturation current as illustrated in the inset.

In all cases, the current—and hence the conductivity—increases under illumination, and saturates after about 180 s (inset of Figure 8). All the nitrogen doped samples show similar photo-response curves. An increased nitrogen content in the film is associated with an increased current change. This behavior indicates that nitrogen doping increases the amount of charge carriers being promoted into the conduction band of  $\text{TiO}_2$ , as also suggested by the TRMC analysis of the nanopowders and the intensities observed for the different doping levels (Figure 7). Unlike in our TRMC analysis, which showed faster charge recombination with doping (Figure 6a), the high voltage biasing of the devices used during the photo-conductivity measurements (bias voltage of 8 V) assists immediate charge transport to the electrodes preventing rapid charge recombination, so that a transient current signal can indeed be recorded. Thus, in this measurement, the limiting factor for the electrical response of the devices is not the charge recombination time but rather the density of recombination centers, e.g., impurities related to surface N atoms. The differences between the N-doped samples are small, as also noticed in the TRMC measurements made under UV excitation. A decrease in the photo-response is, however, observed for sample N-TiO<sub>2</sub>-0.6, which suggests that high nitrogen content is detrimental to current collection. This observation is consistent with the high density of surface nitrogen atoms revealed in this case, and with the high recombination rate evidenced for this sample in the previous section.

Figure 9 presents the current change ( $\Delta I$ ) of N-doped films for an excitation in the visible range provided by a long-pass filtered halogen lamp ( $\lambda > 410$  nm, see Experimental section), as a function of incident light intensity.

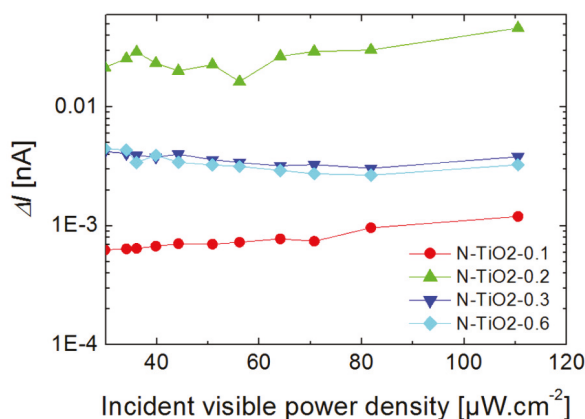


**Figure 9.** Current change associated to N-doped  $\text{TiO}_2$  porous films under visible light illumination as a function of incident light intensity.

The un-doped film is not shown in Figure 9, as it is associated with a very low current level (before the light is switched on) and current change ( $<1$  pA, see Supplementary materials, Figure S10) under illumination by visible light. This behavior is expected as the sample does not significantly absorb the incident light, so that no photo-conductivity is observable. On the opposite side, doped samples rapidly show a significant current change and photo-conductive behavior. We observe that after the initial jump corresponding to the beginning of the illumination, the current experiences a linear increase and no saturation can be observed. This linear increase, which was not observed under UV illumination, can be attributed to thermal effects induced by the infrared wavelengths of the light source. Filtering the infrared part of the lamp is indeed found to completely remove this linear dependency of the photo-response (see Supplementary materials, Figure S11). This effect is an illustration of the important temperature-dependency of  $n_d$ , and hence of  $\Delta I$ .

Keeping this thermal effect in mind, we observe in Figure 9 a larger current level for porous films based on N-doped TiO<sub>2</sub> compared to the un-doped reference. Both the dark current and current change  $\Delta I$  under visible light are enhanced through doping (by about one order of magnitude). Similarly to previous sections, our data suggest that the photo-induced charge transport properties of the porous films are improved through nitrogen doping, especially within the visible range.

### 3. Discussion

Nitrogen-doped porous electrodes can potentially improve the performance of dye-sensitized solar cells. However, although several reports discuss the positive effect of doping on device efficiency [24,32–34], it is also clear that true improvements remain subject to our ability to properly control both the amount and the location of the dopants. In the present study, as well as in our previous report [34], several sets of independent ssDSSC show that improvements in short-circuit current densities, open-circuit voltage, and in overall power conversion efficiencies can be achieved at low doping levels (Table 3). Our fabrication strategy exploits the laser pyrolysis process to grow TiO<sub>2</sub> and N-doped TiO<sub>2</sub> nanopowders of comparable morphologies and crystallinities (Table 1); however, nitrogen location, revealed by XPS analysis, is found to be strongly dependent on the doping level: although interstitial and substitutional N atoms are evident, the fraction of surface nitrogen increases with the doping level. While atoms inserted inside the TiO<sub>2</sub> structure give the metal oxide a visible photo-activity, surface nitrogen can act as electron traps or recombination centers. The resulting surface states are found to be limiting the charge lifetime, as revealed by transient photo-voltage measurements performed at the device level (Figure 5), and by TRMC at the material level (Figure 6). Larger recombination rates are indeed observed for doped electrodes, as soon as nitrogen is incorporated in the material. In parallel, photo-conductivity measurements on porous films prepared from the synthesized TiO<sub>2</sub> nanopowders (similar to device electrodes) show that better transport can be achieved in the doped electrodes, as long as recombination can be reduced through an external applied voltage for example (Figure 8). More specifically, our analysis gives direct evidence for the positive role played by the visible range photo-activity of the doped samples (both using TRMC and photo-response measurements). During illumination within the visible range, a larger fraction of charges can contribute to current collection, which is consistent with the signature observed in the IPCE spectra of the cells around 450 nm (Figure S7). However, in full working devices, such benefit of nitrogen doping remain subject to the competition with the intense recombination processes, which are found to mainly drive device operation. We strongly believe that the main limitation to current generation for the N-doped cells is associated with the preferential location of N atoms on the TiO<sub>2</sub> particle surface. The XPS signatures of such type of nitrogen (Figure 3 and Table 2) start to be clearly observed for sample N-TiO<sub>2</sub>-0.2, when photocurrent also begins to drop. This drop is consistent with the spectral signature observed around 600 nm in the IPCE spectrum of the N-doped devices, which is associated with the influence of surface-related defects induced by the presence of N atoms. Such assumption was also proposed by Lindgren *et al.* for liquid DSSC, for example [28]. For higher doping level up to 0.6 wt %, when recombination is the main limiting factor, we observe a drastic drop of 25% in both photocurrent and device efficiency.

## 4. Materials and Methods

### 4.1. Synthesis of N-Doped TiO<sub>2</sub> Nanocrystals

Nanoparticles doped with different levels of nitrogen were synthesized through laser pyrolysis by varying the NH<sub>3</sub> flow in the precursor mixture composed of titanium tetra-isopropoxide (TTIP) and C<sub>2</sub>H<sub>4</sub>. The details were reported in our previous work [36,38,62]. For the photovoltaic application, the as-prepared nanopowders were annealed at 400 °C for 3h to remove the free carbon phase that remains due to the decomposition of TTIP and/or C<sub>2</sub>H<sub>4</sub>.

#### 4.2. Device Fabrication

TiO<sub>2</sub> and N-doped TiO<sub>2</sub> porous electrodes were deposited on pre-cleaned FTO glass substrates initially covered with a TiO<sub>2</sub> blocking layer deposited by chemical spray pyrolysis, using spin-coating from formulations based on ethanol,  $\alpha$ -terpineol and ethyl-cellulose (EC), as previously described [38]. These films were progressively sintered up to 430 °C during 40 min in air. A TiCl<sub>4</sub> treatment (Aldrich, 0.04 M in deionized water) was performed on these films before a final sintering step at 430 °C in air during 45 min. The 1.8  $\mu$ m thick electrodes were then immersed in D102 dye (Mitsubishi Paper Mills, Tsukuba, Japan) dissolved in an acetonitrile:*tert*-butanol mixture (1:1 in volume) at 80 °C overnight. The sensitized electrodes were rinsed and infiltrated by the hole transporting material (HTM) spiro-OMeTAD (Merck KGaA, Darmstadt, Germany) by spin-coating in ambient conditions, following recipes previously reported [37,38]. Gold counter electrodes were evaporated through a shadow mask at 10<sup>-6</sup> mbar, leading to two independent active areas of 0.18 cm<sup>2</sup> per cell.

#### 4.3. Characterization Techniques

TEM images were recorded on a Philips CM12 microscope to examine the morphology of both the obtained nanoparticles and device cross sections. The crystalline phases were determined by XRD with a Siemens D5000 instrument using the Cu-K $\alpha$  radiation. The specific surface of the nanopowders was determined by the BET method using a Micromeritics FlowsorbII 2300 instrument. The chemical environment of nitrogen atoms in TiO<sub>2</sub> and N-TiO<sub>2</sub> was characterized by X-ray photoelectron spectroscopy (XPS) using a Kratos Analytical Axis Ultra DLD spectrometer (K $\alpha$  X-ray) on the powders. The optical properties of the powders were analyzed using a UV-visible-NIR spectrophotometer (Jasco V-570) in reflectance mode. According to the Kubelka–Munk equation, the optical gap can be estimated from the  $(F(R)/\text{h}\nu)$  plot as a function of photon energy, where  $F(R) = (1 - R)^2/2R$  and  $R$  is the reflection coefficient [63]. The current density-voltage characteristics of the devices were recorded using a Keithley 2400 source-measure unit in the dark and under simulated solar emission (NEWPORT class A solar simulator) at 100 mW·cm<sup>-2</sup> in AM1.5G conditions after spectral mismatch correction.

#### 4.4. Transient Photo-Voltage Measurements

Transient photo-voltage (TPV) decay measurements were measured under open-circuit conditions using a set-up previously described [37]. Two continuous white LEDs (OSRAM) were used to provide the constant illumination of the device up to approximately 100 mW·cm<sup>-2</sup>. An additional pulsed LED ( $\lambda = 550$  nm, Luxeon STAR, 5W), controlled by a solid state switch, generated a small light pulse on the cell. The transient charge population generated by this LED was always below a few percent of the continuous steady-state charge density in the device, ensuring a small-perturbation regime. The photo-voltage of the device was monitored and recorded using a digital oscilloscope (Tektronix DPO 4032) interfaced using a home-made Labview routine. The photo-voltage decays were adjusted using mono-exponential decay functions.

#### 4.5. Time-Resolved Microwave Conductivity Measurements (TRMC)

The charge-carrier lifetimes in the un-doped and N-doped TiO<sub>2</sub> nanopowders after an illumination were determined by microwave absorption experiments using TRMC. The incident microwaves were generated by a Gunn diode of the Ka band at 30 GHz. The pulsed light source was an OPO laser from EKSPILA where the accord ability extends from 200 to 2000 nm. The full width at half-maximum of one pulse was 7 ns and the repetition rate of the experiments was 10 Hz. The light energy density received by the sample depends on the wavelength. To avoid the excitation energy effect on the signals, all the data are divided by the number of photons. Typically, the energy density at 450 nm is  $5.2 \times 10^{-3}$  J·cm<sup>-2</sup>, corresponding to  $1.2 \times 10^{16}$  photons·cm<sup>-2</sup>.

#### 4.6. Photo-Conductivity Measurements

Photo-conductivity characteristics of the samples were studied by illuminating un-doped and N-doped TiO<sub>2</sub> thin films with UV (double peak between 330 and 380 nm, see Supplementary materials, Figure S12) and visible light (long-pass filtered halogen lamp,  $\lambda > 410$  nm, see Supplementary materials, Figure S13) and measuring the photo-response of the conductivity of the film, *i.e.*, the change in the sample conductivity when turning on the light under a constant applied bias voltage. For these experiments, thin porous films were fabricated from the same TiO<sub>2</sub> nanopowders used for the solar cell preparation, except that it was sonicated for 1h using a Hielscher sonicator (UP400s ultrasonicator, Hielscher Ultrasonics GmbH, Teltow, Germany) while cooled in a water path. After sonication, the powder was spin-coated on a glass chip (~1 cm<sup>2</sup>) at 1000 rpm for 1 min. To avoid cracks in the films, they were left to dry for 5 to 10 min before performing a first soft annealing step at 50 °C for 5 min in air. Then, the films were annealed at 430 °C for 35 min. Film deposition, as well as the drying and annealing steps, were performed in a laminar flow hood. Gold contact electrodes (100 nm thick) were evaporated under high vacuum using a thin copper wire (diameter  $\leq 120$   $\mu$ m) placed as a mask across the film. For the photoconductivity measurements, samples were placed in a windowed vacuum chamber at 4–6 mbar to remove most of the ambient moisture. The response of photoconductivity as a function of illumination intensity was measured using Stanford Research Systems voltage and current low-noise preamplifiers (models SR560 and SR570). A MinUVIS 30 W mercury lamp (Desaga #751311, Heidelberg, Germany) and a 50 W halogen lamp (Solux C5 12 V, Rochester, USA) were used for illumination, and light intensity was adjusted by changing the distance between the sample and the light source. The light intensities were measured using PD100M optical power meter (Thorlabs Sweden AB, Mölndal, Sweden) with S302C thermal power head (Thorlabs Sweden AB, Mölndal, Sweden).

#### 5. Conclusions

TiO<sub>2</sub> and N-doped TiO<sub>2</sub> nanoparticles have been synthesized using laser pyrolysis, and used to deposit porous electrodes suitable for solid-state dye-sensitized solar cells. A systematic analysis of the physical properties of the samples as a function of doping level was performed in order to discuss the exact influence of the dopant on material and device photo-physics. At low doping levels, N atoms have been efficiently incorporated in interstitial positions into the metal oxide structure for annealed powders. In this case, device performance is found sensibly improved compared to pure TiO<sub>2</sub>. However, a large fraction of surface nitrogen is also observed at higher doping levels, which was found to be responsible for faster recombination kinetics that clearly reduces device efficiency. At the material scale, charge kinetics is found to be in good correlation with kinetics observed on devices. Both suggest faster electron-hole pair recombination being induced in the presence of N atoms compared to the un-doped powder. Our analysis confirms that the rapid drop in photocurrent observed in our ssDSSC at high doping levels can be associated with the preferential location of nitrogen atoms at the particle surface, which favor interfacial recombination. The visible photo-sensitivity of the samples is confirmed by TRMC measurements, which showed an increasing photo-conductivity of the material in visible range as the nitrogen content increases. This trend was further confirmed through photo-response measurement made on porous TiO<sub>2</sub> and N-TiO<sub>2</sub> films. Once again, the photo-conductivity of the material was found to be largely improved under visible excitation, compared to the pure TiO<sub>2</sub> reference.

Although nitrogen doping remains a relevant strategy to improve the efficiencies of dye-sensitized solar cells, our data show that achieving concrete benefits at the device level from the visible photo-activity of N-doped TiO<sub>2</sub> requires a fine control of the doping level and of the location of N atoms in the metal oxide structure. We also point out an interesting correlation between the photo-physical properties of samples probed at various scales from materials to devices. In light of our investigations, the specific features of the starting nanopowder materials are found to drive the device photo-physics, even when surface treatments and sintering steps are used during solar cell fabrication.

**Supplementary Materials:** The following are available online at <http://www.mdpi.com/2079-4991/6/3/35/s1>. Complementary experimental details, Table S1: Experimental conditions of laser pyrolysis for the synthesis of N-doped TiO<sub>2</sub> powders, Figure S1: XRD patterns of all powders, Figure S2: XPS spectra of TiO<sub>2</sub> nanopowder, Figure S3: XPS spectra as-prepared N-TiO<sub>2</sub>-0.2 and N-TiO<sub>2</sub>-0.6 samples, Table S2: Relative contributions of XPS features for as-prepared N-doped samples, Figure S4: SEM cross-section micrographs of ssDSSC, Figure S5: Absorption coefficient of the dye-sensitized electrodes, Figure S6: J(V) curves of the solar cells in the dark, Figure S7: Normalized IPCE, Figure S8: Photoluminescence spectra of undoped and doped nanopowders, Figure S9: Normalized TRMC signals for different excitation wavelengths, Figure S10: Photoconductivity curves of porous films under visible light excitation, Figure S11: Photoconductivity curves of the porous film under visible light illumination, with and without infrared filter, Figure S12: Emission spectrum of the UV-lamp used in the photoconductivity measurements, Figure S13: Optical spectrum of the long-pass filtered halogen lamp used in the photoconductivity measurements.

**Acknowledgments:** The authors acknowledge the INSIS CNRS Energy program (Noxomix project), Academy of Finland (Projects 263262, 283011, 263526) and CEA-IFA Nanophob project for funding, as well as the support of the “Région Limousin” (thematic project “EVASION”) and NewIndigo ERA-NET NPP2 (“Aquatest” project). This work was performed in the framework of the Energy and Environment thematic of the SIGMA-LIM Laboratory of Excellence. We thank Heikki Häkkinen and Pasi Myllyperkiö for useful discussions.

**Author Contributions:** Jin Wang and Nathalie Herlin-Boime conceived and designed the experiments and supervised the analysis of the data, as well as paper writing; Jin Wang performed the main experiments and participated in the writing of the paper; Monica Scarisoreanu participated in the synthesis by laser pyrolysis of some nanopowders used in this study; Aurélie Habert performed the SEM measurements; Bernard Ratier participated in the interpretation of data and paper writing; Kostu Tapio and Jussi Toppari performed the photoconductivity measurements and contributed to the interpretations of the data; Sébastien Sorgues and Christophe Colbeau-Justin performed the TRMC analyses and contributed to the analysis of the data.

**Conflicts of Interest:** The authors declare no conflict of interest. The founding sponsors had no role in the design of the study; in the collection, analyses, or interpretation of data; in the writing of the manuscript, and in the decision to publish the results.

## References

- Bach, U.; Lupo, D.; Comte, P.; Moser, J.E.; Weissörtel, F.; Salbeck, J.; Spreitzer, H.; Grätzel, M. Solid-state dye-sensitized mesoporous TiO<sub>2</sub> solar cells with high photon-to-electron conversion efficiencies. *Nature* **1998**, *395*, 583–585.
- Burschka, J.; Dualeh, A.; Kessler, F.; Baranoff, E.; Cevey-Ha, N.-L.; Yi, C.; Nazeeruddin, M.K.; Grätzel, M. Tris(2-(1H-pyrazol-1-yl)pyridine)cobalt(III) as p-Type Dopant for Organic Semiconductors and Its Application in Highly Efficient Solid-State Dye-Sensitized Solar Cells. *J. Am. Chem. Soc.* **2011**, *133*, 18042–18045. [CrossRef] [PubMed]
- Xu, B.; Gabrielsson, E.; Safdari, M.; Cheng, M.; Hua, Y.; Tian, H.; Gardner, J.M.; Kloo, L.; Sun, L. 1,1,2,2-Tetrachloroethane (TeCA) as a Solvent Additive for Organic Hole Transport Materials and Its Application in Highly Efficient Solid-State Dye-Sensitized Solar Cells. *Adv. Energy Mater.* **2015**, *5*. [CrossRef]
- Ahmad, S.; Guillén, E.; Kavan, L.; Grätzel, M.; Nazeeruddin, M.K. Metal free sensitizer and catalyst for dye sensitized solar cells. *Energy Environ. Sci.* **2013**, *6*, 3439–3466. [CrossRef]
- Li, L.L.; Diau, E.W.G. Porphyrin-sensitized solar cells. *Chem. Soc. Rev.* **2013**, *42*, 291–304. [CrossRef] [PubMed]
- Liang, M.; Chen, J. Arylamine organic dyes for dye-sensitized solar cells. *Chem. Soc. Rev.* **2013**, *42*, 3453–3488. [CrossRef] [PubMed]
- Stranks, S.D.; Snaith, H.J. Metal-halide perovskites for photovoltaic and light-emitting devices. *Nat. Nano* **2015**, *10*, 391–402. [CrossRef] [PubMed]
- Chen, Q.; de Marco, N.; Yang, Y.; Song, T.-B.; Chen, C.-C.; Zhao, H.; Hong, Z.; Zhou, H. Under the spotlight: The organic–inorganic hybrid halide perovskite for optoelectronic applications. *Nano Today* **2015**, *10*, 355–396. [CrossRef]
- Bui, T.T.; Goubard, F. Small organic molecule hole transporting materials for solid-state dye-sensitized solar cells. *Mater. Tech.* **2013**, *101*. [CrossRef]
- Aulakh, R.K.; Sandhu, S.; Tanvi; Kumar, S.; Mahajan, A.; Bedi, R.K. Designing and synthesis of imidazole based hole transporting material for solid state dye sensitized solar cells. *Synth. Met.* **2015**, *205*, 92–97. [CrossRef]



11. Hsu, C.Y.; Chen, Y.C.; Lin, R.Y.Y.; Ho, K.C.; Lin, J.T. Solid-state dye-sensitized solar cells based on spirofluorene (spiro-OMeTAD) and arylamines as hole transporting materials. *Phys. Chem. Chem. Phys.* **2012**, *14*, 14099–14109. [CrossRef] [PubMed]
12. Chung, I.; Lee, B.; He, J.; Chang, R.P.H.; Kanatzidis, M.G. All-solid-state dye-sensitized solar cells with high efficiency. *Nature* **2012**, *485*, 486–489. [CrossRef] [PubMed]
13. Lee, B.; Stoumpos, C.C.; Zhou, N.; Hao, F.; Malliakas, C.; Yeh, C.-Y.; Marks, T.J.; Kanatzidis, M.G.; Chang, R.P. Air-Stable Molecular Semiconducting Iodosalts for Solar Cell Applications: Cs<sub>2</sub>SnI<sub>6</sub> as a Hole Conductor. *J. Am. Chem. Soc.* **2014**, *136*, 15379–15385. [CrossRef] [PubMed]
14. Freitag, M.; Daniel, Q.; Pazoki, M.; Sveinbjornsson, K.; Zhang, J.; Sun, L.; Hagfeldt, A.; Boschloo, G. High-efficiency dye-sensitized solar cells with molecular copper phenanthroline as solid hole conductor. *Energy Environ. Sci.* **2015**, *8*, 2634–2637. [CrossRef]
15. Bouclé, J.; Ackermann, J. Solid-state dye-sensitized and bulk heterojunction solar cells using TiO<sub>2</sub> and ZnO nanostructures: Recent progress and new concepts at the borderline. *Polym. Int.* **2012**, *61*, 355–373. [CrossRef]
16. Docampo, P.; Guldin, S.; Leijtens, T.; Noel, N.K.; Steiner, U.; Snaith, H.J. Lessons Learned: From Dye-Sensitized Solar Cells to All-Solid-State Hybrid Devices. *Adv. Mater.* **2014**, *26*, 4013–4030. [CrossRef] [PubMed]
17. Chen, H.Y.; Xu, Y.F.; Kuang, D.B.; Su, C.Y. Recent advances in hierarchical macroporous composite structures for photoelectric conversion. *Energy Environ. Sci.* **2014**, *7*, 3887–3901. [CrossRef]
18. Concina, I.; Vomiero, A. Metal oxide semiconductors for dye- and quantum-dot-sensitized solar cells. *Small* **2015**, *11*, 1744–1774. [CrossRef] [PubMed]
19. Gao, C.; Li, X.; Lu, B.; Chen, L.; Wang, Y.; Teng, F.; Wang, J.; Zhang, Z.; Pan, X.; Xie, E. A facile method to prepare SnO<sub>2</sub> nanotubes for use in efficient SnO<sub>2</sub>–TiO<sub>2</sub> core-shell dye-sensitized solar cells. *Nanoscale* **2012**, *4*, 3475–3481. [CrossRef] [PubMed]
20. Antila, L.J.; Heikkilä, M.J.; Mäkinen, V.; Humalamäki, N.; Laitinen, M.; Linko, V.; Jalkanen, P.; Toppari, J.; Aumanen, V.; Kemell, M. ALD grown aluminum oxide submonolayers in dye-sensitized solar cells: The effect on interfacial electron transfer and performance. *J. Phys. Chem. C* **2011**, *115*, 16720–16729. [CrossRef]
21. Liu, Y.; Zhai, H.; Guo, F.; Huang, N.; Sun, W.; Bu, C.; Peng, T.; Yuan, J.; Zhao, X. Synergistic effect of surface plasmon resonance and constructed hierarchical TiO<sub>2</sub> spheres for dye-sensitized solar cells. *Nanoscale* **2012**, *4*, 6863–6869. [CrossRef] [PubMed]
22. Tian, Z.; Wang, L.; Jia, L.; Li, Q.; Song, Q.; Su, S.; Yang, H. A novel biomass coated Ag–TiO<sub>2</sub> composite as a photoanode for enhanced photocurrent in dye-sensitized solar cells. *RSC Adv.* **2013**, *3*, 6369–6376. [CrossRef]
23. Sun, Q.; Zhang, J.; Wang, P.; Zheng, J.; Zhang, X.; Cui, Y.; Feng, J.; Zhu, Y. Sulfur-doped TiO<sub>2</sub> nanocrystalline photoanodes for dye-sensitized solar cells. *J. Renew. Sustain. Energy* **2012**, *4*. [CrossRef]
24. Ma, T.; Akiyama, M.; Abe, E.; Imai, I. High-efficiency dye-sensitized solar cell based on a nitrogen-doped nanostructured titania electrode. *Nano Lett.* **2005**, *5*, 2543–2547. [CrossRef] [PubMed]
25. Wang, H.; Li, H.; Wang, J.; Wu, J.; Li, D.; Liu, M.; Su, P. Nitrogen-doped TiO<sub>2</sub> nanoparticles better TiO<sub>2</sub> nanotube array photo-anodes for dye sensitized solar cells. *Electrochim. Acta* **2014**, *137*, 744–750. [CrossRef]
26. Zhao, B.; Wang, J.; Li, H.; Wang, H.; Jia, X.; Su, P. The influence of yttrium dopant on the properties of anatase nanoparticles and the performance of dye-sensitized solar cells. *Phys. Chem. Chem. Phys.* **2015**, *17*, 14836–14842. [CrossRef] [PubMed]
27. Asahi, R.; Morikawa, T.; Ohwaki, T.; Aoki, K.; Taga, Y. Visible-light photocatalysis in nitrogen-doped titanium oxides. *Science* **2001**, *293*, 269–271. [CrossRef] [PubMed]
28. Lindgren, T.; Mwabora, J.M.; Avandaño, E.; Jonsson, J.; Hoel, A.; Granqvist, C.G.; Lindquist, S.E. Photoelectrochemical and optical properties of nitrogen doped titanium dioxide films prepared by reactive DC magnetron sputtering. *J. Phys. Chem. B* **2003**, *107*, 5709–5716. [CrossRef]
29. Di Valentin, C.; Finazzi, E.; Pacchioni, G.; Selloni, A.; Livraghi, S.; Paganini, M.C.; Giamello, E. N-doped TiO<sub>2</sub>: Theory and experiment. *Chem. Phys.* **2007**, *339*, 44–56. [CrossRef]
30. Di Valentin, C.; Pacchioni, G. Trends in non-metal doping of anatase TiO<sub>2</sub>: B, C, N and F. *Catal. Today* **2013**, *206*, 12–18. [CrossRef]
31. Asahi, R.; Morikawa, T. Nitrogen complex species and its chemical nature in TiO<sub>2</sub> for visible-light sensitized photocatalysis. *Chem. Phys.* **2007**, *339*, 57–63. [CrossRef]



32. Tian, H.; Hu, L.; Zhang, C.; Liu, W.; Huang, Y.; Mo, L.; Guo, L.; Sheng, J.; Dai, S. Retarded charge recombination in dye-sensitized nitrogen-doped TiO<sub>2</sub> solar cells. *J. Phys. Chem. C* **2010**, *114*, 1627–1632. [CrossRef]
33. Di Valentin, C.; Pacchioni, G.; Selloni, A. Origin of the different photoactivity of N-doped anatase and rutile TiO<sub>2</sub>. *Phys. Rev. B* **2004**, *70*. [CrossRef]
34. Melhem, H.; Simon, P.; Wang, J.; di Bin, C.; Ratier, B.; Leconte, Y.; Herlin-Boime, N.; Makowska-Janusik, M.; Kassiba, A.; Bouclé, J. Direct photocurrent generation from nitrogen doped TiO<sub>2</sub> electrodes in solid-state dye-sensitized solar cells: Towards optically-active metal oxides for photovoltaic applications. *Sol. Energy Mater. Sol. Cells* **2013**, *117*, 624–631. [CrossRef]
35. Diker, H.; Varlikli, C.; Stathatos, E. N-doped titania powders prepared by different nitrogen sources and their application in quasi-solid state dye-sensitized solar cells. *Int. J. Energy Res.* **2014**, *38*, 908–917. [CrossRef]
36. Pignon, B.; Maskrot, H.; Ferreol, V.G.; Leconte, Y.; Coste, S.; Gervais, M.; Pouget, T.; Reynaud, C.; Tranchant, J.F.; Herlin-Boime, N. Versatility of laser pyrolysis applied to the synthesis of TiO<sub>2</sub> nanoparticles—Application to UV attenuation. *Eur. J. Inorg. Chem.* **2008**, *2008*, 883–889. [CrossRef]
37. Melhem, H.; Simon, P.; Beouch, L.; Goubard, F.; Boucharef, M.; Di Bin, C.; Leconte, Y.; Ratier, B.; Herlin-Boime, N.; Bouclé, J. TiO<sub>2</sub> Nanocrystals Synthesized by Laser Pyrolysis for the Up-Scaling of Efficient Solid-Stage Dye-Sensitized Solar Cells. *Adv. Energy Mater.* **2011**, *1*, 908–916. [CrossRef]
38. Wang, J.; Lin, Y.; Pinault, M.; Filoramo, A.; Fabert, M.; Ratier, B.; Bouclé, J.; Herlin-Boime, N. Single-Step Preparation of TiO<sub>2</sub>/MWCNT Nanohybrid Materials by Laser Pyrolysis and Application to Efficient Photovoltaic Energy Conversion. *ACS Appl. Mater. Interfaces* **2015**, *7*, 51–56. [CrossRef] [PubMed]
39. Spurr, R.A.; Myers, H. Quantitative analysis of anatase-rutile mixtures with an X-ray diffractometer. *Anal. Chem.* **1957**, *29*, 760–762. [CrossRef]
40. Klug, H.P.; Alexander, L.E. *X-Ray Diffraction Procedures*; Wiley: New York, NY, USA, 1954.
41. Kang, S.H.; Kim, H.S.; Kim, J.Y.; Sung, Y.E. Enhanced photocurrent of nitrogen-doped TiO<sub>2</sub> film for dye-sensitized solar cells. *Mater. Chem. Phys.* **2010**, *124*, 422–426. [CrossRef]
42. Zhang, M.; Lin, G.; Dong, C.; Kim, K.H. Mechanical and optical properties of composite TiO<sub>x</sub>N<sub>y</sub> films prepared by pulsed bias arc ion plating. *Curr. Appl. Phys.* **2009**, *9*, S174–S178. [CrossRef]
43. Amadelli, R.; Samiolo, L.; Borsa, M.; Bellardita, M.; Palmisano, L. N-TiO<sub>2</sub> Photocatalysts highly active under visible irradiation for NO<sub>x</sub> abatement and 2-propanol oxidation. *Catal. Today* **2013**, *206*, 19–25. [CrossRef]
44. Wang, J.; Tafen, D.N.; Lewis, J.P.; Hong, Z.; Manivannan, A.; Zhi, M.; Li, M.; Wu, N. Origin of Photocatalytic Activity of Nitrogen-Doped TiO<sub>2</sub> Nanobelts. *J. Am. Chem. Soc.* **2009**, *131*, 12290–12297. [CrossRef] [PubMed]
45. Guo, W.; Shen, Y.; Wu, L.; Gao, Y.; Ma, T. Effect of N dopant amount on the performance of dye-sensitized solar cells based on N-Doped TiO<sub>2</sub> electrodes. *J. Phys. Chem. C* **2011**, *115*, 21494–21499. [CrossRef]
46. Schmidt-Mende, L.; Bach, U.; Humphry-Baker, R.; Horiuchi, T.; Miura, H.; Ito, S.; Uchida, S.; Grätzel, M. Organic Dye for Highly Efficient Solid-State Dye-Sensitized Solar Cells. *Adv. Mater.* **2005**, *17*, 813–815. [CrossRef]
47. Xie, Y.; Huang, N.; Liu, Y.; Sun, W.; Mehnane, H.F.; You, S.; Wang, L.; Liu, W.; Guo, S.; Zhao, X.-Z. Photoelectrodes modification by N doping for dye-sensitized solar cells. *Electrochim. Acta* **2013**, *93*, 202–206. [CrossRef]
48. Tian, H.; Hu, L.; Zhang, C.; Mo, L.; Li, W.; Sheng, J.; Dai, S. Superior energy band structure and retarded charge recombination for Anatase N, B codoped nano-crystalline TiO<sub>2</sub> anodes in dye-sensitized solar cells. *J. Mater. Chem.* **2012**, *22*, 9123–9130. [CrossRef]
49. Guo, W.; Shen, Y.; Boschloo, G.; Hagfeldt, A.; Ma, T. Influence of nitrogen dopants on N-doped TiO<sub>2</sub> electrodes and their applications in dye-sensitized solar cells. *Electrochim. Acta* **2011**, *56*, 4611–4617. [CrossRef]
50. Guo, W.; Miao, Q.Q.; Xin, G.; Wu, L.Q.; Ma, T.L. Dye-sensitized solar cells based on nitrogen-doped titania electrodes. *Key Eng. Mater.* **2011**, *451*, 21–27. [CrossRef]
51. Guo, W.; Wu, L.; Chen, Z.; Boschloo, G.; Hagfeldt, A.; Ma, T. Highly efficient dye-sensitized solar cells based on nitrogen-doped titania with excellent stability. *J. Photochem. Photobiol. A* **2011**, *219*, 180–187. [CrossRef]
52. Guo, W.; Shen, Y.; Wu, L.; Gao, Y.; Ma, T. Performance of Dye-Sensitized Solar Cells Based on MWCNT/TiO<sub>2-x</sub>N<sub>x</sub> Nanocomposite Electrodes. *Eur. J. Inorg. Chem.* **2011**, *2011*, 1776–1783. [CrossRef]
53. Kolen'ko, Y.V.; Churagulov, B.R.; Kunst, M.; Mazerolles, L.; Colbeau-Justin, C. Photocatalytic properties of titania powders prepared by hydrothermal method. *Appl. Catal. B Environ.* **2004**, *54*, 51–58. [CrossRef]

54. Carneiro, J.T.; Savenije, T.J.; Moulijn, J.A.; Mul, G. How phase composition influences optoelectronic and photocatalytic properties of TiO<sub>2</sub>. *J. Phys. Chem. C* **2011**, *115*, 2211–2217. [CrossRef]
55. Meichtry, J.M.; Colbeau-Justin, C.; Custo, G.; Litter, M.I. Preservation of the photocatalytic activity of TiO<sub>2</sub> by EDTA in the reductive transformation of Cr(VI). Studies by Time Resolved Microwave Conductivity. *Catal. Today* **2014**, *224*, 236–243. [CrossRef]
56. Segal-Peretz, T.; Leman, O.; Nardes, A.M.; Frey, G.L. On the origin of charge generation in hybrid TiO<sub>x</sub>/conjugated polymer photovoltaic devices. *J. Phys. Chem. C* **2012**, *116*, 2024–2032. [CrossRef]
57. Abdi, F.F.; Savenije, T.J.; May, M.M.; Dam, B.; van de Krol, R. The origin of slow carrier transport in BiVO<sub>4</sub> thin film photoanodes: A time-resolved microwave conductivity study. *J. Phys. Chem. Lett.* **2013**, *4*, 2752–2757. [CrossRef]
58. Saeki, A.; Yasutani, Y.; Oga, H.; Seki, S. Frequency-modulated gigahertz complex conductivity of TiO<sub>2</sub> nanoparticles: Interplay of free and shallowly trapped electrons. *J. Phys. Chem. C* **2014**, *118*, 22561–22572. [CrossRef]
59. Katoh, R.; Furube, A.; Yamanaka, K.I.; Morikawa, T. Charge separation and trapping in N-doped TiO<sub>2</sub> photocatalysts: A time-resolved microwave conductivity study. *J. Phys. Chem. Lett.* **2010**, *1*, 3261–3265. [CrossRef]
60. Tang, H.; Prasad, K.; Sanjines, R.; Schmid, P.E.; Levy, F. Electrical and optical properties of TiO<sub>2</sub> anatase thin films. *J. Appl. Phys.* **1994**, *75*, 2042–2047. [CrossRef]
61. Asahi, R.; Taga, Y.; Mannstadt, W.; Freeman, A.J. Electronic and optical properties of anatase TiO<sub>2</sub>. *Phys. Rev. B* **2000**, *61*, 7459–7465. [CrossRef]
62. Simon, P.; Pignon, B.; Miao, B.; Coste-Leconte, S.; Leconte, Y.; Marguet, S.; Jegou, P.; Bouchet-Fabre, B.; Reynaud, C.; Herlin-Boime, N. N-doped titanium monoxide nanoparticles with TiO rock-salt structure, low energy band gap, and visible light activity. *Chem. Mater.* **2010**, *22*, 3704–3711. [CrossRef]
63. Lee, S.; Jeon, C.; Park, Y. Fabrication of TiO<sub>2</sub> tubules by template synthesis and hydrolysis with water vapor. *Chem. Mater.* **2004**, *16*, 4292–4295. [CrossRef]



© 2016 by the authors. Licensee MDPI, Basel, Switzerland. This article is an open access article distributed under the terms and conditions of the Creative Commons Attribution (CC BY) license (<http://creativecommons.org/licenses/by/4.0/>).



Article

# Improving the Photocurrent in Quantum-Dot-Sensitized Solar Cells by Employing Alloy $\text{Pb}_x\text{Cd}_{1-x}\text{S}$ Quantum Dots as Photosensitizers

Chunze Yuan <sup>1,†,‡</sup>, Lin Li <sup>2,†</sup>, Jing Huang <sup>1</sup>, Zhijun Ning <sup>1</sup>, Licheng Sun <sup>2,\*</sup> and Hans Ågren <sup>1,\*</sup>

<sup>1</sup> Department of Theoretical Chemistry and Biology, School of Biotechnology, Royal Institute of Technology, 10691 Stockholm, Sweden; chunze@stanford.edu (C.Y.); jinghuang@theochem.kth.se (J.H.); zhijunning@gmail.com (Z.N.)

<sup>2</sup> Center of Molecular Devices, Department of Chemistry, School of Chemical Science and Engineering, Royal Institute of Technology, 10044 Stockholm, Sweden; lin3@kth.se

\* Correspondence: lichengs@kth.se (L.S.); agre@theochem.kth.se (H.Å.); Tel.: +46-8-5537-8590 (H.Å.)

† These authors contributed equally to the paper.

‡ Present address: Department of Chemistry, Stanford University, Stanford, CA 94305, USA.

Academic Editor: Guanying Chen

Received: 6 April 2016; Accepted: 20 May 2016; Published: 27 May 2016

**Abstract:** Ternary alloy  $\text{Pb}_x\text{Cd}_{1-x}\text{S}$  quantum dots (QDs) were explored as photosensitizers for quantum-dot-sensitized solar cells (QDSCs). Alloy  $\text{Pb}_x\text{Cd}_{1-x}\text{S}$  QDs ( $\text{Pb}_{0.54}\text{Cd}_{0.46}\text{S}$ ,  $\text{Pb}_{0.31}\text{Cd}_{0.69}\text{S}$ , and  $\text{Pb}_{0.24}\text{Cd}_{0.76}\text{S}$ ) were found to substantially improve the photocurrent of the solar cells compared to the single CdS or PbS QDs. Moreover, it was found that the photocurrent increases and the photovoltage decreases when the ratio of Pb in  $\text{Pb}_x\text{Cd}_{1-x}\text{S}$  is increased. Without surface protecting layer deposition, the highest short-circuit current density reaches  $20 \text{ mA/cm}^2$  under simulated AM 1.5 illumination ( $100 \text{ mW/cm}^2$ ). After an additional CdS coating layer was deposited onto the  $\text{Pb}_x\text{Cd}_{1-x}\text{S}$  electrode, the photovoltaic performance further improved, with a photocurrent of  $22.6 \text{ mA/cm}^2$  and an efficiency of 3.2%.

**Keywords:** quantum dot-sensitized solar cells; photocurrent; alloy; PbS

## 1. Introduction

Quantum-dot-sensitized solar cells (QDSCs), which are similar to dye-sensitized solar cells (DSCs) in terms of configuration and working mechanism [1,2], have been intensively investigated in the last decade due to the excellent properties of quantum dots (QDs), *i.e.*, size-dependent spectral tunability, high molar extinction coefficients, and low fabrication cost [3–7]. Especially, QD-based solar cells have shown promising conversion efficiency in the infrared region, where light cannot be effectively harvested by DSCs. In addition, the unique multi-electron generation effect of QDs proposes the theoretically maximum efficiency of QDSCs to be as high as 44% [8]. Therefore, QDSCs have been studied as a promising alternative or supplement to DSCs [9–11]. However, this efficiency is still far from the theoretically highest efficiency [12,13]. To enable the photovoltaic performance of QDSCs to compete with DSCs or other type solar cells, many efforts have been made, *e.g.*, exploring new kinds of QDs with better light harvesting capability, electron injection efficiency, electrolyte and electrode materials in order to alleviate the series resistance between the electrolyte and cathode, as well as the carrier recombination between anode and electrolyte [14–19]. The extension of the light-harvesting region of the photosensitizers to the near-infrared (NIR) region has received more and more attention owing to its critical role to further improve the general solar cell performance [20–22]. Thus, although currently silicon solar cells can harvest light well in the visible region, there is lack of high-performance materials that can efficiently harvest infrared light.

So far, few types of QDs with absorption spectra stretching down to the NIR area have been proven to be effective for QDSCs. The broadening of the absorption spectrum has motivated the development of type-II core/shell-structured QDs, the bandgap of which is the difference between the conduction band (CB) edge of the component with deeper conduction band and the valence band (VB) edge of the component with a smaller VB [23,24]. QDs alloyed with multiple elements serve as another possible approach to broaden the absorption spectrum since they may present lower bandgaps than the corresponding binary QDs by the effect of optical bowing [25]. Another popular approach is to apply some traditional QDs with narrow bandgaps, such as PbS, PbSe, and Ag<sub>2</sub>S [26–28]. PbS QDs have been intensely studied for the solar cell application due to the narrow bandgap (0.41 eV for bulk PbS) and potential multiple exciton collection [29–35]. The Bohr radius of PbS is as large as 18 nm [34], which makes it possible to tune its bandgap in a wide range by modifying the size of QDs.

PbS QDs have been successfully applied in heterojunction solar cells, showing remarkable conversion efficiency up to 10% [36–41]. However, PbS QDSCs show much lower device performance due to the low CB level, heavy charge recombination, and low stability with the presently available liquid electrolytes [30,33]. Coating of CdS or CdPbS shells onto PbS QDs have been explored, showing increased device performance compared with PbS only QDs, as the recombination and corrosion with the electrolyte are then inhibited [30,42]. Alloy QDs have been proposed as a good strategy for improving the optical and electronic properties of QDs by controlling the proportion of their component elements [25,43].

Solution phase *in-situ* ion adsorption by the method of successive ionic-layer adsorption and reaction (SILAR) [5,44] has been widely used for QDSCs and shows promising device performance, due to its convenient fabrication process. SILAR-adsorbed PbS QDs has been explored for QDSCs, albeit giving quite low device performance. Mixed Cd and Pb ions by using Pb(NO<sub>3</sub>)<sub>2</sub> as lead salts for alloy Pb<sub>x</sub>Cd<sub>1-x</sub>S adsorption have been used; however, the device performance remains still low. It still remains unclear how the ratio of Pb: Cd of Pb<sub>x</sub>Cd<sub>1-x</sub>S QDs can influence the photovoltaic performance of QDSCs [45]. Since their bandgaps and CB levels are in between those of PbS and CdS [42], Pb<sub>x</sub>Cd<sub>1-x</sub>S QDs may present a higher CB edge than PbS and a wider absorption spectrum than CdS. By tuning the Pb: Cd ratio of Pb<sub>x</sub>Cd<sub>1-x</sub>S, the bandgap and CB level of the alloy QDs can be adjusted, which should affect the light-harvesting ability, carrier injection, and carrier recombination in the QDSCs. On the other hand, it has been shown that the addition of a certain amount of Cd in PbS QDs can significantly limit the carrier recombination by reducing the trap density without affecting the carrier extraction, which brings much improved device performance [36]. Herein, in this report, we systematically study the effect of the ratio of Pb: Cd. This ratio is varied by controlling the Pb<sup>2+</sup> ion concentration in the cationic precursor solutions, which is used to prepare three kinds of Pb<sub>x</sub>Cd<sub>1-x</sub>S QDs by the SILAR process.

## 2. Results and Discussion

Firstly, a kind of Pb<sub>x</sub>Cd<sub>1-x</sub>S QDs, termed PbCdS-1, was investigated as a photosensitizer compared to the CdS and PbS QDs. PbCdS-1 was prepared by a mixed precursor solution containing 0.004 M PbCl<sub>2</sub> and 0.1 M Cd(NO<sub>3</sub>)<sub>2</sub>. More details are given in the experimental section. The CdS, PbS, and PbCdS-1 were deposited on the TiO<sub>2</sub> electrodes by the SILAR process. The absorption spectra of the CdS, PbS, and PbCdS-1 QD-sensitized TiO<sub>2</sub> electrodes after three SILAR cycles are shown in the inset of Figure 1a. The CdS-sensitized electrode shows the narrowest absorption range (<500 nm), due to its wide bandgap, and the lowest absorbance intensity. In contrast, the PbS electrode shows the highest absorbance intensity and the widest absorption range over 800 nm, due to the considerably narrow bandgap and high molar extinction coefficient. For the PbCdS-1 electrode, the absorbance intensity is slightly lower than for PbS. The absorption performance of the PbCdS-1 QDs is similar to that of the PbS QDs, indicating that PbCdS-1 can harvest similar photon energies as PbS.

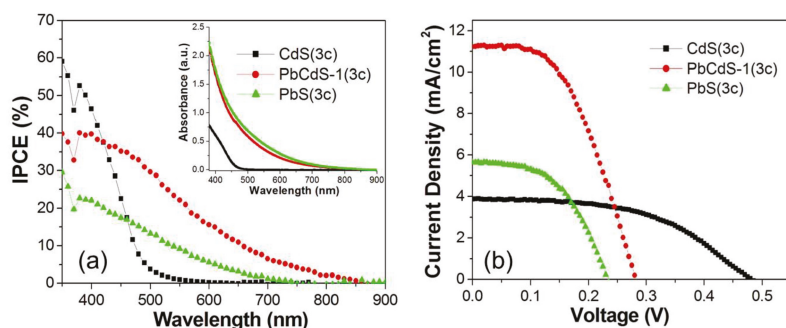


**Figure 1.** Incident photon to current efficiency (IPCE) spectra (a) and current–voltage (I–V) curves (b) of quantum-dot-sensitized solar cells (QDSCs) employing three successive ionic-layer adsorption and reaction (SILAR) cycles of CdS, PbS, and PbCdS-1 as photosensitizers. Inset of (a) is the absorption spectra of three-SILAR-cycle QD-sensitized TiO<sub>2</sub> films. “3C” means three SILAR cycles, and the bare TiO<sub>2</sub> film was used as blank.

Figure 1a shows the incident photon to current efficiency (IPCE) spectra of QDSCs employing CdS, PbS, and PbCdS-1 with three SILAR cycles as photosensitizers. From the absorption spectra, the sizes of three-cycle CdS, PbS, and PbCdS-1 can be estimated to be ~3 nm, ~2 nm, and 2–4 nm, respectively [45–48]. The CdS QDSCs show the highest IPCE and narrowest region (only up to 550 nm). The highest IPCE is due to the high CB energy level of CdS, which leads to a high driving force for electron injection from CB of CdS to TiO<sub>2</sub> [5]. The narrow photocurrent response range of the CdS cell gives an agreement with its absorption spectrum, which is limited by the wide bandgap of CdS. In contrast, the PbS QDSCs present a narrower IPCE range (<700 nm) than their absorption spectra (up to 800 nm), possibly due to the non-radiative decay through deep energy level traps or low CB energy levels. For PbCdS-1 QDSCs, it is clear that the range of photocurrent response extends up to 800 nm, which is in concordance with its absorption spectrum. In addition, Cd cation may be bound to the unpassivated S in PbS, thus removing valence-band-associated trap states [36]. The possible reasons of the much improved efficiency in the infrared region are the higher CB edge and the much reduced trap density of states for the alloy QDs. Compared to PbS, a remarkably improved overall photocurrent response was observed with a maximum IPCE close to 40%. The IPCE is almost double to that of PbS.

Figure 1b shows the current–voltage (I–V) curves of QDSCs employing CdS, PbS, and PbCdS-1 with three SILAR cycles under simulated one sun illumination (AM 1.5, 100 mW/cm<sup>2</sup>). The corresponding parameters of performance are shown in Table S1. Among the three QDs, CdS gives the lowest photocurrent and the highest voltage due to its wide bandgap and high CB edge. PbS offers higher current and much lower voltage than CdS. The relative high current is due to the strong ability of PbS to harvest photons. The low voltage stems from that PbS suffers a serious carrier recombination due to low CB level and high trap densities. When PbCdS-1 was applied, the highest current (11.2 mA/cm<sup>2</sup>) was obtained, while the voltage is larger than that of PbS. The highest current stems mainly from the high IPCE of PbCdS-1 as discussed above. In addition to an efficient photon harvesting ability, there might be other reasons that contribute to the high current and voltage. According to recent publications, Hg- or Cu-doped PbS could push the CB position to a higher energy level, which further promotes the electron injection and leads to a high current [34,49]. In another recent research work, the introduction of Cd into PbS was found to bring a similar result [42,45]. Therefore, one can confirm that the CB edge of PbCdS-1 is much higher than for PbS, which means that the introduction of Cd into PbS is favorable for the electron injection. This favorable electron injection could reduce electron recombination between PbCdS-1 and TiO<sub>2</sub>, which contributes to a higher voltage.

Another reason might be the reduced defects by alloying Cd into PbS that may decrease trap density and restrain the recombination between TiO<sub>2</sub> and QDs.

To study the effect of the proportions of Pb and Cd in the Pb<sub>x</sub>Cd<sub>1-x</sub>S QDs, two more Pb<sub>x</sub>Cd<sub>1-x</sub>S QDs—PbCdS-2 and PbCdS-3—were investigated as photosensitizers for QDSC applications. PbCdS-1, -2, and -3 were prepared with gradually decreased Pb<sup>2+</sup> concentrations of precursor solution, as shown in Table S2. Inductively coupled plasma-atomic emission spectrometry (ICP-AES) was carried out to measure the three kinds of Pb<sub>x</sub>Cd<sub>1-x</sub>S QD electrodes prepared by five SILAR cycles, directly revealing the concentrations of Pb and Cd of Pb<sub>x</sub>Cd<sub>1-x</sub>S QDs listed in Table S3. Therefore, the corresponding chemical formula of PbCdS-1, -2, and -3 can be deduced as Pb<sub>0.54</sub>Cd<sub>0.46</sub>S, Pb<sub>0.31</sub>Cd<sub>0.69</sub>S, and Pb<sub>0.24</sub>Cd<sub>0.76</sub>S, respectively. Although these formulas may not be quite exact for other cycles of Pb<sub>x</sub>Cd<sub>1-x</sub>S QDs, the proportion of Pb in the Pb<sub>x</sub>Cd<sub>1-x</sub>S QDs can be confirmed to be in the order: PbCdS-1 > PbCdS-2 > PbCdS-3.

The absorption spectra of the five-SILAR-cycle QD-sensitized electrodes are shown in Figure 2a. Compared to the inset of Figure 1a, the five-SILAR-cycle CdS, PbS, and PbCdS-1 show stronger absorbance intensities and broader absorption ranges than the corresponding three-SILAR-cycle QDs. Increasing the number of cycles makes the QDs to grow bigger in size, leading to narrower bandgap and stronger and broader absorption. The effect of the proportion of Pb in the Pb<sub>x</sub>Cd<sub>1-x</sub>S QD alloys on the optical properties is illustrated by comparing the absorption spectra of PbCdS-1, PbCdS-2, and PbCdS-3. It is clearly indicated that the absorbance intensity follows the order: PbCdS-1 > PbCdS-2 > PbCdS-3. Moreover, derived from the absorption spectra, the Tauc plots of  $(h\nu\alpha)^2$  vs.  $h\nu$ , drawn in Figure 2b, can be employed to estimate the optical bandgap related by the Tauc equation [48].

$$(h\nu\alpha)^2 \propto (h\nu - E_g^{OP}) \quad (1)$$

where  $E_g^{OP}$  is optical bandgap,  $\nu$  is light frequency, and  $\alpha$  is the absorption coefficient. Therefore, the bandgap is determined by the intersection of the base line and the tangent line.

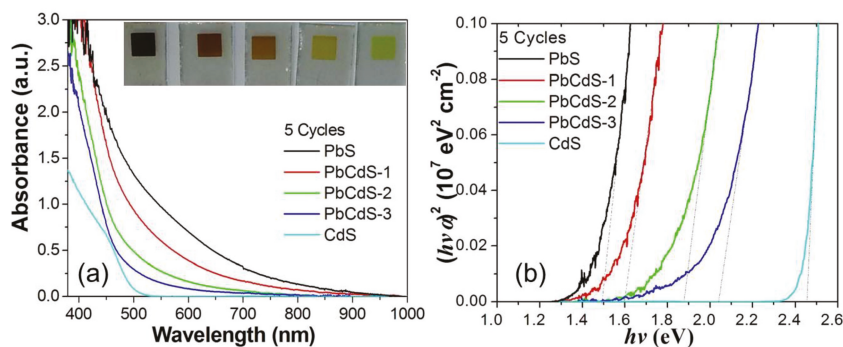


**Figure 2.** Absorption spectra (a) and Tauc plots (b) of five-SILAR-cycle PbS, PbCdS-1, -2, -3, and CdS-sensitized TiO<sub>2</sub> films. The bare TiO<sub>2</sub> film was used as blank in the absorption measurement. Inset images of (a) show the PbS, PbCdS-1, -2, -3, and CdS electrodes in turn from left to right. The dotted tangent lines of the linear region of plots in (b) show the linear fit for the bandgap energy of QDs.

As discussed above, the CB energy level is an important factor affecting the performance of QDs solar cells. In this study, cyclic voltammogram (CV) was carried out in a 0.1 M KCl aqueous solution at pH 6.9, shown in Figure 3. The CB edge can be determined by the onset potential of the reduction current [50,51]. Compared to the CV performance of bare FTO and TiO<sub>2</sub> electrodes (Figure S1), the onset parts of the reduction current surrounded by the dotted line should result from QDs. Therefore, combining the obtained bandgaps and CB edges, the relationship of energy levels



for different QDs and TiO<sub>2</sub> is shown in Scheme 1. The CB edge of TiO<sub>2</sub> was −4.21 eV (*vs.* vacuum) taken from the literature [52]. The CB energy value *vs.* normal hydrogen electrode (NHE) obtained from the CV was converted to the vacuum level by the relation that 0 V *vs.* NHE is equal to −4.5 eV *vs.* vacuum [53]. Clearly, as shown in Scheme 1, the bandgap of Pb<sub>x</sub>Cd<sub>1-x</sub>S QDs is wider than for PbS and narrower than for CdS under the same SILAR cycles, and the higher proportion of Pb in Pb<sub>x</sub>Cd<sub>1-x</sub>S presents a lower bandgap. In other words, increasing the proportion of Pb leads to a higher absorbance intensity and a concomitant shift of the absorption feature towards the higher wavelength because the larger proportion of Pb decreases the bandgap of the QDs. Moreover, it is confirmed that the CB positions of Pb<sub>x</sub>Cd<sub>1-x</sub>S QDs are between PbS and CdS QDs, and PbS QDs have a low CB edge (−4.15 eV) close to the TiO<sub>2</sub> CB edge. Therefore, a higher CB level causes a faster electron injection from QDs into TiO<sub>2</sub>.

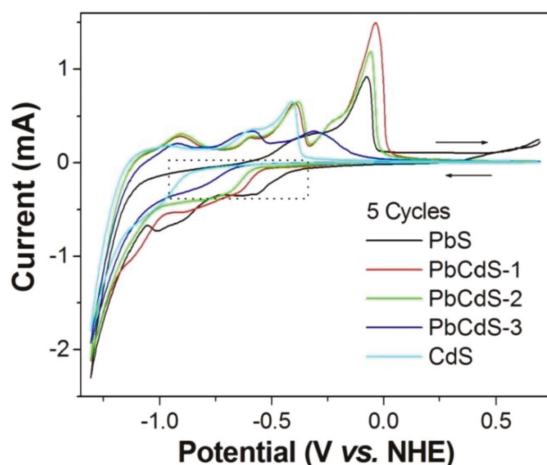
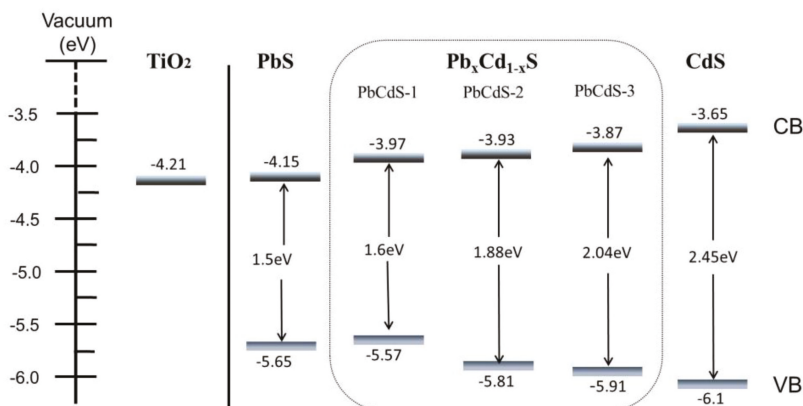


**Figure 3.** Cyclic voltammograms (CVs) of five-SILAR-cycle PbS, PbCdS-1, -2, -3, and CdS-sensitized TiO<sub>2</sub> electrode. CVs were measured with the electrolyte of 0.1 M KCl in deionized water (pH 6.9), and the scan rate was 10 mV/s. The arrows indicate the scan direction. The dotted part in the CV figures is to show the onset potentials of the reduction current varied at the different electrodes.



**Scheme 1.** Schematic diagram of edge energy levels of the conduction band (CB) edge and valence band (VB) edge for TiO<sub>2</sub> and five-SILAR-cycle PbS, CdS, and three kinds of Pb<sub>x</sub>Cd<sub>1-x</sub>S.

Generally, the major factors limiting the conversion efficiency of QDSC are the relatively slow electron transportation within the  $\text{TiO}_2$  film and the slow hole transfer, the main consequence of which is a large carrier loss due to the recombination between the  $\text{TiO}_2$  film and electrolyte [54]. Moreover, the trap states of QDs in the middle position between the  $\text{TiO}_2$  CB edge and the redox level of the electrolyte [3], which are generated by the interfacial effect and inner defects, can aggravate the recombination through back electron transfer via trap states. Therefore, it is vital to reduce the trap density of QDs for improving the performance of QDSCs. As discussed above, the presence of Cd in PbS may reduce the trap states. In order to verify the effect of Cd, dark I–V measurements were carried out, which is a good method to investigate the carrier recombination between  $\text{TiO}_2$  and electrolyte. As shown in Figure 4, the onset of dark current of the devices based on  $\text{Pb}_x\text{Cd}_{1-x}\text{S}$  occurred at a much higher bias-voltage than that of PbS, indicating that the recombination in  $\text{Pb}_x\text{Cd}_{1-x}\text{S}$ -based QDSCs is remarkably reduced. It also suggests that the increase of Cd in  $\text{Pb}_x\text{Cd}_{1-x}\text{S}$  can further reduce the recombination degree. The result proved that the utilization of  $\text{Pb}_x\text{Cd}_{1-x}\text{S}$  can effectively decrease the trap density.

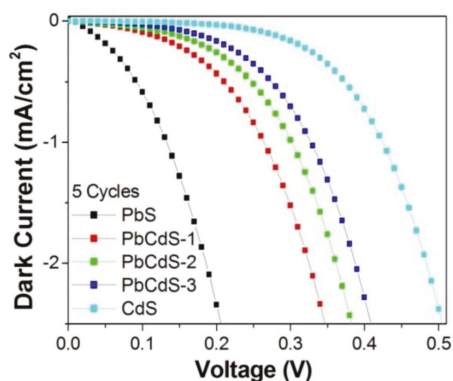


**Figure 4.** Dark I–V curves of QDSCs employing five-SILAR-cycle PbS, PbCdS-1, -2, -3, and CdS.

The optimization of the SILAR cycles is a key factor to boost the performance of the solar cells. Herein, we discuss the effect of SILAR cycles on the photovoltaic performance of the solar cells. The I–V curves of the solar cells of PbS, CdS, and  $\text{Pb}_x\text{Cd}_{1-x}\text{S}$  under one sun illumination are depicted in Figure S2. The photovoltaic parameters are listed in Table S4. In order to analyze the effect of the SILAR cycles, the photovoltaic parameters were presented as a function of the number of such cycles as shown in Figure 5. It was observed that the performance of the PbS solar cells decreases with the increase of SILAR cycles, probably due to the narrower bandgap and the lower CB energy level of the PbS QDs when the SILAR cycles increases after three cycles. The photocurrents of the three kinds of  $\text{Pb}_x\text{Cd}_{1-x}\text{S}$  and CdS are enhanced by increasing SILAR cycles until reaching a number of certain cycles. To further optimize the performance by increasing the cycle number, it was found that 7-cycle PbCdS-1, 7-cycle PbCdS-2, 9-cycle PbCdS-3, and 9-cycle CdS QDSCs provide the best photocurrent. Moreover, the trend of the efficiency is similar to that of the photocurrent. The comparison of the parameters between the different QD solar cells indicates that the QDs with the higher proportion of Pb show the higher short-circuit current and the lower open-circuit voltage.



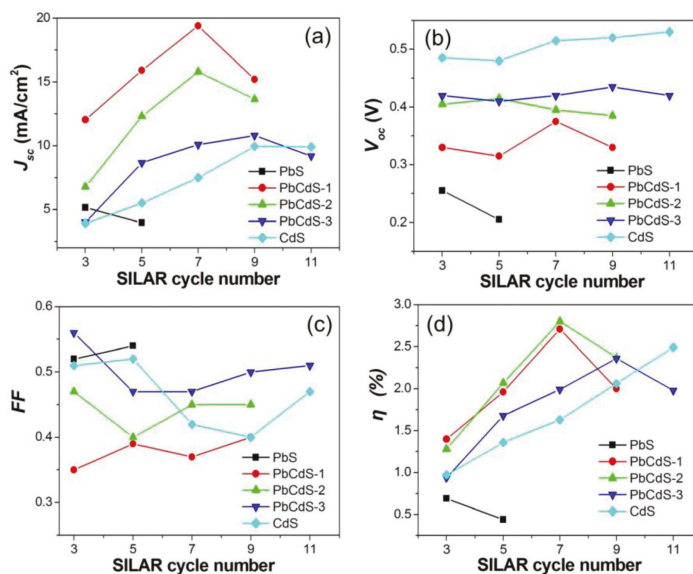


**Figure 5.** The photovoltaic parameters of QDSCs employing CdS, PbS, and three  $Pb_xCd_{1-x}S$  QDs in terms of the number of SILAR cycles. (a) short-circuit current density ( $J_{sc}$ ); (b) open-circuit voltage ( $V_{oc}$ ); (c) fill factor ( $FF$ ); (d) efficiency ( $\eta$ ).

After analyzing the optimization of solar cell parameters, some characteristic trends can be unraveled. In particular, the proportion of Pb and Cd in the  $Pb_xCd_{1-x}S$  alloys will affect these parameters. In order to better understand the effect, the optimized performance of the solar cells based on  $Pb_xCd_{1-x}S$  QDs are re-illustrated and compared in Figure 6; these are the PbCdS-1 (seven SILAR cycles), PbCdS-2 (seven SILAR cycles), and PbCdS-3 (nine SILAR cycles) QDSCs. These three samples show a similar maximum IPCE close to 60%. However, a clear broadening of the IPCE features is observed for the PbCdS-1 solar cell which presents an IPCE range up to more than 900 nm, while the PbCdS-3 only reaches 800 nm. In other words, increasing the proportion of Pb (and thus decreasing the proportion of Cd) in the  $Pb_xCd_{1-x}S$  alloys leads to a significant broadening of the IPCE features. This result is consistent with the absorption performance of the five cycles  $Pb_xCd_{1-x}S$ . Moreover, the IPCE trend also reflects the photocurrent in the I–V curves of the QDSCs. It is clear that the photocurrent follows the trend:  $PbCdS-1 > PbCdS-2 > PbCdS-3$ , something that can be mainly attributed to the light-harvesting ability of the  $Pb_xCd_{1-x}S$  alloys. The highest photocurrent  $J_{sc}$  obtained by the PbCdS-1 QDSCs reaches almost 20 mA/cm<sup>2</sup>. However, the voltage follows the reverse trend:  $PbCdS-1 < PbCdS-2 < PbCdS-3$ . Increasing the proportion of Pb leads to a lower voltage, which is caused by the effect of a lower CB level and higher trap density, as discussed above. PbCdS-2 QDSCs exhibit the efficiency of 2.8%, referring to their moderate photocurrent of 15.8 mA/cm<sup>2</sup> and voltage of 0.4 V. Therefore, controlling the ratio between Pb and Cd in the  $Pb_xCd_{1-x}S$  QDs alloys is very important for the photovoltaic performance of the QDSCs, especially for controlling the photocurrent and voltage.

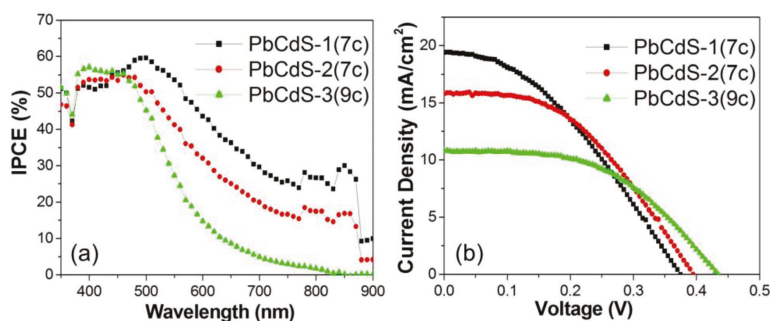


**Figure 6.** (a) IPCE spectra and (b) I–V curves of QDSCs employing PbCdS-1 (seven SILAR cycles), PbCdS-2 (seven SILAR cycles), and PbCdS-3 (nine SILAR cycles).

Furthermore, we also investigated the photovoltaic performance after an extra CdS coating layer was introduced onto the PbCdS-1 QDs, shown in Figure 7. The CB edge of CdS is higher than that of  $Pb_xCd_{1-x}S$ , which will favor the electron injection of CdS to  $TiO_2$  via PbCdS-1. Therefore, it could be observed that the IPCE of seven-cycle PbCdS-1 QDSCs after coating three-cycle CdS QDs improve, especially at wavelengths larger than 500 nm. In addition, CdS coating could serve as a protection layer to prevent the inner layered QDs from the corrosion of electrolyte and reduce the charge recombination [30]. This improvement gives us finally a photocurrent of  $22.6 \text{ mA/cm}^2$  and an efficiency of 3.2% for the QDSC.

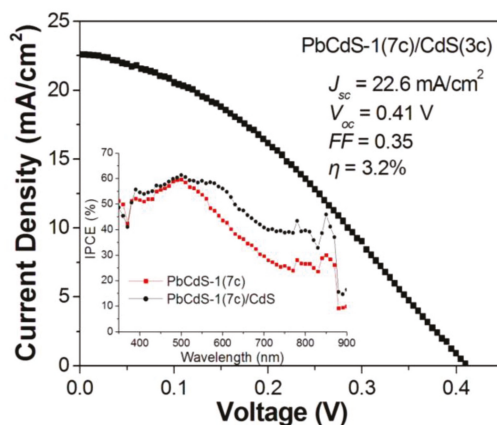


**Figure 7.** I–V curve of QDSC employing a hybrid QDs of PbCdS-1 (seven SILAR cycles) and CdS (three SILAR cycles), where PbCdS-1 was sensitized onto a  $TiO_2$  film, followed by subsequently depositing CdS onto PbCdS-1. Inset: IPCE spectrum of the hybrid QDs compared to the corresponding PbCdS-1 QDs.

### 3. Experimental Section

#### 3.1. Preparation of the QDs-Sensitized Solar Cells

Mesoporous  $TiO_2$  films with a triple-layer structure, containing the compact, transparent, and scattering layer, were prepared according to the procedure reported in [55]. First, fluorine-doped tin oxide (FTO, Solaronix TCO22-7) glass was sequentially cleaned in saturated sodium hydroxide isopropanol solution, absolute ethanol, and deionized (DI) water for 15 min under ultrasonic

treatment. To deposit the first layer, *i.e.*, compact layer, onto the FTO substrate, a freshly aqueous  $\text{TiCl}_4$  solution (40 mM) was used to treat the cleaned FTO glass for 30 min at 70 °C. Subsequently, the transparent and scattering layers were successively deposited by screen printing with  $\text{TiO}_2$  pastes (Solaronix, Ti-Nanoxide T/SP and R/SP), followed by sintering at 500 °C for 30 min in a muffle furnace to remove organic components. The sintered film was post-treated with an aqueous  $\text{TiCl}_4$  solution. The produced  $\text{TiO}_2$  films provided a thickness of 11  $\mu\text{m}$  (7  $\mu\text{m}$  for transparent layer and 4  $\mu\text{m}$  for scattering layer) and a working area of 5 mm  $\times$  5 mm.

QD-sensitized  $\text{TiO}_2$  photoelectrodes were fabricated by growing QDs directly onto a  $\text{TiO}_2$  film according to the method of successive ionic layer adsorption and reaction (SILAR). In this work, PbS, CdS, and  $\text{Pb}_x\text{Cd}_{1-x}\text{S}$  QD alloys were sensitized onto  $\text{TiO}_2$  films to produce the photoanode. In order to sensitize these QDs, several necessary precursor solutions containing different ions should be prepared: 0.1 M  $\text{Cd}(\text{NO}_3)_2$  aqueous solution as a  $\text{Cd}^{2+}$  source, 0.004 M  $\text{PbCl}_2$  aqueous solution as a  $\text{Pb}^{2+}$  source, and 0.1 M  $\text{Na}_2\text{S}$  solution in methanol/DI water (1:1 by volume) as a  $\text{S}^{2-}$  source. The aqueous ionic solution of mixed  $\text{Pb}^{2+}$  and  $\text{Cd}^{2+}$  made by adding 1%–4%  $\text{PbCl}_2$  into 0.1 M  $\text{Cd}(\text{NO}_3)_2$  solution was used as a cationic source to grow  $\text{Pb}_x\text{Cd}_{1-x}\text{S}$  QDs upon reacting with an anionic  $\text{S}^{2-}$  source. In this work, three kinds of  $\text{Pb}_x\text{Cd}_{1-x}\text{S}$  QDs, termed as PbCdS-1, PbCdS-2, and PbCdS-3, were prepared by the mixed precursor solution containing  $\text{Pb}^{2+}$  of 0.004 M, 0.002 M, and 0.001 M, respectively. The typical SILAR procedure is described by using PbS QDs as an example. The  $\text{TiO}_2$  film was alternately immersed into the  $\text{Pb}^{2+}$  source for 2 min and the  $\text{S}^{2-}$  source for another 2 min. The films were washed thoroughly with DI water and methanol to remove excess precursor between each immersion step. Such a single procedure is denoted as one growth cycle, and repeating the cycle to deposit more PbS onto the  $\text{TiO}_2$ . The precursor solutions containing  $\text{Pb}^{2+}$  were replaced by a fresh identical solution for a further immersion process every two SILAR cycles. After QDs sensitization, the surface of the QDs was passivated by depositing a layer coating of ZnS in order to optimize the performance of solar cells. The ZnS coating was prepared by two SILAR cycles using a 0.1 M methanol solution of a  $\text{Zn}(\text{NO}_3)_2$  as  $\text{Zn}^{2+}$  source.

The preparation process of  $\text{Cu}_2\text{S}$  counter electrode is similar to that in the previous report [56]. Briefly, a tailored brass foil was immersed in HCl solution for 5 min at 70 °C, cleaned by DI water, and subsequently dipped into an aqueous polysulfide solution containing 1 M S and 1 M  $\text{Na}_2\text{S}$  to generate a layer of fresh  $\text{Cu}_2\text{S}$  onto the brass substrate. The sandwich structure of QDSCs was fabricated by assembling a QD-sensitized  $\text{TiO}_2$  film and  $\text{Cu}_2\text{S}$  counter electrode with a 50- $\mu\text{m}$  Surlyn film as the sealing thermoplastic material. Polysulfide electrolyte, containing  $\text{Na}_2\text{S}$  (2 M) and S (3 M) in water/methanol (7:3 by volume), was injected to empty space between the two electrodes through a hole on the counter electrode.

### 3.2. Measurement and Equipment

UV-Vis spectra of the QD-deposited  $\text{TiO}_2$  films were measured by a Lambda 750 UV-Vis spectrometer (PerkinElmer, Waltham, MA, USA). The current–voltage (I–V) characteristics of the solar cell were performed by using a Keithley source-meter under AM 1.5 illumination ( $100 \text{ mW} \cdot \text{cm}^{-2}$ ) from a Newport 300 W solar simulator (Newport Corporation, Irvine, CA, USA). The I–V measurement setup was calibrated by using an IR-filtered silicon solar cell (Fraunhofer ISE, Freiburg, Germany). Incident photon-to-current conversion efficiencies (IPCEs) were determined using a measurement system including a 300 W xenon lamp, a 1/8 m monochromator, a Keithley source-meter, and a power meter with a 818-UV detector head. IPCEs were measured by monitoring photocurrent from low to high wavelength every 10 nm. The measured IPCE at higher wavelengths was lower than the actual value because PbS QDSCs are not stable and have slow photoelectric response. The cells with strong photoelectric response at above ~750 nm exhibit a similar fluctuation in IPCE. This should be an equipment problem, possibly resulting from the xenon lamp in the IPCE system. To weaken the light reflection, a black mask (6 mm  $\times$  6 mm) was used for photovoltaic measurements. The inductively coupled plasma-atomic emission spectrometry (ICP-AES) was measured by a Perkin Elmer Model

Optima 7300DV ICP AEOS (PerkinElmer, Waltham, MA, USA). Under each condition, at least three samples were prepared for the measurements in order to obtain a medium value as the final data. Cyclic voltammogram (CV) was carried out at ambient temperature with a electrochemical workstation (model 660A, CH Instruments, Austin, TX, USA) using a regular three-electrode electrochemical cell. The measured sample films were used as the working electrode, a Pt sheet as the counter electrode, and a Ag/AgCl electrode as the reference electrode. The potential conversion of reference from the Ag/AgCl electrode to normal hydrogen electrode by  $E$  (vs. NHE) =  $E$  (vs. Ag/AgCl) + 0.197 V [57].

#### 4. Conclusions

This work was motivated by the fact that, while PbS quantum dots (QDs) have been successfully applied in heterojunction solar cells, showing remarkable conversion efficiency, corresponding PbS QD-sensitized solar cells (QDSCs) still have shown low device performance. One way to improve such QDSCs and utilize the high underlying quantum efficiency is alloying other metals to give a higher quality QDs. We have therefore fabricated ternary alloy  $Pb_xCd_{1-x}S$  photosensitizers for quantum-dot-sensitized solar cells (QDSCs) by the process of successive ionic layer adsorption and reaction (SILAR). The photovoltaic performance of the QDSCs based on three kinds of  $Pb_xCd_{1-x}S$  QDs were explored by the comparison with the corresponding PbS and CdS QDs. Firstly, we found that the three-SILAR-cycle PbCdS-1 ( $Pb_{0.54}Cd_{0.46}S$ ) presents a much higher photocurrent compared to PbS and CdS. Then, by investigation of the absorption spectrum, cyclic voltammogram (CV), and dark I-V current of five-SILAR-cycle QDs, it is suggested that  $Pb_xCd_{1-x}S$  QDs have a wider absorption range compared to the CdS QDs and a higher conduction band (CB) edge and reduced trap density compared to the PbS QDs. This indicates that the  $Pb_xCd_{1-x}S$  QD alloys can overcome the shortcomings of CdS and PbS for QDSC applications. Furthermore, by comparing the PbCdS-1, PbCdS-2 ( $Pb_{0.31}Cd_{0.69}S$ ), and PbCdS-3 ( $Pb_{0.24}Cd_{0.76}S$ ) QDSCs, we found that the solar cells based on the  $Pb_xCd_{1-x}S$  alloy with a higher proportion of Pb exhibit a larger photocurrent and a lower photovoltage. As a result, the PbCdS-1 solar cells present a significant short-circuit current density ( $J_{sc}$ ), up to 20 mA/cm<sup>2</sup>, by the optimization of the SILAR cycles. This indicates that the employment of  $Pb_xCd_{1-x}S$  QD alloys can be a strategy to improve the photocurrent for the PbS and CdS QDSCs. Indeed, the control of the ratio of Pb:Cd in the  $Pb_xCd_{1-x}S$  alloys is very critical for the photovoltaic performance of QDSCs based on  $Pb_xCd_{1-x}S$  QDs. A good proportion and balance of Pb and Cd is thus required for achieving an optimum current and voltage of the solar cells. Finally, a coating layer of CdS deposited onto  $Pb_xCd_{1-x}S$  photoelectrode gives enhancements in the photocurrent to 22.6 mA/cm<sup>2</sup> and in the efficiency to 3.2%. It is reasonable to anticipate the remarkable enhancement of QDSCs by improving QD quality with less or even no defects and developing more effective passivation materials.

**Supplementary Materials:** The following are available online at <http://www.mdpi.com/2079-4991/6/6/97/s1>. Table S1: The photovoltaic parameters of QDSCs employing three SILAR cycles of CdS, PbS, and PbCdS-1 as photosensitizers. Table S2: The concentrations of precursor solutions of cationic sources used in this work. Table S3: The concentrations of Pb and Cd in  $Pb_xCd_{1-x}S$  QDs were assayed by inductively coupled plasma-atomic emission spectrometry (ICP-AES). Table S4: The photovoltaic parameters of QDSCs depending on the number of SILAR cycles, employing CdS, PbS, and  $Pb_xCd_{1-x}S$  as photosensitizers; short-circuit current ( $J_{sc}$ ), open-circuit voltage ( $V_{oc}$ ), fill factor (FF), efficiency ( $\eta$ ). Figure S1: Cyclic voltammograms of the bare FTO glass and TiO<sub>2</sub> electrode measured under the same condition with Figure 3. Figure S2: I-V curves of QDSCs depending on the number of SILAR cycles, employing (a) CdS, (b) PbS, (c) PbCdS-1, (d) PbCdS-2, (e) PbCdS-3 as photosensitizers.

**Acknowledgments:** We acknowledge support from the Swedish Science Research Council, contract nr. C0334701, the Swedish Energy Agency, K & A Wallenberg Foundation, and National Natural Science Foundation of China (21120102036, 91233201).

**Author Contributions:** C.Y. and L.L. conceived, designed, and performed the experiments, as well as analyzed the data and wrote the paper; Z.N. measured ICP-AES, analyzed data, and provided helpful suggestions; J.H. participated in the electrode fabrication and electrochemistry measurements; L.S. and H.Å. contributed to the discussion, the analysis of the data, and the writing of the paper.

**Conflicts of Interest:** The authors declare no conflict of interest.

## References

1. Robel, I.; Subramanian, V.; Kuno, M.; Kamat, P.V. Quantum Dot Solar Cells. Harvesting Light Energy with CdSe Nanocrystals Molecularly Linked to Mesoscopic TiO<sub>2</sub> Films. *J. Am. Chem. Soc.* **2006**, *128*, 2385–2393. [CrossRef] [PubMed]
2. O'Regan, B.; Grätzel, M. A Low-Cost, High-Efficiency Solar Cell Based on Dye-Sensitized Colloidal Titanium Dioxide Films. *Nature* **1991**, *353*, 737–740. [CrossRef]
3. Mora-Sero, I.; Gimenez, S.; Fabregat-Santiago, F.; Gomez, R.; Shen, Q.; Toyoda, T.; Bisquert, J. Recombination in Quantum Dot Sensitized Solar Cells. *Acc. Chem. Res.* **2009**, *42*, 1848–1857. [CrossRef] [PubMed]
4. Hossain, M.A.; Jennings, J.R.; Shen, C.; Pan, J.H.; Koh, Z.Y.; Mathews, N.; Wang, Q. CdSe-Sensitized Mesoscopic TiO<sub>2</sub> Solar Cells Exhibiting >5% Efficiency: Redundancy of CdS Buffer Layer. *J. Mater. Chem.* **2012**, *22*, 16235–16242. [CrossRef]
5. Lee, Y.-L.; Lo, Y.-S. Highly Efficient Quantum-Dot-Sensitized Solar Cell Based on Co-Sensitization of CdS/CdSe. *Adv. Funct. Mater.* **2009**, *19*, 604–609. [CrossRef]
6. Yu, X.-Y.; Liao, J.-Y.; Qiu, K.-Q.; Kuang, D.-B.; Su, C.-Y. Dynamic Study of Highly Efficient CdS/CdSe Quantum Dot-Sensitized Solar Cells Fabricated by Electrodeposition. *ACS Nano* **2011**, *5*, 9494–9500. [CrossRef] [PubMed]
7. Zhang, X.; Huang, X.; Yang, Y.; Wang, S.; Gong, Y.; Luo, Y.; Li, D.; Meng, Q. Investigation on New CuInS<sub>2</sub>/Carbon Composite Counter Electrodes for CdS/CdSe Cosensitized Solar Cells. *ACS Appl. Mater. Interfaces* **2013**, *5*, 5954–5960. [CrossRef] [PubMed]
8. Ellingson, R.J.; Beard, M.C.; Johnson, J.C.; Yu, P.; Micic, O.I.; Nozik, A.J.; Shabaev, A.; Efros, A.L. Highly Efficient Multiple Exciton Generation in Colloidal PbSe and PbS Quantum Dots. *Nano Lett.* **2005**, *5*, 865–871. [CrossRef] [PubMed]
9. Nozik, A.; Beard, M.; Luther, J.; Law, M. Semiconductor Quantum Dots and Quantum Dot Arrays and Applications of Multiple Exciton Generation to Third-Generation Photovoltaic Solar Cells. *Chem. Rev.* **2010**, *110*, 6873–6890. [CrossRef] [PubMed]
10. Yang, Z.; Chen, C.Y.; Roy, P.; Chang, H.T. Quantum Dot-Sensitized Solar Cells Incorporating Nanomaterials. *Chem. Commun.* **2011**, *47*, 9561–9571. [CrossRef] [PubMed]
11. McDaniel, H.; Fuke, N.; Makarov, N.S.; Pietryga, J.M.; Klimov, V.I. An Integrated Approach to Realizing High-Performance Liquid-Junction Quantum Dot Sensitized Solar Cells. *Nat. Commun.* **2013**, *4*. [CrossRef] [PubMed]
12. Wang, G.; Wei, H.; Luo, Y.; Wu, H.; Li, D.; Zhong, X.; Meng, Q. A Strategy to Boost the Cell Performance of CdSe<sub>x</sub>Te<sub>1-x</sub> Quantum Dot Sensitized Solar Cells over 8% by Introducing Mn Modified CdSe Coating Layer. *J. Power Sources* **2016**, *302*, 266–273. [CrossRef]
13. Wang, J.; Li, Y.; Shen, Q.; Izuishi, T.; Pan, Z.; Zhao, K.; Zhong, X. Mn Doped Quantum Dot Sensitized Solar Cells with Power Conversion Efficiency Exceeding 9%. *J. Mater. Chem. A* **2016**, *4*, 877–886. [CrossRef]
14. Ning, Z.; Tian, H.; Yuan, C.; Fu, Y.; Sun, L.; Ågren, H. Pure Organic Redox Couple for Quantum-Dot-Sensitized Solar Cells. *Chem. Eur. J.* **2011**, *17*, 6330–6333. [CrossRef] [PubMed]
15. Lightcap, I.V.; Kamat, P.V. Fortification of CdSe Quantum Dots with Graphene Oxide. Excited State Interactions and Light Energy Conversion. *J. Am. Chem. Soc.* **2012**, *134*, 7109–7116. [CrossRef] [PubMed]
16. Farrow, B.; Kamat, P.V. CdSe Quantum Dot Sensitized Solar Cells. Shuttling Electrons through Stacked Carbon Nanocups. *J. Am. Chem. Soc.* **2009**, *131*, 11124–11131. [CrossRef] [PubMed]
17. Zhang, Q.; Chen, G.; Yang, Y.; Shen, X.; Zhang, Y.; Li, C.; Yu, R.; Luo, Y.; Li, D.; Meng, Q. Toward Highly Efficient CdS/CdSe Quantum Dots-Sensitized Solar Cells Incorporating Ordered Photoanodes on Transparent Conductive Substrates. *Phys. Chem. Chem. Phys.* **2012**, *14*, 6479–6486. [CrossRef] [PubMed]
18. Salant, A.; Shalom, M.; Tachan, Z.; Buhbut, S.; Zaban, A.; Banin, U. Quantum Rod-Sensitized Solar Cell: Nanocrystal Shape Effect on the Photovoltaic Properties. *Nano Lett.* **2012**, *12*, 2095–2100. [CrossRef] [PubMed]
19. Ning, Z.; Yuan, C.; Tian, H.; Hedstrom, P.; Sun, L.; Ågren, H. Quantum Rod-Sensitized Solar Cells. *ChemSusChem* **2011**, *4*, 1741–1744. [CrossRef] [PubMed]
20. Nazeeruddin, M.K.; Pechy, P.; Renouard, T.; Zakeeruddin, S.M.; Humphry-Baker, R.; Comte, P.; Liska, P.; Cevey, L.; Costa, E.; Shklover, V.; *et al.* Engineering of Efficient Panchromatic Sensitizers for Nanocrystalline TiO<sub>2</sub>-Based Solar Cells. *J. Am. Chem. Soc.* **2001**, *123*, 1613–1624. [CrossRef] [PubMed]

21. Kinoshita, T.; Dy, J.T.; Uchida, S.; Kubo, T.; Segawa, H. Wideband Dye-Sensitized Solar Cells Employing a Phosphine-Coordinated Ruthenium Sensitizer. *Nat. Photonics* **2013**, *7*, 535–539. [CrossRef]
22. Yuan, C.Z.; Chen, G.Y.; Prasad, P.N.; Ohulchanskyy, T.Y.; Ning, Z.J.; Tian, H.N.; Sun, L.C.; Ågren, H. Use of Colloidal Upconversion Nanocrystals for Energy Relay Solar Cell Light Harvesting in the near-Infrared Region. *J. Mater. Chem.* **2012**, *22*, 16709–16713. [CrossRef]
23. Kim, S.; Fisher, B.; Eisler, H.-J.; Bawendi, M. Type-II Quantum Dots: CdTe/CdSe(Core/Shell) and CdSe/ZnTe(Core/Shell) Heterostructures. *J. Am. Chem. Soc.* **2003**, *125*, 11466–11467. [CrossRef] [PubMed]
24. Ning, Z.; Tian, H.; Yuan, C.; Fu, Y.; Qin, H.; Sun, L.; Ågren, H. Solar Cells Sensitized with Type-II ZnSe-CdS Core/Shell Colloidal Quantum Dots. *Chem. Commun.* **2011**, *47*, 1536–1538. [CrossRef] [PubMed]
25. Pan, Z.; Zhao, K.; Wang, J.; Zhang, H.; Feng, Y.; Zhong, X. Near Infrared Absorption of CdSe<sub>x</sub>Te<sub>1-x</sub> Alloyed Quantum Dot Sensitized Solar Cells with More Than 6% Efficiency and High Stability. *ACS Nano* **2013**, *7*, 5215–5222. [CrossRef] [PubMed]
26. Tubtintae, A.; Wu, K.-L.; Tung, H.-Y.; Lee, M.-W.; Wang, G.J. Ag<sub>2</sub>S Quantum Dot-Sensitized Solar Cells. *Electrochem. Commun.* **2010**, *12*, 1158–1160. [CrossRef]
27. Parsi Benekohal, N.; González-Pedro, V.; Boix, P.P.; Chavhan, S.; Tena-Zaera, R.; Demopoulos, G.P.; Mora-Seró, I. Colloidal PbS and PbSeS Quantum Dot Sensitized Solar Cells Prepared by Electrophoretic Deposition. *J. Phys. Chem. C* **2012**, *116*, 16391–16397. [CrossRef]
28. Long, R.; Prezhdo, O.V. *Ab Initio* Nonadiabatic Molecular Dynamics of the Ultrafast Electron Injection from a PbSe Quantum Dot into the TiO<sub>2</sub> Surface. *J. Am. Chem. Soc.* **2011**, *133*, 19240–19249. [CrossRef] [PubMed]
29. Sambur, J.B.; Novet, T.; Parkinson, B.A. Multiple Exciton Collection in a Sensitized Photovoltaic System. *Science* **2010**, *330*, 63–66. [CrossRef] [PubMed]
30. Braga, A.; Giménez, S.; Concina, I.; Vomiero, A.; Mora-Seró, I. Panchromatic Sensitized Solar Cells Based on Metal Sulfide Quantum Dots Grown Directly on Nanostructured TiO<sub>2</sub> electrodes. *J. Phys. Chem. Lett.* **2011**, *2*, 454–460. [CrossRef]
31. Ma, W.; Luther, J.M.; Zheng, H.; Wu, Y.; Alivisatos, A.P. Photovoltaic Devices Employing Ternary PbS<sub>x</sub>Se<sub>1-x</sub> Nanocrystals. *Nano Lett.* **2009**, *9*, 1699–1703. [CrossRef] [PubMed]
32. Lee, H.; Leventis, H.C.; Moon, S.-J.; Chen, P.; Ito, S.; Haque, S.A.; Torres, T.; Nüesch, F.; Geiger, T.; Zakeeruddin, S.M.; *et al.* PbS and CdS Quantum Dot-Sensitized Solid-State Solar Cells: “Old Concepts, New Results”. *Adv. Funct. Mater.* **2009**, *19*, 2735–2742. [CrossRef]
33. Gonzalez-Pedro, V.; Sima, C.; Marzari, G.; Boix, P.P.; Gimenez, S.; Shen, Q.; Dittrich, T.; Mora-Sero, I. High Performance PbS Quantum Dot Sensitized Solar Cells Exceeding 4% Efficiency: The Role of Metal Precursors in the Electron Injection and Charge Separation. *Phys. Chem. Chem. Phys.* **2013**, *15*, 13835–13843. [CrossRef] [PubMed]
34. Lee, J.W.; Son, D.Y.; Ahn, T.K.; Shin, H.W.; Kim, I.Y.; Hwang, S.J.; Ko, M.J.; Sul, S.; Han, H.; Park, N.G. Quantum-Dot-Sensitized Solar Cell with Unprecedentedly High Photocurrent. *Sci. Rep.* **2013**, *3*. [CrossRef] [PubMed]
35. Niu, G.; Wang, L.; Gao, R.; Ma, B.; Dong, H.; Qiu, Y. Inorganic Iodide Ligands in *Ex Situ* PbS Quantum Dot Sensitized Solar Cells with I<sup>-</sup>/I<sup>3-</sup> Electrolytes. *J. Mater. Chem.* **2012**, *22*, 16914–16919. [CrossRef]
36. Ip, A.H.; Thon, S.M.; Hoogland, S.; Voznyy, O.; Zhitomirsky, D.; Debnath, R.; Levina, L.; Rollny, L.R.; Carey, G.H.; Fischer, A.; *et al.* Hybrid Passivated Colloidal Quantum Dot Solids. *Nat. Nanotechnol.* **2012**, *7*, 577–582. [CrossRef] [PubMed]
37. Tang, J.; Kemp, K.W.; Hoogland, S.; Jeong, K.S.; Liu, H.; Levina, L.; Furukawa, M.; Wang, X.; Debnath, R.; Cha, D.; *et al.* Colloidal-Quantum-Dot Photovoltaics Using Atomic-Ligand Passivation. *Nat. Mater.* **2011**, *10*, 765–771. [CrossRef] [PubMed]
38. Ning, Z.; Zhitomirsky, D.; Adinolfi, V.; Sutherland, B.; Xu, J.; Voznyy, O.; Maraghechi, P.; Lan, X.; Hoogland, S.; Ren, Y.; *et al.* Graded Doping for Enhanced Colloidal Quantum Dot Photovoltaics. *Adv. Mater.* **2013**, *25*, 1719–1723. [CrossRef] [PubMed]
39. Etgar, L.; Moehl, T.; Gabriel, S.; Hickey, S.G.; Eychmuller, A.; Grätzel, M. Light Energy Conversion by Mesoscopic PbS Quantum Dots/TiO<sub>2</sub> Heterojunction Solar Cells. *ACS Nano* **2012**, *6*, 3092–3099. [CrossRef] [PubMed]
40. Kim, G.H.; Garcia de Arquer, F.P.; Yoon, Y.J.; Lan, X.; Liu, M.; Voznyy, O.; Yang, Z.; Fan, F.; Ip, A.H.; Kanjanaboos, P.; *et al.* High-Efficiency Colloidal Quantum Dot Photovoltaics via Robust Self-Assembled Monolayers. *Nano Lett.* **2015**, *15*, 7691–7696. [CrossRef] [PubMed]



41. Lan, X.; Voznyy, O.; Kiani, A.; Garcia de Arquer, F.P.; Abbas, A.S.; Kim, G.H.; Liu, M.; Yang, Z.; Walters, G.; Xu, J.; *et al.* Passivation Using Molecular Halides Increases Quantum Dot Solar Cell Performance. *Adv. Mater.* **2016**, *28*, 299–304. [CrossRef] [PubMed]
42. Kim, J.; Choi, H.; Nahm, C.; Kim, C.; Ik Kim, J.; Lee, W.; Kang, S.; Lee, B.; Hwang, T.; Hejin Park, H.; *et al.* Graded Bandgap Structure for PbS/CdS/ZnS Quantum-Dot-Sensitized Solar Cells with a  $Pb_xCd_{1-x}S$  Interlayer. *Appl. Phys. Lett.* **2013**, *102*. [CrossRef]
43. Santra, P.K.; Kamat, P.V. Tandem-Layered Quantum Dot Solar Cells: Tuning the Photovoltaic Response with Luminescent Ternary Cadmium Chalcogenides. *J. Am. Chem. Soc.* **2013**, *135*, 877–885. [CrossRef] [PubMed]
44. Lee, H.J.; Wang, M.; Chen, P.; Gamelin, D.R.; Zakeeruddin, S.M.; Grätzel, M.; Nazeeruddin, M.K. Efficient CdSe Quantum Dot-Sensitized Solar Cells Prepared by an Improved Successive Ionic Layer Adsorption and Reaction Process. *Nano Lett.* **2009**, *9*, 4221–4227. [CrossRef] [PubMed]
45. Shu, T.; Zhou, Z.-M.; Wang, H.; Liu, G.-H.; Xiang, P.; Rong, Y.-G.; Zhao, Y.-D.; Han, H.-W. Efficient CdPbS Quantum Dots-Sensitized  $TiO_2$  Photoelectrodes for Solar Cell Applications. *J. Nanosci. Nanotechnol.* **2011**, *11*, 9645–9649. [CrossRef] [PubMed]
46. Singh, N.; Mehra, R.M.; Kapoor, A.; Soga, T. ZnO Based Quantum Dot Sensitized Solar Cell Using CdS Quantum Dots. *J. Renew. Sustain. Energy* **2012**, *4*. [CrossRef]
47. Gocalińska, A.; Saba, M.; Quochi, F.; Marceddu, M.; Szendrei, K.; Gao, J.; Loi, M.A.; Yarema, M.; Seyrkammer, R.; Heiss, W.; *et al.* Size-Dependent Electron Transfer from Colloidal PbS Nanocrystals to Fullerene. *J. Phys. Chem. Lett.* **2010**, *1*, 1149–1154. [CrossRef]
48. Tauc, J.; Menth, A.; Wood, D.L. Optical and Magnetic Investigations of the Localized States in Semiconducting Glasses. *Phys. Rev. Lett.* **1970**, *25*, 749–752. [CrossRef]
49. Huang, Z.; Zou, X.; Zhou, H. A Strategy to Achieve Superior Photocurrent by Cu-Doped Quantum Dot Sensitized Solar Cells. *Mater. Lett.* **2013**, *95*, 139–141. [CrossRef]
50. Haram, S.K.; Kshirsagar, A.; Gujarathi, Y.D.; Ingole, P.P.; Nene, O.A.; Markad, G.B.; Nanavati, S.P. Quantum Confinement in CdTe Quantum Dots: Investigation through Cyclic Voltammetry Supported by Density Functional Theory. *J. Phys. Chem. C* **2011**, *115*, 6243–6249. [CrossRef]
51. Lee, M.S.; Cheon, I.C.; Kim, Y.I. Photoelectrochemical Studies of Nanocrystalline  $TiO_2$  Film Electrodes. *Bull. Korean Chem. Soc.* **2003**, *24*, 1155–1162.
52. Xu, Y.; Schoonen, M.A.A. The Absolute Energy Positions of Conduction and Valence Bands of Selected Semiconducting Minerals. *Am. Mineral.* **2000**, *85*, 543–556. [CrossRef]
53. Grätzel, M. Photoelectrochemical Cells. *Nature* **2001**, *414*, 338–344. [CrossRef] [PubMed]
54. Kamat, P.V. Quantum Dot Solar Cells. The Next Big Thing in Photovoltaics. *J. Phys. Chem. Lett.* **2013**, *4*, 908–918. [CrossRef] [PubMed]
55. Ito, S.; Murakami, T.N.; Comte, P.; Liska, P.; Grätzel, C.; Nazeeruddin, M.K.; Grätzel, M. Fabrication of Thin Film Dye Sensitized Solar Cells with Solar to Electric Power Conversion Efficiency over 10%. *Thin Solid Films* **2008**, *516*, 4613–4619. [CrossRef]
56. Gimenez, S.; Mora-Sero, I.; Macor, L.; Guijarro, N.; Lana-Villarreal, T.; Gomez, R.; Diguna, L.J.; Shen, Q.; Toyoda, T.; Bisquet, J. Improving the Performance of Colloidal Quantum-Dot-Sensitized Solar Cells. *Nanotechnology* **2009**, *20*. [CrossRef] [PubMed]
57. Esswein, A.J.; Surendranath, Y.; Reece, S.Y.; Nocera, D.G. Highly Active Cobalt Phosphate and Borate Based Oxygen Evolving Catalysts Operating in Neutral and Natural Waters. *Energy Environ. Sci.* **2011**, *4*, 499–504. [CrossRef]



© 2016 by the authors. Licensee MDPI, Basel, Switzerland. This article is an open access article distributed under the terms and conditions of the Creative Commons Attribution (CC BY) license (<http://creativecommons.org/licenses/by/4.0/>).



Article

# Numerical Study of Complementary Nanostructures for Light Trapping in Colloidal Quantum Dot Solar Cells

Jue Wei <sup>1,2</sup>, Qiuyang Xiong <sup>1</sup>, Seyed Milad Mahpeykar <sup>1</sup> and Xihua Wang <sup>1,\*</sup>

<sup>1</sup> Department of Electrical and Computer Engineering, University of Alberta, Edmonton, AB T6G 2V4, Canada; weijue@hotmail.com (J.W.); qiuyang@ualberta.ca (Q.X.); mahpeyka@ualberta.ca (S.M.M.)

<sup>2</sup> Key Laboratory of Coherent Light and Atomic and Molecular Spectroscopy of Ministry of Education, College of Physics, Jilin University, Changchun 130012, China

\* Correspondence: xihua@ualberta.ca; Tel.: +1-780-492-3523

Academic Editor: Guanying Chen

Received: 15 February 2016; Accepted: 21 March 2016; Published: 25 March 2016

**Abstract:** We have investigated two complementary nanostructures, nanocavity and nanopillar arrays, for light absorption enhancement in depleted heterojunction colloidal quantum dot (CQD) solar cells. A facile complementary fabrication process is demonstrated for patterning these nanostructures over the large area required for light trapping in photovoltaic devices. The simulation results show that both proposed periodic nanostructures can effectively increase the light absorption in CQD layer of the solar cell throughout the near-infrared region where CQD solar cells typically exhibit weak light absorption. The complementary fabrication process for implementation of these nanostructures can pave the way for large-area, inexpensive light trapping implementation in nanostructured solar cells.

**Keywords:** solar cells; nanostructures; light trapping

## 1. Introduction

In the last few years, colloidal quantum dot (CQD) solar cells have received a great deal of attention due to their potential for large-area, high-throughput, and low-cost manufacturing [1]. Despite all the achievements in CQD synthesis, surface treatment and film deposition technologies [2], the power conversion efficiency of this type of solar cell continues to lag behind traditional silicon solar cells. Because of the lack of long diffusion lengths for photo-generated carriers in CQD films, a CQD film capable of taking advantage of all the incident solar power would be too thick to extract all the generated carriers, leading to an absorption-extraction trade-off [3–5]. Light trapping, or effectively increasing optical path lengths in the absorbing material through structuring without any change in light absorbing material's thickness, is one option to overcome the aforementioned trade-off [6].

Periodic nanostructured gratings have been extensively explored for light trapping in various types of thin-film solar cells and various silicon or metamaterial-based structures have been proposed, such as nanopillar, nanowire, nanohole, and pyramid arrays [7–14]. The downside, however, is that these structures are difficult to fabricate due to their complicated structures or material compositions. Metallic gratings have also been considered for light harvesting enhancement by taking advantage of surface plasmons [15–17]. However, parasitic light absorption intrinsic to metallic structures which can compete against useful absorption in light absorbing layer has severely limited the application of metallic nanostructures in photovoltaic devices [18].



Recently, we reported on periodic nano-branch indium-doped tin oxide (ITO) electrodes as diffraction gratings for light absorption enhancement in CQD solar cells [19]. Using numerical simulations, a significant polarization-independent broadband light absorption enhancement was observed for two-dimensional ITO nano-branch gratings and the absorption enhancement was demonstrated to be almost independent of common fabrication flaws in nano-branch structure. On the other hand, current fabrication technologies are unable to implement the fabrication of such nanostructures due to the difficulty of keeping the periodicity of the structure over a large area and also incorporation of CQDs into such porous structure.

In order to be able to apply a periodic nanostructure for practical and tangible light trapping in solar cells, maintaining the periodicity of the structure over a large area is the key requirement. Therefore, the fabrication process used to impose the periodic pattern must be able to produce periodic patterns over large areas and also inexpensive at the same time. Recent advances in large-scale nanofabrication techniques have allowed sophisticated nanostructures to be employed in solar cells and photodetectors with impressive results [20,21]. In this work, in order to fully satisfy the large-area requirement of light trapping structures, we consider two experimentally available nanostructures (nanocavity and nanopillar) for light absorption enhancement in CQD solar cells due to their potential for easy large-area fabrication and CQD incorporation. A facile fabrication process is performed to achieve large-area periodic pattern of the nanocavity and nanopillar structures. The simulation results show that compared to the reference flat structure, our proposed structures can achieve relatively high absorption enhancement in CQD solar cells.

## 2. Results and Discussion

### 2.1. Structure Design

The main reason that nanocavity and nanopillar arrays are proposed as nanostructured electrodes to improve absorption enhancement in PbS CQD solar cells is that such nanostructures can be easily fabricated over large areas by a low-cost pattern transfer method known as nanosphere lithography (NSL). As a proof of concept, PDMS nanopillar and silver nanocavity arrays were fabricated utilizing nanosphere lithography. The proposed process steps for fabrication of nanocavity and nanopillar arrays is presented schematically in Figure 1a. Firstly, colloidal nanosphere mask is deposited on a Si substrate. After nanosphere mask formation, oxygen plasma is employed to shrink the nanospheres to ideal diameter needed for the intended structure through reactive ion etching (RIE). The next step is to deposit the desired material, in this case silver (Ag), on the sample covered by colloidal mask. The final step is to lift off the nanosphere mask, which is usually done in ultrasonic bath with organic solvents such as acetone, after which the nanocavity array is formed on the substrate. In addition to being a standalone light trapping structure, the fabricated nanocavity array can be utilized for fabrication of nanopillar array through PDMS casting and peel off. This is possible because the nanocavity array can act as a mold for formation of nanopillar array. The Scanning Electron Microscope (SEM) images of the cavity and pillar arrays fabricated using the described fabrication process are shown in Figure 1b. We believe a similar procedure with minimal modification can be used to fabricate well-defined ITO nanocavity and nanopillar electrodes. Substituting the silver with ITO in material deposition step will easily lead to ITO nanocavity structure and depositing ITO on top of fabricated PDMS nanopillars can form the desired ITO nanopillars suitable for light absorption enhancement in CQD solar cells.

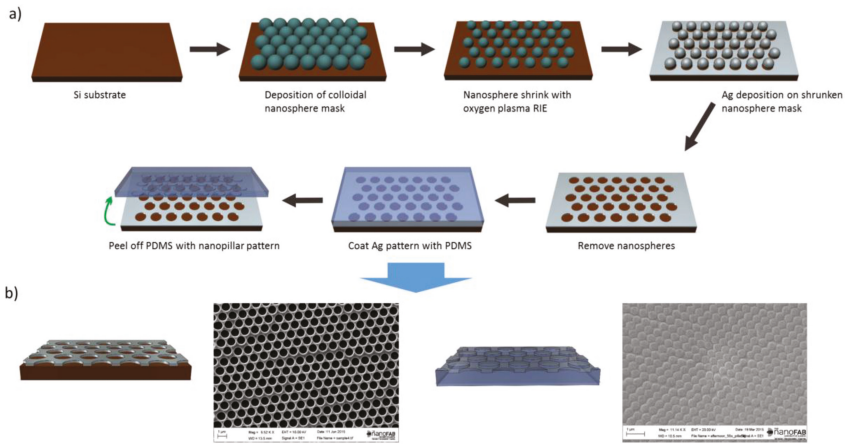


**Figure 1.** (a) The proposed process flow for fabrication of nanocavity and nanopillar arrays. (b) Top view scanning electron microscope (SEM) images and cross-sectional schematic of the nanocavity (left) and nanopillar (right) arrays fabricated using the proposed process.

The periodic ITO electrodes proposed in this work are designed for a typical depleted heterojunction CQD solar cell structure. The depleted heterojunction architecture utilizes a  $\text{TiO}_2$  layer as the n-side of the junction and p-type PbS quantum dots as the p-side. The bottom contact to the junction is formed on a glass substrate and consists of a thin transparent conductive ITO layer. The top contact employs a deep work function metal such as gold to collect photo-excited holes and also reflect back any unabsorbed photons into the light absorbing layer. A conformal layer of  $\text{TiO}_2$  with thickness of 50 nm was considered as a layer between ITO electrode and active layer. The designed periodic nanostructures are implemented at the interface between the ITO bottom contact and PbS QDs. Figure 2a shows the schematic of the structure of PbS QD solar cell with patterned ITO electrode used for simulation. As depicted in the figure, when the light is normally incident on ITO diffraction gratings through the transparent substrate, forward diffraction of light can induce light trapping by effectively increasing optical path lengths inside the absorbing material especially for higher diffracted orders supported by the grating structure. Optical constants of the materials used in the simulation model are shown in Figure 2b.

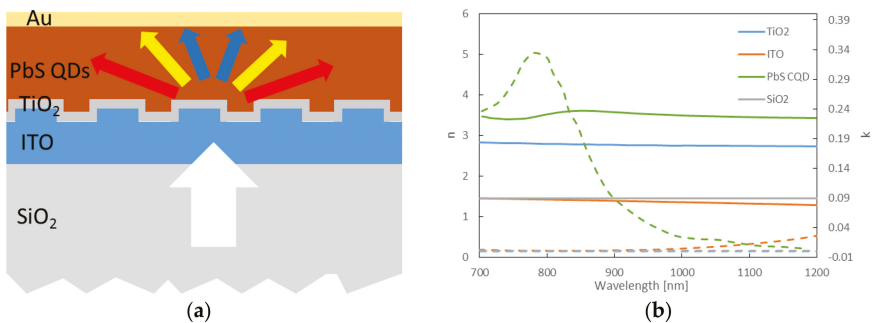


**Figure 2.** (a) Schematic of light diffraction in PbS quantum dot (QD) solar cell with patterned indium-doped tin oxide (ITO) electrode. (b) Optical constants of the materials used in the simulation model.

## 2.2. Light Trapping Analysis

Grating far-field projection analysis [22] was firstly used to analyze the diffraction behavior of the proposed periodic grating structures in PbS CQD solar cells. The resulting transmission efficiencies of the simulated patterned structures are illustrated in Figure 3. As is clear from the figure, both cavity and pillar structures demonstrate high transmission efficiency in wavelength range of 700 nm to 900 nm. On the other hand, the amount of transmitted power is not significant beyond 900 nm. This trend, however, is broken for both nanocavity and nanopillar arrays at around the wavelength of 950 nm with a strong increase in the amount of transmitted power. The same behavior is also observed in the case of the cavity array at wavelength of 1080 nm, the intensity of which, however, is not as strong as the peak at 950 nm. This sudden increase in transmitted power can be attributed to the resonant coupling of the incident light into wave guiding modes supported by the PbS CQD layer located adjacent to the ITO grating structures due to the periodic nature of their structure [19]. Although throughout the spectrum, a portion of incident light is not diffracted (shown as the order (0,0)), by paying close attention to the total transmission values and their difference with order (0,0), it is obvious that a significant amount of energy is diffracted into higher orders, especially at resonance wavelengths. This can greatly contribute to light absorption enhancement in CQD layer by increasing the optical path length of the light inside the layer or light trapping through resonant coupling with the incident light [19]. The transmission efficiencies of two of the strongest diffracted orders (1,1) and (2,0) are plotted in Figure 3.

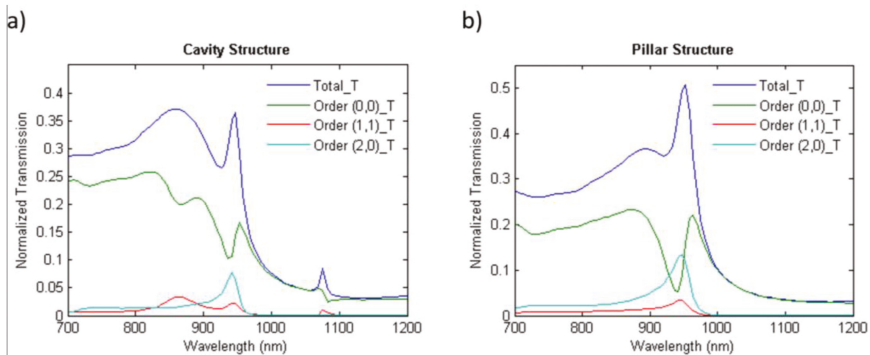


**Figure 3.** The normalized transmission spectra of simulated patterned ITO structures: (a) nanocavity, (b) nanopillar. The plot shows the relative power transmitted into different diffracted orders and the net total transmitted power normalized to the simulation source power. Two of the strongest diffracted orders (1,1) and (2,0) are plotted. (0,0) represents the part of incident power not being diffracted by the structures.

Figure 4 depicts the simulated light absorption spectra for PbS CQD layer of the modelled depleted heterojunction solar cell normalized to the AM1.5G solar spectrum (Figure 4a) and simulation light source (Figure 4b). In order to be able to compare the effect of proposed structures on absorption enhancement in PbS CQD layer, a flat ITO layer was considered as the reference. The available power from AM1.5G spectrum is also included in the figure for comparison. As is obvious from the figure, both nanocavity and nanopillar arrays can induce more light absorption in CQD layer than the flat ITO layer within most parts of the near-infrared region. It is also noticeable that both proposed structures have achieved almost perfect absorption in the range of 720 nm to 850 nm by absorbing all the power available from the sun in this range. As for beyond this range, especially in the case of cavity structure, the resonant coupling of the incident light into guided modes supported by CQD layer is the major responsible for strong but narrowband absorption enhancements at resonant peaks,

previously predicted by grating projection analysis. This is possible because of the major difference in refractive indices of the CQD layer and the ITO layer which can form an efficient waveguide in the middle of the cell's structure.

In order to have an overall evaluation for the light absorption enhancement performance of the proposed structures, the average absorption enhancement of the structures over the entire simulated spectrum was measured against the flat reference structure using the following equation:

$$\text{Absorption Enhancement (\%)} = (P_g - P_r)/P_r \times 100 \quad (1)$$

where  $P_g$  depicts the total power absorbed by the cell with grating structure and  $P_r$  denotes the power absorbed by the reference flat structure. According to the equation, the calculated absorption enhancement factors for nanocavity and nanopillar grating structures compared to the flat structure are 15.0% and 13.6%, respectively. This amount of absorption enhancement can significantly boost charge carrier generation and thus short-circuit current density of a CQD solar cell which can ultimately lead to remarkable improvement in power conversion efficiency of the cell.

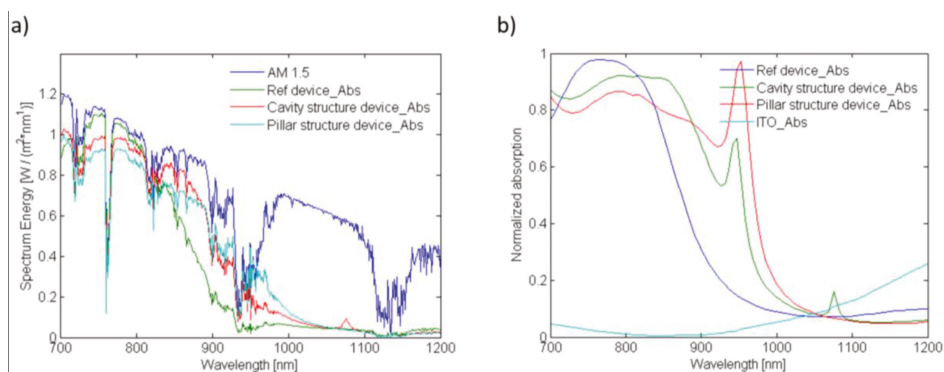


**Figure 4.** The light absorption spectra for PbS colloidal quantum dot (CQD) layer incorporated into different ITO structures normalized to (a) AM1.5G spectra and (b) simulation light source. The absorption enhancement for both cavity and pillar structures over the reference flat structure is obvious especially at resonance wavelengths of 950 nm for both structures and 1080 nm for cavity arrays. A slight absorption loss by ITO layer was also observed, as shown in Figure 4b.

To clearly demonstrate the influence of nanocavity and nanopillar resonance effect on absorption enhancement in CQD layer, the electric field distributions inside the PbS CQD layer with patterned structures were investigated and are shown in Figure 5. The on resonance profiles for nanocavity and nanopillar structures are plotted at wavelength of 950 nm and the off resonant profile wavelength is chosen at 1000 nm for both structures. The on resonance profiles for both structures reveal various absorption hot spots for on-resonance wavelengths where as in the case of off resonance profiles, no hot spot is visible at off-resonance wavelengths. It is obvious that the presence of high intensity E-field spots (hot spots) indicates the occurrence of strong absorption inside PbS CQD layer. In addition, the periodic pattern of the hot spots observed in the obtained profiles discloses the type of resonance to be the guided mode kind usually excited by periodic dielectric nanostructures [6]. The difference in field distribution observed between on and off resonance profiles implies the impressive light trapping performance of the proposed structures at resonance wavelengths. This confirms the superiority of the proposed structures for absorption enhancement in CQD solar cells through resonant coupling of the incident light with supported waveguide modes inside the CQD layer.

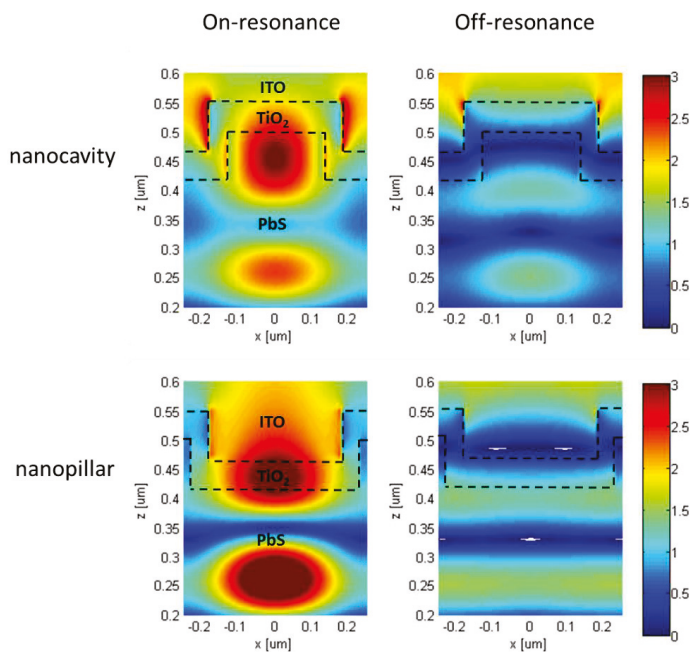


**Figure 5.** Simulated electric field distributions inside the PbS QDs layer with patterned structures. The hot spots present at resonance wavelengths (950 nm for both structures) with high field intensity indicate strong absorption inside PbS CQD. No hot spots are observed at off resonance wavelengths (1000 nm for both structures) suggesting the importance of resonant coupling of the incident into CQD layer for significant absorption enhancement.

### 3. Materials and Methods

#### 3.1. Complementary Structure Fabrication

Self-assembly of nanospheres in Si substrate was accomplished by the air/water interface self-assembly process [23]. The etching of deposited nanospheres was done by using a 20 W O<sub>2</sub> plasma at 5 sccsm oxygen flow for 1 min. E-beam evaporation was used for Silver deposition. The nanosphere mask was removed through sonication in acetone for 10 min. PDMS nanopillars were fabricated by mixing silicone elastomer with curing agent from a Sylgard 184 kit (Dow Corning, Midland, MI, USA) in 10 wt % ratio. The mixture was then degassed in a desiccator for 30 min and was spin-coated on the nanocavity structures at 200 rpm for 30 s. The resulting film was then cured on a hot plate at 80 °C for 2 h after which it was peeled off using a doctor blade. The SEM images were obtained by a Ziess EVO Scanning Electron Microscope (Carl Zeiss, Oberkochen, Germany).

#### 3.2. Simulation Methods

The Lumerical FDTD Solutions software (Lumerical Solutions Inc, Vancouver, Canada) was used for simulations in this work. A period of 500 nm was chosen for both cavity and pillar structures which is same as the diameter of nanospheres used for pattern generation. A cavity depth and pillar height of 80 nm and a diameter of 360 nm for both structures was found to be an optimum value. The PbS QD layer was considered to be a quasi-bulk homogeneous film (QDs were not considered as individual particles) without any voids and its thickness (excluding the nanostructure) is chosen to be 300 nm, which is usually considered the maximum thickness for efficient photo-generated

carrier collection. The TiO<sub>2</sub> layer was assumed to be 50 nm thick. Both gold and SiO<sub>2</sub> glass layers are considered with infinite thickness for ease of modeling. The optimum thickness of ITO layer (excluding the nanostructure) was found to be 500 nm. It should be noted here that the periodic grating structure layer consists of both ITO and PbS materials. The multi-coefficient fitting tool inside the simulation software was utilized to model optical constants of materials from available experimental data [24–27]. In the case of PbS QDs, the optical constants of commonly used QDs with a bandgap of 1.3 eV were used for simulations.

The light source was considered a planewave source placed inside the substrate (SiO<sub>2</sub> layer) to simplify the simulations. The wavelength range of 700–1200 nm was chosen as the simulation wavelength span because PbS CQD solar cells are currently in need of absorption enhancement mostly in this region of sunlight [27]. For directions perpendicular to the incident light propagation direction, Bloch boundary conditions and for directions parallel to the light propagation direction, perfectly matched layer (PML) boundary conditions were defined. The amount of absorption inside the CQD layer was measured by placing two power monitors at the either sides of the layer. This configuration can calculate the power flow entering and exiting the layer and thus the power absorbed inside the layer can be obtained by calculating the difference between the measurements from the two monitors. In the case of transmission measurements, all the shown powers are normalized with respect to the power from the light source. For absorption spectra, however, the absorbed powers are normalized to AM1.5G solar spectrum data available from NREL [28].

#### 4. Conclusions

In this work, ITO nanocavity and nanopillar diffraction gratings are proposed as light trapping structures in CQD solar cells to realize absorption enhancement and power conversion efficiency improvement. A facile fabrication process is demonstrated for patterning these periodic nanostructures over a large area which is a critical requirement of practical light trapping structures designed for photovoltaic devices. The simulation results show that both proposed periodic structures can effectively increase the light absorption in CQD layer of the solar cell throughout the near-infrared region where CQD solar cells typically exhibit weak light absorption. The overall absorption enhancement of 15.0% and 13.6% was achieved for nanocavity and nanopillar structures, respectively. It is verified that the two nanostructures are useful for enhancing the efficiency of photovoltaics as large-area, inexpensive light trapping structures.

#### Abbreviations

The following abbreviations are used in this manuscript:

CQD	Colloidal Quantum Dot
ITO	Indium-doped Tin Oxide
NSL	Nano Sphere Lithography
RIE	Reactive Ion Etching
SEM	Scanning Electron Microscope
PDMS	Polydimethylsiloxane
FDTD	Finite Difference Time Domain

**Acknowledgments:** This work was supported by the Natural Sciences and Engineering Research Council of Canada (NSERC) Discovery Grant, the University of Alberta Start-Up Fund, and the IC-IMPACTS Centres of Excellence. J.W. also gratefully acknowledges financial support from China Scholarship Council.

**Author Contributions:** J.W. and X.W. conceived and designed the study; J.W. and Q.X. performed the experiments; J.W. and S.M.M. performed and analyzed the simulations; All the authors contributed to the preparation of the manuscript.

**Conflicts of Interest:** The authors declare no conflict of interest.



## References

- Chang, L.Y.; Lunt, R.R.; Brown, P.R.; Bulovic, V.; Bawendi, M.G. Low-temperature solution-processed solar cells based on PbS colloidal quantum dot/CdS heterojunctions. *Nano Lett.* **2013**, *13*, 994–999. [CrossRef] [PubMed]
- Tang, J.; Sargent, E.H. Infrared colloidal quantum dots for photovoltaics: Fundamentals and recent progress. *Adv. Mater.* **2011**, *23*, 12–29. [CrossRef] [PubMed]
- Clifford, J.P.; Konstantatos, G.; Johnston, K.W.; Hoogland, S.; Levina, L.; Sargent, E.H. Fast, sensitive and spectrally tuneable colloidal-quantum-dot photodetectors. *Nat. Nanotechnol.* **2009**, *4*, 40–44. [CrossRef] [PubMed]
- Zhitomirsky, D.; Voznyy, O.; Hoogland, S.; Sargent, E.H. Measuring charge carrier diffusion in coupled colloidal quantum dot solids. *ACS Nano* **2013**, *7*, 5282–5290. [CrossRef] [PubMed]
- Labelle, A.J.; Thon, S.M.; Kim, J.Y.; Lan, X.; Zhitomirsky, D.; Kemp, K.W.; Sargent, E.H. Conformal fabrication of colloidal quantum dot solids for optically enhanced photovoltaics. *ACS Nano* **2015**, *9*, 5447–5453. [CrossRef] [PubMed]
- Brongersma, M.L.; Cui, Y.; Fan, S. Light management for photovoltaics using high-index nanostructures. *Nat. Mater.* **2014**, *13*, 451–460. [CrossRef] [PubMed]
- Cao, S.; Yu, W.; Wang, T.; Xu, Z.; Wang, C.; Fu, Y.; Liu, Y. Two-dimensional subwavelength meta-nanopillar array for efficient visible light absorption. *Appl. Phys. Lett.* **2013**, *102*, 161109. [CrossRef]
- Han, Q.; Jin, L.; Fu, Y.Q.; Yu, W.X. Si substrate-based metamaterials for ultrabroadband perfect absorption in visible regime. *J. Nanomater.* **2014**, *2014*, 893202.
- Han, S.E.; Chen, G. Optical absorption enhancement in silicon nanohole arrays for solar photovoltaics. *Nano Lett.* **2010**, *10*, 1012–1015. [CrossRef] [PubMed]
- Lin, C.; Povinelli, M.L. Optical absorption enhancement in silicon nanowire arrays with a large lattice constant for photovoltaic applications. *Opt. Express* **2009**, *17*, 19371–19381. [CrossRef] [PubMed]
- Adachi, M.M.; Labelle, A.J.; Thon, S.M.; Lan, X.; Hoogland, S.; Sargent, E.H. Broadband solar absorption enhancement via periodic nanostructuring of electrodes. *Sci. Rep.* **2013**, *3*. [CrossRef] [PubMed]
- Fu, Y.; Dinku, A.G.; Hara, Y.; Miller, C.W.; Vrouwenvelder, K.T.; Lopez, R. Modeling photovoltaic performance in periodic patterned colloidal quantum dot solar cells. *Opt. Express* **2015**, *23*, A779–A790. [CrossRef] [PubMed]
- Kim, J.; Koh, J.K.; Kim, B.; Kim, J.H.; Kim, E. Nanopatterning of mesoporous inorganic oxide films for efficient light harvesting of dye-sensitized solar cells. *Angew. Chem. Int. Ed.* **2012**, *51*, 6864–6869. [CrossRef] [PubMed]
- Na, J.; Kim, Y.; Park, C.; Kim, E. Multi-layering of a nanopatterned TiO<sub>2</sub> layer for highly efficient solid-state solar cells. *NPG Asia Mater.* **2015**, *7*, E217. [CrossRef]
- Atwater, H.A.; Polman, A. Plasmonics for improved photovoltaic devices. *Nat. Mater.* **2010**, *9*, 205–213. [CrossRef] [PubMed]
- Ding, I.-K.; Zhu, J.; Cai, W.; Moon, S.-J.; Cai, N.; Wang, P.; Zakeeruddin, S.M.; Grätzel, M.; Brongersma, M.L.; Cui, Y.; *et al.* Plasmonic dye-sensitized solar cells. *Adv. Energy Mater.* **2011**, *1*, 52–57. [CrossRef]
- Min, C.; Li, J.; Veronis, G.; Lee, J.-Y.; Fan, S.; Peumans, P. Enhancement of optical absorption in thin-film organic solar cells through the excitation of plasmonic modes in metallic gratings. *Appl. Phys. Lett.* **2010**, *96*, 133302. [CrossRef]
- Raman, A.; Yu, Z.; Fan, S. Dielectric nanostructures for broadband light trapping in organic solar cells. *Opt. Express* **2011**, *19*, 19015–19026. [CrossRef] [PubMed]
- Mahpeykar, S.M.; Xiong, Q.; Wang, X. Resonance-induced absorption enhancement in colloidal quantum dot solar cells using nanostructured electrodes. *Opt. Express* **2014**, *22*, 1576–1588. [CrossRef] [PubMed]
- Hall, A.S.; Friesen, S.A.; Mallouk, T.E. Wafer-scale fabrication of plasmonic crystals from patterned silicon templates prepared by nanosphere lithography. *Nano Lett.* **2013**, *13*, 2623–2627. [CrossRef] [PubMed]
- Yang, S.; Lapsley, M.I.; Cao, B.; Zhao, C.; Zhao, Y.; Hao, Q.; Kiraly, B.; Scott, J.; Li, W.; Wang, L.; *et al.* Large-scale fabrication of three-dimensional surface patterns using template-defined electrochemical deposition. *Adv. Funct. Mater.* **2013**, *23*, 720–730. [CrossRef]
- Lumerical Solutions Inc. Grating Projections. Available online: [http://docs.lumerical.com/en/solvers\\_grating\\_projections.html](http://docs.lumerical.com/en/solvers_grating_projections.html) (accessed on 15 February 2016).



23. Yu, J.; Geng, C.; Zheng, L.; Ma, Z.; Tan, T.; Wang, X.; Yan, Q.; Shen, D. Preparation of high-quality colloidal mask for nanospherolithography by a combination of air/water interface self-assembly and solvent vapor annealing. *Langmuir* **2012**, *28*, 12681–12689. [CrossRef] [PubMed]
24. Synowicki, R.A. Spectroscopic ellipsometry characterization of indium tin oxide film microstructure and optical constants. *Thin Solid Films* **1998**, *313–314*, 394–397. [CrossRef]
25. Palik, E.D. *Handbook of Optical Constants of Solids*; Academic Press: Cambridge, MA, USA, 1998; pp. 12–24.
26. SOPRA Refractive Index Database. Available online: <http://www.soprasteria.com> (accessed on 15 February 2016).
27. Wang, X.; Koleilat, G.I.; Tang, J.; Liu, H.; Kramer, I.J.; Debnath, R.; Brzozowski, L.; Barkhouse, D.A.R.; Levina, L.; Hoogland, S.; *et al.* Tandem colloidal quantum dot solar cells employing a graded recombination layer. *Nat. Photon.* **2011**, *5*, 480–484. [CrossRef]
28. Reference Solar Spectral Irradiance: ASTM G-173. Available online: <http://rredc.nrel.gov/solar/spectra/am1.5/ASTMG173/ASTMG173.html> (accessed on 15 February 2016).



© 2016 by the authors. Licensee MDPI, Basel, Switzerland. This article is an open access article distributed under the terms and conditions of the Creative Commons Attribution (CC BY) license (<http://creativecommons.org/licenses/by/4.0/>).

Article

# Correlation between CdSe QD Synthesis, Post-Synthetic Treatment, and BHJ Hybrid Solar Cell Performance

Michael Eck <sup>1</sup> and Michael Krueger <sup>2,\*</sup>

<sup>1</sup> Department of Microsystems Engineering (IMTEK), University of Freiburg, Georges-Köhler-Allee 103, 79110 Freiburg, Germany; eck@imtek.de

<sup>2</sup> Department of Physics, Carl von Ossietzky University of Oldenburg, Carl-von-Ossietzky-Straße 9-11, 26129 Oldenburg, Germany

\* Correspondence: michael.krueger@uni-oldenburg.de; Tel.: +49-441-798-3153

Academic Editors: Guanying Chen, Zhijun Ning and Hans Agren

Received: 20 April 2016; Accepted: 6 June 2016; Published: 14 June 2016

**Abstract:** In this publication we show that the procedure to synthesize nanocrystals and the post-synthetic nanocrystal ligand sphere treatment have a great influence not only on the immediate performance of hybrid bulk heterojunction solar cells, but also on their thermal, long-term, and air stability. We herein demonstrate this for the particular case of spherical CdSe nanocrystals, post-synthetically treated with a hexanoic acid based treatment. We observe an influence from the duration of this post-synthetic treatment on the nanocrystal ligand sphere size, and also on the solar cell performance. By tuning the post-synthetic treatment to a certain degree, optimal device performance can be achieved. Moreover, we show how to effectively adapt the post-synthetic nanocrystal treatment protocol to different nanocrystal synthesis batches, hence increasing the reproducibility of hybrid nanocrystal:polymer bulk-heterojunction solar cells, which usually suffers due to the fluctuations in nanocrystal quality of different synthesis batches and synthesis procedures.

**Keywords:** bulk heterojunction solar cells; hybrid solar cells; nanocrystals; quantum dots; conjugated polymers; post-synthetic treatment; thermal annealing; long-term stability

## 1. Introduction

Solar cells possessing a photoactive layer made out of semiconducting nanocrystals (NCs) and a conjugated polymer blend are called hybrid bulk heterojunction (BHJ) solar cells. Their photoactive layer typically possesses a thickness of around 100 nm, and is deposited from a NC/polymer dispersion [1]. A typical device structure is shown in Figure 1a. Within the photoactive layer, the polymer is mostly utilized as donor material for the electrons arising from the photo-induced excitons, while the NCs serve as electron acceptors and extraction material. Already the seminal work of Greenham *et al.* [2] published in 1996 has acknowledged the crucial negative impact of the insulating NC synthesis ligands on the solar cell performance, and a post-synthetic pyridine treatment of NCs was reported to improve overall solar cell performance. Since then, hybrid BHJ solar cells have undergone a remarkable development over the years (see Figure 1b), now exceeding efficiencies of 4% [3–6]; the currently best hybrid solar cells using NCs of different shapes have in common the usage of the low-bandgap polymer PCPDTBT (poly[2,6-(4,4-bis-(2-ethylhexyl)-4H-cyclopenta[2,1-b;3,4-b']dithiophene)-alt-4,7-(2,1,3-benzothiadiazole)]) and of CdSe as NC material. Moreover, the best solar cells of the respective NC shape (spherical [6], elongated [5], multibranch [4]) all utilize the attachment of a thiol group to the CdSe NC surface. Thereby, high open circuit voltages of 0.71–0.74 V are achieved, leading to power conversion efficiencies (PCE) of 4.05%–4.7%.

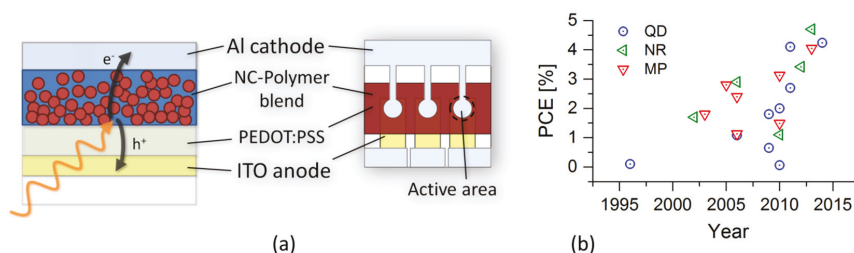


**Figure 1.** (a) Working principle and device structure shown on the cross-sectional and on the top view of the investigated hybrid bulk heterojunction (BHJ) solar cell with the active area size of  $0.07 \text{ cm}^2$ . (b) Power conversion efficiencies of selected hybrid BHJ solar cells published over the years from nanocrystals (NCs) of different shape: quantum dots (QD) [2,3,6–12], nanorods (NR) [5,10,13–15], multipods (MP) [4,10,16–20].

Nevertheless, despite almost reaching the PCEs of (poly[2,6-(4,4-bis-(2-ethylhexyl)-4H-cyclopenta[2,1-b;3,4-b']dithiophene)-alt-4,7-(2,1,3-benzothiadiazole)]) (PCPDTBT):fullerene-based BHJ solar cells, which are up to 5.24%–5.5% [21,22], the utilization of NCs as electron acceptors has the aforementioned disadvantage of requiring post-synthetic NC treatment to reduce and/or exchange the initial synthesis ligands. This treatment, however, may result in the partial destruction of the NC surface [23]—leading to increased charge recombination—and to the formation of NC aggregates, which might introduce shortcuts over the thin active layer. Hence, several publications on hybrid BHJ solar cells report the filtration of the post-synthetically treated NC dispersion, in order to remove large NC aggregates [4,20]. The approach we follow is to avoid NC aggregation within the process of post-synthetic NC treatment prior to incorporation into the polymer:NC blend dispersion. We achieve this by a gradual reduction of the NC ligand sphere [11,15,24] through a protonation step of the hexadecylamine (HDA) capping ligands with hexanoic acid (HA) and their subsequent solvation with the polar solvent methanol. We observed an influence from the post-synthetic treatment duration on the NC ligand sphere size (see Figure 4). Therefore, we believe that we are able to minimize the post-synthetically induced number of NC surface defects, which is supported by the excellent ideality factor of 1.22–1.33 for our CdSe/PCPDTBT solar cells [6], which is relatively close to unity compared to other hybrid BHJ solar cells [25–28], even when compared to organic BHJ photovoltaic cells [29,30].

## 2. Results and Discussion

### 2.1. NC Synthesis

CdSe QDs, capped with HDA and trioctylphosphine oxide (TOPO) ligands, were synthesized according to Yuan *et al.* [31]. An exemplary transmission electron microscopy (TEM) picture of the spherical CdSe NCs with a typical diameter of about 6.5 nm as well as the ultraviolet-visible (UV-Vis) absorption and photoluminescence (PL) spectrum are given in Figure 2.

In order to increase the NC size uniformity, the precursor concentration was increased from a 100:1:1 (hexadecylamine/trioctylphosphine oxide):(cadmium-stearic acid):(trioctylphosphine-selenide) (HDA/TOPO:Cd-SA:TOP-Se) molar ratio to a 100:2:2 ratio [24]. Furthermore, to study the influence of unintentionally occurring fluctuations of practically utilized precursor ratios for the NC synthesis, the Cd:Se precursor ratio was varied from 3:2, over 2:2, to 2:3. The parameters of PL intensity, PL peak position, and full width at half maximum (FWHM) were measured and compared to aliquots taken during the NC synthesis at different reaction times and are depicted in Figure 3.

From the parameters of the CdSe quantum dots (QDs)—determined from extracted samples during 2 different syntheses for each precursor ratio—shown in Figure 3, one can observe that indeed a lower minimal FWHM is observed when using higher precursor concentrations. Moreover, a tendency of lower minimum FWHM is also observed for the increased Se precursor concentration; this synthesis

furthermore exhibits a higher PL quantum yield in the synthesis brightpoint (point where the PL intensity reaches its maximum during synthesis). These observations confirm the findings firstly described by Qu *et al.* [32]. The properties of CdSe QDs in their brightpoint of different precursor concentrations—utilized for BHJ hybrid solar cell fabrication—are summarized in Table 1.

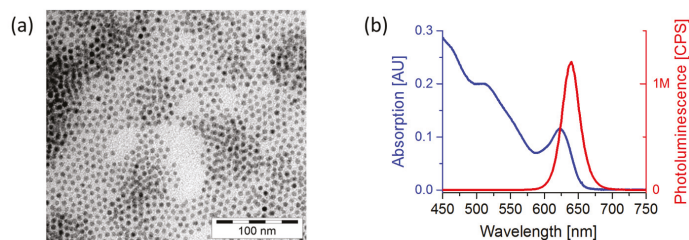


**Figure 2.** (a) Transmission electron microscopy (TEM) image of CdSe nanocrystals (NCs) used for the investigation from a 100:3:2 (hexadecylamine/trioctylphosphine oxide):(cadmium-stearic acid):(trioctylphosphine-selenid) ((HDA/TOPO):(Cd-SA):(TOP-Se)) ratio, synthesized for 30 min at 300 °C by wet-chemical hot injection NC synthesis with an average diameter of 6.5 nm. (b) Ultraviolet-visible (UV-Vis) absorption spectrum (blue line) and photoluminescence spectrum of CdSe nanocrystals (NCs) synthesized by a hot injection method recorded at an excitation of 575 nm (red line).

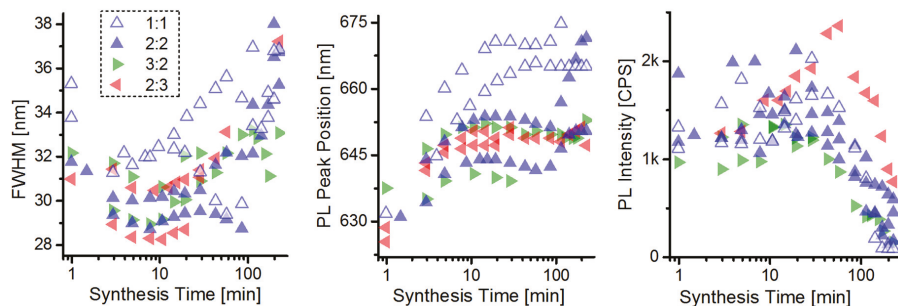


**Figure 3.** Different Cd:Se precursor ratios and concentrations—full width at half maximum (FWHM), photoluminescence (PL) peak position, and PL intensity evolution during the NC syntheses.

**Table 1.** Cd:Se precursor ratios, position of the photoluminescence (PL) brightpoint during the nanocrystal (NC) synthesis; average spectral PL peak position, PL full width at half maximum (FWHM), and average PL quantum yield (QY) of utilized quantum dots (QDs); and average power conversion efficiency (PCE) of hybrid bulk heterojunction poly[2,6-(4,4-bis-(2-ethylhexyl)-4H-cyclopenta[2,1-b;3,4-b']dithiophene)-alt-4,7-(2,1,3-benzothiadiazole)]:CdSe (BHJ PCPDTBT:CdSe) QD solar cells found for the optimal post-synthetic hexanoic acid washing time of CdSe QDs.

Cd:Se Precursor Ratio	Brightpoint (min)	PL Peak Position (nm)	FWHM (nm)	PL QY (%)	Optimal HA Washing Time (min)	PCE with Optimal NC Treatment Time (%)
3:2	17	647 ± 7	30.7 ± 0.8	24 ± 5	21	2.4 ± 0.10
2:2	21	650 ± 3	27.0 ± 0.7	25 ± 5	18	2.8 ± 0.18
2:3	60	646 ± 5	32.2 ± 0.9	37 ± 8	60	1.7 ± 0.04

## 2.2. Post-Synthetic NC Treatment

As mentioned before, CdSe QDs were taken from the PL brightpoint, since we expect an optimal NC quality in this point, according to Qu *et al.* [32]. A hexanoic acid-based treatment was applied on CdSe QDs synthesized at three different Cd:Se ratios as described in the methods section. As we

have presented in previous publications [11,15,33], the NC possesses a sphere of weakly associated ligands, which crystallize after the cool-down of the synthesis reaction around the initial ligand layer chemisorbed to the NC surface. To demonstrate the physical influence of the post-synthetic treatment on the CdSe QDs, the PL intensity and the ligand sphere size were determined for different hexanoic acid (HA) washing times (Figure 4). The peak PL intensity was determined from PL spectroscopy measurements of re-dispersed CdSe QDs, while the ligand sphere size was determined by measuring the hydrodynamic QD diameter (corresponding to the ligand sphere size [34]) by dynamic light scattering (DLS) of the same samples.

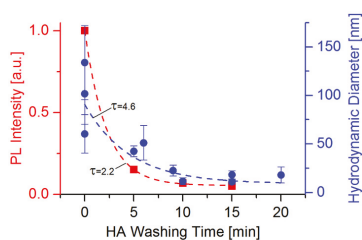


**Figure 4.** Red squares: Development of PL intensity over the HA washing time for CdSe QDs synthesized in hexadecylamine/trioctylphosphine oxide (HDA/TOPO) (100:3:2, 30 min at 300 °C). Blue dots: Respective development of the hydrodynamic diameter together with the standard deviation for CdSe QDs measured by dynamic light scattering (DLS). For both, the half-life  $\tau$  in min is given for the respective fitted exponential decay.

It can be seen that both the hydrodynamic diameter and the PL intensity seem to decrease exponentially with increasing HA washing time, corresponding to the facile removal of the outer, weakly associated ligand shell. The DLS measurements of untreated QD samples show a relatively wide value distribution, which might also partially result from QD aggregation to superstructures. Nevertheless, from the DLS measurements we can draw the conclusion that the NC ligand sphere diameter is decreasing with increasing HA washing time, while from the PL intensity measurements one can assume that the original ligand passivation of the NC surface is either reduced or changed (*i.e.*, by a ligand exchange with HA and/or MeOH).

### 2.3. Optimal Initial Solar Cell Performance

Using CdSe QDs taken from the brightpoint of the respective NC synthesis (*i.e.*, from 21 min synthesis time for the 100:2:2 ratio, 16 min for 100:3:2, and 60 min for 100:2:3), hybrid BHJ Solar cells were fabricated and characterized according to the methods section. In order to obtain the best solar cell performance, the optimal post-synthetic NC treatment time had to be found (see Figure 5).

From these experiments the post-synthetic NC treatment times, resulting in the optimal hybrid solar cell power conversion efficiency (PCE), were determined for 3 differently synthesized QDs. A summary of the optimal NC treatment time based on the experiments presented in Figure 5, the resulting average optimal PCE and the initial properties of the utilized QDs are presented in Table 1.

The parameters summarized in Table 1 show that there is a correlation in between the initial PL QY of CdSe QDs, and the required post-synthetic treatment time for creating the most efficient hybrid solar cell: a high PL QY requires a long post-synthetic NC treatment time. Furthermore, one can see that low PL FWHM leads to high PCEs for BHJ hybrid solar cells. Hence, the PL QY is an indicator of the required post-synthetic treatment time but not for the achievable solar cell performance. This is determined—given that the post-synthetic treatment is optimized—by the FWHM for comparable NC sizes, as they were in this investigation. Lower FWHM results in a higher PCE, and higher FWHM results in a lower PCE. This is reasonable, since a low FWHM presumably corresponds to a high intrinsic uniform NC quality.

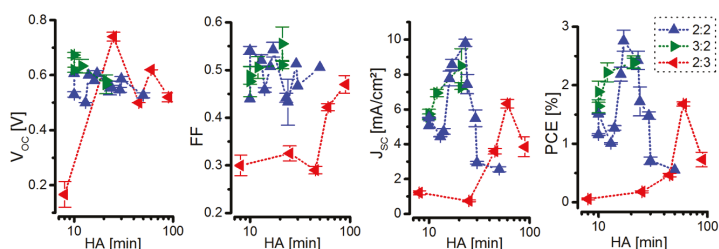


**Figure 5.** Dependency of open-circuit voltage ( $V_{OC}$ ), fill factor (FF), short-circuit current density ( $J_{sc}$ ) and PCE on the HA washing time at 105 °C for hybrid BHJ solar cells containing CdSe NCs taken from the respective PL brightpoint of the NC hot-injection syntheses performed at 300 °C with a 100:3:2, 100:2:2, and 100:2:3 ratio of (HDA/TOPO):(Cd-SA):(TOP-Se). The results are obtained from two synthesis batches for each ratio and from 60 solar cells, which were thermally post-annealed until reaching their optimal performance.

#### 2.4. Influence of the Post-Synthetic NC Treatment on the Device Annealing Time, and Guidance for NC Treatment

To obtain the optimal solar cell performances presented in the prior paragraph, besides the optimal NC treatment time, an optimal time for the thermal solar cell annealing is also necessary. This optimal annealing time is however different for different NC post-synthetic treatment times as shown in Figure 6.

When taking a closer look at this behavior (see Figures 7 and 8), one can even identify indications for finding the optimal NC treatment time with a reduced number of initial experiments.

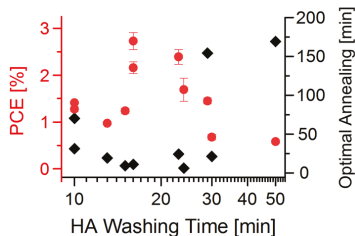


**Figure 6.** Power conversion efficiencies (PCEs) (red spherical points) obtained from 36 hybrid BHJ solar cells containing CdSe QDs (100:2:2) washed for different times in HA, and the optimal annealing time (black rhombic points) required to reach this efficiency.

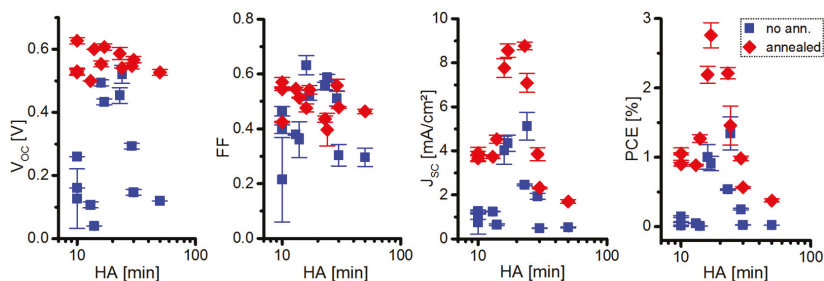


**Figure 7.** Differently long HA washed CdSe QDs (100:2:2) exhibit different performances when incorporated inside hybrid BHJ solar cells both without annealing and with 10 min of thermal annealing at 145 °C (results obtained from 36 cells).

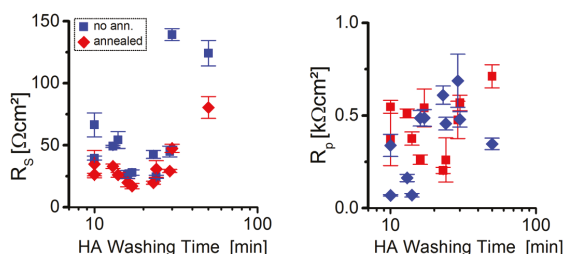


**Figure 8.** Incorporating differently long HA washed CdSe QDs (100:2:2) into BHJ hybrid solar cells results in different series resistance ( $R_s$ ) and parallel resistance ( $R_p$ ) values before and after 10 min of thermal annealing.

As depicted in Figure 7, the short-circuit current density and the open-circuit voltage are already relatively high, near the optimal HA treatment time, even before the thermal annealing step. This is since the series resistance—representing the active layer resistivity and to a lesser extent also the contact resistances [35]—has its lowest values for longer HA washing times (see Figure 8). The reason for this is probably the decreasing NC ligand sphere diameter, measured during the first 15 min of the NC treatment (see Figure 4), leading to an increased conductivity of the QD phase within the active layer and a more intimate NC packing, improving electron hopping processes.

The parallel resistance, which is an indicator for the active layer morphology (e.g., formation of “dead zones” from which no electrons can be extracted, and also to trap-assisted recombination [36]), tends to steadily increase with increased NC washing time, pointing towards an improved active layer morphology (*i.e.*, finer phase segregation and better charge extraction pathways). For post-synthetic NC treatment times exceeding the optimal duration, the parallel resistance tends to remain high in the resulting solar cells, but series resistance greatly increases, supposedly due to destruction of the NC surface by the washing procedure.

After performing a thermal annealing step on a hotplate inside a nitrogen filled glovebox for 10 min at 145 °C, a strong increase in  $J_{SC}$  (and accordingly a decrease in  $R_s$ ) is observed especially for shorter washed QDs, which is probably mostly attributed to the enhanced intermolecular polymer-chain packing according to organic BHJ solar cell literature [36], but here a thermally induced *in situ* reduction of the NC ligand shell might also play a role. The series resistance for the longest washed NCs, however, strongly profits (despite still being of relatively high values) from thermal annealing, which might arise from a partial re-passivation of the NC surface. On the other side, the parallel resistance generally only appears to change after thermal annealing for solar cells containing shortly washed QDs, which we attribute to a higher morphological stability of the active layer of solar cells containing stronger ligand shell-size reduced QDs.

Briefly, after performing a first thermal annealing step on the solar cell, one can conclude whether one has to add to the NC washing time, or further reduce it for the next solar cell. This is, since the  $J_{SC}$  increase is stronger after annealing for short-time-washed NCs, accompanied with a typical strong increase of  $R_p$ . Moreover, solar cells containing short-time-washed NCs exhibit a higher  $V_{OC}$  after the same thermal annealing, compared to long-time-washed NCs containing cells.

## 2.5. Influence of NC Treatment on Solar Cell Long-Term Performance Stability

As we have previously shown, the post-synthetic NC treatment influences the immediate solar cell performance and the thermal stability of BHJ hybrid solar cells. As we will subsequently show, the post-synthetic NC treatment also influences the long-term performance of solar cells. Figure 9 shows the behavior of BHJ hybrid solar cells containing shorter (10 min and 12 min) and longer washed (21 min) CdSe QDs before being incorporated into the active layer.



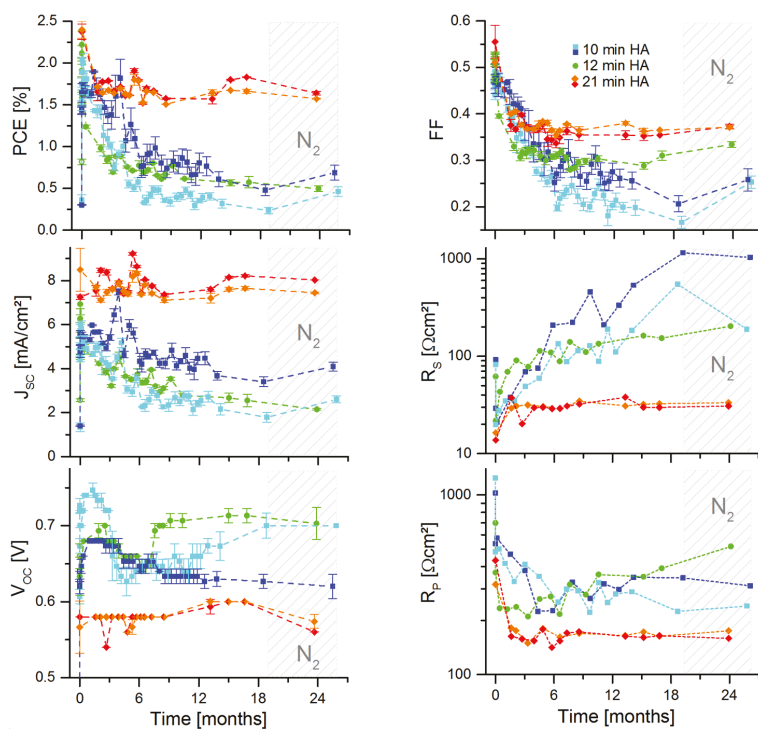


**Figure 9.** Parameters of PCPDTBT:CdSe QD solar cells from QDs washed by HA for 10 min (turquoise & blue squares), 12 min (green spherical points), and 21 min (orange & red rhombic points), stored in the dark inside a glovebox and periodically illuminated by a sun-simulator (AM 1.5 G spectrum) and characterized inside the same glovebox.

As a result, we observe improved performance stability for solar cells containing longer-time-washed QDs, with a decrease of the PCE from 2.4% to 1.6% (−33%) compared to a decrease from 2.1% to 0.55% (−74%), during 2 years of investigation. The series resistance  $R_s$  increases only slightly for long-time-washed NCs, but continuously increases for solar cells with shorter washed NCs. Possible explanations for this behavior would be the facilitated oxygen penetration through a supposedly less dense active layer for solar cells with higher ligand content, leading to increased oxidation of the CdSe QDs and of the polymer. However, the diffusion of ligands towards the electrodes, forming there an insulating layer would also be a possible explanation for the increasing  $R_s$ .  $R_p$  and  $V_{oc}$  are already low for long-time-washed NCs, possibly due to more shunts within the active layer by presumably more aggregated NCs, and induced surface defects introduced by long NC washing, hence increasing charge recombination processes.

It is also worth mentioning that the short-circuit current has shown a clear dependency on the oxygen concentration, which fluctuated during the first 19 months around 25 ppm  $O_2$  with extremes of 0 ppm and 36 ppm, before the glovebox was continuously flushed with nitrogen for the following 5 months (the  $H_2O$  concentration was of <5 ppm at all time). We have observed  $J_{sc}$  to decrease with increasing oxygen concentration inside the glovebox, and  $J_{sc}$  to be recovered after the oxygen concentration has decreased. This observed reversibility does not occur immediately, but rather slowly (within several days). Hence, the origin of  $J_{sc}$  recovery might be due to oxygen depletion within the active layer by  $O_2$  diffusion.

## 2.6. Influence of NC Treatment on the Solar Cell Performance Stability in Air

We have also performed a short investigation of the influence the difference in NC treatment time has on the stability of non-encapsulated glass/ITO/PEDOT:PSS/PCPDTBT: CdSe/Al solar cells taken into air and measured under AM 1.5G illumination. Three different solar cells were used herein. The CdSe QDs utilized in this investigation received a HA-based treatment for 15 min (short washed) and 22 min (long washed). To this comparison, also an organic PC<sub>61</sub>BM:PCPDTBT solar cell, with the active layer composed out of a 2.5:1 weight ratio between PC<sub>61</sub>BM (Phenyl C<sub>61</sub> butyric acid methyl ester, Sigma-Aldrich, Saint Louis, MS, USA, >99.5%) and PCPDTBT was added to specifically investigate the influence of the NCs.

According to Figure 10, a decreasing  $J_{SC}$  is observed for both hybrid and organic solar cells when taking the devices from the glovebox out into air. Possible reasons for the reduced  $J_{SC}$  are the (partially) reversible uptake of oxygen within the polymer phase [37], the oxidation of the aluminum cathode [38], and the uptake of water into the hygroscopic Poly(3,4-ethylenedioxythiophene):poly(styrenesulfonic acid) (PEDOT:PSS) layer [39,40]. We also observe that the  $J_{SC}$  decrease is more similar to the organic solar cell, when utilizing long-washed NCs; this might be due to the fact that the oxygen diffusion within the higher-density NC ligand depleted active layer is slowed down. The  $V_{OC}$  shows a strong increase for hybrid solar cells containing short washed NCs, while a  $V_{OC}$  increase is seen much later with long washed NCs, and not at all for organic solar cells—as has already been reported for organic solar cells [40,41]. Hence, we assume that the  $V_{OC}$  increase in air is connected to the utilization of NCs, and possibly due to adsorption of H<sub>2</sub>O onto CdSe NCs.

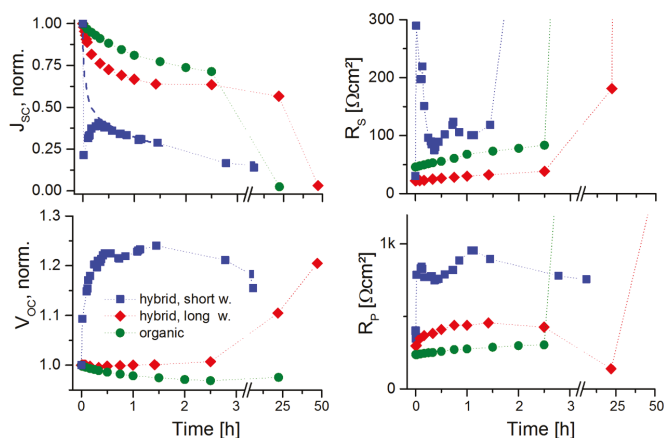


**Figure 10.** Development by time of short circuit current densities, series resistances, open circuit voltages, and parallel resistances for hybrid BHJ CdSe/PCPDTBT solar cells with short-time HA washed and long-time HA washed NCs, and for an organic BHJ PC<sub>61</sub>BM/PCPDTBT solar cell for comparison when taken into air. Since the  $J_{SC}$  of the solar cell containing short washed QDs displayed a fast initial decrease from its original value, an extrapolated graph has been added to guide the eye.

## 3. Methods

### 3.1. Post-Synthetic NC Treatment

The post-synthetic NC treatment was performed in the following way: a portion of the synthesis product containing 1 mg of CdSe QDs was dissolved in 2.5 mL hexanoic acid ( $\geq 99.5\%$ , Sigma-Aldrich, Saint Louis, MS, USA), stirred for several minutes in a snap-cap glass tube at 110 °C on a hot plate. Subsequently a double volume (compared to HA) of methanol (anhydrous, 99.8%, Sigma-Aldrich, Saint Louis, MS, USA) was added to reduce the QD concentration to 1/3rd of its initial value.

The stirring was continued with the added methanol at 110 °C for half the stirring time compared to that in pure HA. Then, the dispersion was centrifuged by an Eppendorf MiniSpin® plus centrifuge (Eppendorf AG, Hamburg, Germany) for 1 min at 14.5 krpm with the rotor-pre heated in a furnace to 90 °C in order to hinder the re-crystallization of the ligands. Afterwards the QDs were redispersed in chloroform (CHCl<sub>3</sub>) with a concentration of 2 mg/mL and stirred at 105 °C for 1 min. Consequently, triple the volume of methanol was added, and the NCs were further stirred for 3 min at 105 °C for precipitation. Afterwards, the NCs were collected by centrifugation for 30 s at 14.5 krpm. Chlorobenzene (anhydrous, 99.8%, Sigma-Aldrich, Saint-Louis, MS, USA) was then added to obtain a CdSe QD dispersion of 24 mg/mL. Hence, when mentioning the HA washing times throughout this publication, one must also consider the rest of the NC washing protocol subsequently executed, which additionally includes half the HA washing time with added MeOH, 1 min stirring in CHCl<sub>3</sub>, and finally 3 min stirring in MeOH. For example, 20 min of HA washing means: 20 min HA plus 10 min MeOH, centrifugation, redispersion, 1 min CHCl<sub>3</sub> plus 3 min MeOH, centrifugation, and final redispersion in chlorobenzene (CB).

### 3.2. Solar Cell Fabrication

The obtained CdSe QD/CB dispersion was mixed in a weight ratio of 88:12 (QD:polymer) with a 20 mg/mL solution of PCPDTBT (Mn = 10–20 kDa, 1-Material, Dorval, Canada) in CB. The final ink was spun cast by a WS400-6NPP-Lite spin coater from Laurell Technologies (North Wales, PA, USA) with 800 rpm for 30 s followed by a 60 s drying step at 1800 rpm, resulting in an active layer thickness of about 80 nm. The spin coating was done on a structured  $\leq 10 \Omega_{\text{sq}}$  ITO substrate from Präzisions Glas & Optik GmbH (Iserlohn, Germany), which was treated for 5 min with oxygen plasma and spin coated with Baytron AI4083 PEDOT:PSS from HC Starck GmbH (Goslar, Germany) at 2000 rpm for 30 s and dried for 20 min at 160 °C, to form a 70 nm thick hole blocking layer. After thermal evaporation of an 80 nm aluminum layer as electrode, the cells were thermally annealed for different times at 145 °C on a hot plate. The solar cells were usually annealed for 10 min and subsequently characterized. This procedure was repeated until the solar cell PCE started to decrease.

### 3.3. Solar Cell Characterization

The solar cells were characterized inside a nitrogen filled glovebox by a computer controlled Keithley 2602A source-meter (Keithley Instruments, Solon, OH, USA). The cells were individually illuminated by a LS0400 LOT-Oriel sun simulator (LOT-QuantumDesign GmbH, Darmstadt, Germany), housing a xenon lamp and using an AM 1.5G filter. The light intensity is adjusted by a calibrated silicon reference solar cell to match 100 mW/cm<sup>2</sup>.

### 3.4. Dynamic Light Scattering (DLS)

DLS measurements were performed with a Zetasizer Nanosizer ZS of Malvern Instruments Ltd (Malvern, UK). The investigated QDs were dispersed in chloroform to obtain a dispersion with an absorbance of 0.1 A.U. at the first excitonic peak. For the measurements a Hellma® fluorescence cuvette out of Suprasil® quartz glass (Hellma, Müllheim, Germany) was utilized.

## 4. Conclusions

The optimal NC treatment time before integration into BHJ hybrid solar cells can be determined by systematic analysis of the resulting solar cell device performances. NCs of higher PL QY require a longer post-synthetic NC treatment time. The optimal thermal annealing time for solar cell devices is different for different NC treatment times, and provides crucial information for tuning the NC treatment time in the right direction. Hybrid BHJ solar cells containing stronger ligand sphere reduced QDs exhibit an improved performance stability in the long term and in air. Further investigations would have to be conducted into the influence of the post-synthetic NC treatment on the active layer morphology and on the induced trap density on the NCs and inside the solar cell. We have shown

in this publication that the QD synthesis procedure can lead to decisive influences on the optimal post-synthetic NC treatment before integration into hybrid BHJ solar cells and determine the overall solar cell performance. This might be one reason for the widely scattered results of groups working in this field and for QD batch to batch variations, since properties of nanomaterials are often determined by surface properties such as surface defects or ligand attachment and arrangement, which are hard to control and cannot be determined by TEM and UV-Vis spectroscopy, which are the methods of choice for QD characterization. We also believe that our findings for CdSe QDs are also of general importance for other QD systems and for the development of respective post-synthetic treatment protocols before integration into various applications.

**Acknowledgments:** We thank the German Science Foundation (DFG) Graduate School “Micro Energy Harvesting” (GRK1322) for funding.

**Author Contributions:** M.E. and M.K. conceived and designed the experiments; M.E. performed the experiments and analyzed the data; M.E. and M.K. wrote the paper; all authors read and approved the final manuscript.

**Conflicts of Interest:** The authors declare no conflict of interests.

## Abbreviations

The following abbreviations are used in this manuscript:

NC	Nanocrystal
BHJ	Bulk heterojunction
PCPDTBT	(poly[2,6-(4,4-bis-(2-ethylhexyl)-4H-cyclopenta[2,1-b;3,4-b']dithiophene)-alt-4,7-(2,1,3-benzothiadiazole)])
PEDOT:PSS	(Poly(3,4-ethylenedioxythiophene):poly(styrenesulfonic acid))
PCE	Power conversion efficiency
QD	Quantum dot
NR	Nanorod
MP	Multipod
HDA	Hexadecylamine
TOPO	Trioctylphosphine oxide
HA	Hexanoic acid
PL	Photoluminescence
Cd-SA	Cadmium-stearic acid
TOP-Se	Trioctylphosphine-selenid
UV-Vis	Ultraviolet-visible
FWHM	Full width at half maximum
CB	Chlorobenzene
MeOH	Methanol
DLS	Dynamic light scattering
A.U.	Absorbance units
ITO	Indium tin oxide
QY	Quantum yield
$V_{OC}$	Open-circuit voltage
FF	Fill factor
$J_{SC}$	Short-circuit current density
$R_S$	Series resistance
$R_P$	Parallel resistance

## References

1. Zhou, Y.; Eck, M.; Krueger, M. Bulk-heterojunction hybrid solar cells based on colloidal nanocrystals and conjugated polymers. *Energy Environ. Sci.* **2010**, *3*, 1851–1864. [CrossRef]
2. Greenham, N.C.; Peng, X.; Alivisatos, A.P. Charge separation and transport in conjugated-polymer/semiconductor-nanocrystal composites studied by photoluminescence quenching and photoconductivity. *Phys. Rev. B* **1996**, *54*, 17628–17637. [CrossRef]

3. Ren, S.; Chang, L.-Y.; Lim, S.-K.; Zhao, J.; Smith, M.; Zhao, N.; Bulović, V.; Bawendi, M.; Gradečak, S. Inorganic–organic hybrid solar cell: Bridging quantum dots to conjugated polymer nanowires. *Nano Lett.* **2011**, *11*, 3998–4002. [CrossRef]
4. Greaney, M.J.; Araujo, J.; Burkhart, B.; Thompson, B.C.; Brutchey, R.L. Novel semi-random and alternating copolymer hybrid solar cells utilizing CdSe multipods as versatile acceptors. *Chem. Commun.* **2013**, *49*, 8602. [CrossRef] [PubMed]
5. Zhou, R.; Stalder, R.; Xie, D.; Cao, W.; Zheng, Y.; Yang, Y.; Plaisant, M.; Holloway, P.H.; Schanze, K.S.; Reynolds, J.R.; *et al.* Enhancing the efficiency of solution-processed polymer: Colloidal nanocrystal hybrid photovoltaic cells using ethanedithiol treatment. *ACS Nano* **2013**, *7*, 4846–4854. [CrossRef] [PubMed]
6. Eck, M.; van Pham, C.; Züfle, S.; Neukom, M.; Sessler, M.; Scheunemann, D.; Erdem, E.; Weber, S.; Borchert, H.; Ruhstaller, B.; *et al.* Improved efficiency of bulk heterojunction hybrid solar cells by utilizing CdSe quantum dot-graphene nanocomposites. *Phys. Chem. Chem. Phys.* **2014**, *16*, 12251–12260. [CrossRef] [PubMed]
7. Han, L.; Qin, D.; Jiang, X.; Liu, Y.; Wang, L.; Chen, J.; Cao, Y. Synthesis of high quality zinc-blende CdSe nanocrystals and their application in hybrid solar cells. *Nanotechnology* **2006**, *17*, 4736–4742. [CrossRef] [PubMed]
8. Heinemann, M.D.; von Maydell, K.; Zutz, F.; Kolny-Olesiak, J.; Borchert, H.; Riedel, I.; Parisi, J. Photo-induced charge transfer and relaxation of persistent charge carriers in polymer/nanocrystal composites for applications in hybrid solar cells. *Adv. Funct. Mater.* **2009**, *19*, 3788–3795. [CrossRef]
9. Olson, J.D.; Gray, G.P.; Carter, S.A. Optimizing hybrid photovoltaics through annealing and ligand choice. *Sol. Energy Mater. Sol. Cells* **2009**, *93*, 519–523. [CrossRef]
10. Dayal, S.; Reese, M.O.; Ferguson, A.J.; Ginley, D.S.; Rumbles, G.; Kopidakis, N. The effect of nanoparticle shape on the photocarrier dynamics and photovoltaic device performance of poly(3-hexylthiophene):CdSe nanoparticle bulk heterojunction solar cells. *Adv. Funct. Mater.* **2010**, *20*, 2629–2635. [CrossRef]
11. Zhou, Y.; Riehle, F.S.; Yuan, Y.; Schleiermacher, H.-F.; Niggemann, M.; Urban, G.A.; Krueger, M. Improved efficiency of hybrid solar cells based on non-ligand-exchanged CdSe quantum dots and poly(3-hexylthiophene). *Appl. Phys. Lett.* **2010**, *96*. [CrossRef]
12. Zhou, Y.; Eck, M.; Veit, C.; Zimmermann, B.; Rauscher, F.; Niyamakom, P.; Yilmaz, S.; Dumsch, I.; Allard, S.; Scherf, U.; *et al.* Efficiency enhancement for bulk-heterojunction hybrid solar cells based on acid treated CdSe quantum dots and low bandgap polymer PCPDTBT. *Sol. Energy Mater. Sol. Cells* **2011**, *95*, 1232–1237. [CrossRef]
13. Huynh, W.U.; Dittmer, J.J.; Alivisatos, A.P. Hybrid nanorod-polymer solar cells. *Science* **2002**, *295*, 2425–2427. [CrossRef] [PubMed]
14. Sun, B.; Greenham, N.C. Improved efficiency of photovoltaics based on CdSe nanorods and poly(3-hexylthiophene) nanofibers. *Phys. Chem. Chem. Phys.* **2006**, *8*, 3557–3560. [CrossRef] [PubMed]
15. Celik, D.; Krueger, M.; Veit, C.; Schleiermacher, H.F.; Zimmermann, B.; Allard, S.; Dumsch, I.; Scherf, U.; Rauscher, F.; Niyamakom, P. Performance enhancement of CdSe nanorod-polymer based hybrid solar cells utilizing a novel combination of post-synthetic nanoparticle surface treatments. *Sol. Energy Mater. Sol. Cells* **2012**, *98*, 433–440. [CrossRef]
16. Sun, B.Q.; Marx, E.; Greenham, N.C. Photovoltaic devices using blends of branched CdSe nanoparticles and conjugated polymers. *Nano Lett.* **2003**, *3*, 961–963. [CrossRef]
17. Sun, B.; Snaith, H.J.; Dhoot, A.S.; Westenhoff, S.; Greenham, N.C. Vertically segregated hybrid blends for photovoltaic devices with improved efficiency. *J. Appl. Phys.* **2005**, *97*. [CrossRef]
18. Zhou, Y.; Li, Y.; Zhong, H.; Hou, J.; Ding, Y.; Yang, C.; Li, Y. Hybrid nanocrystal/polymer solar cells based on tetrapod-shaped CdSe<sub>x</sub>Te<sub>1-x</sub> nanocrystals. *Nanotechnology* **2006**, *17*, 4041–4047. [CrossRef] [PubMed]
19. Wang, P.; Abrusci, A.; Wong, H.M.P.; Svensson, M.; Andersson, M.R.; Greenham, N.C. Photoinduced charge transfer and efficient solar energy conversion in a blend of a red polyfluorene copolymer with CdSe nanoparticles. *Nano Lett.* **2006**, *6*, 1789–1793. [CrossRef] [PubMed]
20. Dayal, S.; Kopidakis, N.; Olson, D.C.; Ginley, D.S.; Rumbles, G. Photovoltaic devices with a low band gap polymer and CdSe nanostructures exceeding 3% efficiency. *Nano Lett.* **2010**, *10*, 239–242. [CrossRef] [PubMed]
21. Dennler, G.; Scharber, M.C.; Brabec, C.J. Polymer-fullerene bulk-heterojunction solar cells. *Adv. Mater.* **2009**, *21*, 1323–1338. [CrossRef]

22. Peet, J.; Kim, J.Y.; Coates, N.E.; Ma, W.L.; Moses, D.; Heeger, A.J.; Bazan, G.C. Efficiency enhancement in low-bandgap polymer solar cells by processing with alkane dithiols. *Nat. Mater.* **2007**, *6*, 497–500. [CrossRef] [PubMed]
23. Zillner, E.; Fengler, S.; Niyamakom, P.; Rauscher, F.; Köhler, K.; Dittrich, T. Role of ligand exchange at CdSe quantum dot layers for charge separation. *J. Phys. Chem. C* **2012**, *116*, 16747–16754. [CrossRef]
24. Riehle, F.S. The Rational Synthesis Of Defect-Free CdE (E=S,Se) Nanocrystals. From Precursor Reactivity to Surface Stability. Ph.D. Thesis, University of Freiburg, Freiburg im Breisgau, Germany, 2013.
25. Gao, F.; Li, Z.; Wang, J.; Rao, A.; Howard, I.A.; Abrusci, A.; Massip, S.; McNeill, C.R.; Greenham, N.C. Trap-induced losses in hybrid photovoltaics. *ACS Nano* **2014**, *8*, 3213–3221. [CrossRef] [PubMed]
26. Zhu, L.; Richardson, B.J.; Yu, Q. Inverted hybrid CdSe-polymer solar cells adopting PEDOT:PSS/MoO<sub>3</sub> as dual hole transport layers. *Phys. Chem. Chem. Phys.* **2016**, *18*, 3463–3471. [CrossRef] [PubMed]
27. Ramar, M.; Suman, C.K.; Manimozhi, R.; Ahamad, R.; Srivastava, R. Study of Schottky contact in binary and ternary hybrid CdSe quantum dot solar cells. *RSC Adv.* **2014**, *4*, 32651–32657. [CrossRef]
28. Lek, J.Y.; Lam, Y.M.; Niziol, J.; Marzec, M. Understanding polycarbazole-based polymer: CdSe hybrid solar cells. *Nanotechnology* **2012**, *23*. [CrossRef] [PubMed]
29. Kippelen, B.; Brédas, J.-L. Organic photovoltaics. *Energy Environ. Sci.* **2009**, *2*, 251–261. [CrossRef]
30. Steinmann, V.; Kronenberg, N.M.; Lenze, M.R.; Graf, S.M.; Hertel, D.; Meerholz, K.; Bürckstümmer, H.; Tulyakova, E.V.; Würthner, F. Simple, highly efficient vacuum-processed bulk heterojunction solar cells based on merocyanine dyes. *Adv. Energy Mater.* **2011**, *1*, 888–893. [CrossRef]
31. Yuan, Y.; Riehle, F.-S.; Gu, H.; Thomann, R.; Urban, G.; Krueger, M. Critical parameters for the scale-up synthesis of quantum dots. *J. Nanosci. Nanotechnol.* **2010**, *10*, 6041–6045. [CrossRef] [PubMed]
32. Qu, L.; Peng, X. Control of photoluminescence properties of CdSe nanocrystals in growth. *J. Am. Chem. Soc.* **2002**, *124*, 2049–2055. [CrossRef] [PubMed]
33. Krueger, M.; Eck, M.; Zhou, Y.; Riehle, F.-S. Semiconducting nanocrystal/conjugated polymer composites for applications in hybrid polymer solar cells. In *Semiconducting Polymer Composites*; Wiley-VCH Verlag GmbH & Co. KGaA: Weinheim, Germany, 2012; pp. 361–397.
34. Eichhöfer, A.; Hänisch, C.V.; Jacobsohn, M.; Banin, U. Dynamic light scattering at CdSe nanocrystals and CdSe cluster-molecules. In Proceedings of the MRS Fall Meeting 2000, Boston, MA, USA, 27–30 November 2000; Karim, A., Merhari, L., Norris, D.J., Rogers, J.A., Xia, Y., Eds.; Cambridge University Press: Cambridge, UK, 2000; pp. D9.53.1–D9.53.9.
35. Shen, Y.; Li, K.; Majumdar, N.; Campbell, J.C.; Gupta, M.C. Bulk and contact resistance in P3HT:PCBM heterojunction solar cells. *Sol. Energy Mater. Sol. Cells* **2011**, *95*, 2314–2317. [CrossRef]
36. Kim, M.-S.; Kim, B.-G.; Kim, J. Effective variables to control the fill factor of organic photovoltaic cells. *ACS Appl. Mater. Interfaces* **2009**, *1*, 1264–1269. [CrossRef] [PubMed]
37. Schafferhans, J.; Baumann, A.; Wagenpahl, A.; Deibel, C.; Dyakonov, V. Oxygen doping of P3HT:PCBM blends: Influence on trap states, charge carrier mobility and solar cell performance. *Org. Electron.* **2010**, *11*, 1693–1700. [CrossRef]
38. Tang, J.; Wang, X.; Brzozowski, L.; Barkhouse, D.A.; Debnath, R.; Levina, L.; Sargent, E.H. Schottky quantum dot solar cells stable in air under solar illumination. *Adv. Mater.* **2010**, *22*, 1398–1402. [CrossRef] [PubMed]
39. Kwon, S.; Lim, K.-G.; Shim, M.; Moon, H.C.; Park, J.; Jeon, G.; Shin, J.; Cho, K.; Lee, T.-W.; Kim, J.K. Air-stable inverted structure of hybrid solar cells using a cesium-doped ZnO electron transport layer prepared by a sol-gel process. *J. Mater. Chem. A* **2013**, *1*. [CrossRef]
40. Züfle, S.; Neukom, M.T.; Altazin, S.; Zinggeler, M.; Chrapa, M.; Offermans, T.; Ruhstaller, B. An effective area approach to model lateral degradation in organic solar cells. *Adv. Energy Mater.* **2015**, *5*. [CrossRef]
41. Kawano, K.; Pacios, R.; Poplavskyy, D.; Nelson, J.; Bradley, D.D.; Durrant, J.R. Degradation of organic solar cells due to air exposure. *Sol. Energy Mater. Sol. Cells* **2006**, *90*, 3520–3530. [CrossRef]



Review

# Graphene and Carbon Quantum Dot-Based Materials in Photovoltaic Devices: From Synthesis to Applications

Sofia Paulo <sup>1,2</sup>, Emilio Palomares <sup>1,3,\*</sup> and Eugenia Martinez-Ferrero <sup>2,\*</sup>

<sup>1</sup> Institut Català d'Investigació Química (ICIQ), The Barcelona Institute of Science and Technology, Avda. Països Catalans 16, Tarragona 43007, Spain; spaulo@iciq.es

<sup>2</sup> Fundació Eurecat, Avda. Ernest Lluch 36, Mataró 08302, Spain

<sup>3</sup> ICREA, Passeig Lluís Companys 23, Barcelona 08010, Spain

\* Correspondence: epalomares@iciq.es (E.P.); emartinez@eurecat.org (E.M.-F.); Tel.: +34-977-920-241 (E.P.); +34-937-419-100 (E.M.-F.)

Academic Editor: Guanying Chen

Received: 24 May 2016; Accepted: 10 August 2016; Published: 25 August 2016

**Abstract:** Graphene and carbon quantum dots have extraordinary optical and electrical features because of their quantum confinement properties. This makes them attractive materials for applications in photovoltaic devices (PV). Their versatility has led to their being used as light harvesting materials or selective contacts, either for holes or electrons, in silicon quantum dot, polymer or dye-sensitized solar cells. In this review, we summarize the most common uses of both types of semiconducting materials and highlight the significant advances made in recent years due to the influence that synthetic materials have on final performance.

**Keywords:** quantum dots; graphene; carbon; photovoltaics; solar cells

## 1. Introduction

Converting solar energy efficiently into either electrical or fuel sources remains one of mankind's biggest challenges [1]. Despite the rapid progress that has been made in recent years in research into third generation solar cells, silicon is still the biggest and most important player in the PV industry. Even so, such new technologies as mixed halide perovskite solar cells are quickly catching-up in efficiency (the current record of efficiency is above 22% at 1 sun) [2,3]. Dye-sensitized and organic solar cells (which include polymer- and small organic molecule-based solar cells) have already shown their potential for applications like building integrated photovoltaics. Whereas semiconductor-based quantum dots, typically composed of cadmium or lead derivatives, have such excellent optical properties that they have been used in a wide array of optoelectronic devices such as solar cells, light emitting diodes, bioimaging or optical sensors [4–6].

In this context, carbon-based quantum dots have emerged as potential candidates for application in such devices. Since their discovery early 2000s, carbon-based quantum dots have been the focus of intensive research because of their excellent luminescent properties, good solubility and biocompatibility [7,8]. This research effort increased exponentially after the Nobel Prize awarded to Novoselov and Geim for discovering graphene and describing its properties [9].

These carbon-based nanostructures are in fact two different allotropes (Figure 1). On the one hand, carbon quantum dots (CDs) are quasi-spherical nanoparticles less than 10 nm in diameter, formed by crystalline sp<sup>2</sup> graphite cores, or amorphous aggregations, which have a quantum confinement effect. On the other hand, there are dots—the so-called graphene quantum dots (GDs)—made up of single or very few graphene lattices (<10) that have quantum confinement effect and edge effects. GDs are



usually more crystalline than CDs because their conjugated domains are larger and their structure regular. Both allotropes are functionalized with complex surface groups, specially oxygen-related molecules such as carboxylates or hydroxylate derivatives that remain after the synthetic procedure and enhance the optical properties and the solubility of the particles [10,11]. It should be pointed out that variability in the fabrication of these materials results in different surface functionalization and the addition of complexity to the hybridization of the carbon atoms.

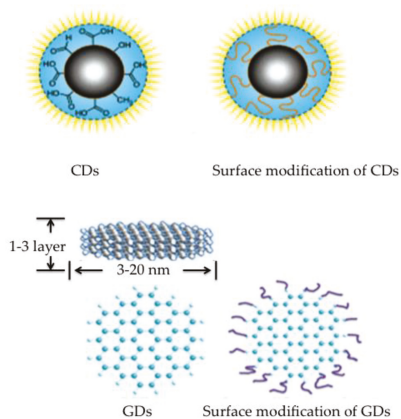


**Figure 1.** Illustration of CD (top) and GD (bottom) structures. Reproduced with permission of [12–14].

Carbon-based dots have many advantages over non-carbon dots because of their chemical inertness and lower cytotoxicity photobleaching and cost. For instance, they can be produced from biomass. In recent years, carbon-based dots have been tested as fluorescent probes, in light emitting diodes, solar cells, biosensors, supercapacitors, lithium ion batteries and catalysts [15–20] and have even been combined with non-carbon dots in optoelectronic applications [21]. Despite their excellent optical properties, they have not performed in photovoltaics as well as non-carbon based quantum dot solar cells. As far as we know, no exhaustive review has been made of carbon-based dots used in photovoltaics. Therefore, in an attempt to understand why these nanostructures have so far failed to realize their potential, in this review we analyze the main achievements in the link between functionality and the synthesis of the material. We aim to give a general overview of how these promising carbon nanostructures can be applied in PV dividing this feature article into the following parts:

1. General synthetic approaches.
2. Photonic properties.
3. Graphene quantum dots in photovoltaic devices.
4. Carbon quantum dots in photovoltaic devices.
5. Outlook and perspectives.

At the end of the manuscript, we have included a list of the abbreviations used throughout the text and Tables 1 and 2 summarize the research done on graphene and carbon quantum dots in photovoltaics, respectively.

**Table 1.** Summary of the synthetic techniques of CDs included in this article, the resulting size and functional groups and the performance of the photovoltaic cells in which they are used.

Synthesis <sup>1</sup>	Carbon Source	Average Size (nm)	Surface Groups	Solar Cell <sup>2</sup>	Jsc (mA/cm <sup>2</sup> )	Voc (V)	FF (%)	$\eta$ (%)	Effect	R <sup>3</sup>
H	$\gamma$ -butyrolactone	9 ± 6	Sulfonate, carboxyl, hydroxyl, alkyl	DSSC	0.53	0.38	64	0.13	Emissive traps on the dot surface and enhancement of recombination	[22]
H	Citric acid	1–2	carboxyl	SMOPV PSC	13.32 9.98	0.904 0.609	63.7 54.8	7.67 3.42	Increment in exciton separation and charge collection	[23]
H	CCl <sub>4</sub>	1.5–3.3	Amino, carboxylic	DSSC	0.33	0.370	43	0.13	Contribution to light absorption	[24,25]
H	Polystyrene-co-maleic anhydride	---	---	PSC	13.61	0.870	59.5	7.05	Improvement of absorption in the UV and charge transport	[26]
M	Citric acid	200 <sup>4</sup> 1.2 <sup>5</sup>	Carboxylic, primary amines	QDSC	16.6 <sup>4</sup> 2.0 <sup>5</sup>	0.708 <sup>4</sup> 0.550 <sup>5</sup>	46.4 <sup>4</sup> 16 <sup>5</sup>	5.4 <sup>4</sup> 0.18 <sup>5</sup>	Improved charge extraction	[27]
E	Graphite rods	<4	Hydroxyl, carboxyl, aromatic groups, epoxide/ether	DSSC	0.02	0.580	35	0.0041	Non-optimized electrolyte and electrode	[28]
H	Biomass (chitin, chitosan, glucose)	14.1 ± 2.4 chitin 8.1 ± 0.3 chitosan 2.37 ± 0.04 glucose	Amine, amide, hydroxyl	DSSC	0.674 <sup>6</sup>	0.265 <sup>6</sup>	43 <sup>6</sup>	0.077 <sup>6</sup>	Influence of surface groups	[29]
E	Graphite rod	4.5	---	Si	30.09	0.510	59.3	9.1	Improvement of absorption in the UV and decrease of recombination	[30]
H	Ascorbic acid	3–4	Carboxylic, hydroxyl	DSSC	8.40	0.610	62	3.18	Improvement of light absorption	[31]
S	Citric acid	1.5	Aldehyde, carboxylic	PSC	0.288	1.588	48.5	0.23	Insulating character of oleylamine ligand	[32]
H	Glucose	16	---	QDSC	1.88	0.605	31	0.35	Increment of charge transfer and decrease of recombination	[33]
E	Graphite rods	<10	---	DSSC	0.64	0.500	---	0.147	Improvement of absorption in the UV and decrease of recombination	[34]
H	Citric acid	2–3	---	PerSC	7.83	0.515	74	3.00	Non-optimized device	[35]

<sup>1</sup> H: hydrothermal, M: microwave, E: electrochemical, S: soft template synthesis; <sup>2</sup> DSSC: dye-sensitized solar cell, SMOPV: small molecule organic solar cell, PSC: polymer-based organic solar cells, Si: silicon-based solar cell, QDSC: quantum dot sensitized solar cell, PerSC: perovskite-based solar cell; <sup>3</sup> R: reference; <sup>4</sup>: CDs-Au particles; <sup>5</sup>: CDs; <sup>6</sup>: best results obtained from the combination of chitosan- and chitin-derived CDs.

**Table 2.** Summary of the synthetic techniques of GDs included in this article, the resulting size and functional groups and the performance of the photovoltaic cells in which they are used.

Synthesis <sup>1</sup>	Carbon Source	Size (nm)	Surface Groups	Solar Cell <sup>2</sup>	J <sub>sc</sub> (mA/cm <sup>2</sup> )	Voc (V)	FF (%)	η (%)	Effect	R <sup>3</sup>
H	Bromobenzoic acid	13.5	1,3,5 trialkyl phenyl	DSSC	0.2	0.48	58	0.055	Poor charge injection due to low affinity of GDs to titania	[36]
M	Glucose	3.4	---	Si	37.47	0.61	72.51	16.55	Improvement of absorption in the UV	[37]
E	Graphite rod	5–10	Hydroxyl, epoxy, carboxylic, carbonyl	PerSC	17.06	0.957	63.5	10.15	Improvement of charge extraction	[38]
E	Graphene film	3–5	Hydroxyl, carbonyl	PSC	6.33	0.67	30	1.28	Increment of exciton separation and charge transport. Non-optimized morphology	[39]
A	Graphite	8.5	---	DSSC	0.45	0.8	50	0.2	Inefficient hole collection due to non-optimized thickness of GD layer	[40]
M	Glucose	2.9	---	Si	36.26	0.57	63.87	13.22	Improvement of absorption in the UV and conductivity	[41]
A+H	Graphene oxide	2–6	Epoxy, carbonyl	Si	23.38	0.51	55	6.63	Reduction in current leakage	[42,43]
A	Carbon black	10	Hydroxyl, carbonyl	DSSC	14.36	0.723	50.8	5.27	Reduction in internal resistance and increment of charge transfer	[44]
A+H	Graphene oxide	<1	Epoxy, carbonyl, hydroxyl	PSC	15.2	0.74	67.6	7.6	Increment in conductivity	[45]
A+H	Graphene sheets	9	Carboxyl <sup>4</sup>	PSC	3.51	0.61	53	1.14	Increase in exciton separation and charge transport	[46]
A+H	Graphene oxide	50	PEG	DSSC	14.07	0.66	59	6.1	Increase in light absorption	[47]
M	Glucosamine hydrochloride	4.3	amine	DSSC	5.58	0.583	66	2.15	Increase in light absorption and decrease of recombination	[48]
A	Carbon fibers	20–30	---	PSC SMOPV	10.2 11.36	0.52 0.92	66.3 65.2	3.5 6.82	Increase in conductivity	[49,50]

<sup>1</sup> H: hydrothermal, M: microwave, E: electrochemical, A: acidic oxidation, <sup>2</sup> DSSC: dye sensitized solar cell, SMOPV: small molecule organic solar cell, PSC: polymer-based organic solar cells, Si: silicon-based solar cell, QDSC: quantum dot sensitized solar cell, PerSC: perovskite-based solar cell, <sup>3</sup> R: reference, <sup>4</sup> surface groups attached after chemical treatment.

## 2. General Synthetic Approaches

Numerous papers describe synthetic procedures for preparing carbon and graphene quantum dots. Two main approaches can be distinguished: bottom-up and top-down synthesis. The bottom-up route builds nanostructures from small organic molecular precursors by pyrolysis, combustion or hydrothermal methods while the top-down approach is based on cutting small sheets via physical, chemical or electrochemical techniques until the required particle size is reached (Figure 2). In both cases, post treatment is done to purify or modify the surface functionalization and improve the performance of the dots. For example, the quantum yield increases after surface passivation of CDs or functionalization because the emissive traps on the nanoparticle surface disappear. Likewise, doping with heteroatoms such as nitrogen and phosphor, or metals such as Au or Mg improves the electrical conductivity and solubility of CDs and GDs [24,27].

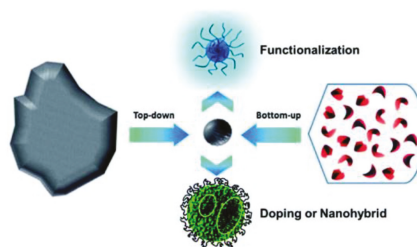


**Figure 2.** Schematic representation of both synthetic approaches. Reproduced with permission of [16].

In this review, we have focused exclusively on the synthetic procedures described for carbon-based dots applied in photovoltaic devices. Of course, other excellent reviews on the vast number of applications of carbon and graphene quantum dots can be found in [16,17,51], and the references cited therein.

### 2.1. Bottom-up Approach

#### 2.1.1. Hydrothermal/Solvothermal Synthesis

Hydrothermal synthesis is a widespread procedure that consists of a one-step synthetic technique in which an organic precursor is heated in a Teflon line to achieve high temperature and pressure. Using various organic precursors and modifying the temperature, the optoelectronic properties of the dots are tuned. It is, thus, a low-cost, non-toxic method. In addition, hydrothermal methods produce dots with a diameter of 10 nm, which are bigger than dots produced by other techniques such as electrochemical preparations (3–5 nm).

Pioneering work by Mirtchev and coworkers introduced the use of carbon quantum dots as sensitizers in dye-sensitized solar cells (DSSC) prepared by dehydrating  $\gamma$ -butyrolactone [22]. In contrast, Yan et al. synthesized graphene dots from bromobenzoic acid using well-known Suzuki-Miyaura reaction conditions (Figure 3). In order to prepare large graphene dots and avoid aggregation, they covalently attached 1,3,5-trialkyl phenyl moieties to the edge of the graphene, shielding them in the three dimensions [36]. Last but not least, Zhang et al. prepared the CDs from citric acid and ethylenediamine in aqueous solution heated for 10 h at 250 °C obtaining uniform 1–2 nm size particles [23], whereas Liu et al. synthesized the CDs combining polystyrene-co-maleic and ethylenediamine dissolved in DMF at 200 °C for 5 h [26].

The nanoparticles are nitrogen doped by this route as well. Zhang et al. used carbon tetrachloride and sodium amide as starting materials and methylbenzene as the solvent, heating at 200 °C for different periods of time to prepare well-dispersed crystalline CDs. By controlling the reaction time, the authors tuned the size and the nitrogen content of the dots in such a way that prolonged reaction

times favored the incorporation of nitrogen into the carbon framework and the increase in the particle size. Regardless of the reaction time, the dots had amino functional groups on their surface [24].

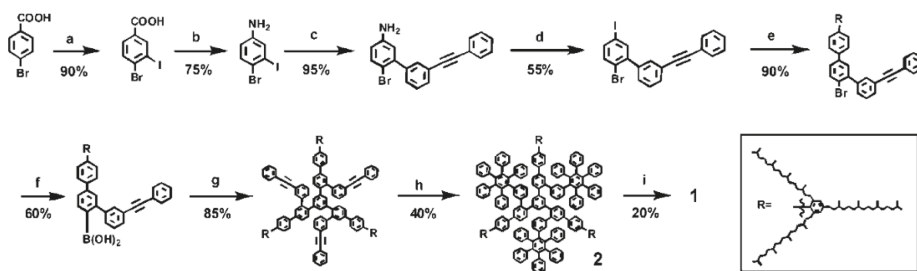


**Figure 3.** Suzuki reaction followed to prepare graphene dots (described as product number 1 in the reaction scheme) from bromobenzoic acid. Reproduced with permission of [36]. Steps are as follows: (a)  $\text{NaIO}_4$ ,  $\text{I}_2$ , concentrated  $\text{H}_2\text{SO}_4$ , room temperature; (b) Heated with diphenylphosphoryl azide in triethylamine and tert-butanol at  $80\text{ }^\circ\text{C}$ , followed by treatment with  $\text{CF}_3\text{COOH}$  in dichloromethane at room temperature; (c) Suzuki condition with 3-(phenylethynyl)phenylboronic acid,  $\text{Pd}(\text{PPh}_3)_4$ ,  $\text{K}_2\text{CO}_3$  in water, ethanol, and toluene mixture,  $60\text{ }^\circ\text{C}$ ; (d) Iodine and tert-butyl nitrite in benzene,  $5\text{ }^\circ\text{C}$  to room temperature; (e) Suzuki condition with substituted phenyl boronic acid,  $\text{Pd}(\text{PPh}_3)_4$ ,  $\text{K}_2\text{CO}_3$  in water, ethanol, and toluene mixture,  $80\text{ }^\circ\text{C}$ ; (f) Treatment with butyllithium in tetrahydrofuran (THF) at  $-78\text{ }^\circ\text{C}$ , then with triisopropyl borate at  $-78\text{ }^\circ\text{C}$ , followed by treatment with acidic water at room temperature; (g) Suzuki condition with 1,3,5-triiodobenzene,  $\text{Pd}(\text{PPh}_3)_4$ ,  $\text{K}_2\text{CO}_3$  in water and toluene mixture,  $80\text{ }^\circ\text{C}$ ; (h) Tetraphenylcyclopentadienone in diphenylether,  $260\text{ }^\circ\text{C}$ ; (i)  $\text{FeCl}_3$  in nitromethane and dichloromethane mixture, room temperature.

### 2.1.2. Microwave Irradiation Synthesis

As well as the speed of the synthesis, another important advantage that microwave synthetic methods have over hydrothermal synthesis is that they can be used at lower temperatures. Dao et al. obtained high quality CDs by this synthetic approach. They mixed citric acid and urea in distilled water and the solution was then heated in a microwave oven at 700 W for 4 min. The supernatant was neutralized with sodium bicarbonate and cleaned with distilled water [27]. The resulting dots were doped with Au by chemical reduction of  $\text{HAuCl}_4$  with formic acid to prepare three dimensional raspberry-like particles with a diameter of 200 nm formed by gold branches that originated high surface areas. In addition, Tsai et al. synthesised water soluble GDs by microwave irradiation using glucose as the carbon source and water as solvent heating at 700 W for 11 min. The as-prepared dots measured 3.4 nm in diameter, as observed by AFM (Atomic Force Microscopy) and TEM (Transmission Electron Microscopy) [37].

### 2.1.3. Soft Template Method

In this approach, reported by Kwon et al., CDs are made into an emulsion that acts as a self-assembled soft template because the size of the dots is controlled by regulating the amount of the emulsifier. Synthesis in a non aqueous medium favors organic-based surface capping and size tuning. For that, the authors mix oleylamine and octadecene with citric acid solved in water. The water droplets, stabilized by the oleylamine, are eliminated heating at  $250\text{ }^\circ\text{C}$  forcing the intermolecular dehydration of citric acid molecules which form polymer-like structures. Further carbonization render organic soluble carbon dots capped by oleylamine molecules that are chemically bound to the dot surface carbonyl groups. The concentration of oleylamine determines the final size of the dots [32].

## 2.2. Top-down Approach

### Electrochemical Methods

Electrochemical methods make it possible to fine tune carbon nanostructures by controlling the voltage/current applied. For instance, applying a controlled bias to a bulk of carbon precursors leads to electrochemical corrosion reactions over the carbon reactants and subsequently to carbon nanostructures. It is important to notice that this particular technique does not require high temperatures, is easy to scale-up and can proceed under aqueous or non-aqueous solutions. It is one of the fastest routes for preparing graphene sheets [52]. For example, Sun et al. prepared carbon quantum dots by combining the electrochemical method with etching methods [28]. In brief, they used graphite rods as both electrodes whereas the reaction was conducted by applying an alternate bias between 100 and 150 V during 10 h in the presence of an ethanol solution of NaOH (Figure 4). Then they added  $MgSO_4$  followed by stirring, deposition, centrifugation and drying of the solvent in order to obtain the uniform and monodisperse dots.

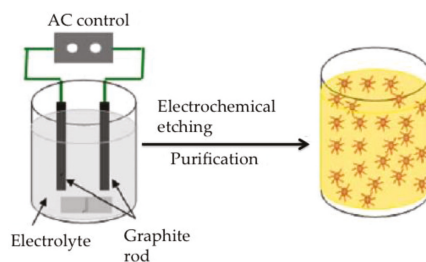


**Figure 4.** Schematic view of the obtention of CDs by electrochemical methods. Reproduced with permission of [28].

More recently, Zhu and co-workers obtained graphene dots. In this case, the electrolysis took place under a current intensity between 80 and 200  $mA/cm^2$  with a graphite rod as anode in a basic solution and Pt foil as the counter electrode. In order to finish the reaction, they added 1 mL of 80% hydrazine hydrate and stirred the solution for 8h. It was then centrifuged and dialyzed in water for one day [38,53]. Yan Li and co-workers prepared homogeneous GDs by electrochemical methods from graphene films [39]. For that, graphene films, prepared by the filtration method and treated in oxygen plasma to improve its hydrophilicity, were used as working electrodes in combination with Pt wire and Ag/AgCl that acted as counter and reference electrode, respectively, in phosphate buffer solution. After CV scan rate of 0.5 V/s within  $\pm 3$  V in 0.1 M PBS, water soluble GDs with uniform 3–5 nm size were obtained.

### 2.3. Acidic Oxidation or Chemical Ablation

In essence, this two-step procedure consists of the exfoliation of graphite powder using concentrated mineral acids and oxidizing agents under refluxing conditions. This approach, also known as Hummers method, is one of the most popular procedures described for obtaining graphite oxide. The first step is often followed by further chemical reduction to prepare the quantum dots. For example, Dutta et al. treated graphite with sodium nitrate in aqueous sulfuric acid solution with potassium permanganate stirring for four days. Once the graphite oxide was ready, ultrasonication of the sample in water produced graphene oxide, which was converted to graphene dots by reduction in hydrazine solution [40]. Pan et al. prepared GDs from graphene oxide that was transformed to graphene sheets by the Hummer's method. For the second step, they applied a hydrothermal treatment in basic solution (heating at 200 °C for 10 h at pH 8) to cut the graphene sheets into dots that were further purified by dialysis [43].

Carbon black has also been used as a carbon source. Chen et al. prepared GDs by oxidation of the carbon black in nitric acid under reflux conditions overnight. After cooling and centrifugation, the supernatant was heated to recover the dots [44]. An alternative source are carbon fibers, as reported by Peng et al. [49]. In this case, the fibers were sonicated and heated for 30 h at 100 °C in acidic medium. After being cooled, the mixture was diluted in water, the pH tuned to 7 and the solution dialyzed.

### 3. Photonic Properties

It is a remarkable fact that both structures show quantum confinement effects, which means that the energy band gap is determined by the size and shape of the structure (Figure 5). In addition, the optical properties are also influenced by the fabrication variability, which results in a wide array of sizes and surface functionalizing groups and/or defects. Therefore, the determination of the origin of the material's optical properties is one of the most controversial topics in research into carbon and graphene quantum dots.

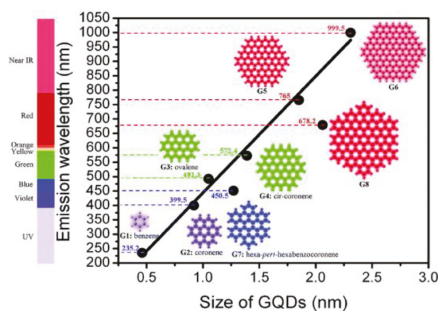


**Figure 5.** Estimated variation of the emission wavelength with the size for GDs. Reproduced with permission of [54].

#### 3.1. Light Absorption

Both CDs and GDs have an absorbance band in the UV region between 260 and 320 nm assigned to the  $\pi-\pi^*$  transition of C=C bonds with  $sp^2$  hybridization and, sometimes, a weaker shoulder at 270–400 nm attributed to  $\delta-\pi^*$  transitions of the C=O bonds, with a tail extending into the visible wavelengths. Graphene quantum dots also have extinction coefficients in the UV region from 10 to  $200 \times 10^3 \text{ M}^{-1}\text{cm}^{-1}$ , which is larger than common fluorophores and comparable to other quantum dots [53,54].

#### 3.2. Light Emission

The photoluminescence (PL) mechanism in CDs and GDs is still an open question and different processing methods cause PL of different origins. In fact, PL has been reported to be influenced by the dot size, the excitation wavelength, the degree of surface functionalization or oxidation, the pH during synthesis, the solvent polarity and the doping with heteroatoms. Both CDs and GDs show strong photoluminescent emission that is mostly exciton dependent, which means that the emission peak moves as the excitation wavelength is changed. The origin of fluorescence emission has been intensively studied and assigned to quantum confinement effects, triplet carbenes at zigzag edges or edge defects, excitonic transitions, surface states or functional groups [55–59].

### 4. Graphene Quantum Dots in Photovoltaics

Researchers have already found various applications for graphene dots in solar cells, mainly in silicon-based solar cells, dye-sensitised solar cells, organic solar cells (OSC) and, more recently, perovskite solar cells. Silicon diodes (either crystalline, c-Si, or amorphous, a-Si) are based on silicon p-n



junctions that act both as light absorbers and charge transport carriers. Although Si diodes dominate the PV market because of their high efficiency (recently reported to be 25.6%) [2] and long lifetime, the incorporation of graphene sheets as transparent electrodes has already been explored to improve the performance of the diodes [60].

The device structure of DSSC, which are photo-electrochemical solar cells, is more complex. The electron transport layer is often based on mesoporous nanocrystalline metal oxide films, usually TiO<sub>2</sub> or ZnO, supported on a conducting substrate. The electron transport layer can be configured as planar, mesoporous or columnar morphologies. The mesoporous metal oxide film is sensitized to absorb visible light after the adsorption of a dye monolayer. Examples of popular dyes are Ru(II)-containing polypyridyls, porphyrins, phthalocyanines, squarines or organic dyes [61]. The device is filled with an electrolyte that regenerates the sensitizer, normally iodide/tri-iodide redox electrolyte, defined as hole transport layer (HTL) and a platinum coated counter electrode (Figure 6a). DSSCs have attracted considerable attention since the landmark paper in 1991 by Gratzel and O'Regan [62]. Because of their potential low cost, environmentally friendly components, ease of fabrication in air and such optical properties as transparency and colour, which depends on the dye selected, DSSCs have attracted attention for building-integrated photovoltaic applications. Record efficiencies of 13% have recently been achieved with the molecularly engineered porphyrin dye SM315 [63]. A solid state version of the DSSC can be achieved by replacing the liquid electrolyte with a solid hole transport material such as spiro-OMeTAD or a semiconductor polymer [64].

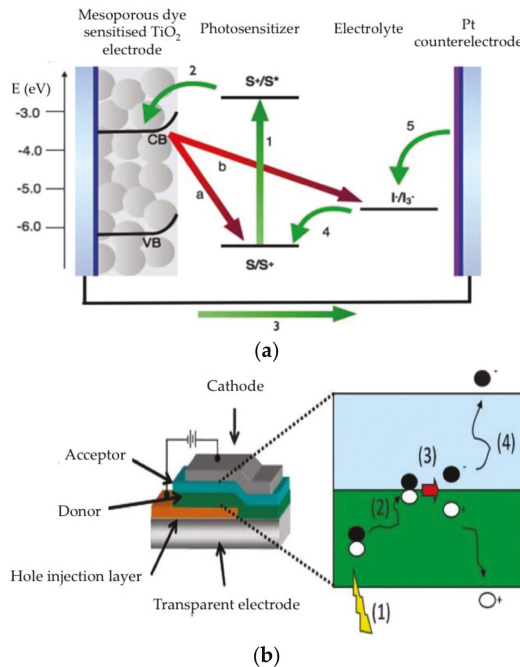


**Figure 6.** Schematic representation of the composition and charge transfer processes in (a) DSSC [(1) light absorption; (2) electron injection; (3) electron collection; (4) reduction of the oxidized dye cation by the redox couple; (5) regeneration of the electrolyte at the counterelectrode] and (b) OSC [(1) Light absorption and creation of an exciton; (2) exciton diffusion; (3) exciton splitting at the interface; (4) diffusion and collection of charges]. Reproduced with permission of [61,65], respectively.

Organic photovoltaics (OSCs) combine carbon-based semiconductor materials and molecules, which play the roles of light absorption and carrier transport sandwiched between selective metal electrodes. Depending on the molecular weight of the organic material, OSCs are classified as polymer (PSC) or small-molecule solar cells (SMOPV). The former are processed from solution in organic solvents to form bulk heterojunctions in the photoactive layer in conjunction with either the electron or hole acceptor material. The latter can also be processed using high vacuum techniques. It is well established that the intermixing of the donor and the acceptor optimizes the exciton separation and subsequent carrier collection (Figure 6b) [65,66]. For many years, the most efficient, and widely used, electron acceptor materials were those based on such fullerene derivatives as PCBM. In fact, record efficiencies above 11% have recently been reported using PffBT4T-derivatives as donors and C71-fullerene derivatives as acceptors [67,68]. Only recently has it been shown that other electron acceptor materials can be used to match the high efficiency obtained with fullerene derivatives [69].

In both types of solar cell, DSSC and OSC, which differ from silicon solar cells in the materials they use to transport the hole and the electron carriers, carbon nanomaterials can be easily adapted to have different roles, as described below.

#### 4.1. Light Harvesting

Even though thin film layers of CDs and GDs have been used more as selective contacts in molecular solar cells, several groups have tried using these materials as light harvesting components. For example, Dutta and coworkers sensitized ZnO nanowires with graphene dots to prepare the structure of AZO/ZnO nanowires/GDs/TPD/Au. Graphene quantum dots participated in the charge transfer to the ZnO nanowires (nw). This is reflected in the increase of  $J_{sc}$  and  $V_{oc}$  compared to the control (ZnO nw without dots) and has an efficiency of 0.2%. This low value was attributed to inefficient hole collection by TPD originated by the non-optimized thickness of the graphene layer [40]. For the deposition of GD into mesoporous layers of titania, Yan and colleagues prepared large dots functionalized with 1,3,5-trialkyl-substituted phenyl moieties (at the 2-position) at the edges of the dots to favour solubilization into common solvents and avoid aggregation. The  $V_{oc}$  and FF of the as-prepared  $TiO_2$ /GDs/ $I_3^-/I^-$  diodes were comparable to those obtained with the widely used Ru-based sensitizer (0.48 V, 58%, respectively). However,  $J_{sc}$  was much lower, which was attributed to the low affinity of the dots to the oxide surface, which resulted in poor physical adsorption and subsequent poor charge injection [36]. In addition, the dot size may have prevented effective packaging on the surface. Taking into account that graphene dots have a limited spectral absorption range in the visible, co-sensitization of the device with dyes to cover all the visible range of the spectrum emerges as an effective alternative. In this regard, the work of Fang and colleagues combined GDs with the well-known N719 dye. The dots, synthesized by acidic and hydrothermal methods from graphene oxide, were surface-passivated with PEG so carboxyl and hydroxyl groups on the surface promoted the linkage to the titania surface. Tests done with different concentrations of GDs showed that higher loadings resulted in agglomeration. The best results gave an efficiency of 6.1% due to higher  $J_{sc}$  and  $V_{oc}$  than the reference, which gave 5.1% [47]. In a second example provided by Mihalache et al., N3 was combined with GDs prepared by microwave-assisted synthesis. They used this method to obtain dots with higher quantum yields and a self-passivated surface with amino functional groups to improve the affinity for the titania surface. The resulting device had better  $J_{sc}$  than the  $TiO_2$ /N3 devices due to the expansion of the absorption range, which was confirmed by the increase in the IPCE throughout the range. However, the  $V_{oc}$  was lower, although the overall efficiency of 2.15% was higher than the 1.92% of the reference. The efficiency improved as a result of the crossover between two mechanisms: first, a Foster Resonance Energy Transfer (FRET) dominant process in the blue part of the spectrum because of the significant overlap between the emission spectra of the GDs and the absorption spectrum of N3, and second, a charge transfer mediated by GDs towards the red part of the spectrum due to the cascaded energy level alignment of the LUMO levels of N3-GDs- $TiO_2$  (2.98, 3.16, 4 eV, respectively), which increased the rate of electron injection [48]. Photovoltage decay analyses

confirmed the hypothesis that the GDs inhibited the back electron transfer from N3 to the electrolyte. Therefore, the dots were playing a dual role in these devices as active absorbers and reductors of the recombination reactions.

Li and coworkers tested the GDs as alternatives to the popular fullerene derivative acceptors for application in organic solar cells. They reported the preparation of monodisperse graphene dots by electrochemical methods between 3 and 5 nm in size. Surface groups such as hydroxyl, carbonyl and carboxylic acid groups facilitated dispersion in common organic solvents and subsequent mixing with polymers leading to the structure ITO/PEDOT:PSS/P3HT-GQD/Al [39]. The value of the LUMO level (4.2–4.4 eV) of the GDs led to the formation of an electron transport cascade in the system P3HT-GDs-Al. Compared to P3HT-only devices, the GDs increased the exciton separation and carrier transport leading to an efficiency of 1.28%. However, the efficiency was lower than that of devices prepared with fullerenes as electron acceptors because of lower electron affinity and the non-optimized morphology, which resulted in lower FF. Similar experiments made by Gupta et al. compared the effect of graphene dots, synthesized by acidic and hydrothermal methods, and graphene sheets, both functionalized with aniline, as electron acceptors in the structure ITO/PEDOT:PSS/P3HT:ANI-GQD/LiF/Al [46]. They combined P3HT with increasing amounts of GDs in order to optimize the devices. Results were best with 1 wt. % for which efficiencies were 1.14%. Dots gave higher  $J_{sc}$  values than graphene sheets because their homogenous and uniform distribution within P3HT enhanced exciton separation and transport towards electrodes, which resulted, in turn, in higher FF. Another paper by Kim et al. compared the effects of GDs with different oxidation degrees on OSC [45]. The dots, prepared using Hummers' method, were oxidized, and then hydrothermally reduced for 5 h or for 10 h before being added to the PTB7:PC71BM bulk heterojunction. During reduction, the oxygen-related functional groups were gradually removed while the size remained unaltered below 1 nm. In addition, the reduction had a negative effect on the light absorption but enhanced conductivity. After optimizing the concentration of dots in the BHJ, the researchers found that the positive effect of GDs varies with their reduction time, because  $J_{sc}$  increased with the oxidized dots whereas FF increased with the dots reduced for 5 h. This agreed with the observations made about the morphology and composition of the dots and shows that the functional groups, richer in oxidized GDs, play a positive role in light harvesting while  $sp^2$  carbon-richer reduced samples make a beneficial contribution to charge conductivity, decreasing the leakage current and enhancing shunt resistance and FF. The maximum efficiency, 7.6%, was thus achieved with 5 h-reduced GDs.

Finally, Tsai et al. combined GDs with n-type silicon heterojunction solar cells to expand the spectral range absorption and decrease the number of wasted photons in the UV region. To do so, they added GDs at different concentrations by solution processing on top of Ag/ITO/a-Si/ITO/Ag devices where the silicon wafer is structured as a micro pyramid [37]. The results demonstrated that the addition of GDs increased the  $J_{sc}$  and the FF, reaching a record efficiency of 16.55% when 0.3 wt. % concentration was used.

#### 4.2. Counterelectrode

Platinum is the most popular material used as the counterelectrode in DSSC because its energy levels are suitable and it is easy to prepare. However, platinum is a rare precious metal and this increases the cost of the device. It is, therefore, prone to be substituted. In this regard, graphene sheets emerge as an excellent alternative nanomaterial because of their high carrier mobility, surface area and optical transparency. Examples of the use of plain graphene or composites of graphene with polymers, metals or carbon nanotubes can be found in the review by Wang et al. [70]. The defects and the functional groups of the sheets play a critical role in the electrocatalytic sites of the counterelectrode, making research on this topic necessary if understanding and efficiencies are to be increased. Chen and coworkers proposed a composite made of GDs embedded in polypyrrol (PPy) in the structure FTO/TiO<sub>2</sub>/N719/I<sub>3</sub><sup>-</sup>/I<sup>-</sup>/GD-PPy as an effective method to lower the cost of the device. PPy is cheap and easy to produce although high charge transfer resistance has prevented it from being used

in optoelectronic devices. Graphene dots containing  $-\text{COOH}$  and  $-\text{OH}$  groups on the edge interacted electrostatically with the N sites of the pyrrol, giving rise to highly porous structures. Cells were built with amounts of GDs ranging between 3% and 30%. Performance was best with 10%. The efficiency reached 5.27%, which is 20% more than when the pure PPy counterelectrode was used and is lower than when the electrode was Pt (efficiencies 4.46% and 6.02%, respectively). The amount of GD had to be finely tuned since increasing concentrations at low values increased the  $J_{sc}$  and the FF by reducing the internal resistance and enhancing charge transfer, whereas higher doping rates increased the charge recombination at the counterelectrode resulting in lower  $J_{sc}$  and  $V_{oc}$  values [44].

#### 4.3. Hole Collector

GDs such as HTL have been added to silicon solar cells and polymer solar cells because of their excellent charge transport properties and transparency. Since the fabrication of large area graphene sheets involves complicated deposition and transfer processes, research has also focused on solution processed GDs. Recently, Gao and coworkers reported the structure In-Ga/c-Si/GD/Au in which dots were prepared from graphene sheets with final sizes ranging between 2 and 6 nm. Epoxy, carboxyl and other oxygenous functional groups have been detected in the edges. c-Si was also passivated to improve the interaction between the two materials. Of all the options the methyl group showed the best results due to the reduction of surface carrier recombination. The diodes were prepared in air by solution processing and gave an efficiency of 6.63% which is higher than the 2.26% obtained without GDs. The dots increased  $J_{sc}$  and  $V_{oc}$  because the current leakage reduced after recombination was suppressed at the anode. Although the GDs show strong absorption in the UV, the contribution to the  $J_{sc}$  could not be observed when the EQE was measured [42]. Moreover, the addition of GDs resulted in good stability of the c-Si/GDs cells after storage for half a year. Tsai et al. added an extra layer of PEDOT:PSS and GDs to micro-structured amorphous silicon heterojunctions leading to the configuration Al/a-Si/PEDOT:PSS-GDs/Ag. The dots, prepared by microwave methods, measured 2.9 nm, roughly 12 layers of graphene. The  $J_{sc}$  and FF of the diodes increased with increasing concentrations of GDs up to 0.5%, at which point the efficiency started to decline because of increased recombination reactions probably arising from the formation of GD aggregates. Therefore, a record performance of 13.22% was achieved due to the contribution of the GDs to light harvesting below 400 nm and the improvement in conductivity and the subsequent carrier collection efficiency [41].

Searching for enhanced stability and lifetime, Li and colleagues used GDs in polymer solar cells to substitute the hygroscopic PEDOT:PSS in the configuration ITO/GDs/P3HT:PCBM/LiF/Al. The dots were created by acid treatment of carbon fibers. Optimization of the HTL thickness between 1.5 and 2 nm resulted in devices that had efficiency values similar to those of the cells prepared with PEDOT:PSS, 3.5%, due to the homogeneous morphology and good conductivity of the GDs. Moreover, measurements of efficiency in air showed that decay was slower when GDs were used. The same experiments performed on small molecule solar cells based on DR3TBDT:PC71BM gave efficiencies similar to PEDOT:PSS containing devices (6.9% efficiency), thus demonstrating the capability of GDs to act as a hole collector [50].

#### 4.4. Electron Collector

Perovskite-based solar cells have recently attracted the research community because of their broad spectral absorption and conducting properties. These molecules have been applied in planar and mesoscopic heterojunctions and have shown efficiencies over 22% [3,71]. Meanwhile, GDs have shown ultrafast hot-electron extraction faster than 15 fs through the GDs-TiO<sub>2</sub> interface [72], although their application in DSSC has given low efficiencies. However, to further improve performance, Zhu et al. inserted an ultrathin layer of GDs between the perovskite and the titania layer in the configuration FTO/TiO<sub>2</sub> dense/TiO<sub>2</sub> mesoporous/CH<sub>3</sub>NH<sub>3</sub>PbI<sub>3</sub>/GDs/spiro-OMeTAD/Au (Figure 7). The dots, prepared by electrochemical methods, measured between 5 and 10 nm and were homogeneously distributed onto the titania layer. Optimization of the thin layer thickness led to efficiencies of 10.15%,

which is higher than the 8.81% reported for the reference cell without GDs. Whereas the FF and Voc showed values similar to the reference, the Jsc increased due to faster charge extraction. Involvement of the GDs in light harvesting was discarded since the strong absorption of the perovskite dominates absorption and no contribution from the GDs could be detected [38].

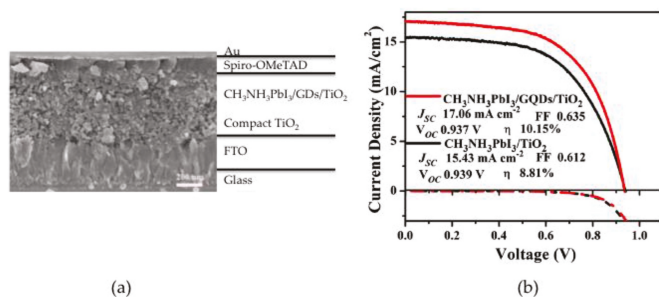


**Figure 7.** (a) Cross-sectional view of the SEM image; (b) JV curve of the devices comparing the effect of the insertion of the GDs. Reproduced with permission of [38].

## 5. Carbon Dots in Photovoltaics

The light harvesting abilities and conducting properties of carbon dots have prompted researchers to use them in a variety of roles in solar cells.

### 5.1. Light Harvesting

The spectral absorption features of the carbon dots in the ultraviolet region have led to their application as single absorbers in several photovoltaic cells. Briscoe and co-workers studied the construction of low-cost sustainable structured cells making use of carbon dots (CDs) obtained from biomass. They prepared the dots by hydrothermal carbonization of chitin, chitosan or glucose which led to samples with features that reflected the parent reactant. Thus, chitin and chitosan led to N-doped CDs (10% and 8% doping, respectively). The surface was functionalized by amides if chitin was used, amines if chitosan was used and hydroxyl if glucose was used. The differences remained during deposition onto ZnO nanorods because the best coverages were obtained with chitosan and glucose. Finally, CuSCN was added as HTL giving rise to the cell configuration FTO/ZnO nanorod/CDs/CuSCN/Au. Efficiencies were best (0.061%) with chitosan-derived CDs. It was observed that the nature of the precursor and surface functionalization heavily influences the performance of the diodes. For further optimization, the authors combined two types of CD to merge their best properties and increase optical absorption. However, the combination needed to be done with great care to prevent the series resistance from increasing and the Jsc from decreasing. Therefore, results were best with a combination of chitosan and chitin-derived carbon dots, for which efficiency was 0.077 [29].

Mirtchev et al. explored CD- DSSC with mesoporous titania. The dots were prepared by dehydration of  $\gamma$ -butyrolactone and contained sulfonate, carboxylate and hydroxyl groups on the surface, thus mimicking the anchoring groups of common Ru-based sensitizers. The device was built by immersing titania in CD solution for 48 h and was completed with  $I_3^-/I^-$  as HTL to give the structure FTO/TiO<sub>2</sub>/CDs/I<sub>3</sub><sup>-</sup>/I<sup>-</sup>/P [22]. In comparison with typical Ru-sensitizers, Jsc is the factor that limits better efficiencies because of the emissive trap sites on the surface of the dot that could act as recombination centers and because of the lower capacity of the dot to inject charges into TiO<sub>2</sub>. The authors suggested maximizing the titania surface coverage by using smaller dots or bifunctional linker molecules to enhance the efficiency [22]. Sun et al. used a similar device configuration with titania nanotubes. The dots were prepared by electrochemical-etching methods and

added to the nanotubes by impregnation for several hours. Assembly between the small dots and the titania was possible through the oxygen functional groups present on the surface of the carbon material. The device, which has a low efficiency of 0.0041%, served as proof-of-concept of the light harvesting properties of the CDs. The authors expected that optimizing the electrolyte and the electrodes would give better results [28].

Zhang et al. developed hierarchical microspheres of rutile built by uniform nanorods to prepare solar cells made of metal-free sensitizers. They synthesized nitrogen-doped carbon dots (NCDs) by one-pot solvothermal methods and anchor them to the rutile structures by means of the surface groups. The configuration of the cell was  $\text{TiO}_2/\text{NCDs}/\text{I}_3^-/\text{I}^-/\text{Pt}$  and the  $J_{sc}$  values were higher than those of similar devices prepared without NCDs. The final efficiency was 0.13% [25].

CDs have also been applied in nanostructured silicon solar cells. Xie et al. intended to broaden the absorption range of the silicon nanowires (Si nw) by creating core/shell heterojunctions with carbon dots. The nanoparticles were synthesized by electrochemical etching methods and added to the silicon wires to form a homogeneous and continuous shell of 23 nm corresponding to 5 layers of dots. The overall structure of the device was In-Ga/Si nw/CD/Au and reached an efficiency of 9.1% which is much higher than the references prepared with planar silicon and five layers of CDs (4.05%) or silicon nanowires without CDs (1.58%) [30]. The reasons for the enhanced performance of the device were the increase in optical absorption in the UV region and the fact that recombination was lower because of the electron blocking layer action of the CDs (Figure 8).

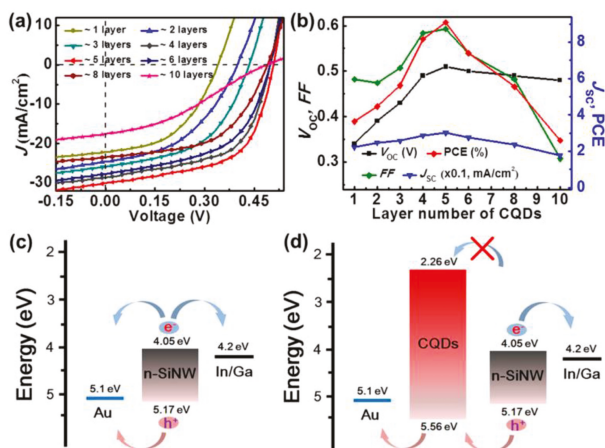


**Figure 8.** Variation of the JV curve (a) and cell parameters (b) with increasing layers of CDs; Energy level alignments of the cells without (c) and with (d) CDs. Reproduced with permission of [30].

An innovative approach has recently been reported by Huang et al. who prepared composites of CDs and polysiloxane to coat the substrate of the solar cells, which had the configuration CD-polysiloxane/ITO/ZnO/P3HT:PCBM/MoO<sub>3</sub>/Ag [31]. The dots were prepared by a one-step reaction with ascorbic acid as the carbon source and KH791 as the stabilizing and passivating agent and source of the siloxane polymer. The composite contributed to light harvesting in the UV part of the spectrum and increased the efficiency by about 12% compared to the polymer:fullerene solar cell (3.18% and 2.85%, respectively). Similar observations are reported by Liu et al. who added increasing amounts of CDs to the active layer in the cell configuration ITO/TiO<sub>2</sub>/PCDTBT:PCBM:CDs/MoO<sub>3</sub>/Ag. The increase in absorption in the UV region, together with the improvement in charge transport resulted in enhanced FF and  $J_{sc}$  when 0.062 wt. % ratio was used leading to efficiencies of 7.05% [26].



### 5.2. Counterelectrode

Dao et al. studied different options for the counterelectrode (CE) component of quantum dot solar cells looking for lower resistance and higher reduction rates of the redox electrolyte. They compared sputtered gold, CDs and CD-containing gold particles in the ZnO nanowire/CdS/CdSe/polysulfide electrolyte/CE configuration. The Cd-Au structures were formed by a dense array of gold rods covered by small 1.2 nm CDs in a 200 nm wide raspberry-like superstructure. When applied as the CE, they showed enhanced redox activity toward the polysulfide electrolyte that increased the efficiency to 5.4% whereas CDs and the sputtered gold gave efficiencies of 0.18 and 3.6%, respectively. These results are explained by the larger surface area of the Au-CD structures and the reduced internal charge transfer resistance of the material that contributed to the increment of  $J_{sc}$  and the FF [27].

### 5.3. Hole Collection

CDs have also been tested in the charge transport layers of perovskite solar cells as alternatives to the expensive hole transporter spiro-OMeTAD in the configuration FTO/TiO<sub>2</sub> dense/TiO<sub>2</sub> mesoporous/CH<sub>3</sub>NH<sub>3</sub>PbI<sub>3-x</sub>Cl<sub>x</sub>/CDs/Au [35]. The dots were prepared by polymerization-carbonization of citric acid using p-phenylenediamine as passivating agent and deposited by solution processing onto the perovskite layer. The resulting devices performed better than the control without HTL, although  $J_{sc}$ ,  $V_{oc}$  and FF values were lower than those of the spiro-OMeTAD device. The poorer performance (3% vs. 8% efficiencies for the CDs and the spiro-OMeTAD-containing devices, respectively) was attributed to non-optimized device fabrication.

### 5.4. Electron Collection

The potential contribution of CDs to the charge transport in the solar cells led to the nanocrystals being used as electron acceptors. Kwon and coworkers tested oleylamine-capped CDs in combination with the electron donor P3HT to form the structure ITO/PEDOT:PSS/P3HT:CDs/Al [32]. Compared to the 1.99% efficiency of the P3HT/PCBM reference, the 0.23% obtained points to the insulating character of oleylamine as the origin of the lower  $J_{sc}$  values. Zhang et al. in addition, worked on organic solar cells and tested the ability of the CDs as electron acceptors. They prepared the configuration ITO/PEDOT:PSS/DR3TBDT:PC71BM/ETL/Al (ETL: electron transport layer) and observed that the efficiency of the devices increased to 7.67% when CDs replaced the widely used LiF in the ETL. In addition, extended lifetimes due to the air stability of the dots were also reported. When the small molecular light harvesters were replaced by P3HT:PCBM, the efficiency was also higher when CDs were used instead of LiF (3.42% vs. 3.38%, respectively) [23]. The improvement was attributed in both cases to the balance of the charge transport by decreasing the series resistance and increasing the shunt resistance resulting in the increase of charge collection.

Another strategy for enhancing the charge transport is to combine CDs with electron acceptor molecules. Narayanan et al. described a device made of quantum dots ZnS/CdS/ZnS, which act as an exciton generator, and the small molecule CuPc as an electron acceptor (Figure 9). The quantum dots absorbed light in the blue-green region of the spectrum and transferred the energy via Förster resonance to the red absorber phthalocyanine. The addition of the CDs to the heterojunction accelerated the charge transfer towards the electrode and decreased the electron recombination rate, which was reflected in the increase in IPCE. Thus, the resulting  $J_{sc}$  was 5.76 times higher than the reference prepared without CDs.  $V_{oc}$  was also enhanced, and the efficiency increased to 0.35%. The carbon nanocrystals measured 16 nm and were closely connected to CDs and CuPc, as observed by HRTEM [33].



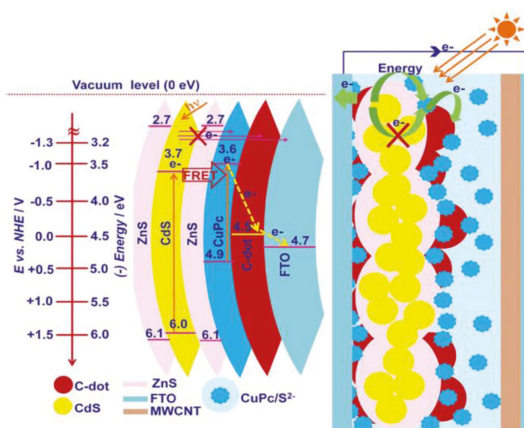


**Figure 9.** Energy band diagram showing possible paths for energy and charge transport and structure of the FTO/ZnS-CdS-ZnS/CDs/CuPc/S<sup>2-</sup>/MWCNT devices. Reproduced with permission of [33].

Similar results were observed by Ma et al. when they added CDs to titania functionalized with the rhodamine B sensitizer in the system FTO/TiO<sub>2</sub>/RhB/CQD/I<sub>3</sub><sup>-</sup>/I<sup>-</sup>/Pt [34]. The combination of the dots with rhodamine increased light harvesting in the UV region and suppressed electron recombination leading to 0.147% efficiency. Therefore, electrochemically generated CDs were responsible for the 7-fold increase in the J<sub>sc</sub>.

## 6. Outlook and Perspectives

Carbon-based materials are an exciting challenge in the area of materials chemistry and nanotechnology. Needless to say, they are abundant and they are also inert, non-toxic and, when scaled-up, cost effective. However, at present their applications are limited due to the numerous physical and chemical phenomena that are still unexplored. This review aimed to give a general overview of the enormous potential graphene and carbon dots have in photovoltaic applications. There are, of course, more applications, but the ones discussed here will help researchers interested in exploring the boundaries of graphene and carbon nanoform research.

For instance, the absorption ability of the carbon nanostructures in the UV region complements light harvesting in those cells where absorption is confined to the visible region. The increased number of captured photons leads to the boost of the IPCE and the J<sub>sc</sub>. On the other hand, their redox characteristics accelerate charge transfer from the absorber to the electrode. Therefore, electron recombination diminishes whereas Voc increases. These beneficial effects are influenced by the synthetic approach, which determines the size of the particles and the functional groups found on the surface and edges of the crystals. These groups have a major influence on the optical properties and the interactions with the materials of which the devices are made. In this regard, some authors have investigated on the addition of specific functionalities to enhance the interaction between the dots and other components of the device. However, the synthetic variability hinders reproducibility and affects the efficiency. The examples reported in this review highlight the need for further optimization of the structure and linkage; so consequently, the size and surface molecules need to be fine tuned if efficient devices are to be prepared. Nonetheless, these materials are expected to play an important role in energy-harvesting devices that help to decrease CO<sub>2</sub> emissions and lower the cost of renewable energy.

**Acknowledgments:** E.M.F. thanks Spanish MINECO for funding through the Ramon y Cajal fellowship RYC-2010-06787 and project MAT2012-31570. SP acknowledges financial support from ICIQ and EURECAT. EP would like to thank AGAUR for the SGR-2014-763 grant, as well as the Spanish MINECO for the SEVERO OCHOA Excellence Accreditation 2014.20188SEV-2013-0319 and the CTQ2013-47183-R project.

**Author Contributions:** All the authors contributed to the preparation of the manuscript.

**Conflicts of Interest:** The authors declare no conflict of interest. The founding sponsors had no role in the design of the study; in the collection, analyses, or interpretation of data; in the writing of the manuscript, or in the decision to publish the results.

## Abbreviations

The following abbreviations are used in this manuscript:

AFM	Atomic force microscope
AZO	Aluminum-doped zinc oxide
CDs	Carbon quantum dots
DSSC	Dye-sensitised solar cells
DR3TBDT	3-ethyl rhodanine benzo[1,2-b:4,5-b']dithiophene
ETL	Electron transport layer
GDs	Graphene dots
HTL	Hole transport layer
HRTEM	High resolution transmission electron microscopy
KH791	(N-(2-aminoethyl)-3-aminopropyl)tris-(2-ethoxy) silane
N719	Di-tetrabutylammonium cis-bis(isothiocyanato) bis (2,2'-bipyridyl -4,4'- dicarboxylato) ruthenium(II)
N3	Cis-Bis(isothiocyanato) bis(2,2'-bipyridyl-4,4'-dicarboxylato ruthenium(II)
MWCNT	Multiwall carbon nanotubes
NCDs	Nitrogen-doped carbon dots
OSC	Organic solar cells
P3HT	Poly(3-hexyl thiophene)
PEDOT:PSS	Poly(3,4-ethylenedioxythiophene) polystyrene sulfonate
PCBM	[6,6]-phenyl-C61-butyric acid methyl ester
PfBT4T-2OD	Poly [(5,6-difluoro-2,1,3-benzothiadiazol-4,7-diyl)-alt-(3,3'''-di (2-octyldodecyl)-2, 2'; 5', 2''; 5'', 2'''-quaterthiophen-5,5'''-diyl)
Ppy	Polypyrrol
PSC	Polymer solar cell
SMOPV	Small molecule organic photovoltaics
TC71BM	[6,6]-2-Thienyl-C71-butyric acid methyl ester
TPD	NN'-diphenyl-N-N'-bis(3-methylphenyl)-1,1'-biphenyl)-4,4'-diamine
Spiro-OMeTAD	N2,N2,N2',N2',N7,N7',N7',N7'-octakis(4-methoxyphenyl)-9,9'-spiro bi[9H-fluorene]-2,2',7,7'-tetramine

## References

1. Armaroli, N.; Balzani, V. Solar Electricity and Solar Fuels: Status and Perspectives in the Context of the Energy Transition. *Chem. A Eur. J.* **2016**, *22*, 32–57. [CrossRef] [PubMed]
2. Green, M.A.; Emery, K.; Hishikawa, Y.; Warta, W.; Dunlop, E.D. Solar cell efficiency tables (version 47). *Prog. Photovolt. Res. Appl.* **2016**, *24*, 3–11. [CrossRef]
3. National Center for Photovoltaics. Available online: <http://www.nrel.gov/ncpv/> (accessed on 23 August 2016).
4. Albero, J.; Clifford, J.N.; Palomares, E. Quantum dot based molecular solar cells. *Coord. Chem. Rev.* **2014**, *263–264*, 53–64. [CrossRef]
5. Medintz, I.L.; Uyeda, H.T.; Goldman, E.R.; Mattoussi, H. Quantum dot bioconjugates for imaging, labelling and sensing. *Nat. Mater.* **2005**, *4*, 435–446. [CrossRef] [PubMed]
6. Nurmikko, A. What future for quantum dot-based light emitters? *Nat. Nanotechnol.* **2015**, *10*, 1001–1004. [CrossRef] [PubMed]
7. Xu, X.; Ray, R.; Gu, Y.; Ploehn, H.J.; Gearheart, L.; Raker, K.; Scrivens, W.A. Electrophoretic analysis and purification of fluorescent single-walled carbon nanotube fragments. *J. Am. Chem. Soc.* **2004**, *126*, 12736–12737. [CrossRef] [PubMed]

8. Sun, Y.P.; Zhou, B.; Lin, Y.; Wang, W.; Fernando, K.A.S.; Pathak, P.; Meziani, M.J.; Harruff, B.A.; Wang, X.; Wang, H.; et al. Quantum-sized carbon dots for bright and colorful photoluminescence. *J. Am. Chem. Soc.* **2006**, *128*, 7756–7757. [CrossRef] [PubMed]
9. Novoselov, K.S.; Geim, A.K.; Morozov, S.V.; Jiang, D.; Zhang, Y.; Dubonos, S.V.; Grigorieva, I.V.; Firsov, A.A. Electric Field Effect in Atomically Thin Carbon Films. *Science* **2011**, *306*, 666–669. [CrossRef] [PubMed]
10. Ding, C.; Zhu, A.; Tian, Y. Functional surface engineering of C-dots for fluorescent biosensing and in vivo bioimaging. *Acc. Chem. Res.* **2014**, *47*, 20–30. [CrossRef] [PubMed]
11. Li, H.; Kang, Z.; Liu, Y.; Lee, S.-T. Carbon nanodots: Synthesis, properties and applications. *J. Mater. Chem.* **2012**, *22*, 24230–24253. [CrossRef]
12. Zheng, X.T.; Ananthanarayanan, A.; Luo, K.Q.; Chen, P. Glowing graphene quantum dots and carbon dots: Properties, syntheses, and biological applications. *Small* **2015**, *11*, 1620–1636. [CrossRef] [PubMed]
13. Baker, S.N.; Baker, G.A. Luminescent carbon nanodots: Emergent nanolights. *Angew. Chem. Int. Ed.* **2010**, *49*, 6726–6744. [CrossRef] [PubMed]
14. Shen, J.; Zhu, Y.; Yang, X.; Li, C. Graphene quantum dots: Emergent nanolights for bioimaging, sensors, catalysis and photovoltaic devices. *Chem. Commun.* **2012**, *48*, 3686–3699. [CrossRef] [PubMed]
15. Ding, H.; Yu, S.-B.; Wei, J.-S.; Xiong, H.-M. Full-Color Light-Emitting Carbon Dots with a Surface-State-Controlled Luminescence Mechanism. *ACS Nano* **2015**, *10*, 484–491. [CrossRef] [PubMed]
16. Wang, Y.; Hu, A. Carbon quantum dots: Synthesis, properties and applications. *J. Mater. Chem. C* **2014**, *2*, 6921–6939. [CrossRef]
17. Li, X.M.; Rui, M.C.; Song, J.Z.; Shen, Z.H.; Zeng, H.B.; Li, X.M.; Rui, M.C.; Song, J.Z.; Shen, Z.H.; Zeng, H.B. Carbon and Graphene Quantum Dots for Optoelectronic and Energy Devices: A Review. *Adv. Funct. Mater.* **2015**, *25*, 4929–4947. [CrossRef]
18. Zhang, Z.; Zhang, J.; Chen, N.; Qu, L. Graphene quantum dots: An emerging material for energy-related applications and beyond. *Energy Environ. Sci.* **2012**, *5*, 8869–8890. [CrossRef]
19. Miao, P.; Han, K.; Tang, Y.; Wang, B.; Lin, T.; Cheng, W. Recent advances in carbon nanodots: Synthesis, properties and biomedical applications. *Nanoscale* **2015**, *7*, 1586–1595. [CrossRef] [PubMed]
20. Fan, Z.; Li, S.; Yuan, F.; Fan, L. Fluorescent graphene quantum dots for biosensing and bioimaging. *RSC Adv.* **2015**, *5*, 19773–19789. [CrossRef]
21. Van Pham, C.; Madsuha, A.F.; Nguyen, T.V.; Krueger, M. Graphene-quantum dot hybrid materials on the road to optoelectronic applications. *Synth. Met.* **2016**, *219*, 33–43. [CrossRef]
22. Mirtchev, P.; Henderson, E.J.; Soheilnia, N.; Yip, C.M.; Ozin, G.A. Solution phase synthesis of carbon quantum dots as sensitizers for nanocrystalline TiO<sub>2</sub> solar cells. *J. Mater. Chem.* **2012**, *22*, 1265–1269. [CrossRef]
23. Zhang, H.; Zhang, Q.; Li, M.; Kan, B.; Ni, W.; Wang, Y.; Yang, X.; Du, C.; Bc, X.W.; Chen, Y. Investigation of the enhanced performance and lifetime of organic solar cells using solution-processed carbon dots as the electron transport layers. *J. Mater. Chem. C* **2015**, *3*, 12403–12409. [CrossRef]
24. Zhang, Y.-Q.; Ma, D.-K.; Zhuang, Y.; Zhang, X.; Chen, W.; Hong, L.-L.; Yan, Q.-X.; Yu, K.; Huang, S.-M. One-pot synthesis of N-doped carbon dots with tunable luminescence properties. *J. Mater. Chem.* **2012**, *22*, 16714–16718. [CrossRef]
25. Zhang, Y.Q.; Ma, D.K.; Zhang, Y.G.; Chen, W.; Huang, S.M. N-doped carbon quantum dots for TiO<sub>2</sub>-based photocatalysts and dye-sensitized solar cells. *Nano Energy* **2013**, *2*, 545–552. [CrossRef]
26. Liu, C.; Chang, K.; Guo, W.; Li, H.; Shen, L.; Chen, W.; Yan, D. Improving charge transport property and energy transfer with carbon quantum dots in inverted polymer solar cells. *Appl. Phys. Lett.* **2014**, *105*, 073306. [CrossRef]
27. Dao, V.D.; Kim, P.; Baek, S.; Larina, L.L.; Yong, K.; Ryoo, R.; Ko, S.H.; Choi, H.S. Facile synthesis of carbon dot-Au nanoraspberries and their application as high-performance counter electrodes in quantum dot-sensitized solar cells. *Carbon* **2016**, *96*, 139–144. [CrossRef]
28. Sun, M.; Ma, X.; Chen, X.; Sun, Y.; Cui, X.; Lin, Y. A nanocomposite of carbon quantum dots and TiO<sub>2</sub> nanotube arrays: Enhancing photoelectrochemical and photocatalytic properties. *RSC Adv.* **2014**, *4*, 1120–1127. [CrossRef]
29. Briscoe, J.; Marinovic, A.; Sevilla, M.; Dunn, S.; Titirici, M. Biomass-Derived Carbon Quantum Dot Sensitizers for Solid-State Nanostructured Solar Cells. *Angew. Chem. Int. Ed.* **2015**, *54*, 4463–4468. [CrossRef] [PubMed]

30. Xie, C.; Nie, B.; Zeng, L.; Liang, F.X.; Wang, M.Z.; Luo, L.; Feng, M.; Yu, Y.; Wu, C.Y.; Wu, Y.; et al. Core-shell heterojunction of silicon nanowire arrays and carbon quantum dots for photovoltaic devices and self-driven photodetectors. *ACS Nano* **2014**, *8*, 4015–4022. [CrossRef] [PubMed]
31. Huang, J.J.; Zhong, Z.F.; Rong, M.Z.; Zhou, X.; Chen, X.D.; Zhang, M.Q. An easy approach of preparing strongly luminescent carbon dots and their polymer based composites for enhancing solar cell efficiency. *Carbon* **2014**, *70*, 190–198. [CrossRef]
32. Kwon, W.; Lee, G.; Do, S.; Joo, T.; Rhee, S.W. Size-controlled soft-template synthesis of carbon nanodots toward versatile photoactive materials. *Small* **2014**, *10*, 506–513. [CrossRef] [PubMed]
33. Narayanan, R.; Deepa, M.; Srivastava, A.K. Forster resonance energy transfer and carbon dots enhance light harvesting in a solid-state quantum dot solar cell. *J. Mater. Chem. A* **2013**, *1*, 3907–3918. [CrossRef]
34. Ma, Z.; Zhang, Y.L.; Wang, L.; Ming, H.; Li, H.; Zhang, X.; Wang, F.; Liu, Y.; Kang, Z.; Lee, S.T. Bioinspired photoelectric conversion system based on carbon-quantum-dot-doped dye-semiconductor complex. *ACS Appl. Mater. Interfaces* **2013**, *5*, 5080–5084. [CrossRef] [PubMed]
35. Paulo, S.; Stoica, G.; Cambarau, W.; Martinez-Ferrero, E.; Palomares, E. Carbon quantum dots as new hole transport material for perovskite solar cells. *Synth. Met.* **2016**. [CrossRef]
36. Yan, X.; Cui, X.; Li, B.; Li, L.S. Large, solution-processable graphene quantum dots as light absorbers for photovoltaics. *Nano Lett.* **2010**, *10*, 1869–1873. [CrossRef] [PubMed]
37. Tsai, M.-L.; Tu, W.-C.; Tang, L.; Wei, T.-C.; Wei, W.-R.; Lau, S.P.; Chen, L.-J.; He, J.-H. Efficiency Enhancement of Silicon Heterojunction Solar Cells via Photon Management Using Graphene Quantum Dot as Downconverters. *Nano Lett.* **2016**, *16*, 309–313. [CrossRef] [PubMed]
38. Zhu, Z.; Ma, J.; Wang, Z.; Mu, C.; Fan, Z.; Du, L.; Bai, Y.; Fan, L.; Yan, H.; Phillips, D.L.; et al. Efficiency enhancement of perovskite solar cells through fast electron extraction: The role of graphene quantum dots. *J. Am. Chem. Soc.* **2014**, *136*, 3760–3763. [CrossRef] [PubMed]
39. Li, Y.; Hu, Y.; Zhao, Y.; Shi, G.; Deng, L.; Hou, Y.; Qu, L. An electrochemical avenue to green-luminescent graphene quantum dots as potential electron-acceptors for photovoltaics. *Adv. Mater.* **2011**, *23*, 776–780. [CrossRef] [PubMed]
40. Dutta, M.; Sarkar, S.; Ghosh, T.; Basak, D. ZnO/graphene quantum dot solid-state solar cell. *J. Phys. Chem. C* **2012**, *116*, 20127–20131. [CrossRef]
41. Tsai, M.-L.; Wei, W.-R.; Tang, L.; Chang, H.-C.; Tai, S.-H.; Yang, P.-K.; Lau, S.P.; Chen, L.-J.; He, J.-H. 13% Efficiency Si Hybrid Solar Cells via Concurrent Improvement in Optical and Electrical Properties by Employing Graphene Quantum Dots. *ACS Nano* **2016**, *10*, 815–821. [CrossRef] [PubMed]
42. Gao, P.; Ding, K.; Wang, Y.; Ruan, K.; Diao, S.; Zhang, Q.; Sun, B.; Jie, J. Crystalline Si/graphene quantum dots heterojunction solar cells. *J. Phys. Chem. C* **2014**, *118*, 5164–5171. [CrossRef]
43. Pan, D.; Zhang, J.; Li, Z.; Wu, M. Hydrothermal route for cutting graphene sheets into blue-luminescent graphene quantum dots. *Adv. Mater.* **2010**, *22*, 734–738. [CrossRef] [PubMed]
44. Chen, L.; Guo, C.X.; Zhang, Q.; Lei, Y.; Xie, J.; Ee, S.; Guai, G.; Song, Q.; Li, C.M. Graphene quantum-dot-doped polypyrrole counter electrode for high-performance dye-sensitized solar cells. *ACS Appl. Mater. Interfaces* **2013**, *5*, 2047–2052. [CrossRef] [PubMed]
45. Kim, J.K.; Park, M.J.; Kim, S.J.; Wang, D.H.; Cho, S.P.; Bae, S.; Park, J.H.; Hong, B.H. Balancing light absorptivity and carrier conductivity of graphene quantum dots for high-efficiency bulk heterojunction solar cells. *ACS Nano* **2013**, *7*, 7207–7212. [CrossRef] [PubMed]
46. Gupta, V.; Chaudhary, N.; Srivastava, R.; Sharma, G.D.; Bhardwaj, R.; Chand, S. Luminescent graphene quantum dots for organic photovoltaic devices. *J. Am. Chem. Soc.* **2011**, *133*, 9960–9963. [CrossRef] [PubMed]
47. Fang, X.; Li, M.; Guo, K.; Li, J.; Pan, M.; Bai, L.; Luoshan, M.; Zhao, X. Graphene quantum dots optimization of dye-sensitized solar cells. *Electrochim. Acta* **2014**, *137*, 634–638. [CrossRef]
48. Mihalache, I.; Radoi, A.; Mihaila, M.; Munteanu, C.; Marin, A.; Danila, M.; Kusko, M.; Kusko, C. Charge and energy transfer interplay in hybrid sensitized solar cells mediated by graphene quantum dots. *Electrochim. Acta* **2015**, *153*, 306–315. [CrossRef]
49. Peng, J.; Gao, W.; Gupta, B.K.; Liu, Z.; Romero-Aburto, R.; Ge, L.; Song, L.; Alemany, L.B.; Zhan, X.; Gao, G.; et al. Graphene quantum dots derived from carbon fibers. *Nano Lett.* **2012**, *12*, 844–849. [CrossRef] [PubMed]

50. Li, M.; Ni, W.; Kan, B.; Wan, X.; Zhang, L.; Zhang, Q.; Long, G.; Zuo, Y.; Chen, Y. Graphene quantum dots as the hole transport layer material for high-performance organic solar cells. *Phys. Chem. Chem. Phys.* **2013**, *15*, 18973–18978. [CrossRef] [PubMed]
51. Li, L.; Wu, G.; Yang, G.; Peng, J.; Zhao, J.; Zhu, J.-J. Focusing on luminescent graphene quantum dots: Current status and future perspectives. *Nanoscale* **2013**, *5*, 4015–4039. [CrossRef] [PubMed]
52. Low, C.T.J.; Walsh, F.C.; Chakrabarti, M.H.; Hashim, M.A.; Hussain, M.A. Electrochemical approaches to the production of graphene flakes and their potential applications. *Carbon* **2013**, *54*, 1–21. [CrossRef]
53. Zhang, M.; Bai, L.; Shang, W.; Xie, W.; Ma, H.; Fu, Y.; Fang, D.; Sun, H.; Fan, L.; Han, M.; et al. Facile synthesis of water-soluble, highly fluorescent graphene quantum dots as a robust biological label for stem cells. *J. Mater. Chem.* **2012**, *22*, 7461–7467. [CrossRef]
54. Sk, M.A.; Ananthanarayanan, A.; Huang, L.; Lim, K.H.; Chen, P. Revealing the tunable photoluminescence properties of graphene quantum dots. *J. Mater. Chem. C* **2014**, *2*, 6954–6960. [CrossRef]
55. Song, Y.; Zhu, S.; Yang, B. Bioimaging based on fluorescent carbon dots. *RSC Adv.* **2014**, *4*, 27184–27200. [CrossRef]
56. Gan, Z.; Xiong, S.; Wu, X.; Xu, T.; Zhu, X.; Gan, X.; Guo, J.; Shen, J.; Sun, L.; Chu, P.K. Mechanism of photoluminescence from chemically derived graphene oxide: Role of chemical reduction. *Adv. Opt. Mater.* **2013**, *1*, 926–932. [CrossRef]
57. Hong, G.; Diao, S.; Antaris, A.L.; Dai, H. Carbon Nanomaterials for Biological Imaging and Nanomedicinal Therapy. *Chem. Rev.* **2015**, *115*, 10816–10906. [CrossRef] [PubMed]
58. Gan, Z.; Xu, H.; Hao, Y. Mechanism for excitation-dependent photoluminescence from graphene quantum dots and other graphene oxide derivatives: Consensus, debates and challenges. *Nanoscale* **2016**, *7*, 7794–7807. [CrossRef] [PubMed]
59. Ritter, K.A.; Lyding, J.W. The influence of edge structure on the electronic properties of graphene quantum dots and nanoribbons. *Nat. Mater.* **2009**, *8*, 235–242. [CrossRef] [PubMed]
60. Xie, C.; Zhang, X.; Wu, Y.; Zhang, X.; Zhang, X.; Wang, Y.; Zhang, W.; Gao, P.; Han, Y.; Jie, J. Surface passivation and band engineering: A way toward high efficiency graphene-planar Si solar cells. *J. Mater. Chem. A* **2013**, *1*, 8567–8574. [CrossRef]
61. Clifford, J.N.; Martínez-Ferrero, E.; Viterisi, A.; Palomares, E. Sensitizer molecular structure-device efficiency relationship in dye sensitized solar cells. *Chem. Soc. Rev.* **2011**, *40*, 1635–1646. [CrossRef] [PubMed]
62. O'Regan, B.; Grätzel, M. A low-cost, high-efficiency solar cell based on dye-sensitized colloidal TiO<sub>2</sub> films. *Nature* **1991**, *353*, 737–740. [CrossRef]
63. Mathew, S.; Yella, A.; Gao, P.; Humphry-Baker, R.; Curchod, B.F.E.; Ashari-Astani, N.; Tavernelli, I.; Rothlisberger, U.; Khaja, N.; Grätzel, M. Dye-sensitized solar cells with 13% efficiency achieved through the molecular engineering of porphyrin sensitizers. *Nat. Chem.* **2014**, *6*, 242–247. [CrossRef] [PubMed]
64. Weickert, J.; Dunbar, R.B.; Hesse, H.C.; Wiedemann, W.; Schmidt-Mende, L. Nanostructured organic and hybrid solar cells. *Adv. Mater.* **2011**, *23*, 1810–1828. [CrossRef] [PubMed]
65. Brabec, C.J.; Heeney, M.; McCulloch, I.; Nelson, J. Influence of blend microstructure on bulk heterojunction organic photovoltaic performance. *Chem. Soc. Rev.* **2011**, *40*, 1185–1199. [CrossRef] [PubMed]
66. Lu, L.; Zheng, T.; Wu, Q.; Schneider, A.M.; Zhao, D.; Yu, L. Recent Advances in Bulk Heterojunction Polymer Solar Cells. *Chem. Rev.* **2015**, *115*, 12666–12731. [CrossRef] [PubMed]
67. Liu, Y.; Zhao, J.; Li, Z.; Mu, C.; Ma, W.; Hu, H.; Jiang, K.; Lin, H.; Ade, H.; Yan, H. Aggregation and morphology control enables multiple cases of high-efficiency polymer solar cells. *Nat. Commun.* **2014**, *5*, 5293. [CrossRef] [PubMed]
68. Zhao, J.; Li, Y.; Yang, G.; Jiang, K.; Lin, H.; Ade, H.; Ma, W.; Yan, H. Efficient organic solar cells processed from hydrocarbon solvents. *Nat. Energy* **2016**, *1*, 15027. [CrossRef]
69. Zhao, W.; Qian, D.; Zhang, S.; Li, S.; Inganäs, O.; Gao, F.; Hou, J. Fullerene-Free Polymer Solar Cells with over 11% Efficiency and Excellent Thermal Stability. *Adv. Mater.* **2016**, *28*, 4737–4739. [CrossRef] [PubMed]
70. Wang, H.; Hu, Y.H. Graphene as a counter electrode material for dye-sensitized solar cells. *Energy Environ. Sci.* **2012**, *5*, 8182–8188. [CrossRef]

71. Yang, W.S.; Noh, J.H.; Jeon, N.J.; Kim, Y.C.; Ryu, S.; Seo, J.; Seok, S., II. High-performance photovoltaic perovskite layers fabricated through intramolecular exchange. *Science* **2015**, *348*, 1234–1237. [CrossRef] [PubMed]
72. Williams, K.J.; Nelson, C.A.; Yan, X.; Li, L.-S.; Zhu, X. Hot Electron Injection from Graphene Quantum Dots to TiO<sub>2</sub>. *ACS Nano* **2013**, *7*, 1388–1394. [CrossRef] [PubMed]



© 2016 by the authors. Licensee MDPI, Basel, Switzerland. This article is an open access article distributed under the terms and conditions of the Creative Commons Attribution (CC BY) license (<http://creativecommons.org/licenses/by/4.0/>).



Article

# The Influence of Fluorination on Nano-Scale Phase Separation and Photovoltaic Performance of Small Molecular/PC<sub>71</sub>BM Blends

Zhen Lu <sup>1</sup>, Wen Liu <sup>1</sup>, Jingjing Li <sup>1</sup>, Tao Fang <sup>2</sup>, Wannin Li <sup>1</sup>, Jicheng Zhang <sup>2</sup>, Feng Feng <sup>1,\*</sup> and Wenhua Li <sup>2,\*</sup>

<sup>1</sup> College of Chemistry and Environmental Engineering, ShanXi DaTong University, Datong 037009, China; luzhen0313@aliyun.com (Z.L.); liuwen19701021@163.com (W.L.); lijingjing8150@163.com (J.L.); liwannin2016@163.com (W.L.)

<sup>2</sup> Beijing Key Laboratory of Energy Conversion and Storage Materials, College of Chemistry, Beijing Normal University, Beijing 100875, China; fangtao@bnu.edu.cn (T.F.); zhangjichengbnu@hotmail.com (J.Z.)

\* Correspondence: feng-feng64@263.net (F.F.); liwenhua@bnu.edu.cn (W.L.); Tel.: +86-0352-6090018 (F.F.); +86-010-62207699 (W.L.)

Academic Editor: Guanying Chen

Received: 5 February 2016; Accepted: 11 April 2016; Published: 22 April 2016

**Abstract:** To investigate the fluorination influence on the photovoltaic performance of small molecular based organic solar cells (OSCs), six small molecules based on 2,1,3-benzothiadiazole (BT), and diketopyrrolopyrrole (DPP) as core and fluorinated phenyl (DFP) and triphenyl amine (TPA) as different terminal units (DFP-BT-DFP, DFP-BT-TPA, TPA-BT-TPA, DFP-DPP-DFP, DFP-DPP-TPA, and TPA-DPP-TPA) were synthesized. With one or two fluorinated phenyl as the end group(s), HOMO level of BT and DPP based small molecular donors were gradually decreased, inducing high open circuit voltage for fluorinated phenyl based OSCs. DFP-BT-TPA and DFP-DPP-TPA based blend films both displayed stronger nano-scale aggregation in comparison to TPA-BT-TPA and TPA-DPP-TPA, respectively, which would also lead to higher hole motilities in devices. Ultimately, improved power conversion efficiency (PCE) of 2.17% and 1.22% was acquired for DFP-BT-TPA and DFP-DPP-TPA based devices, respectively. These results demonstrated that the nano-scale aggregation size of small molecules in photovoltaic devices could be significantly enhanced by introducing a fluorine atom at the donor unit of small molecules, which will provide understanding about the relationship of chemical structure and nano-scale phase separation in OSCs.

**Keywords:** small molecule; fluorinated phenyl (DFP) groups; organic solar cell; solution process; nanoscale phase separation

## 1. Introduction

Recently, organic solar cells (OSCs) have received great attention due to their advantages of solution processability, light weight, low cost, and flexibility [1–4]. Generally, bulk-heterojunction architecture was adopted with the electron-efficient conjugated polymer or small molecule as the donor and electron-deficient fullerene derivative such as (6,6)-phenyl-C<sub>71</sub>-butyric acid methyl ester (PC<sub>71</sub>BM) as the acceptor [5–7]. In comparison to widely investigated polymeric counterparts, small molecule-based OSCs have distinct advantages of well-defined chemical structures, easy purification, and high purity without batch-to-batch variation [5,6,8,9]. Therefore, small molecule-based materials are more suitable for mass production compared to polymer based ones. Driven by the developing of high efficiency small molecular donors and the investigation



of nano-scale phase separation at donor/acceptor interfaces, power conversion efficiency (PCE) of nearly 10% for small molecule-based single-junction OSCs has been achieved [10,11].

Due to the strong electron-withdrawing capability, the introducing of fluorine atoms onto the conjugated backbones of small molecules could reduce the HOMO energy levels, resulting in higher open circuit voltage ( $V_{oc}$ ) in OSCs [12–19]. Furthermore, the intra-molecular interaction of F–S and F–H could also induce closed packing properties and lead to superior hole mobiles [17,20–22]. Fluorinated molecules also showed good thermal and electrochemical stability, which would be helpful in the future commercial application. Although fluorinated small molecules have been broadly studied, fluorine atoms were mostly introduced to the acceptor unit of donor materials [18,19,23–25], works focus on the investigation of small molecules with a fluorine atom at the donor unit were still rare. Triphenylamine (TPA) based small molecules were common donor materials in organic semiconductor devices [8,26–30]. Nevertheless, the inferior planarity of TPA unit would induce weak intramolecular packing of small molecules and lead to a relatively low hole mobility in OSCs [31–33]. Conjugating a fluorine unit could therefore enhance the aggregation of TPA based small molecules and result in an appropriate nano-scale phase separation when blended with PC<sub>71</sub>BM. As a result, higher hole motilities and PCE were expected.

In this contribution, six small molecules (DFP-BT-DFP, DFP-BT-TPA, TPA-BT-TPA, DFP-DPP-DFP, DFP-DPP-TPA, and TPA-DPP-TPA) based on 2,1,3-benzothiadiazole (BT) or diketopyrrolopyrrole (DPP) (Chart 1) as the core and TPA or fluorinated phenyl (DFP) groups as the flanks were synthesized and applied as the donors in OSCs [34–36]. BT or DPP groups were chosen as the acceptor units due to their uniquely planarity and remarkably electron-withdrawing capabilities, and various DFP groups were conjugated as the end groups to investigate the influence of fluorinated donor unit on the performance of small molecule based OSCs. With one or two DFP as the end group(s), the HOMO level of BT-based small molecular donors TPA-BT-TPA, DFP-BT-TPA, and DFP-BT-DFP were gradually decreased; DPP-based small molecular donors also exhibited similar tendency, which would be beneficial to achieve high  $V_{oc}$  in OSCs. Due to the inferior solubility of DFP-BT-DFP and DFP-DPP-DFP, only TPA-BT-TPA, TPA-DPP-TPA, DFP-BT-TPA, and DFP-DPP-TPA were used as donor materials in OSCs. DFP-BT-TPA and DFP-DPP-TPA based blend films both displayed stronger nano-scale aggregation in comparison to TPA-BT-TPA and TPA-DPP-TPA, respectively, leading to higher hole motilities in devices. Ultimately, a PCE of 2.17% with a  $V_{oc}$  of 0.90 V and a PCE of 1.22% with a  $V_{oc}$  of 0.78 V was acquired for DFP-BT-TPA and DFP-DPP-TPA-based devices, respectively. Our results demonstrated that the nano-scale aggregation size of small molecules in photovoltaic devices could be significantly enhanced by introducing a fluorine atom at the donor unit of small molecules, which provided useful information in the further design of high efficiency small molecular donors for OSCs.

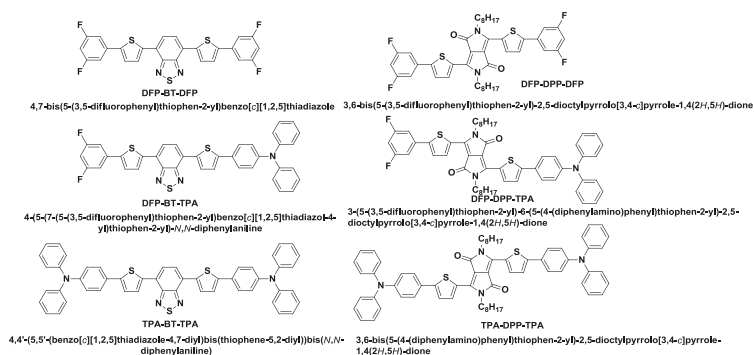
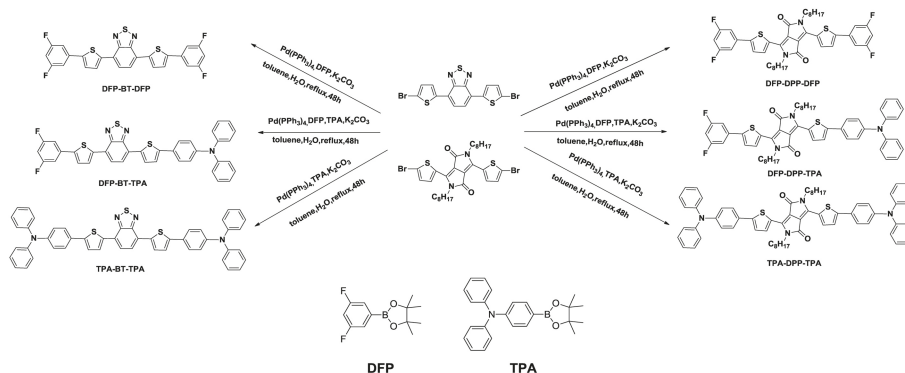


**Chart 1.** Chemical structures of small molecules (DFP-BT-DFP, DFP-BT-TPA, TPA-BT-TPA, DFP-DPP-DFP, DFP-DPP-TPA, and TPA-DPP-TPA). DFP: fluorinated phenyl; BT: 2,1,3-benzothiadiazole; DPP: diketopyrrolopyrrole; TPA: triphenyl amine.

## 2. Results and discussions

### 2.1. Synthesis

The synthesis route of six small molecules (DFP-BT-DFP, DFP-BT-TPA, TPA-BT-TPA, DFP-DPP-DFP, DFP-DPP-TPA, and TPA-DPP-TPA) is outlined in Scheme 1. All small molecules were synthesized by using the Suzuki cross-coupling reaction between a boronic acid ester and a brominated aromatic compound in toluene and  $K_2CO_3$  aqueous solution under  $N_2$  with  $Pd(PPh_3)_4$  as the catalyst procedure. DFP-BT-TPA, TPA-BT-TPA, DFP-DPP-TPA, and TPA-DPP-TPA show good solubility in common organic solvents such as chloroform ( $CHCl_3$ ), tetrahydrofuran (THF), and chlorobenzene (CB). However, DFP-BT-DFP and DFP-DPP-DFP showed poor solubility in these solvents, which might be ascribed to the fluorinated and symmetric molecular structure. As shown in Figure S1, DSC images demonstrated that all these small molecules were crystalline, which might be beneficial for the closed packing properties when blended with  $PC_{71}BM$ . As shown in Figure S2 and Table 1, DFP-BT-DFP, DFP-BT-TPA, TPA-BT-TPA, DFP-DPP-DFP, DFP-DPP-TPA, and TPA-DPP-TPA all exhibited good thermal stability with a 5% weight loss of 350, 450, 461, 374, 400, and 408 °C, respectively. Our results revealed TPA-based small molecules possess better thermal stability than DFP based small molecules, which is beyond our expectation. The 5% weight loss temperature of DFP-BT-TPA and TPA-BT-TPA could reach to around 450 °C, making them very stable in the application of OSCs.



**Scheme 1.** Synthetic route of six small molecules (DFP-BT-DFP, DFP-BT-TPA, TPA-BT-TPA, DFP-DPP-DFP, DFP-DPP-TPA, and TPA-DPP-TPA).

**Table 1.** Optical, electrochemical, and physical properties of small molecules.

Donor	$\lambda_{abs}(S)$ (nm) <sup>a</sup>	$\lambda_{abs}(F)$ (nm) <sup>b</sup>	$\lambda_{onset}$ (nm)	$E_{g,opt}(ev)$	HOMO <sup>c</sup>	LUMO <sup>d</sup>	$T_m$ (°C)	$T_g$ (°C)
DFP-BT-DFP	488	505	636	1.95	-5.73	-3.78	246.6	350
DFP-BT-TPA	525	530	643	1.93	-5.34	-3.41	248.8	450
TPA-BT-TPA	544	547	659	1.88	-5.17	-3.29	254.4	461
DFP-DPP-DFP	598	616, 663	715	1.73	-5.59	-3.86	216.9	374
DFP-DPP-TPA	619	583, 627	746	1.66	-5.13	-3.47	195.3	400
TPA-DPP-TPA	634	588, 656	760	1.63	-5.07	-3.44	217.3	408

<sup>a</sup> S stands for in solutions; <sup>b</sup> F stands for as films; <sup>c</sup> HOMO means highest occupied molecular orbital; <sup>d</sup> LUMO means lowest unoccupied molecular orbital.

### 2.2. Optical Properties

The normalized ultraviolet-visible spectroscopy (UV-VIS) absorption spectra of six small molecules in dilute CB solution and as thin films at 25 °C are shown in Figure 1. These small molecules exhibit a broad absorption in the range from 300 to 700 nm with two distinguishable absorption bands, which could be attributed to the  $\pi$ - $\pi^*$  transition and the internal charge transfer (ICT) interaction

between the donor and the acceptor units [4,21,28]. Upon going from solution to the solid state, the absorption spectra become broader and redshift 17 nm for DFP-BT-DFP, 5 nm for DFP-BT-TPA, and 5 nm for TPA-BT-TPA, respectively, which can be attributed to the closer  $\pi$ - $\pi$  stacking in solid state. The onsets of film absorption spectra are 636, 643, and 659 nm, respectively, for these small molecules, and optical band gaps ( $E_{g, opt}$ ) were calculated to be 1.95, 1.93, and 1.88 eV, respectively. Similar to BT based small molecules, DFP-DPP-DFP, DFP-DPP-TPA, TPA-DPP-TPA show broader absorption over the range from 300 to 750 nm with two distinguishable absorption bands. Specifically, the absorption for DFP-DPP-DFP showed stronger shoulder peaks, revealing more ordered molecular stacking capabilities in the solid state [37,38]. From the absorption onsets, the optical band gaps were estimated to be 1.73, 1.66, and 1.63 eV for DFP-DPP-DFP, DFP-DPP-TPA, and TAP-DPP-TPA, respectively.

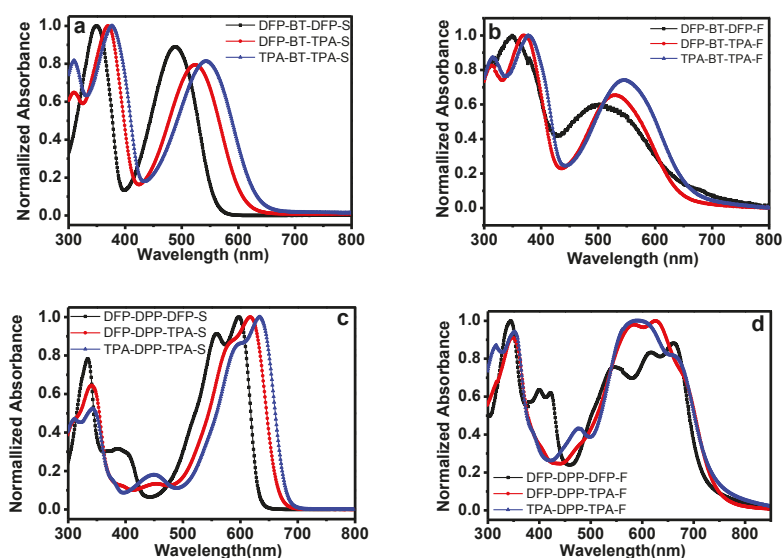


**Figure 1.** Normalized ultraviolet-visible spectroscopy (UV-VIS) absorption spectra of the six small molecules. (a,c) in dilute chlorobenzene (CB) solution; (b,d) as thin film on a quartz substrate.

### 2.3. Cyclic Voltammetry

Cyclic voltammetry (CV) experiments were carried out to evaluate electrochemical characteristics of these small molecules. As shown in Figure 2, the onset oxidation potentials ( $E_{ox}$ ) were 1.02, 0.63, 0.46 V for DFP-BT-DFP, DFP-BT-TPA, and TPA-BT-TPA, respectively, According to the equation  $E_{HOMO} = -(4.71 + E_{ox})$  (eV), highest occupied molecular orbital (HOMO) energy levels of these small molecules could be determined to be  $-5.73$ ,  $-5.34$ , and  $-5.17$  eV. With the combination of the optical band gap and the equation  $E_{LUMO} = E_{HOMO} + E_{g, opt}$ , [39] the lowest unoccupied molecular orbital (LUMO) energy levels were calculated to be  $-3.78$ ,  $-3.41$ , and  $-3.29$  eV for DFP-BT-DFP, DFP-BT-TPA, and TPA-BT-TPA, respectively. Similarly, the HOMO and LUMO energy levels were determined to be  $-5.59$ ,  $-5.13$ ,  $-5.07$  and  $-3.86$ ,  $-3.47$ ,  $-3.44$  eV for DFP-DPP-DFP, DFP-DPP-TPA, and TAP-DPP-TPA, respectively. These results demonstrated that the incorporation of fluorine atom could significantly decrease the HOMO energy levels of small molecules, which would be beneficial to achieve high  $V_{oc}$  in OSCs. The data are also summarized in Table 1.

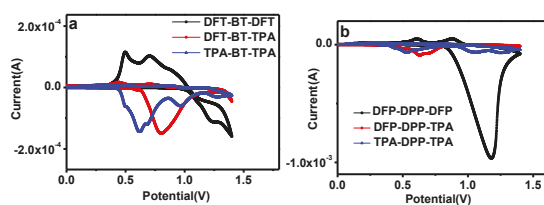


**Figure 2.** Cyclic voltammograms of small molecules. (a) DFT-BT-DFT, DFT-BT-TPA, TPA-BT-TPA; and (b) DFP-DPP-DFP, DFP-DPP-TPA, TPA-DPP-TPA.

#### 2.4. Photovoltaic Properties

Photovoltaic properties of these small molecules were investigated by a general device structure of indium tin oxides (ITO)/poly(3,4-ethylenedioxythiophene):poly(styrenesulfonate) (PEDOT:PSS)/donor:PC<sub>71</sub>BM/LiF/Al. Different spin-coating speeds and weight ratios of small molecules to PC<sub>71</sub>BM in a CB solution were screened to optimize the photovoltaic performance. Due to the inferior solubility of DFP-BT-DFP and DFP-DPP-DFP, typical cluster structures with boosted big domains could be easily observed by naked eyes. As a result, photovoltaic performance of these two small molecules based devices would not be discussed. For other small molecules, the current density-voltage (*J-V*) curves are shown in Figure 3a and device characteristics are summarized in Table 2. After optimization, superior PCE values could be achieved with a weight ratio of 1:4 (*w/w*) for all devices, and a PCE of 1.95% with a  $V_{oc}$  of 0.82 V,  $J_{sc}$  of 5.97 mA·cm<sup>-2</sup> and fill factor (FF) of 0.40 was achieved for TPA-BT-TPA devices. When one TPA unit was replaced by one DFP group, increased  $V_{oc}$  of 0.90 V and  $J_{sc}$  of 6.12 mA·cm<sup>-2</sup> were obtained for DFP-BT-TPA based device, leading to higher PCE of 2.17%. Similarly, DFP-DPP-TPA based solar cells exhibited a higher PCE of 1.22% with a  $V_{oc}$  of 0.78 V than that of TPA-DPP-TPA based devices. This improvement could be attributed to the increase of  $V_{oc}$  and  $J_{sc}$ . Since  $V_{oc}$  is related to the offset between HOMO level of donor materials and LUMO level of PC<sub>71</sub>BM, the decrease of HOMO levels for DFP based small molecules would lead to higher  $V_{oc}$  [3]. Meanwhile, DFP based small molecules also possesses bigger nano-scale aggregates, and resulting higher hole mobilities in the active layer (*vide infra*), which would also lead to higher  $J_{sc}$  in devices.

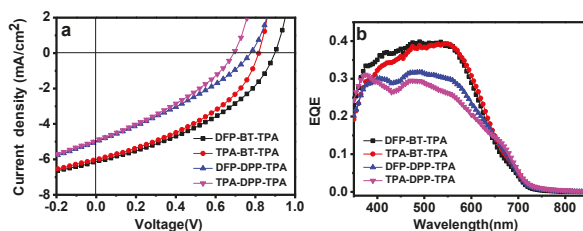


**Figure 3.** *J-V* characteristics (a) and external quantum efficiency (EQE) curves (b) of devices fabricated from the blend of small molecule: PC<sub>71</sub>BM.

**Table 2.** Photovoltaic performance and hole mobilities of small molecule-based devices. FF: fill factor; PCE: power conversion efficiency; SCLC: space charge limited current.

Donor Molecule	$V_{oc}$ (V)	$J_{sc}$ (mA·cm <sup>-2</sup> )	FF	PCE (max/ave) <sup>a</sup> (%)	Thickness (nm)	SCLC (cm <sup>2</sup> ·V <sup>-1</sup> ·s <sup>-1</sup> )
DFP-BT-TPA	0.90	6.12	0.39	2.17/2.08	76	3.81 × 10 <sup>-4</sup>
TPA-BT-TPA	0.82	5.97	0.40	1.95/1.85	82	4.42 × 10 <sup>-5</sup>
DFP-DPP-TPA	0.78	4.95	0.32	1.22/1.17	70	9.35 × 10 <sup>-5</sup>
TPA-DPP-TPA	0.70	4.90	0.34	1.15/1.02	85	3.26 × 10 <sup>-5</sup>

<sup>a</sup> Average value recorded over 20 devices.

To verify the  $J_{sc}$  obtained from  $J$ - $V$  measurement, the external quantum efficiencies (EQEs) of devices were measured. As shown in Figure 3b, the EQE images of devices all displayed a broad response in the range from 350 to 600 nm, and the maximum EQE value of DFP-BT-TPA and TPA-BT-TPA-based devices are both 40%, which are higher than that of DFP-DPP-TPA and TPA-DPP-TPA.  $J_{sc}$  values integrated from EQE curves all agreed approximately with that obtained from  $J$ - $V$  measurement.

The hole mobilities of these devices were measured by the space charge limited current (SCLC) method. Hole-only devices were fabricated with a structure of ITO/PEDOT:PSS/donor:PC<sub>71</sub>BM/Au and resulting hole mobility value ( $\mu$ ) was calculated from the dark  $J$ - $V$  experiments. Dark  $J$ - $V$  curves were fitted by using the Mott–Gurney equation:  $J = 9\epsilon_0\epsilon_r\mu V^2/8L^3$ , where  $J$  is the space charge limited current,  $\epsilon_0$  is the vacuum permittivity,  $\epsilon_r$  is the permittivity of the active layer,  $\mu$  is the hole mobility of small molecules, and  $L$  is the thickness of the active layer.  $\mu$  of devices based on DFP-BT-TPA and DFP-DPP-TPA were evaluated to be  $3.81 \times 10^{-4}$  and  $9.35 \times 10^{-5}$  cm<sup>2</sup>·V<sup>-1</sup>·s<sup>-1</sup>, respectively, and  $\mu$  of TPA-BT-TPA and TPA-DPP-TPA based devices were determined to be  $4.42 \times 10^{-5}$  and  $3.26 \times 10^{-5}$  cm<sup>2</sup>·V<sup>-1</sup>·s<sup>-1</sup>, respectively.  $\mu$  of DFP based devices were obviously higher than that of TPA based ones, which might be attributed to their planar chemical structure and resulting bigger nano-scale aggregation in the blend films.

### 2.5. Film Morphology

Atomic force microscopy (AFM) experiments were carried out to investigate the surface morphology of the active layer. Well-mixed blend films were in favor of exciton dissociation in devices, whereas appropriate nano-scale aggregation of small molecules was also important for the charge transport. Therefore, suitable nano-scale phase separation is critical to obtain a superior photovoltaic performance [40,41]. As shown in Figure 4, blend films based on TPA-BT-TPA and TPA-DPP-TPA were both uniform and smooth with a root-mean-square (RMS) roughness value of 0.78 and 0.65 nm, which might be ascribed to the inferior packing properties of TPA group. For devices based on DFP-BT-TPA and DFP-DPP-TPA, rougher blend film surface with a RMS roughness value of 2.35 nm and 0.84 nm were acquired, demonstrating the domain size of DFP-BT-TPA and DFP-DPP-TPA were higher than TPA-BT-TPA and TPA-DPP-TPA in devices. Our results demonstrated that incorporating a DFT group as the end groups could enhance the nano-scale aggregation in the devices, which would be beneficial to the charge transport in the blend films, and lead to higher  $J_{sc}$  and PCE.

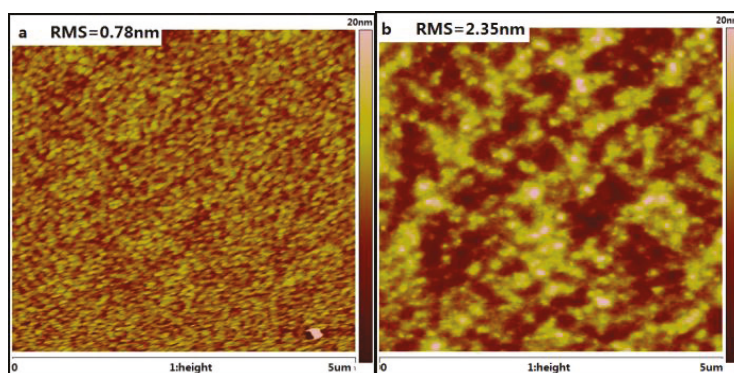
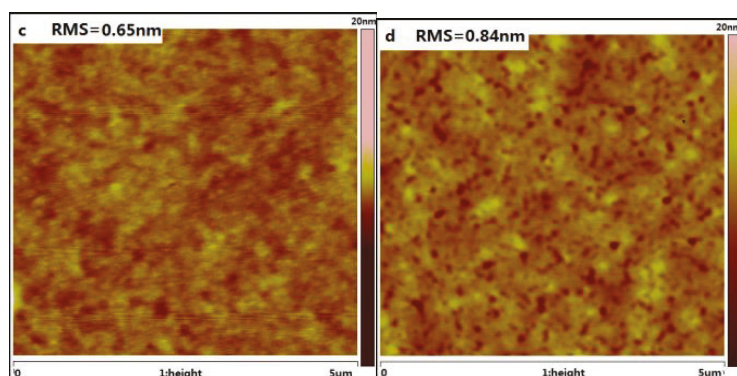


Figure 4. Cont.



**Figure 4.** Atomic force microscopy (AFM) ( $5 \times 5 \mu\text{m}^2$ ) height images of blend films. (a) TPA-BT-TPA:PC<sub>71</sub>BM; (b) DFP-BT-TPA:PC<sub>71</sub>BM; (c) TPA-DPP-TPA:PC<sub>71</sub>BM; and (d) DFP-DPP-TPA:PC<sub>71</sub>BM.

### 3. Experimental Section

#### 3.1. Materials

All chemicals were purchased from commercial sources and used without further purification, and all solvents were purified by standard techniques. Additionally, all reactions were carried out under the nitrogen atmosphere unless otherwise stated. The catalyst procedure Pd(PPh<sub>3</sub>)<sub>4</sub> [34], 4,7-bis(5-bromothiophen-2-yl)benzo[c][1,2,5]thiadiazole [35] and 3,6-bis(5-bromothiophen-2-yl)-2,5-dioctylpyrrolo[3,4-c]pyrrole-1,4-dione [36] were synthesized according to the literature procedures.

#### 3.2. Measurements and Characterization

All reactions were monitored by thin layer chromatography (TLC) on silica gel 60 F254 (Merck, Beijing, China, 0.2 mm), and column chromatography was performed on silica gel (200–300 mesh). <sup>1</sup>H and <sup>13</sup>C NMR spectra were recorded on a Bruker AV 400 spectrometer (Saarbrücken, Germany) using CDCl<sub>3</sub> as the solvents. Differential scanning calorimetry (DSC) measurements were performed on the Perkin-Elmer Diamond DSC instrument (Shanghai, China) under a nitrogen atmosphere with a heating rate of 20 °C/min. UV-VIS absorption spectra was recorded on the PerkinElmer UV-VIS spectrometer model Lambda 750 (Shanghai, China). The electrochemical behavior of small molecules was achieved using CHI 630A electrochemical analyzer (Beijing, China) with a standard three-electrode electrochemical cell in 0.1 M Bu<sub>4</sub>NPF<sub>6</sub> in CH<sub>3</sub>CN solution. A glassy carbon working electrode, a Pt wire counter electrode, and an Ag/AgNO<sub>3</sub> (0.01 M in CH<sub>3</sub>CN) reference electrode were used. Elemental analyses were performed on a Flash EA 1112 analyzer (Lakewood, CO, USA), and atomic force microscopy (AFM) measurements were carried out in the tapping mode using a Digital Instrument Multimode Nanoscope IIIA (Plainview, TX, USA). The thickness of the active layers was determined by the Dektak 6 M surface profilometer (Beijing, China).

#### 3.3. Fabrication and Characterization of SCLC

Devices used to measure the space charge limited current (SCLC) were fabricated with a configuration of ITO/PEDOT:PSS/small molecule:PC<sub>71</sub>BM/Au. The conductivity of ITO was 20 Ω. PEDOT:PSS is Baytron Al 4083 from H.C.Starck (Leverkusen, Germany) and filtered with a 0.45 μm polyethersulfone (PES) film before use. The PEDOT:PSS was spin-coated on top of a ITO substrate from a speed of 3000 rpm/s for 60 s and dried at 130 °C for 15 min on a hotplate. The thickness of the PEDOT:PSS layer was about 40 nm. Small molecule and PC<sub>71</sub>BM was dissolved in chlorobenzene (CB) at 110 °C overnight, and then spin-coated onto the PEDOT:PSS layer. The top electrode was



subsequently thermally evaporated with a 100 nm of gold under a pressure of  $10^{-4}$  Pa by a shadow mask. Dark current-voltage characteristics were recorded using an Agilent B2902A Source (Taiwan) under darkness in a range of 0 V to 5.0 V.

### 3.4. Fabrication and Characterization of PSCs

PSCs were fabricated with the device configuration of ITO/PEDOT:PSS/small molecule:PC<sub>71</sub>BM/LiF/Al. ITO glasses with a conductivity of 20  $\Omega$  were cleaned before use. PEDOT:PSS is Baytron AI 4083 from H.C.Starck, and filtered with a 0.45  $\mu$ m PES film before use. The thin layer of PEDOT:PSS was spin-coated on top of a cleaned ITO substrate at 3000 rpm/s for 60 s and dried subsequently at 130  $^{\circ}$ C for 15 min on a hotplate. The thickness of the PEDOT:PSS layer was about 40 nm. The active layer was subsequently prepared by spin-coating the blend solution of small molecule and PC<sub>71</sub>BM on the top of ITO/PEDOT:PSS. The top electrode was thermally evaporated with a 0.6 nm LiF layer, and followed by 100 nm of aluminum under a pressure of  $10^{-4}$  Pa through a shadow mask. Five cells were fabricated on one substrate with an effective area of 0.04 cm<sup>2</sup>. The current-voltage (*I-V*) curves of devices were completed by a computer-controlled Keithley 236 Source Measure Unit. An AM 1.5G AAA class solar simulator (model XES-301S, SAN-EI) in an intensity of 100 mW/cm<sup>2</sup> was used as the simulative sun light source, and the light intensity of the light was calibrated under a standard single-crystal Si photovoltaic cell.

### 3.5. General Procedure for the Synthesis of Small Molecules

The general procedure for the synthesis were shown in Scheme 1, A solution of BT or DPP, DFP or TPA, K<sub>2</sub>CO<sub>3</sub>, toluene (50 mL), and H<sub>2</sub>O (5 mL) was carefully gas and degassed before and after Pd(PPh<sub>3</sub>)<sub>4</sub> was added, and the mixture was stirring at 100  $^{\circ}$ C for two days. After the reaction, the mixture was poured into water (100 mL) and extracted with CHCl<sub>3</sub>. The organic layer was washed with water three times, and then dried by MgSO<sub>4</sub>. After evaporating to dryness, the pure product was obtained from column chromatography by a silica gel.

4,7-bis(5-(3,5-difluorophenyl)thiophen-2-yl)benzo[c][1,2,5]thiadiazole (DFP-BT-DFP): BT (0.96 g, 2.1 mmol), DFP (1.01 g, 4.2 mmol), K<sub>2</sub>CO<sub>3</sub> (1.38 g, 10.0 mmol), and Pd(PPh<sub>3</sub>)<sub>4</sub> (127.1 mg, 0.11 mmol) were used. Yield: 0.73 g, 66% purple crystal. <sup>1</sup>H NMR (400 MHz, CDCl<sub>3</sub>)  $\delta$ . 8.12 (d, 1H), 7.94 (s, 1H), 7.44 (d, 1H) 7.52 (m, 2H), 6.77 (m, 1H). <sup>13</sup>C NMR (100 MHz, CDCl<sub>3</sub>)  $\delta$ . 155.61, 151.55, 148.01, 143.27, 142.00, 137.55, 131.73, 120.63, 116.91. Analyze (Anal.) Calcd for C<sub>26</sub>H<sub>12</sub>F<sub>4</sub>N<sub>2</sub>S<sub>3</sub>: C, 59.53; H, 2.31; N, 5.34; Found: C, 59.42; H, 2.40; N, 5.26. MALDI-TOF: calculated for C<sub>26</sub>H<sub>12</sub>F<sub>4</sub>N<sub>2</sub>S<sub>3</sub> 524.6, found 523.8.

4-(5-(7-(5-(3,5-difluorophenyl)thiophen-2-yl)benzo[c][1,2,5]thiadiazol-4-yl)thiophen-2-yl)-*N,N*-diphenylaniline (DFP-BT-TPA): BT (1.15 g, 2.5 mmol), DFP (0.60 g, 2.5 mmol), TPA (0.93 g, 2.5 mmol), K<sub>2</sub>CO<sub>3</sub> (1.38 g, 10.0 mmol), and Pd(PPh<sub>3</sub>)<sub>4</sub> (144.3 mg, 0.11 mmol) were used. Yield: 0.67 g, 41% purple crystal. <sup>1</sup>H NMR (400 MHz, CDCl<sub>3</sub>)  $\delta$ . 8.14 (d, 1H), 8.08 (d, 1H), 7.90 (t, 2H) 7.57 (d, 2H), 7.43 (d, 1H), 7.34 (d, 1H), 7.29 (t, 3H), 7.22 (d, 2H), 7.16–7.00 (m, 8H), 6.75 (t, 1H). <sup>13</sup>C NMR (100 MHz, CDCl<sub>3</sub>)  $\delta$ . 161.66, 158.56, 153.96, 145.33, 143.04, 139.03, 132.72, 129.49, 127.99, 124.80, 123.41, 123.32, 115.51. Anal. Calcd for C<sub>38</sub>H<sub>23</sub>F<sub>2</sub>N<sub>3</sub>S<sub>3</sub>: C, 69.60; H, 3.54; N, 6.41 Found: C, 69.45; H, 3.52; N, 6.40. MALDI-TOF: calculated for C<sub>38</sub>H<sub>23</sub>F<sub>2</sub>N<sub>3</sub>S<sub>3</sub> 655.8, found 654.9.

4,4'-(5,5'-(benzo[c][1,2,5]thiadiazole-4,7-diyl)bis(thiophene-5,2-diyl))bis(*N,N*-diphenylaniline) (TPA-BT-TPA): BT (1.01 g, 2.2 mmol), TPA (1.63 g, 4.4 mmol), K<sub>2</sub>CO<sub>3</sub> (1.22 g, 8.8 mmol), and Pd(PPh<sub>3</sub>)<sub>4</sub> (127.1 mg, 0.11 mmol) were used. Yield: 1.30 g, 75% purple crystal. <sup>1</sup>H NMR (400 MHz, CDCl<sub>3</sub>)  $\delta$ . 8.11 (s, 2H), 7.85 (s, 2H), 7.56 (m, 4H), 7.29 (m, 10H), 7.08 (m, 16H). <sup>13</sup>C NMR (100 MHz, CDCl<sub>3</sub>)  $\delta$ . 152.57, 147.58, 147.39, 129.35, 128.67, 128.03, 126.60, 125.61, 125.14, 124.64, 123.46, 123.23. Anal. Calcd for C<sub>50</sub>H<sub>34</sub>N<sub>4</sub>S<sub>3</sub>: C, 76.30; H, 4.35; N, 7.12. Found: C, 76.17; H, 4.36; N, 7.02. MALDI-TOF: calculated for C<sub>50</sub>H<sub>34</sub>N<sub>4</sub>S<sub>3</sub> 787.0, found 785.9.



3,6-bis(5-(3,5-difluorophenyl)thiophen-2-yl)-2,5-dioctylpyrrolo[3,4-c]pyrrole-1,4(2H,5H)-dione(DFP-DPP-DFP): DPP (1.37 g, 2.0 mmol) and DFP (0.96 g, 4.0 mmol),  $K_2CO_3$  (1.11 g, 8.0 mmol), and  $Pd(PPh_3)_4$  (115.5 mg, 0.11 mmol) were used. Yield: 0.91 g, 66% gray solid.  $^1H$  NMR (400 MHz,  $CDCl_3$ )  $\delta$ : 8.94 (d, 2H), 7.48 (d, 2H), 7.19 (d, 4H), 6.82 (t, 2H), 4.11 (t, 4H), 1.77 (t, 4H), 1.46–1.28 (m, 20H), 0.86 (t, 6H)  $^{13}C$  NMR (100 MHz,  $CDCl_3$ )  $\delta$ : 161.26, 155.77, 155.15, 149.36, 146.58, 139.32, 136.46, 129.90, 125.89, 109.15, 108.85, 42.32, 31.79, 30.01, 29.28, 29.21, 26.90, 22.63, 14.07. Anal. Calcd for  $C_{42}H_{44}F_4N_2O_2S_2$ : C, 67.36; H, 5.92; N, 3.74. Found: C, 67.12; H, 5.92; N, 3.73. MALDI-TOF: calculated for  $C_{42}H_{44}F_4N_2O_2S_2$  748.9, found 748.1.

3-(5-(3,5-difluorophenyl)thiophen-2-yl)-6-(5-(4-(diphenylamino)phenyl)thiophen-2-yl)-2,5-dioctylpyrrolo pyrrole-1,4(2H,5H)-dione(DFP-DPP-TPA): DPP (1.91 g, 2.8 mmol), DFP (0.67 g, 2.8 mmol) and TPA (1.04 g, 2.8 mmol),  $K_2CO_3$  (3.33 g, 14.0 mmol), and  $Pd(PPh_3)_4$  (161.7 mg, 0.14 mmol) were used. Yield: 0.76 g, 31% gray solid.  $^1H$  NMR (400 MHz,  $CDCl_3$ )  $\delta$ : 9.04 (s, 1H), 8.87 (s, 1H), 7.52 (s, 2H), 7.44 (s, 1H), 7.36 (s, 1H), 7.30 (t, 4H), 7.14 (d, 6H), 7.08 (dd, 4H), 6.78 (s, 1H), 4.09 (t, 4H), 1.76 (t, 4H), 1.45–1.26 (m, 20H), 0.85 (t, 6H).  $^{13}C$  NMR (100 MHz,  $CDCl_3$ )  $\delta$ : 148.74, 147.02, 137.71, 129.47, 126.99, 126.30, 125.09, 123.80, 123.64, 122.58, 109.05, 108.77, 42.32, 31.82, 30.04, 29.27, 29.22, 26.94, 22.64, 14.12. Anal. Calcd for  $C_{55}H_{59}F_2N_3O_2S_2$ : C, 73.71; H, 6.64; N, 4.69. Found: C, 73.25; H, 6.35; N, 4.73. MALDI-TOF: calculated for  $C_{55}H_{59}F_2N_3O_2S_2$  896.2, found 895.3.

3,6-bis(5-(4-(diphenylamino)phenyl)thiophen-2-yl)-2,5-dioctylpyrrolo[3,4-c]pyrrole-1,4(2H,5H)-dione (TPA-DPP-TPA): DPP (1.30 g, 1.9 mmol) and TPA (1.41 g, 3.8 mmol),  $K_2CO_3$  (1.31 g, 9.5 mmol), and  $Pd(PPh_3)_4$  (115.5 mg, 0.10 mmol) were used. Yield: 1.35 g, 70% gray solid.  $^1H$  NMR (400 MHz,  $CDCl_3$ )  $\delta$ : 7.30 (t, 15H), 7.10 (d, 17H), 4.10 (t, 4H), 1.80 (t, 4H), 1.46–1.26 (m, 20H), 0.84 (t, 6H).  $^{13}C$  NMR (100 MHz,  $CDCl_3$ )  $\delta$ : 162.54, 160.20, 155.76, 148.66, 147.40, 132.11, 129.44, 126.93, 124.82, 123.60, 123.69, 122.72, 110.77, 42.28, 31.81, 30.03, 29.24, 29.22, 26.93, 22.63, 14.10. Anal. Calcd for  $C_{66}H_{66}N_4O_2S_2$ : C, 78.38; H, 6.58; N, 5.54. Found: C, 78.17; H, 6.61; N, 5.38. MALDI-TOF: calculated for  $C_{66}H_{66}N_4O_2S_2$  1011.4, found 1010.1.

#### 4. Conclusions

In conclusion, six small molecules (DFP-BT-DFP, DFP-BT-TPA, TPA-BT-TPA, DFP-DPP-DFP, DFP-DPP-TPA, and TPA-DPP-TPA) based on 2,1,3-benzothiadiazole (BT) or diketopyrrolopyrrole (DPP) as the core and TPA or fluorinated phenyl (DFP) as the end groups were designed and synthesized as the donors in OSCs. To investigate the influence of fluorinated donor unit on the photovoltaic performance of devices, various DFP groups were conjugated. With one or two DFP as the end group(s), HOMO level of TPA-BT-TPA, DFP-BT-TPA, and DFP-BT-DFP was gradually decreased; similar tendency could also be observed for DPP based small molecular donors, inducing high  $V_{oc}$  for DFP based OSCs. DFP-BT-TPA and DFP-DPP-TPA based blend films both displayed stronger nano-scale aggregation in comparison to TPA-BT-TPA and TPA-DPP-TPA, respectively, which would also lead to higher hole mobilities in devices. Ultimately, a PCE of 2.17% with a  $V_{oc}$  of 0.90 V was acquired for DFP-BT-TPA based devices. Our results demonstrated that the nano-scale aggregation size of small molecules in photovoltaic devices could be significantly enhanced by introducing a fluorine atom at the donor unit of small molecules. Although the PCE is not attractive enough, this work will provide understanding about the relationship of chemical structure and nano-scale phase separation in OSCs.

**Supplementary Materials:** The following are available online at <http://www.mdpi.com/2079-4991/6/4/80/s1>.

**Acknowledgments:** Financial support from PhD Research Startup Foundation of Shanxi Datong University (2013-B-01), School foundation of Shanxi Datong University (XDC2014110), the NSF of China (91233205), the NSF of China (51403021), the NSF of China (21375083) and Beijing Natural Science Foundation (2152017).

**Author Contributions:** The experimental design was planned by Feng Feng and Wenhua Li. The experimental work and data analysis were performed by Zhen Lu, Wen Liu, Jingjing Li, Tao Fang, Wannin Li and Jicheng Zhang.

**Conflicts of Interest:** The authors declare no conflict of interest.

## References

- Liang, Y.; Xu, Z.; Xia, J.; Tsai, S.-T.; Wu, Y.; Li, G.; Ray, C.; Yu, L. For the Bright Future—Bulk Heterojunction Polymer Solar Cells with Power Conversion Efficiency of 7.4%. *Adv. Mater.* **2010**, *22*, E135–E138. [CrossRef] [PubMed]
- Lu, L.; Zheng, T.; Wu, Q.; Schneider, A.M.; Zhao, D.; Yu, L. Recent Advances in Bulk Heterojunction Polymer Solar Cells. *Chem. Rev.* **2015**, *115*, 12666–12731. [CrossRef] [PubMed]
- Chen, J.; Cao, Y. Development of Novel Conjugated Donor Polymers for High-Efficiency Bulk-Heterojunction Photovoltaic Devices. *Acc. Chem. Res.* **2009**, *42*, 1709–1718. [CrossRef] [PubMed]
- Li, Y. Molecular Design of Photovoltaic Materials for Polymer Solar Cells: Toward Suitable Electronic Energy Levels and Broad Absorption. *Acc. Chem. Res.* **2012**, *45*, 723–733. [CrossRef] [PubMed]
- Lin, Y.; Li, Y.; Zhan, X. Small molecule semiconductors for high-efficiency organic photovoltaics. *Chem. Soc. Rev.* **2012**, *41*, 4245–4272. [CrossRef] [PubMed]
- Cui, C.; Guo, X.; Min, J.; Guo, B.; Cheng, X.; Zhang, M.; Brabec, C.J.; Li, Y. High-Performance Organic Solar Cells Based on a Small Molecule with Alkylthio-Thienyl-Conjugated Side Chains without Extra Treatments. *Adv. Mater. (Deerfield Beach Fla.)* **2015**, *27*, 7469–7475. [CrossRef] [PubMed]
- Liu, C.; Yi, C.; Wang, K.; Yang, Y.L.; Bhatta, R.S.; Tsige, M.; Xiao, S.Y.; Gong, X. Single-Junction Polymer Solar Cells with Over 10% Efficiency by a Novel Two-Dimensional Donor-Acceptor Conjugated Copolymer. *ACS Appl. Mater. Interfaces* **2015**, *7*, 4928–4935. [CrossRef] [PubMed]
- Shang, H.; Fan, H.; Liu, Y.; Hu, W.; Li, Y.; Zhan, X. A Solution-Processable Star-Shaped Molecule for High-Performance Organic Solar Cells. *Adv. Mater.* **2011**, *23*, 1554–1557. [CrossRef] [PubMed]
- Sun, Y.; Welch, G.C.; Leong, W.L.; Takacs, C.J.; Bazan, G.C.; Heeger, A.J. Solution-processed small-molecule solar cells with 6.7% efficiency. *Nat. Mater.* **2012**, *11*, 44–48. [CrossRef] [PubMed]
- Zhang, Q.; Kan, B.; Liu, F.; Long, G.; Wan, X.; Chen, X.; Zuo, Y.; Ni, W.; Zhang, H.; Li, M.; et al. Small-molecule solar cells with efficiency over 9%. *Nat. Photonics* **2015**, *9*, 35–41. [CrossRef]
- Kan, B.; Zhang, Q.; Li, M.; Wan, X.; Ni, W.; Long, G.; Wang, Y.; Yang, X.; Feng, H.; Chen, Y. Solution-Processed Organic Solar Cells Based on Dialkylthiol-Substituted Benzodithiophene Unit with Efficiency near 10%. *J. Am. Chem. Soc.* **2014**, *136*, 15529–15532. [CrossRef] [PubMed]
- Ni, W.; Li, M.; Kan, B.; Zuo, Y.; Zhang, Q.; Long, G.; Feng, H.; Wan, X.; Chen, Y. Open-circuit voltage up to 1.07 V for solution processed small molecule based organic solar cells. *Organic Electron.* **2014**, *15*, 2285–2294. [CrossRef]
- Carsten, B.; Szarko, J.M.; Son, H.J.; Wang, W.; Lu, L.; He, F.; Rolczynski, B.S.; Lou, S.J.; Chen, L.X.; Yu, L. Examining the Effect of the Dipole Moment on Charge Separation in Donor-Acceptor Polymers for Organic Photovoltaic Applications. *J. Am. Chem. Soc.* **2011**, *133*, 20468–20475. [CrossRef] [PubMed]
- Chen, H.Z.; Ling, M.M.; Mo, X.; Shi, M.M.; Wang, M.; Bao, Z. Air stable *n*-channel organic semiconductors for thin film transistors based on fluorinated derivatives of perylene diimides. *Chem. Mater.* **2007**, *19*, 816–824. [CrossRef]
- Li, K.; Li, Z.; Feng, K.; Xu, X.; Wang, L.; Peng, Q. Development of Large Band-Gap Conjugated Copolymers for Efficient Regular Single and Tandem Organic Solar Cells. *J. Am. Chem. Soc.* **2013**, *135*, 13549–13557. [CrossRef] [PubMed]
- Schroeder, B.C.; Huang, Z.; Ashraf, R.S.; Smith, J.; D'Angelo, P.; Watkins, S.E.; Anthopoulos, T.D.; Durrant, J.R.; McCulloch, I. Silaindacenodithiophene-Based Low Band Gap Polymers—The Effect of Fluorine Substitution on Device Performances and Film Morphologies. *Adv. Funct. Mater.* **2012**, *22*, 1663–1670. [CrossRef]
- Shewmon, N.T.; Watkins, D.L.; Galindo, J.F.; Zerdan, R.B.; Chen, J.; Keum, J.; Roitberg, A.E.; Xue, J.; Castellano, R.K. Enhancement in Organic Photovoltaic Efficiency through the Synergistic Interplay of Molecular Donor Hydrogen Bonding and  $\pi$ -Stacking. *Adv. Funct. Mater.* **2015**, *25*, 5166–5177. [CrossRef]
- Wang, L.; Yin, L.; Ji, C.; Li, Y. Tuning the photovoltaic performance of BT-TPA chromophore based solution-processed solar cells through molecular design incorporating of bithiophene unit and fluorine-substitution. *Dyes Pigments* **2015**, *118*, 37–44. [CrossRef]
- Sonar, P.; Ng, G.-M.; Lin, T.T.; Dodabalapur, A.; Chen, Z.-K. Solution processable low bandgap diketopyrrolopyrrole (DPP) based derivatives: Novel acceptors for organic solar cells. *J. Mater. Chem.* **2010**, *20*, 3626–3636. [CrossRef]

20. Cui, R.; Fan, L.; Yuan, J.; Jiang, L.; Chen, G.; Ding, Y.; Shen, P.; Li, Y.; Zou, Y. Effect of fluorination on the performance of poly(thieno[2,3-f]benzofuran-co-benzothiadiazole) derivatives. *RSC Adv.* **2015**, *5*, 30145–30152. [CrossRef]
21. Guo, S.; Ning, J.; Koerstgens, V.; Yao, Y.; Herzig, E.M.; Roth, S.V.; Mueller-Buschbaum, P. The Effect of Fluorination in Manipulating the Nanomorphology in PTB7:PC<sub>71</sub>BM Bulk Heterojunction Systems. *Adv. Energy Mater.* **2015**, *5*. [CrossRef]
22. Jo, J.W.; Jung, J.W.; Jung, E.H.; Ahn, H.; Shin, T.J.; Jo, W.H. Fluorination on both D and A units in D-A type conjugated copolymers based on difluorobithiophene and benzothiadiazole for highly efficient polymer solar cells. *Energy Environ. Sci.* **2015**, *8*, 2427–2434. [CrossRef]
23. Kim, H.G.; Kang, B.; Ko, H.; Lee, J.; Shin, J.; Cho, K. Synthetic Tailoring of Solid-State Order in Diketopyrrolopyrrole-Based Copolymers via Intramolecular Noncovalent Interactions. *Chem. Mater.* **2015**, *27*, 829–838. [CrossRef]
24. Wang, J.-L.; Wu, Z.; Miao, J.-S.; Liu, K.-K.; Chang, Z.-F.; Zhang, R.-B.; Wu, H.-B.; Cao, Y. Solution-Processed Diketopyrrolopyrrole-Containing Small-Molecule Organic Solar Cells with 7.0% Efficiency: In-Depth Investigation on the Effects of Structure Modification and Solvent Vapor Annealing. *Chem. Mater.* **2015**, *27*, 4338–4348. [CrossRef]
25. Cho, A.; Kim, Y.; Song, C.E.; Moon, S.-J.; Lim, E. Synthesis and Characterization of Fluorinated Benzothiadiazole-Based Small Molecules for Organic Solar Cells. *Sci. Adv. Mater.* **2014**, *6*, 2411–2415. [CrossRef]
26. Paek, S.; Cho, N.; Song, K.; Jun, M.J.; Lee, J.K.; Ko, J. Efficient Organic Semiconductors Containing Fluorine-Substituted Benzothiadiazole for Solution-Processed Small Molecule Organic Solar Cells. *J. Phys. Chem. C* **2012**, *116*, 23205–23213. [CrossRef]
27. Cho, N.; Song, K.; Lee, J.K.; Ko, J. Facile Synthesis of Fluorine-Substituted Benzothiadiazole-Based Organic Semiconductors and Their Use in Solution-Processed Small-Molecule Organic Solar Cells. *Chem. Eur. J.* **2012**, *18*, 11433–11439. [CrossRef] [PubMed]
28. Dutta, P.; Yang, W.; Eom, S.H.; Lee, S.-H. Synthesis and characterization of triphenylamine flanked thiazole-based small molecules for high performance solution processed organic solar cells. *Organic Electron.* **2012**, *13*, 273–282. [CrossRef]
29. Li, Z.; Dong, Q.; Li, Y.; Xu, B.; Deng, M.; Pei, J.; Zhang, J.; Chen, F.; Wen, S.; Gao, Y.; Tian, W. Design and synthesis of solution processable small molecules towards high photovoltaic performance. *J. Mater. Chem.* **2011**, *21*, 2159–2168. [CrossRef]
30. Lin, Y.; Cheng, P.; Li, Y.; Zhan, X. A 3D star-shaped non-fullerene acceptor for solution-processed organic solar cells with a high open-circuit voltage of 1.18 V. *Chem. Commun.* **2012**, *48*, 4773–4775. [CrossRef] [PubMed]
31. Vijay Kumar, C.; Cabau, L.; Koukaras, E.N.; Sharma, G.D.; Palomares, E. Efficient solution processed D<sub>1</sub>-A-D<sub>2</sub>-A-D<sub>1</sub> small molecules bulk heterojunction solar cells based on alkoxy triphenylamine and benzo[1,2-*b*:4,5-*b'*]thiophene units. *Organic Electron.* **2015**, *26*, 36–47. [CrossRef]
32. Patil, H.; Chang, J.; Gupta, A.; Bilic, A.; Wu, J.; Sonar, P.; Bhosale, S.V. Isoindigo-Based Small Molecules with Varied Donor Components for Solution-Processable Organic Field Effect Transistor Devices. *Molecules* **2015**, *20*, 17362–17377. [CrossRef] [PubMed]
33. Bagde, S.S.; Park, H.; Yang, S.-N.; Jin, S.-H.; Lee, S.-H. Diketopyrrolopyrrole-based narrow band gap donors for efficient solution-processed organic solar cells. *Chem. Phys. Lett.* **2015**, *630*, 37–43. [CrossRef]
34. Mikroyannidis, J.A.; Stylianakis, M.M.; Suresh, P.; Balraju, P.; Sharma, G.D. Low band gap vinylene compounds with triphenylamine and benzothiadiazole segments for use in photovoltaic cells. *Organic Electron.* **2009**, *10*, 1320–1333. [CrossRef]
35. Tolman, C.A.; Seidel, W.C.; Gerlach, D.H. Triarylphosphine and ethylene complexes of zerovalent nickel, palladium, and platinum. *J. Am. Chem. Soc.* **1972**, *94*, 2669–2676. [CrossRef]
36. Kato, S.-I.; Matsumoto, T.; Ishi-i, T.; Thiemann, T.; Shigeiwa, M.; Gorohmaru, H.; Maeda, S.; Yamashita, Y.; Mataka, S. Strongly red-fluorescent novel donor- $\pi$ -bridge-acceptor- $\pi$ -bridge-donor (D- $\pi$ -A- $\pi$ -D) type 2,1,3-benzothiadiazoles with enhanced two-photon absorption cross-sections. *Chem. Commun.* **2004**, *20*, 2342–2343. [CrossRef] [PubMed]
37. Zou, Y.; Gendron, D.; Badrou-Aïch, R.; Najari, A.; Tao, Y.; Leclerc, M. A High-Mobility Low-Bandgap Poly(2,7-carbazole) Derivative for Photovoltaic Applications. *Macromolecules* **2009**, *42*, 2891–2894. [CrossRef]

38. Huang, J.; Zhan, C.; Zhang, X.; Zhao, Y.; Lu, Z.; Jia, H.; Jiang, B.; Ye, J.; Zhang, S.; Tang, A.; *et al.* Solution-Processed DPP-Based Small Molecule that Gives High Photovoltaic Efficiency with Judicious Device Optimization. *ACS Appl. Mater. Interfaces* **2013**, *5*, 2033–2039. [CrossRef] [PubMed]
39. Uhrich, C.; Schueppel, R.; Petrich, A.; Pfeiffer, M.; Leo, K.; Brier, E.; Kilickiran, P.; Baeuerle, P. Organic Thin-Film Photovoltaic Cells Based on Oligothiophenes with Reduced Bandgap. *Adv. Funct. Mater.* **2007**, *17*, 2991–2999. [CrossRef]
40. Lu, Z.; Li, C.-H.; Du, C.; Gong, X.; Bo, Z.-S. 6,7-dialkoxy-2,3-diphenylquinoxaline based conjugated polymers for solar cells with high open-circuit voltage. *Chin. J. Polym. Sci.* **2013**, *31*, 901–911. [CrossRef]
41. Shang, Y.; Hao, S.; Liu, J.; Tan, M.; Wang, N.; Yang, C.; Chen, G. Synthesis of Upconversion beta-NaYF<sub>4</sub>:Nd<sup>3+</sup>/Yb<sup>3+</sup>/Er<sup>3+</sup> Particles with Enhanced Luminescent Intensity through Control of Morphology and Phase. *Nanomaterials* **2015**, *5*, 218–232. [CrossRef]



© 2016 by the authors. Licensee MDPI, Basel, Switzerland. This article is an open access article distributed under the terms and conditions of the Creative Commons Attribution (CC BY) license (<http://creativecommons.org/licenses/by/4.0/>).

Communication

# Morphology-Controlled High-Efficiency Small Molecule Organic Solar Cells without Additive Solvent Treatment

Il Ku Kim <sup>1,\*</sup>, Jun Hyung Jo <sup>2</sup> and Jung-Ho Yun <sup>3</sup>

<sup>1</sup> National Photonics Semiconductor Lab, National Photonics Semiconductor Inc., Suwon-Si 17113, Korea

<sup>2</sup> School of Information and Communication Technology, Griffith University, Southport QLD 4222, Australia; j.jo@griffith.edu.au

<sup>3</sup> Nanomaterials Centre, School of Chemical Engineering, University of Queensland, Brisbane QLD 4072, Australia; j.yun1@uq.edu.au

\* Correspondence: cto.np@npsemi.com; Tel.: +82-31-907-7950

Academic Editor: Guanying Chen

Received: 23 February 2016; Accepted: 29 March 2016; Published: 8 April 2016

**Abstract:** This paper focuses on nano-morphology-controlled small-molecule organic solar cells without solvent treatment for high power-conversion efficiencies (PCEs). The maximum high PCE reaches up to 7.22% with a bulk-heterojunction (BHJ) thickness of 320 nm. This high efficiency was obtained by eliminating solvent additives such as 1,8-diiodooctane (DIO) to find an alternative way to control the domain sizes in the BHJ layer. Furthermore, the generalized transfer matrix method (GTMM) analysis has been applied to confirm the effects of applying a different thickness of BHJs for organic solar cells from 100 to 320 nm, respectively. Finally, the study showed an alternative way to achieve high PCE organic solar cells without additive solvent treatments to control the morphology of the bulk-heterojunction.

**Keywords:** small molecule; organic solar cell; bulk-heterojunction; optical simulation

## 1. Introduction

During the last decades, bulk-heterojunction (BHJ) small-molecule organic solar cells (OSCs) have received more research attention [1–9]. BHJ OSCs have interpenetrating networks in a blend of conjugated organic donors and fullerene-derivative acceptors for their alternative potential in obtaining low-cost clean energy solutions [1–6]. Among the many research issues, surface morphology control is an essential part of the spin-coating process to form thin films to get high-efficiency OSCs [2]. In the BHJ photoactive layer, the ultrafast photo-induced charge transfer at the interface of the phase-separated acceptor and donor is also needed for the high performance of OSCs before charge recombination has happened [10–12]. However, despite polymeric BHJ OSCs reported with high power conversion efficiencies (PCEs), others have pointed out some drawbacks. For instance, the organic polymer has batch-to-batch variations, molecular weight differences, polydispersity and impurity which could lead to a major obstacle for high-performance organic solar cells [2,13–15]. To address the above issues, small-molecule BHJs (SM BHJs) were introduced [1–5,8].

In contrast, it has been reported that solution-processed small-molecule BHJ solar cells have a well-defined molecular structure with intermediate dimensions [1,2]. Examples of solution-processed SM BHJ OSCs with PCEs ranging from 6.7% to 8.01% have been reported with a 1,8-diiodooctane (DIO) additive solution [1–4]. These results were mainly obtained from the morphological control of the BHJ layer in terms of the additive solvent treatment. However, there are major concerns surrounding morphology control by using an additive solution such as the optimization of solution ratio control,

and a limited number of applicable matching solutions (*i.e.*, chlorobenzene, 1,2-dichlorobenzene) [1–4]. In addition, the usage of a solvent additive affects unexpected solar cell performance. To avoid this, a study suggests the treatment of the active layer by drying speed or washout with methanol [16]. However, this is also not the fundamental method to solve the additional solvent problem issue. Therefore, it does not always guarantee a high efficiency of OSCs. Furthermore, strong aggregation is another problem during the spin-coating process used to produce a high quality of thin film for SM BHJs [2].

In this paper, we report solution-processed high-efficiency SM BHJ OSCs without a DIO additive solvent treatment. For that, a well-developed small-molecular donor (*p*-DTS(FBTTh<sub>2</sub>)<sub>2</sub>) will be applied [1–5]. This small-molecule donor has good characteristics of excellent solubility in organic solvents, strong optical absorption (600–800 nm) and a good hole mobility ( $\approx 0.1 \text{ cm}^2/\text{Vs}$ ) [2]. Furthermore, a generalized transfer matrix method (GTMM) for the optical modeling analysis result will be introduced to confirm the behavior of light absorption in the BHJ photoactive layer of different thicknesses [17–19].

## 2. Experimental Section

To address the particular issues mentioned above, OSCs fabricated through the incorporation of a donor-acceptor blend of *p*-DTS(FBTTh<sub>2</sub>)<sub>2</sub> and [6,6]-phenyl-C<sub>71</sub>-butyric-acid-methyl-ester (PC<sub>70</sub>BM) to form a BHJ photoactive layer. Chemical structures for OSC showed in Figure 1a. *p*-DTS(FBTTh<sub>2</sub>)<sub>2</sub> and PC<sub>70</sub>BM were dissolved in chlorobenzene (CB) and stirred over 24 h with a total concentration of 50 mg/mL. Indium tin oxide (ITO)-coated glass substrates were cleaned sequentially by ultrasonic treatment in Alconox detergent, deionized water, acetone and isopropyl alcohol. A polymeric conducting thin layer of PEDOT:PSS (40 nm) was spun-cast on top of the ITO-coated glass substrate. Before spin-coating of BHJ thin film, co-dissolved donor-acceptor blend was heated at 100 °C for 30 min. Then the *p*-DTS(FBTTh<sub>2</sub>)<sub>2</sub>:PC<sub>70</sub>BM BHJ layer was spin-cast from the heated and blended solution with different spin speed to form a different thickness of BHJs from 300 to 2000 rpm. During the solution preparation and film formation processes, 1,8-diiodooctane (DIO) additive solvent treatment was avoided. Finally, Ca (5 nm) and Al (100 nm) electrodes were deposited on top of BHJ photoactive layer (Figure 1b). Post-annealing process is also not applied for all devices. The energy band diagram of SM BHJ OSC showed in Figure 1c. Electrical characterization of all OSCs had done in the air after encapsulation. A commercial *J-V* and external quantum efficiency (EQE) characterization system was supplied by PV Measurement Inc. (Boulder, CO, USA) to obtain the data. A GTMM analysis was accomplished to calculate and analyse the multi-layered interface OSCs. For transfer matrix analysis, optical constants of all layers have been obtained by the ellipsometry method. Finally, the nano-morphology of BHJ film was investigated by atomic force microscopy (AFM).

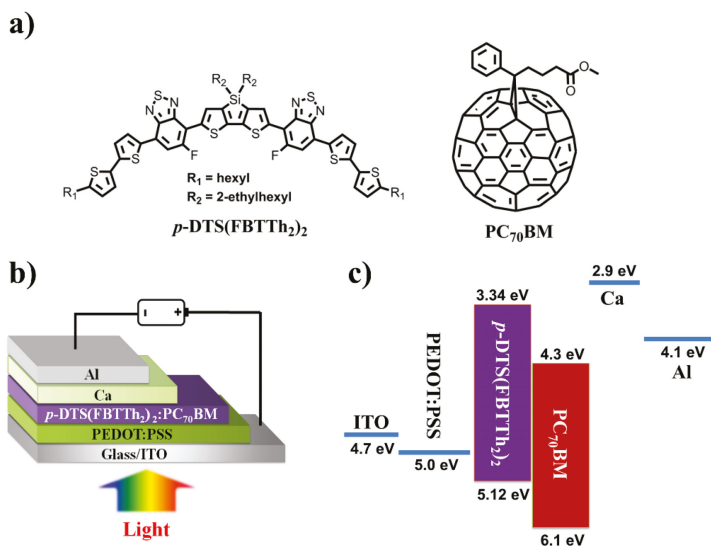


**Figure 1.** (a) Chemical structures of  $p$ -DTS(FBTTh<sub>2</sub>)<sub>2</sub> and PC<sub>70</sub>BM; (b) device architecture for small-molecule bulk-heterojunction organic solar cells (SM BHJ OSCs); (c) band diagram of SM BHJ OSCs.

### 3. Results and Discussion

SM BHJ OSCs have been tested under simulated 100 mW/cm<sup>2</sup> Air Mass (AM) 1.5G illumination. The optimized ratio of the small molecule donor ( $p$ -DTS(FBTTh<sub>2</sub>)<sub>2</sub>) to PC<sub>70</sub>BM was chosen to be the same as the reported ratio (60:40  $w/w$ ) [1]. Device current density/voltage ( $J$ - $V$ ) characteristics of SM BHJ OSCs, in terms of BHJ without DIO treatment, with different photoactive thicknesses are shown in Figure 2.

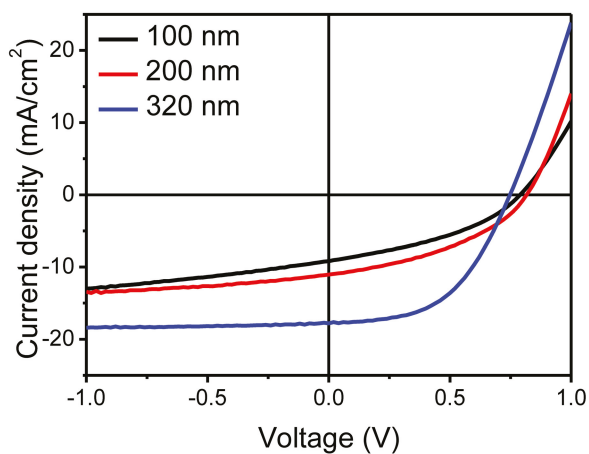


**Figure 2.** Measured density/voltage ( $J$ - $V$ ) curves of SM BHJ OSCs.

A  $V_{oc}$  as high as 0.74 V was observed in all devices. Combined with its high  $J_{sc}$  and fill factor ( $FF$ ), a high power conversion efficiency (PCE) of 6.83% on average was measured with 320-nm-thick



devices and the highest PCE was measured at 7.22% ( $V_{oc} = 0.74$  V,  $J_{sc} = 18.23$  mA/cm<sup>2</sup>,  $FF = 0.54$ ). The measured PCE of our device (2.78%) is much greater than the reported PCE value (1.8%) with the same BHJ thickness of 100 nm [1]. It is strong evidence to confirm that an additive solvent such as DIO is not an essential part for controlling the device performance, while the majority of the research groups have focused on using an additive solvent to control the *p*-DTS(FBTTh<sub>2</sub>)<sub>2</sub> and small molecule donor materials.

The EQE spectra were obtained to confirm the accuracy of the SM BHJ OSC's photo-generated *J*-*V* result. The results are shown in Figure 3. Significantly, an EQE over 70% was achieved with a 320 nm SM BHJ photoactive layer from a wavelength range of 350–700 nm. A 1.5 G spectrum was applied to calculate the  $J_{sc}$  value by integrating the EQE data. The calculated  $J_{sc}$  values are in good agreement with the directly measured values. Furthermore, these EQE spectra confirm Beer-Lambert law by increasing the photoactive layer thicknesses. It is good to note that EQE spectra results obtained much better results to compare with the literature [1,3,4,8]. A summary of the SM BHJ OSCs' performance is shown in Table 1.

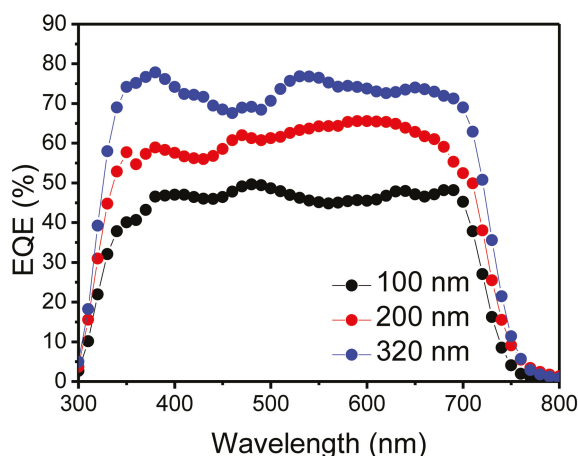


**Figure 3.** Measured external quantum efficiency (EQE) spectra of SM BHJ OSCs.

**Table 1.** A summary of SM BHJ OSC performances with changes of BHJ thickness. (PCE: Power conversion efficiency.)

BHJ Thickness	$V_{oc}$ (V)	$J_{sc}$ (mA/cm <sup>2</sup> )	Fill Factor	PCE (%)
100 nm	0.78	9.2	0.39	2.78
200 nm	0.80	11.1	0.41	3.64
320 nm	0.74	17.8	0.52	6.83

Figure 4 shows the calculated charge generation rate (in s<sup>-1</sup>.cm<sup>-3</sup>) of SM BHJ OSCs obtained by the generalized transfer matrix method (GTMM). These calculated charge generation rate results provide a further explanation as to why a thicker junction of OSC has a higher  $J_{sc}$  value than a thinner junction of OSCs. From Figure 4a, the peak charge generation rate is located in the middle of the SM BHJ. In comparison with Figure 4b,c, the charge generation rate has the highest value in 100-nm-thick BHJ. However, under the thin junction circumstance, there is interference between the forward direction waves by absorption from the glass side and the backward direction waves by reflections from the electrodes in the photoactive layer. Therefore, the interference effect brings a low  $J_{sc}$  value in thin junction OSCs. By increasing the photoactive layer thickness containing BHJ, the OSC follows

Beer-Lambert law. Therefore, the photo-generation rate is exponentially decreased by increasing the photoactive layer thickness.

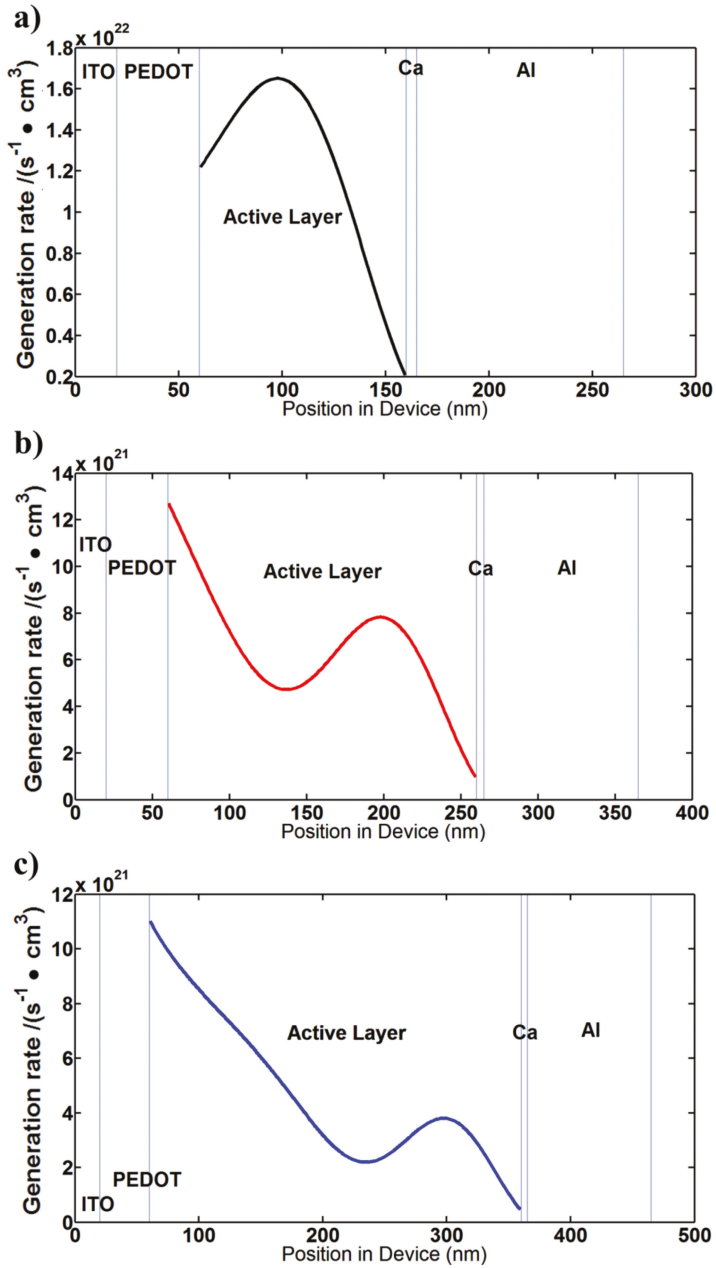


**Figure 4.** Simulation results of charge generation rates of SM BHJ OSCs: (a) BHJ active layer = 100 nm; (b) BHJ active layer = 200 nm; (c) BHJ active layer = 320 nm.

An AFM two-dimensional (2D) topography image of the *p*-DTS(FBTTh<sub>2</sub>)<sub>2</sub>:PC<sub>70</sub>BM BHJ film (thickness = 320 nm) is shown in Figure 5a. As reported, conjugated small molecules tend to aggregate strongly and form a crystalline structure [1–4,8,20]. Therefore, we assumed that the smaller domains in the device allow for a higher donor-acceptor interface area [1–4,8]. Finally, it has more efficient generations of charge carriers. From the literature, it has been suggested that below 15 nm, morphology control of the high efficiency of the small molecular solar cell is guaranteed [1–4,8]. In Figure 5b, it confirms that avoiding solvent treatment is effectively working in the control of the BHJ domains within 3 nm. Therefore, this would be strong and robust evidence of the morphology control of BHJ films without DIO solvent treatment.

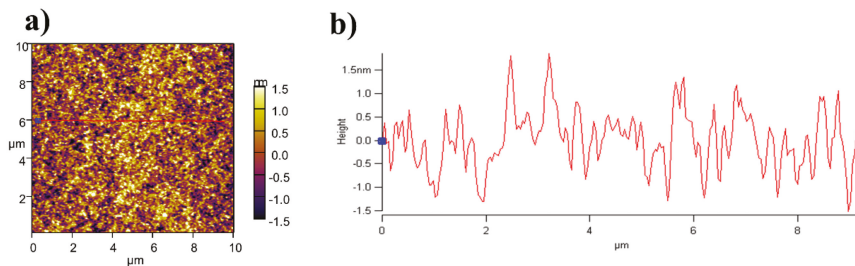


**Figure 5.** Measured atomic force microscopy (AFM) image of BHJ with a thickness of 320 nm: (a) top view of AFM; (b) measured cross-section of BHJ.

#### 4. Conclusions

In conclusion, we studied the high performance of small-molecule organic solar cells without additive solvent treatment on the control of the photoactive layer in nano-morphology. Significantly, we have obtained small-molecule organic solar cells with a comparable PCE of 7.22% by eliminating the DIO additional solvent treatment. Also, GTMM analysis was accomplished to confirm the effect of the thickness variations of SM BHJ OSCs. Lastly, AFM measurement also confirms that smaller domains have achieved efficient charge generation. These results provide significant progress in showing that solution-processed small-molecule organic solar cells without solvent treatment can be an alternative method to having a high-PCE device with polymeric and/or small-molecule counterparts.

**Author Contributions:** I.K.K. and J.H.J. conceived and designed the experiments; I.K.K. performed the experiments; I.K.K. and J.H.J. analyzed the data; J.H.Y. contributed AFM analysis; I.K.K. wrote the paper.

**Conflicts of Interest:** The authors declare no conflict of interest.

#### References

1. Van der Poll, T.S.; Love, J.A.; Nguyen, T.Q.; Bazan, G.C. Non-Basic High-Performance Molecules for Solution-Processed Organic Solar Cells. *Adv. Mater.* **2012**, *24*, 3646–3649. [CrossRef] [PubMed]
2. Sun, Y.; Welch, G.C.; Leong, W.L.; Takacs, C.J.; Bazan, G.C.; Heeger, A.J. Solution-processed small-molecule solar cells with 6.7% efficiency. *Nat. Mater.* **2012**, *11*, 44–48. [CrossRef] [PubMed]
3. Kyaw, A.K.K.; Wang, D.H.; Gupta, V.; Leong, W.L.; Ke, L.; Bazan, G.C.; Heeger, A.J. Intensity dependence of current-voltage characteristics and recombination in high-efficiency solution-processed small-molecule solar cells. *ACS Nano* **2013**, *7*, 4569–4577. [CrossRef] [PubMed]
4. Gupta, V.; Kyaw, A.K.K.; Wang, D.H.; Chand, S.; Bazan, G.C.; Heeger, A.J. Barium: An efficient cathode layer for bulk-heterojunction solar cells. *Sci. Rep.* **2013**, *3*. [CrossRef] [PubMed]
5. Zhang, Q.; Kan, B.; Liu, F.; Long, G.; Wan, X.; Chen, X.; Zuo, Y.; Ni, W.; Zhang, H.; Li, M. Small-molecule solar cells with efficiency over 9%. *Nat. Photon.* **2015**, *9*, 35–41. [CrossRef]
6. Zhao, J.; Li, Y.; Yang, G.; Jiang, K.; Lin, H.; Ade, H.; Ma, W.; Yan, H. Efficient organic solar cells processed from hydrocarbon solvents. *Nat. Energy* **2016**, *1*. [CrossRef]

7. Li, W.; Hendriks, K.H.; Roelofs, W.; Kim, Y.; Wienk, M.M.; Janssen, R.A. Efficient small bandgap polymer solar cells with high fill factors for 300 nm thick films. *Adv. Mater.* **2013**, *25*, 3182–3186. [CrossRef] [PubMed]
8. Kyaw, A.K.K.; Wang, D.H.; Gupta, V.; Zhang, J.; Chand, S.; Bazan, G.C.; Heeger, A.J. Efficient Solution-Processed Small-Molecule Solar Cells with Inverted Structure. *Adv. Mater.* **2013**, *25*, 2397–2402. [CrossRef] [PubMed]
9. Sharenko, A.; Proctor, C.M.; van der Poll, T.S.; Henson, Z.B.; Nguyen, T.Q.; Bazan, G.C. A High-Performing Solution-Processed Small Molecule: Perylene Diimide Bulk Heterojunction Solar Cell. *Adv. Mater.* **2013**, *25*, 4403–4406. [CrossRef] [PubMed]
10. Koster, L.; Smits, E.; Mihaiiletschi, V.; Blom, P. Device model for the operation of polymer/fullerene bulk heterojunction solar cells. *Phys. Rev. B* **2005**, *72*. [CrossRef]
11. Street, R.; Cowan, S.; Heeger, A. Experimental test for geminate recombination applied to organic solar cells. *Phys. Rev. B* **2010**, *82*. [CrossRef]
12. Cowan, S.R.; Street, R.; Cho, S.; Heeger, A. Transient photoconductivity in polymer bulk heterojunction solar cells: competition between sweep-out and recombination. *Phys. Rev. B* **2011**, *83*. [CrossRef]
13. Walker, B.; Kim, C.; Nguyen, T.Q. Small molecule solution-processed bulk heterojunction solar cells. *Chem. Mater.* **2010**, *23*, 470–482. [CrossRef]
14. Coffin, R.C.; Peet, J.; Rogers, J.; Bazan, G.C. Streamlined microwave-assisted preparation of narrow-bandgap conjugated polymers for high-performance bulk heterojunction solar cells. *Nat. Chem.* **2009**, *1*, 657–661. [CrossRef] [PubMed]
15. Tong, M.; Cho, S.; Rogers, J.T.; Schmidt, K.; Hsu, B.B.Y.; Moses, D.; Coffin, R.C.; Kramer, E.J.; Bazan, G.C.; Heeger, A.J. Higher molecular weight leads to improved photoresponsivity, charge transport and interfacial ordering in a narrow bandgap semiconducting polymer. *Adv. Func. Mater.* **2010**, *20*, 3959–3965. [CrossRef]
16. Ye, L.; Jing, Y.; Guo, X.; Sun, H.; Zhang, S.; Zhang, M.; Huo, L.; Hou, J. Remove the residual additives toward enhanced efficiency with higher reproducibility in polymer solar cells. *J. Phys. Chem. C* **2013**, *117*, 14920–14928. [CrossRef]
17. Burkhard, G.F.; Hoke, E.T.; McGehee, M.D. Accounting for interference, scattering, and electrode absorption to make accurate internal quantum efficiency measurements in organic and other thin solar cells. *Adv. Mater.* **2010**, *22*, 3293–3297. [CrossRef] [PubMed]
18. Zhao, X.; Li, Z.; Zhu, T.; Mi, B.; Gao, Z.; Huang, W. Structure optimization of organic planar heterojunction solar cells. *J. Phys. D* **2013**, *46*. [CrossRef]
19. Jo, J.H.; Chun, Y.-S.; Kim, I. Optical Modeling-Assisted Characterization of Polymer: Fullerene Photodiodes. *IEEE Photonics J.* **2014**, *6*, 1–7.
20. Liu, Y.; Zhao, J.; Li, Z.; Mu, C.; Ma, W.; Hu, H.; Jiang, K.; Lin, H.; Ade, H.; Yan, H. Aggregation and morphology control enables multiple cases of high-efficiency polymer solar cells. *Nat. Commun.* **2014**, *5*. [CrossRef] [PubMed]



© 2016 by the authors. Licensee MDPI, Basel, Switzerland. This article is an open access article distributed under the terms and conditions of the Creative Commons Attribution (CC BY) license (<http://creativecommons.org/licenses/by/4.0/>).



Article

# Enhancing the Photocurrent of Top-Cell by Ellipsoidal Silver Nanoparticles: Towards Current-Matched GaInP/GaInAs/Ge Triple-Junction Solar Cells

Yiming Bai <sup>1,\*</sup>, Lingling Yan <sup>1</sup>, Jun Wang <sup>2</sup>, Lin Su <sup>1</sup>, Zhigang Yin <sup>3</sup>, Nuofu Chen <sup>1,\*</sup> and Yuanyuan Liu <sup>3</sup>

<sup>1</sup> State Key Laboratory of Alternate Electrical Power System with Renewable Energy Sources, North China Electric Power University, Beijing 102206, China; dgunwung@163.com (L.Y.); 18229799348@163.com (L.S.)

<sup>2</sup> Institute of Information Photonics and Optical Communications, Beijing University of Posts and Telecommunications, Beijing 100876, China; wangjun@semi.ac.cn

<sup>3</sup> Key Laboratory of Semiconductor Materials Science, Institute of Semiconductors, Chinese Academy of Sciences, P.O. Box 912, Beijing 100083, China; yzhg@semi.ac.cn (Z.Y.); liuyy@semi.ac.cn (Y.L.)

\* Correspondence: ymbai@ncepu.edu.cn (Y.B.); nfchen@ncepu.edu.cn (N.C.);  
Tel.: +86-10-6177-2455 (Y.B. & N.C.); Fax: +86-10-6177-2816 (Y.B. & N.C.)

Academic Editors: Guanying Chen, Zhijun Ning and Hans Agren

Received: 6 April 2016; Accepted: 16 May 2016; Published: 25 May 2016

**Abstract:** A way to increase the photocurrent of top-cell is crucial for current-matched and highly-efficient GaInP/GaInAs/Ge triple-junction solar cells. Herein, we demonstrate that ellipsoidal silver nanoparticles (Ag NPs) with better extinction performance and lower fabrication temperature can enhance the light harvest of GaInP/GaInAs/Ge solar cells compared with that of spherical Ag NPs. In this method, appropriate thermal treatment parameters for Ag NPs without inducing the dopant diffusion of the tunnel-junction plays a decisive role. Our experimental and theoretical results confirm the ellipsoidal Ag NPs annealed at 350 °C show a better extinction performance than the spherical Ag NPs annealed at 400 °C. The photovoltaic conversion efficiency of the device with ellipsoidal Ag NPs reaches 31.02%, with a nearly 5% relative improvement in comparison with the device without Ag NPs (29.54%). This function of plasmonic NPs has the potential to solve the conflict of sufficient light absorption and efficient carrier collection in GaInP top-cell devices.

**Keywords:** GaInP/GaInAs/Ge triple-junction solar cells; Ag ellipsoidal nanoparticles; thermal treatment parameters; current-match

## 1. Introduction

Currently, GaInP/GaInAs/Ge triple-junction solar cells (TJSCs) for space and terrestrial concentrator applications have attracted increasing attention for their very high conversion efficiencies [1–3] and dramatic reduction in cost [4]. Such TJSCs with different subcell bandgaps divide the broad solar spectrum into three narrower sections, each of which can be converted to electricity more efficiently [5,6], while the 50% theoretical efficiency have not been obtained as expected due to the current mismatch among the subcells [7,8]. There are two aspects of this problem that have to be addressed. The first involves the Ge subcell, which absorbs approximately two times that photons than that needed for current matching with the GaInP and GaAs subcells [6]. The second problem relates to the lowest photocurrent of GaInP top-cells, which limits the efficiency of TJSCs greatly [9]. To the former, some reports suggest that the Ge bottom-cell would be replaced by a material with a bandgap of 1.0 eV, such as GaInNAs [10], but it is confined by the requirements of lattice matching

with the other junctions and a higher epitaxy technique. Hence, improving the photocurrent of GaInP top-cell to approach other subcells is an effective way for enhancing the conversion efficiency of TJSCs.

For the commercialized case of the lattice-matched  $\text{Ga}_{0.49}\text{In}_{0.51}\text{P}/\text{Ga}_{0.99}\text{In}_{0.01}\text{As}/\text{Ge}$  TJSCs, the bandgap energies are 1.9, 1.4, and 0.67 eV, respectively, which means each subcell has its very specific absorption spectrum [11–13]. Hence, the maximum number of photons absorbed by each subcell seems to be expected only if their optical thickness was thick enough. However, the short minority carrier lifetime of a few nanoseconds present in GaInP film limits the typical minority carrier diffusion lengths [14]. Consequently, the thickness of GaInP top-cell is generally allowed in the order of hundreds of nanometers for carrier collection other than its theoretical optical thickness of micrometers, resulting in unsatisfactory absorption of incident solar radiation [15]. Meanwhile, taking the material consumption into account, it also motivates a reduction in thickness of the active region of solar cells [16]. Therefore, a feasible and effective approach should be explored urgently for solving the puzzle between sufficient light absorption and efficient carrier collection in GaInP top-cell.

Most recently, an appealing approach involves the plasmonic nanostructures. The advantages of surface plasmon excitations is attributed to two aspects. The first involves an obviously increased material extinction for incident light arising from an enhanced local electromagnetic field near the nanostructures [17]. The other relates to the extended incident light path owing to a strong scattering of incident light into the active region of solar cells, with a result of increase in absorption and the promotion of photovoltaic conversion efficiency [18]. To date, many studies provide insights into the metal plasmonic nanostructures and, therefore, contribute greatly to practical photovoltaic applications [19–23]. However, few investigations are available on clarifying the feasibility of plasmonic nanostructures for GaInP/GaInAs/Ge TJSCs because the thermal treatment process for fabrication nanoparticles (NPs) is easy to cause the dopant diffusion in the highly-doped tunnel junction [24]. It is well known that annealing metal film is the simplest method to obtain metal nanoparticles. Unfortunately, too low an annealing temperature is not suitable for the formation of metal NPs, and too high an annealing temperature will greatly degrade the performance of TJSCs derived from the diffusion of dopant in TJSCs [25]. However, double hetero-structure tunnel junctions with wider bandgaps and lower diffusion coefficients are known for effectively suppressing impurity diffusion [13], so the problem of impurity diffusion in tunnel junctions is not an insurmountable barrier for improving the photocurrent of GaInP top-cells. Therefore, exploiting appropriate thermal treatment conditions for silver (Ag) NPs without inducing the dopant diffusion is an important strategy needing further study. Herein, the present work was aimed at promoting the photocurrent of GaInP top-cell using plasmonic nanostructures and, therefore, the efficiency of TJSCs.

In this work, Ag NPs were adopted because their extinction spectral range [26] is almost perfectly matched with the absorption range of the GaInP top-cell, and a series of experiments on annealing temperature, exposure time, and heating rate were proceeded to facilitate the light absorption of GaInP top-cell. We found that both the experimental and theoretical study confirmed the ellipsoidal Ag NPs annealed at 350 °C show a better extinction performance than the spherical Ag NPs annealed at 400 °C. The photovoltaic conversion efficiency of the device with ellipsoidal Ag NPs reaches 31.02%, with a nearly 5% relative improvement in comparison with the device without Ag NPs. The findings provide a feasible, cost-effective solution to solve the puzzle between the carrier collection and optical absorption in GaInP top-cells.

## 2. Experiments

The material growth of TJSCs on a p-type Ge substrate was performed by metal-organic vapor phase epitaxy (MOVPE) and the growth conditions were similar to those described elsewhere [27]. Figure 1a shows a schematic illustration of the material structure of the GaInP/GaInAs/Ge TJSCs evaluated in this work. The overall layer structure for the cell contains three pn-junctions and two tunnel junctions between the subcells. The  $\text{Ga}_{0.51}\text{In}_{0.49}\text{P}$  top-cell,  $\text{Ga}_{0.99}\text{In}_{0.01}\text{As}$  middle-cell, and Ge bottom-cell are all lattice-matched, which can effectively avoid the formation of dislocations

and ensure excellent material quality. The three subcells were series connected with two highly-doped and ultra-thin tunnel junctions, which are favorable for a low resistance and high current density. The device processing on ohmic contacts, wet etching, and anti-reflection coatings were performed after the theoretical design of electrode patterns and anti-reflection coatings. The cell size was  $10 \times 11 \text{ mm}^2$  and 1 mm grid pitch of electrode was designed for an optimal electrode distribution under one-sun operation. The performance characterization of current density-voltage ( $J$ - $V$ ) characteristic curves and external quantum efficiency (EQE) for devices without Ag NPs has been measured. The device parameters of short-circuit current density, open circuit voltage, and efficiency are averaged from 12 individual devices with spherical or ellipsoidal NPs, respectively.

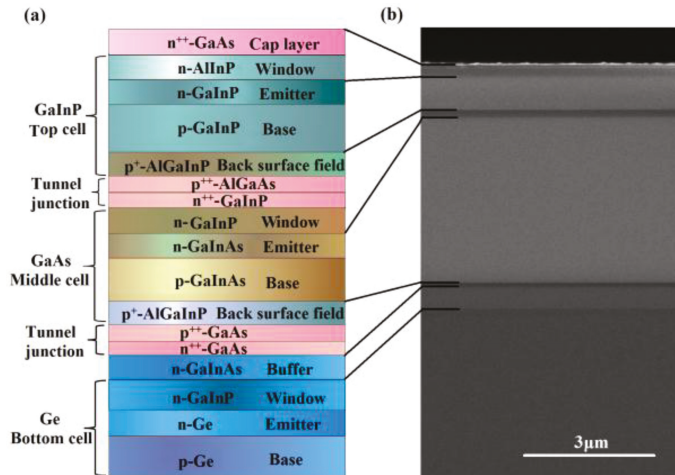


**Figure 1.** (a) Schematic layer structure and (b) cross-sectional view scanning electron microscope (SEM) image of the epitaxial structure of GaInP/GaInAs/Ge triple-junction solar cells (TJSCs).

Then, Ag films with 7 nm thickness were deposited on TJSCs at room temperature by magnetron sputtering, and the detailed fabrication processes can be referred to our previous work [18]. In consideration of the growth temperature for epitaxial layers is about 600–700 °C, the annealing temperature and temperature fluctuation for Ag film were strictly controlled. To the former, it is no higher than 450 °C, and to the latter, it is no more than 10 °C according to the computer supervising system. A series of experiments were performed for obtaining an optimal annealing temperature, exposure time, and heating rate. Lastly, the parameters were given as the following: the Ag films were annealed at 350 and 400 °C for 10 min under a nitrogen atmosphere with a heating rate of 150 °C/s. The resulting samples of ellipsoidal and spherical Ag NPs were shown in Figure 2.

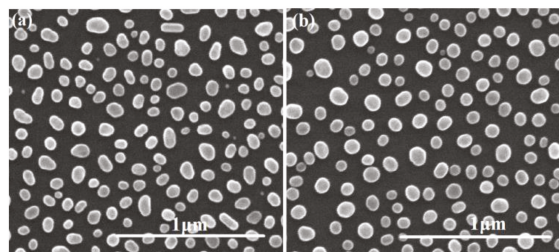


**Figure 2.** Plane-view SEM images of (a) ellipsoidal and (b) spherical Ag NPs.



Surface morphologies of Ag NPs were observed by a NOVA NANOSEM 650 scanning electron microscopy (SEM, FEL, Brno, Czech Republic). The optical properties were measured by an ultraviolet-visible spectrophotometer (UV spectrophotometer, Cary 5000, Varian, Palo Alto, CA, USA). The current density versus voltage ( $J$ - $V$ ) characteristic was tested by New-port 92250A Solar Simulator (Newport, Irvine, CA, USA) under one-sun AM1.5 ( $1000 \text{ W/m}^2$ ,  $25^\circ\text{C}$ ) standard test conditions. The light response property of the devices was further investigated using Qtest-2000 external quantum efficiency (EQE) systems (Crowntech, PA, USA).

### 3. Results and Discussion

#### 3.1. Epitaxial Structure and Performance of GaInP/GaInAs/Ge TJSCs

Figure 1b demonstrates the cross-sectional view SEM image of the epitaxial structure of the GaInP/GaInAs/Ge TJSCs. As can be seen, the cell has a clear configuration and distinct interfaces, and the epitaxial structure mainly includes a  $0.40\text{-}\mu\text{m}$ -thick GaInAs buffer layer, a  $3.75\text{-}\mu\text{m}$ -thick middle-cell and a  $0.75\text{-}\mu\text{m}$ -thick top-cell, as well as two  $0.03\text{-}\mu\text{m}$ -thick tunnel junctions. The thickness of each layer, the doping concentration level and the material composition are based on the theoretical optimization. The  $J$ - $V$  characteristic curve of TJSCs without Ag NPs under AM 1.5G solar irradiation ( $100 \text{ mW/cm}^2$ ) is presented in Figure 3a. As can be seen, the short-circuit current density ( $J_{sc}$ ), open circuit voltage ( $V_{oc}$ ), and photovoltaic conversion efficiency ( $\eta$ ) are  $13.56 \text{ mA/cm}^2$ ,  $2.57 \text{ V}$  and  $29.54\%$ , respectively.

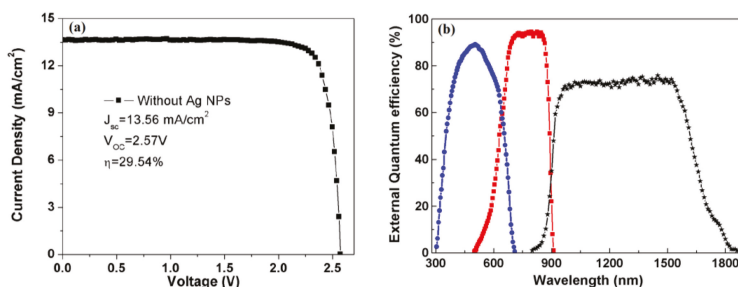


**Figure 3.** (a) Current-voltage ( $J$ - $V$ ) characteristic curve and (b) external quantum efficiency of the GaInP/GaInAs/Ge device.

Previous researches demonstrate that the  $J_{sc}$  of TJSCs is limited by one of the subcells [28,29], but the  $J_{sc}$  of each subcell cannot be directly obtained by  $J$ - $V$  measurement. Therefore, the light response property of the devices was measured to calculate the  $J_{sc}$  of each subcell using EQE. Figure 3b exhibits the EQE of GaInP, GaInAs, and Ge subcells for the TJSCs without Ag NPs. Here, the absorption edges of GaInP, GaInAs, and Ge subcells are  $670$ ,  $900$ , and  $1800 \text{ nm}$ , respectively. The EQE curves of the top- and middle-cell both drop rapidly near their absorption edges versus the gradual-decreasing modes of Ge bottom cell when wavelength ranges from  $1600$  to  $1800 \text{ nm}$ , which stems from the severe back surface recombination of Ge bottom-cell. The integrated current density for top-, middle- and bottom-cell is  $13.70$ ,  $14.21$ , and  $18.35 \text{ mA/cm}^2$ , respectively, which is in good agreement with the  $J_{sc}$  ( $13.56 \text{ mA/cm}^2$ ) of the  $J$ - $V$  measurement. It can be concluded that the  $J_{sc}$  of the TJSCs is limited by the GaInP top-cell, and an appropriate approach of increasing photocurrent of the top-cell is indispensable for high-performance TJSCs.

#### 3.2. Morphology and Optical Properties of Ag NPs

Figure 2 presents the plane-view SEM images of the samples of Ag films annealed at  $350$  and  $400^\circ\text{C}$ , respectively. As seen in Figure 2a, the Ag film was transformed into ellipsoid-like Ag NPs with

smooth surface after annealing at 350 °C. The average principal axes length  $2a-c$  of these ellipsoidal particles are 76, 94, and 76 nm. While the Ag NPs annealed at 400 °C appear very nearly spherical in shape with an average diameter  $D$  of 88 nm, as shown in Figure 2b. The average sizes of those ellipsoidal and spherical particles in Figure 2a,b are statistically determined by ImageJ software (National Institutes of Health, Bethesda, MD, USA). Hence, the Ag NPs exhibit obviously different morphology features at the two annealing temperatures of 350 and 400 °C, and the shape the Ag NPs tends to be ellipsoid-like at lower annealing temperatures.

The insights into the metal plasmonic nanostructures require a deep understanding of their optical properties. Figure 4 displays both the experimental and theoretical extinction spectra for ellipsoidal and spherical Ag NPs. For comparison, the experimental results are marked with solid lines and the theoretical extinction spectra are marked with dashed lines. Samples of those Ag NPs fabricated on glass with similar process conditions were used to carry out the extinction spectra measurement. The theoretical extinction efficiency was calculated by the discrete dipole approximation (DDA) method [30]. In our calculation, both the perpendicular and parallel polarizations were assumed to have the same proportion of 50%, and the dielectric constant of Ag nanoparticles was extracted from [31].

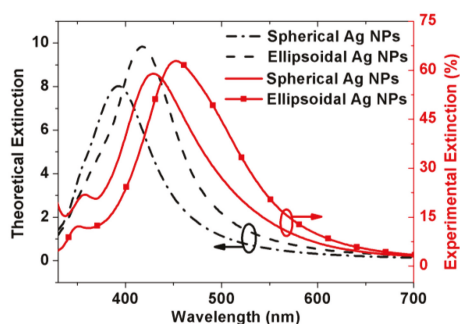


**Figure 4.** Theoretical (dotted lines) and experimental (solid lines) extinction spectra of spherical Ag NPs with  $D = 88$  nm and ellipsoidal Ag NPs with  $2a/2b/2c = 76/94/76$  nm.

As shown here, the theoretical calculation is comparatively consistent with the experimental result. The most significant aspect is that both the theoretical and measured extinction spectrum ranges are almost perfectly matched with the absorption wavelength range of GaInP top-cell [26], especially the measured one. The second aspect is that ellipsoidal Ag NPs demonstrate better extinction performance than that of spherical Ag NPs. Finally, the increased extinction ability almost disappears for wavelength beyond 600 nm.

Meanwhile, there are two different features exhibited in Figure 4. Firstly, the theoretical dipole extinction peaks are located at 393 and 418 nm for ellipsoidal and spherical Ag NPs, respectively, and the corresponding experimental dipole extinction peaks are located at 429 and 453 nm. Apparently, a red-shift of about 35-nm, both for the experimental extinction peak of ellipsoidal and spherical Ag NPs, appears, which can be attributed to the retardation effects occurred on the particles [32] and the practical wider size distribution. Secondly, the broadening of full width at half maximum (FWHM) of experimental results can be explicated by the wide size distribution of NPs. Overall, the features of the red-shift, the broader FWHM, and higher peak intensity are beneficial for harvesting more incident sunlight.

### 3.3. Enhanced Performance of GaInP/GaInAs/Ge TJSCs by Ag NPs

Since the extinction spectra of Ag NPs cover from 300 to 600 nm, we speculate that the plasmonic nanostructures have little effect on the middle- and bottom-cell. To verify the impact of plasmonic nanostructures, the EQE of GaInP/GaInAs/Ge TJSCs with Ag NPs was measured. As expected,

only the spectral response characteristic of GaInP top-cell is affected by Ag NPs. Hence, Figure 5 gives the EQE of GaInP top-cell with and without Ag NPs. As shown in Figure 5, the EQEs of devices with Ag NPs are higher than that of device without Ag NPs. The improved EQE for a device with spherical Ag NPs mainly locates from 390 to 490 nm, which is in accordance with the extinction spectra. Similarly, the excellent extinction performance of ellipsoidal Ag NPs leads to a higher EQE of the top-cell in a broader spectral range. The integrated current for devices without and with spherical and ellipsoidal Ag NPs is 13.70, 14.09, and 14.31 mA/cm<sup>2</sup>, respectively. Definitely, distinct photocurrent enhancements are obtained both for spherical and ellipsoidal Ag NPs compared with that of the device without Ag NPs, especially for the latter. The results allow the conclusion that ellipsoidal Ag NPs with better extinction property can obviously enhance the performance of TJSCs.

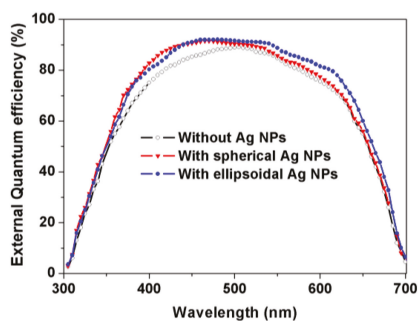


Figure 5. External quantum efficiency of GaInP top-cell in TJSCs.

Figure 6 presents the  $J$ - $V$  characteristic curves of TJSCs with and without Ag NPs under AM 1.5G solar irradiation. As demonstrated in Figure 6, there is no obvious difference in the  $V_{oc}$  for all devices, but their  $J_{sc}$  and  $\eta$  increase when Ag NPs are incorporated into the TJSCs. This could be attributed to the increased material extinction of Ag NPs within the spectral range from 300 to 600 nm. For the device without Ag NPs, the  $J_{sc}$  and  $\eta$  are 13.56 mA/cm<sup>2</sup> and 29.54%, respectively. The  $\eta$  for devices with spherical and ellipsoidal Ag NPs is improved from 30.27% to 31.02%, respectively. This can be attributed to the key factor of  $J_{sc}$ , which increases from 13.94 to 14.17 mA/cm<sup>2</sup> and is in accordance with the EQE results discussed in the previous part. From the results, we conclude that Ag NPs, especially ellipsoidal Ag NPs, are obviously beneficial for the performance of TJSCs, but it is still a challenge to fabricate of metal NPs without inducing the dopant diffusion of tunnel junctions.

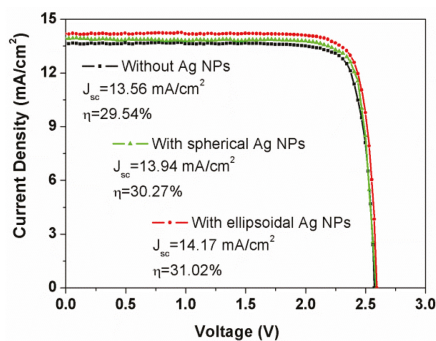


Figure 6.  $J$ - $V$  characteristics of GaInP/GaInAs/Ge triple-junction solar cells at one-sun AM 1.5G, 25 °C. The measurement was performed on the 1.1 cm<sup>2</sup> solar cell devices.

#### 4. Conclusions

In conclusion, we demonstrated a simple approach for increasing the photocurrent of the top-cell using plasmonic nanostructures for current-matched GaInP/GaInAs/Ge TJSCs. The devices with ellipsoidal Ag NPs display an enhanced photocurrent due to the remarkably increased material extinction. Both the experimental and theoretical results verify the ellipsoidal Ag NPs with the lower annealing temperature of 350 °C show excellent optical properties. Under the illumination of AM 1.5G 100 mW·cm<sup>-2</sup>, the photovoltaic conversion efficiency of the device with ellipsoidal Ag NPs reaches 31.02%, with a nearly 5% relative improvement in comparison with the device without Ag NPs (29.54%). The findings of this study elucidate that plasmonic nanoparticles located on the illuminated surface of a solar cell is a promising structure for resolving the puzzle between carrier collection and optical absorption in GaInP top-cells and facilitating the light trapping of TJSCs.

**Acknowledgments:** The authors acknowledge financial support from the National Natural Science Foundation of China (Grant Nos. 61006050, 51573042), the Natural Science Foundation of Beijing (No. 21511004), the Fundamental Research Funds for the Central Universities (Grant No. 2016MS50).

**Author Contributions:** All the authors together designed the scope of the work. Yiming Bai contributed to the idea, discussion and writing the manuscript. Lingling Yan and Lin Su performed the experiments and analyzed the data. Jun Wang, Zhigang Yin and Yuanyuan Liu contributed to the performance characterization. Nuofu Chen reviewed and finalized the paper.

**Conflicts of Interest:** The authors declare no conflicts of interest.

#### References

- Green, M.A.; Emery, K.; Hishikawa, Y.; Warta, W.; Dunlop, E.D. Solar cell efficiency tables (version 46). *Prog. Photovolt. Res. Appl.* **2015**, *23*, 805–812. [CrossRef]
- Green, M.A.; Keevers, M.J.; Thomas, I.; Lasich, J.B.; Emery, K.; King, R.R. 40% efficient sunlight to electricity conversion. *Prog. Photovolt. Res. Appl.* **2015**, *23*, 685–691. [CrossRef]
- Li, S.L.; Bi, J.F.; Li, M.Y.; Yang, M.J.; Song, M.H.; Liu, G.Z.; Xiong, W.P.; Li, Y.; Fang, Y.Y.; Chen, C.Q.; *et al.* Investigation of GaInAs strain reducing layer combined with InAs quantum dots embedded in Ga(In)As subcell of triple junction GaInP/Ga(In)As/Ge solar cell. *Nanoscale Res. Lett.* **2015**, *10*. [CrossRef] [PubMed]
- Paraskeva, V.; Hadjipanayi, M.; Norton, M.; Pravettoni, M.; Georghiou, G.E. Voltage and light bias dependent quantum efficiency measurements of GaInP/GaInAs/Ge triple junction devices. *Sol. Energy Mater. Sol. Cells* **2013**, *116*, 55–60. [CrossRef]
- Barrigon, E.; Espinet-Gonzalez, P.; Contreras, Y.; Rey-Stolle, I. Implications of low breakdown voltage of component subcells on external quantum efficiency measurements of multijunction solar cells. *Prog. Photovolt. Res. Appl.* **2015**, *23*, 1597–1607. [CrossRef]
- Geisz, J.F.; Kurtz, S.; Wanlass, M.W.; Ward, J.S.; Duda, A.; Friedman, D.J.; Olson, J.M.; McMahon, W.E.; Moriarty, T.E.; Kiehl, J.T. High-efficiency GaInP/GaAs/InGaAs triple-junction solar cells grown inverted with a metamorphic bottom junction. *Appl. Phys. Lett.* **2007**, *91*. [CrossRef]
- Dimroth, F.; Grave, M.; Beutel, P.; Fiedeler, U.; Karcher, C.; Tibbits, T.N.D.; Oliva, E.; Siefert, G.; Schachtner, M.; Wekkeli, A.; *et al.* Wafer bonded four-junction GaInP/GaAs/GaInAsP/GaInAs concentrator solar cells with 44.7% efficiency. *Prog. Photovolt. Res. Appl.* **2014**, *22*, 277–282. [CrossRef]
- Guter, W.; Schone, J.; Philipps, S.P.; Steiner, M.; Siefert, G.; Wekkeli, A.; Welsler, E.; Oliva, E.; Bett, A.W.; Dimroth, F. Current-matched triple-junction solar cell reaching 41.1% conversion efficiency under concentrated sunlight. *Appl. Phys. Lett.* **2009**, *94*. [CrossRef]
- Kurtz, S.; Geisz, J. Multijunction solar cells for conversion of concentrated sunlight to electricity. *Opt. Express* **2010**, *18*, A73–A78. [CrossRef] [PubMed]
- Pham, N.D.; Kim, J.T.; Jung, T.I.; Han, J.H.; Oh, I. Direct solar water splitting enabled by monolithic III–V triple junction integrated with low-cost catalyst. *Sci. Adv. Mater.* **2016**, *8*, 241–246. [CrossRef]
- Braun, A.; Katz, E.A.; Gordon, J.M. Basic aspects of the temperature coefficients of concentrator solar cell performance parameters. *Prog. Photovolt. Res. Appl.* **2013**, *21*, 1087–1094. [CrossRef]

12. Meusel, M.; Baur, C.; Létay, G.; Bett, A.W.; Warta, W.; Fernandez, E. Spectral response measurements of monolithic GaInP/Ga(In)As/Ge triple-junction solar cells: Measurement artifacts and their explanation. *Prog. Photovolt. Res. Appl.* **2003**, *11*, 499–514. [CrossRef]
13. Sogabe, T.; Ogura, A.; Okada, Y. Analysis of bias voltage dependent spectral response in Ga<sub>0.51</sub>In<sub>0.49</sub>P/Ga<sub>0.99</sub>In<sub>0.01</sub>As/Ge triple junction solar cell. *J. Appl. Phys.* **2014**, *115*. [CrossRef]
14. Cotal, H.; Fetzer, C.; Boisvert, J.; Kinsey, G.; King, R.; Hebert, P.; Yoon, H.; Karam, N. III-V multijunction solar cells for concentrating photovoltaics. *Energy Environ. Sci.* **2009**, *2*, 174–192. [CrossRef]
15. Conibeer, G. Third-generation photovoltaics. *Mater. Today* **2007**, *10*, 42–50. [CrossRef]
16. Lee, S.M.; Kwong, A.; Jung, D. High performance ultrathin GaAs solar cells enabled with heterogeneously integrated dielectric periodic nanostructures. *ACS Nano* **2015**, *9*, 10356–10365. [CrossRef] [PubMed]
17. Okamoto, H.; Imura, K. Near-field optical imaging of enhanced electric fields and plasmon waves in metal nanostructures. *Prog. Surf. Sci.* **2009**, *84*, 199–229. [CrossRef]
18. Bai, Y.M.; Gao, Z.; Chen, N.F.; Liu, H.; Yao, J.X.; Ma, S.; Shi, X.Q. Elimination of small-sized Ag nanoparticles via rapid thermal annealing for high efficiency light trapping structure. *Appl. Surf. Sci.* **2014**, *315*. [CrossRef]
19. Yang, L.; Pillai, S.; Green, M.A. Can plasmonic Al nanoparticles improve absorption in triple junction solar cells? *Sci. Rep.* **2015**, *5*. [CrossRef] [PubMed]
20. Zhang, Z.C.; Han, S.; Wang, C.; Li, J.P.; Xu, G.B. Single-walled carbon nanohorns for energy applications. *Nanomaterials* **2015**, *5*, 1732–1755. [CrossRef]
21. Bai, Y.M.; Wang, J.; Yin, Z.G.; Chen, N.F.; Zhang, X.W.; Zhen, F.; Yao, J.X.; Li, N.; Guli, M.N. Ag nanoparticles preparation and their light trapping performance. *Sci. China Technol. Sci.* **2013**, *56*, 109–114. [CrossRef]
22. Stratakis, E.; Kymakis, E. Nanoparticle-based plasmonic organic photovoltaic devices. *Mater. Today* **2013**, *16*, 133–146. [CrossRef]
23. Lee, D.S.; Kim, W.; Cha, B.G.; Kwon, J.; Kim, S.J.; Kim, M.; Kim, J.; Wang, D.H.; Park, J.H. Self-position of Au NPs in perovskite solar cells: Optical and electrical contribution. *ACS Appl. Mater. Interfaces* **2015**, *8*, 449–454. [CrossRef] [PubMed]
24. Keding, R.; Stuwe, D.; Kamp, M.; Kamp, M.; Reichel, C.; Wolf, A.; Woehl, R.; Borchert, D.; Reinecke, H.; Biro, D. Co-diffused back-contact back-junction silicon solar cells without gap regions. *IEEE J. Photovolt.* **2013**, *3*, 1236–1242. [CrossRef]
25. Simrick, N.J.; Kilner, J.A.; Atkinson, A. Thermal stability of silver thin films on zirconia substrates. *Thin Solid Films* **2012**, *520*, 2855–2867. [CrossRef]
26. Hu, P.F.; Cao, Y.L.; Jia, D.Z.; Li, Q.; Liu, R.L. Engineering the metathesis and oxidation-reduction reaction in solid state at room temperature for nanosynthesis. *Sci. Rep.* **2014**, *4*. [CrossRef] [PubMed]
27. Fetzer, C.M.; King, R.R.; Colter, P.C.; Edmondson, K.M.; Law, D.C.; Stavrides, A.P.; Yoon, H.; Ermer, J.H.; Romero, M.J.; Karam, N.H. High-efficiency metamorphic GaInP/GaInAs/Ge solar cells grown by MOVPE. *J. Cryst. Growth* **2004**, *261*, 341–348. [CrossRef]
28. King, R.R.; Law, D.C.; Edmondson, K.M.; Fetzer, C.M.; Kinsey, G.S.; Yoon, H.; Sherif, R.A.; Karam, N.H. 40% efficient metamorphic GaInP/GaInAs/Ge multijunction solar cells. *Appl. Phys. Lett.* **2007**, *90*. [CrossRef]
29. Hoheisel, R.; Fernandez, J.; Dimroth, F.; Bett, A.W. Investigation of radiation hardness of germanium photovoltaic cells. *IEEE Trans. Electron Devices* **2010**, *57*, 2190–2194. [CrossRef]
30. Draine, B.T.; Flatau, P.J. User guide for the discrete dipole approximation code DDSCAT (Version 7.1). 2010. Available online: <http://arxiv.org/abs/1002.1505> (accessed on 28 January 2016).
31. Palik, E.D. *Handbook of Optical Constants of Solids*; Academic Press: Washington, DC, USA, 1985.
32. Gao, H.L.; Zhang, X.W.; Yin, Z.G.; Tan, H.R.; Zhang, S.G.; Meng, J.H.; Liu, X. Plasmon enhanced polymer solar cells by spin-coating Au nanoparticles on indium-tin-oxide substrate. *Appl. Phys. Lett.* **2012**, *101*. [CrossRef]





Review

# Enhancing Solar Cell Efficiency Using Photon Upconversion Materials

Yunfei Shang<sup>1</sup>, Shuwei Hao<sup>1,2</sup>, Chunhui Yang<sup>1,2,\*</sup> and Guanying Chen<sup>1,3,\*</sup>

<sup>1</sup> School of Chemical Engineering and Technology, Harbin Institute of Technology, Harbin 150001, China; shangyunfei@hit.edu.cn (Y.S.); haosw@hit.edu.cn (S.H.)

<sup>2</sup> Harbin Huigong Technology Co., Ltd., Harbin 150001, China

<sup>3</sup> Institute for Lasers, Photonics, and Biophotonics, University at Buffalo, State University of New York, Buffalo, NY 14260, USA

\* Authors to whom correspondence should be addressed; yangchh@hit.edu.cn (G.Y.); chenguanying@hit.edu.cn or guanying@buffalo.edu (G.C.).

Academic Editor: Jiye Fang

Received: 27 August 2015; Accepted: 10 October 2015; Published: 27 October 2015

**Abstract:** Photovoltaic cells are able to convert sunlight into electricity, providing enough of the most abundant and cleanest energy to cover our energy needs. However, the efficiency of current photovoltaics is significantly impeded by the transmission loss of sub-band-gap photons. Photon upconversion is a promising route to circumvent this problem by converting these transmitted sub-band-gap photons into above-band-gap light, where solar cells typically have high quantum efficiency. Here, we summarize recent progress on varying types of efficient upconversion materials as well as their outstanding uses in a series of solar cells, including silicon solar cells (crystalline and amorphous), gallium arsenide (GaAs) solar cells, dye-sensitized solar cells, and other types of solar cells. The challenge and prospect of upconversion materials for photovoltaic applications are also discussed.

**Keywords:** photovoltaic; upconversion; efficiency

## 1. Introduction

Fossil fuels (coal, oil, and natural gas) form the major energy source for meeting current human needs [1–4], yet cause a range of serious environmental issues. Moreover, the ever-growing consumption rate outpaces their regeneration rate, endangering the exhaustion of fossil fuels on earth. Dealing with the energy crisis is an urgent need [5,6]. Among all new competing energy sources (biomass, wind, hydroelectricity, geothermal energy, and nuclear energy), solar energy is considered to be the most abundant, renewable, and environment-friendly energy form [7,8]. The total solar power that strikes the Earth's surface is about 100,000 terawatts, which is 10,000 times more than that consumed globally [9,10]. If just 0.1% of the sunlight that reaches the Earth's surface could be converted by photovoltaic (PV) devices, with an average conversion efficiency of 10%, the amount would be sufficient to meet our current energy demands. The achievement of PV technology in recent decades has been tremendous [11–13]. The high-cost per kilowatt delivered by PV stations, however, limits its competitiveness with other sources. This is caused mainly by the inferior power conversion efficiencies of PV devices. The inability to absorb infrared (IR) light (700–2500 nm), which constitutes 52% of the energy of the entire solar spectrum, forms the major energy loss mechanism of conventional solar cells. This fundamental issue is set by the sizable bandgap of light-absorbing materials in PV devices. Crystalline silicon (c-Si) photovoltaic (PV) cells are the most used among all types of solar cells on the market, representing about 90% of the world's total PV cell production in 2008 [14]. However, even for single crystalline silicon (Si) PV cells with a rather small semiconductor band-gap

(1.12 eV, corresponding to a wavelength of  $\sim 1100$  nm), the transmission loss of sub-band-gap photons can still amount to about 20% of the sun's energy irradiated onto the Earth's surface [15]. For PV cells with a larger band-gap, such as amorphous Si (1.75 eV) solar cells, which are limited to absorb sunlight with wavelengths below 708 nm, they manifest even higher near infrared transmission losses.

Photon upconversion (UC) provides a means to circumvent transmission loss by converting two sub-band-gap photons into one above-band-gap photon, where the PV cell has high light responsivity. This technology enables us to break the Shockley–Queisser limit of a single-junction PV cell (about 31% for non-concentrated sunlight irradiation for a semiconductor material with an optimized band-gap of around 1.35 eV) by transforming the solar spectrum [16]. Indeed, Trupke *et al.* demonstrated through a detailed balance model that modification of the solar spectrum with an up-converter could elevate the upper theoretical efficiency limit of a single-junction crystalline silicon PV cell to be as high as 40.2% under non-concentrated sunlight irradiation [17]. This value is far beyond the Shockley–Queisser limit for crystalline silicon solar cells ( $\sim 1.1$  eV bandgap) of approximately 30%. Figure 1 schematically illustrates the use of upconversion processes to convert the solar spectrum in the IR-Near IR (NIR)-short visible range into the peak ( $\sim 500$  nm) of sun radiation. There are three typical photon upconversion materials under investigation now outlined. (1) Rare-earth-doped micro- and nano-crystals (RED-UC), which usually work with wavelengths above 800 nm, but also possibly below 800 nm with appropriate composition design [18–24]. The abundant electronic states of trivalent lanthanide ions enable upconverting a range of IR wavelengths by selecting varied types of rare earth ions [25,26]. (2) Triplet–triplet annihilation upconversion (TTA-UC, response range  $\lambda < 800$  nm) [27–29], whereby the triplet states of two organic molecules interact with each other, exciting one molecule to its emitting state to produce fluorescence. The excitation power density required for TTA UC is quite low, a few  $\text{mW}/\text{cm}^2$ , which is comparable to that of sun radiation. (3) Upconversion in Quantum Nanostructures (QN-UC, response range  $\lambda < 800$  nm) [30–32]. This process leans on the use of a unique design comprising a compound semiconductor nanocrystal, which incorporates two quantum dots with different bandgaps separated by a tunneling barrier. Upconversion occurs by excitation of an electron in the lower energy transition, followed by intra-band absorption of the hole, allowing it to cross the barrier to a higher energy state. Detailed mechanisms of these three types of upconversion materials are discussed in Section 2. These upconversion materials are now emerging in use to improve PV efficiency in the real world.

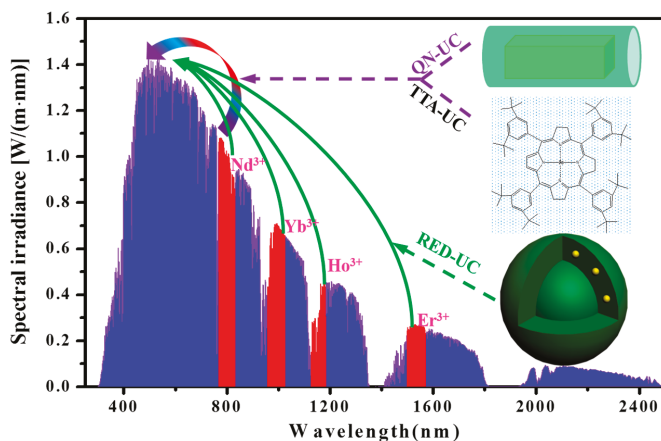


**Figure 1.** The absorption and emission range of three types of upconversion materials in reference to AM 1.5 spectrum (QN-UC (purple): upconversion in quantum nanostructures; TTA-UC (purple): triplet-triplet annihilation upconversion; RED-UC (green): Rare-earth-doped upconversion materials).



## 2. Upconversion Materials

### 2.1. Rare-Earth-Doped Upconversion Materials

The rare-earth family is comprised of 17 elements, which includes 15 lanthanide elements (from La to Lu) plus the elements of yttrium (Y) and scandium (Sc). The trivalent lanthanide ions possess a  $4f^n 5s^2 5p^6$  electronic structure with 14 available orbitals ( $0 < n < 14$ ), offering 14 possible electronic group configurations. The quantum interaction of involved electrons endows lanthanide elements with abundant energy levels covering a spectral range of NIR, visible and ultraviolet (UV) [33–37]. In addition, the perfect shielding of  $4f$  electrons by outer complete  $5s$  and  $5p$  shells enables electronic transitions to occur with limited influence from the surrounding environment, thus exhibiting high resistance to processes of photobleaching and photochemical degradation. As the symmetries of involved quantum states are identical, the intra- $4f$  electronic transitions of lanthanide ions are electric-dipole forbidden, yet can be relaxed due to local-crystal-field-induced intermixing of the  $f$  states with higher electronic configurations. The primary forbidden nature yields metastable energy levels of lanthanide ions (lifetime can be as long as tens of milliseconds), thus favoring the occurrence of sequential excitations in excited states of a single lanthanide ion as well as permitting favorable ion-ion interactions in excited states to allow energy transfers between two or more lanthanide ions.

There are four main basic mechanisms for rare-earth ions based upconversion processes, comprising of excited state absorption (ESA), energy transfer upconversion (ETU), photon avalanche (PA) and energy migration-mediated upconversion (EMU) (Figure 2). Excited state absorption (ESA) takes the form of successive absorption of pump photons by a single ion utilizing the ladder-like structure of a simple multi-level system as portrayed in Figure 2a. Figure 2a illustrates a simplified three level system for two sequential photon absorption processes. The ETU process involves at least two types of ions, namely a sensitizer and an activator. In this process, ion I known as the sensitizer is firstly excited from the ground state to its metastable level by absorbing a pump photon; it then successively transfers its harvested energy to the ground state and the first excited state of ion II, known as the activator, exciting ion II to its upper emitting state, which is followed by radiative decay to its ground state. The PA in Figure 2c is a looping process that involves an efficient cross relaxation mechanism between ion I in the ground state and ion II in the second excited state, resulting in generation of two ion IIs in the metastable state. The population of ion II in the second excited state is created through absorption of laser photons at its metastable state (the first excited state), which is initially populated through non-resonant weak ground state absorption. When the looping process ensues, an avalanche population of ion II will be created at its metastable state, producing avalanche upconverted luminescence from the emitting state. The generation of PA UC typically occurs above a certain threshold of excitation density. Below the threshold, very little up-converted fluorescence is produced, while the luminescence intensity increases by orders of magnitude above the pump threshold. In addition, the looping nature enables the evoked UC luminescence to be strongly dependent on the laser pump power, especially around the threshold laser power. The lanthanide ions designed for realizing energy migration-mediated upconversion (EMU) comprise four types: the sensitizers (type I), the accumulators (type II), the migrators (type III), and the activators (type IV; Figure 2d). A sensitizer ion is used to harvest excitation photons and subsequently promotes a neighboring accumulator ion to its excited states. A migrator ion extracts the excitation energy from high-lying energy states of the accumulator, followed by random energy hopping through the migrator ion sublattice and trapping of the migrating energy by an activator ion that produces luminescence by decaying to the ground state. The excitation density for RED-UC is typically in the range of  $10^{-1}$ – $10^2$  W/cm<sup>2</sup>.

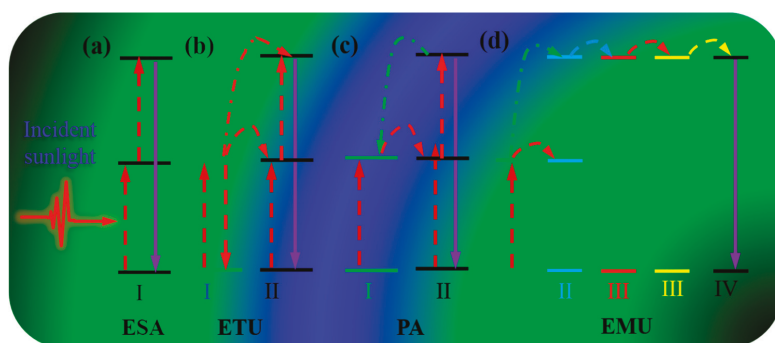


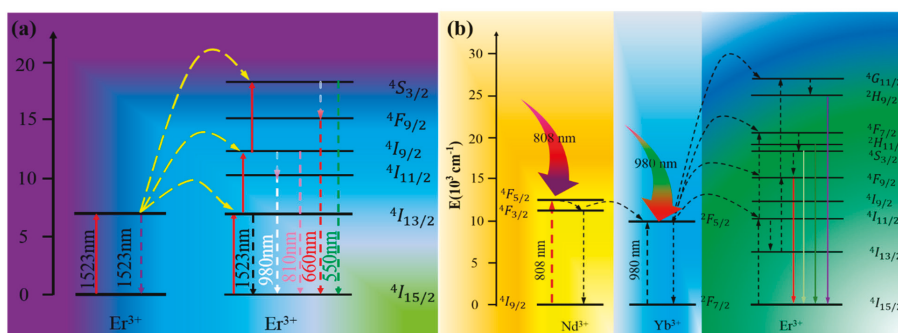
**Figure 2.** A schematic illustration of four typical upconversion processes: (a) Excited state absorption (ESA); (b) Energy transfer upconversion (ETU); (c) Photon avalanche (PA); (d) Energy migration-mediated upconversion (EMU).

Rare-earth-doped upconversion materials typically consist of an appropriate dielectric host matrix and doped  $\text{Ln}^{3+}$  ions that are dispersed as the guest in the lattice of the host matrix. Host materials with low phonon energy are able to produce upconversion luminescence at high efficiency, as multiphonon-assisted nonradiative relaxations between the closely spaced energy levels can be minimized, thus yielding increased lifetime of intermediate energy levels. Investigated low phonon energy host materials typically include fluorides, chlorides, iodides, and bromides [38], while high phonon energy host materials such as silicates, borates, and phosphates are also under study [39]. In general, host materials with low phonon energy are hygroscopic, while the high phonon energy ones are robust even under acute environment (strong acid, base, high temperature, *etc.*). Yet, the type of fluoride host material is unique and has attracted a lot of attentions in recent years. This is because fluoride host lattice not only has low phonon energy but also shows excellent chemical stability. In particular, hexagonal  $\text{NaYF}_4$  lattice is considered to be one of the most efficient host materials to date [40–42]. Interestingly, even for cubic phase  $\text{NaYF}_4$ , a well-defined distribution of  $\text{Na}^+$  and  $\text{Y}^{3+}$  ions in the crystal lattice can enable ultrahigh upconversion luminescence [43].

The  $\text{Ln}^{3+}$  dopants provide light harvesting ability as well as upconverting ability for RED UC. Among  $\text{Ln}^{3+}$  ions, the research for enhancing the efficiency of solar cells explores the use of single  $\text{Ln}^{3+}$  doping such as  $\text{Er}^{3+}$ ,  $\text{Ho}^{3+}$ ,  $\text{Tm}^{3+}$ , and  $\text{Pr}^{3+}$  to upconvert IR light. Meanwhile, a utilization of  $\text{Yb}^{3+}$  ions as co-dopants can provide new, strong absorption at  $\sim 980$  nm ( ${}^2F_{7/2} \rightarrow {}^2F_{5/2}$ ). The  $\text{Yb}^{3+}$  ions are able to sensitize most lanthanide activator ions, typically,  $\text{Er}^{3+}$ ,  $\text{Ho}^{3+}$ ,  $\text{Tm}^{3+}$ , resulting in intense upconversion when excited. Recently,  $\text{Nd}^{3+}$  ion has been proposed as another extraordinary sensitizer. It provides a new absorption at 808 nm and is able to sensitize the  $\text{Yb}^{3+}$  ion. This further broadens the absorption range of RED upconversion for PV application. Table 1 summarizes some selected upconverting materials which can be excited, utilizing light with wavelength longer than 800 nm. (1) Single  $\text{Er}^{3+}$  doped UC materials can convert light at 1523 nm to green (550 nm) and red (650 nm) (Figure 3a) [44–47]; (2)  $\text{Yb}^{3+}/\text{Er}^{3+}$  codoped system can produce green (525 nm, 542 nm), red (655 nm), as well as purple (415 nm, weak) emissions under 980 nm laser excitation [42,48–53]; (3)  $\text{Yb}^{3+}/\text{Tm}^{3+}$  pairs are able to convert light at 980 nm into UV (345 nm), blue (480 nm) and NIR (800 nm) emissions [54–58]; (4)  $\text{Nd}^{3+}/\text{Yb}^{3+}/\text{Ln}^{3+}$  ( $\text{Ln} = \text{Er}, \text{Tm}, \text{Ho}, \text{etc.}$ ) tri-doped UC materials can convert 808 nm NIR light to visible luminescence [57–62]. As an example, the energy transfer processes for  $\text{Nd}^{3+}$ ,  $\text{Yb}^{3+}$ , and  $\text{Er}^{3+}$  are depicted in Figure 3b for illustration. The  $\text{Er}^{3+}$  ion emits in the green and red range after absorbing the excitation energy by either the  $\text{Nd}^{3+}$  or the  $\text{Yb}^{3+}$  ions. Simultaneous use of  $\text{Nd}^{3+}$ ,  $\text{Yb}^{3+}$  and  $\text{Er}^{3+}$  ions enables light harvesting at  $\sim 800$  nm,  $\sim 980$  nm, as well as  $\sim 1523$  nm, covering broader spectral range for upconversion.

**Table 1.** Some selected upconverters excitable with wavelength longer than 800 nm.

Dopant Ion	Host Material	Excitation (nm)	Emission (nm)	References
Er <sup>3+</sup>	NaYF <sub>4</sub>	1523	550, 660, 800, 980	[63]
Yb <sup>3+</sup> -Er <sup>3+</sup>	NaYbF <sub>4</sub>	980	520, 540, 654	[64]
Yb <sup>3+</sup> -Er <sup>3+</sup>	NaYF <sub>4</sub>	980	410, 522, 540, 650	[65–67]
Yb <sup>3+</sup> -Er <sup>3+</sup>	NaYF <sub>4</sub> @NaYF <sub>4</sub>	980	510–570, 640–680	[68]
Yb <sup>3+</sup> -Er <sup>3+</sup>	NaYF <sub>4</sub> @NaYF <sub>4</sub> :Nd <sup>3+</sup>	808/980	520, 540, 655	[69]
Yb <sup>3+</sup> -Tm <sup>3+</sup>	NaYF <sub>4</sub>	980	375, 450, 475, 679, 800	[70,71]
Yb <sup>3+</sup> -Ho <sup>3+</sup>	NaYF <sub>4</sub>	980	545, 650	[72]
Yb <sup>3+</sup> -Er <sup>3+</sup> -Nd <sup>3+</sup>	NaYF <sub>4</sub>	808/980	410, 520, 545, 650	[60]

**Figure 3.** The upconversion mechanisms for (a) single Er<sup>3+</sup> doped upconversion particles (UCNPs) excited under 1523 nm laser excitation; (b) Nd<sup>3+</sup>-Yb<sup>3+</sup>-Er<sup>3+</sup> tridoped system under 808 nm or 980 nm laser excitation.

## 2.2. Triplet-Triplet Annihilation Upconversion Materials

Triplet-triplet annihilation (TTA) up-conversion is a process occurring in a pair of sensitizer-annihilator dyes, as portrayed in Figure 4. Light harvesting is enabled by the sensitizer, followed by populating its singlet excited state ( $S_0 \rightarrow S_1$ ). The intersystem crossing process (ISC,  $S_1 \rightarrow T_1$ ) allows the triplet excited state of the sensitizer (organo-metallic type) to be efficiently populated thanks to the heavy atom effect of the transition metal atom. Subsequently, a transfer of the energy in the triplet to a neighboring acceptor (annihilator) at  $S_0$  state *via* a Dexter energy transfer (DET) process, can excite the acceptor (annihilator) to its triplet state. Two nearby acceptor (annihilator) molecules in the triplet states collide with each other, and results in one acceptor molecule being excited to the higher singlet state ( $S_1$ ), while the other one returns to the ground singlet state ( $S_0$ ). A radiative decay from the generated singlet excited state of the acceptor produces an upconverted fluorescence, which is called triplet-triplet annihilation (TTA) upconversion. Furthermore, the wavelength of light harvesting can be varied by selecting the sensitizer, while the emission wavelength of TTA up-conversion can be tuned by selection of the triplet acceptor (annihilator). Since sun radiation can be utilized in a direct way to induce TTA UC, this type of upconversion is promising for applications in PV solar cells. Yet, the inability to produce efficient TTA UC in long visible as well as in the IR range, limits its impact on PV technology. To address this challenge, Kimizuka *et al.* [73] and Bardeen *et al.* [74] extended the absorption wavelength beyond 850 nm by using metallonaphthalocyanines and semiconductor nanocrystals as triplet sensitizers. However, the upconversion quantum efficiency of TTA-UC remains rather low. To address the low efficiency problem, F. Meinardi and co-workers [75] combined organic TTA with fluorescent semiconductor nanocrystals that not only broaden the absorption but also lower the excitation intensity. The same group [76] synthesized a series of sensitizers with tuned absorption and achieved a conversion efficiency of 10% under broadband

AM 1.5 irradiation. Kimizuka *et al.* [77] demonstrated a novel metal-organic framework, in which donor-acceptor position could be precisely tailored to achieve a high UC efficiency even under a weak excitation (less than that of sunlight).

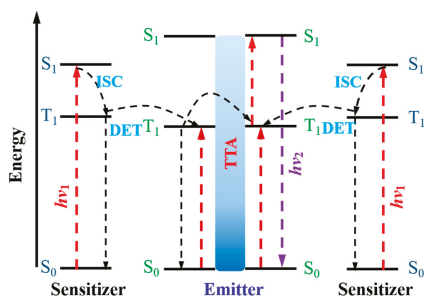


**Figure 4.** The working principle of the triplet-triplet annihilation upconversion.

TTA UC is highly sensitive to oxygen molecules, as the generated triplet states of TTA dye pairs can be easily quenched by them, producing reactive oxygen species (ROS). These ROS species are exceptionally reactive, which can cause the chemical degradation of the paired dyes. As a result, TTA upconversion will be deactivated by oxygen molecules, posing another problem for their PV applications. To address this issue, Kimizuka and co-workers prepared a solvent-free liquid TTA UC system that can function well even under aerated conditions [78]. Subsequently, they reported a series of air-stable TTA upconversion in supramolecular organogel [79], supramolecular self-assemblies [80], and ionic liquids [81], providing a new approach to solve the problem of the sensitivity to oxygen molecules. Alternatively, Weder *et al.* demonstrated TTA upconversion in molecular glasses and organogels where oxygen-induced upconversion fluorescence quenching could also be prevented [82,83].

### 2.3. Upconversion in Quantum Nanostructures

Upconversion in quantum nanostructures is realized through a design of a compound semiconductor nanocrystal, which incorporates two quantum dots with different bandgaps separated and connected by a tunneling barrier (a semiconductor rod). The implementation of upconversion is through a two-step absorption of two subsequent photons. The first photon generates an electron-hole pair via interband absorption in the lower-energy core (small band-gap dots), leaving a confined hole and a delocalized electron in the compound semiconductor nanocrystal. The second absorbed photon can lead, either directly or indirectly, to further excitation of the hole, enabling it to cross the barrier layer. The direct way is through an intraband absorption of the photon by the confined hole at the lower-energy core (Figure 5a), while the indirect way is via an Auger mediated energy transfer process (Figure 5b). The Auger process describes a recombination of the second electron-hole pair, generated by absorbing the second photon, while simultaneously allowing nonradiative energy transfer to the confined hole at the lower energy core (small band-gap dots), empowering it to cross the barrier to the higher energy quantum dot (large band-gap dots). This, in turn, is followed by a radiative recombination with the delocalized electron, producing upconverted luminescence. This system combines the stability of an inorganic crystalline structure, with the spectral tunability afforded by quantum confinement. Since the absorption, emission, and lifetime of the semiconductor nanocrystals can be controlled by variation of their size, shape, as well as composition, upconversion in quantum nanostructures holds prime promise for applications in PV devices. However, a relative high excitation density ( $\sim 10^4$  W/cm<sup>2</sup>) is needed to activate this type of upconversion. Lowering the excitation density to the range of sun irradiation ( $\sim 10^{-1}$  W/cm<sup>2</sup>) is an inviting direction, which could produce a pronounced impact for PV applications in a straightforward way.

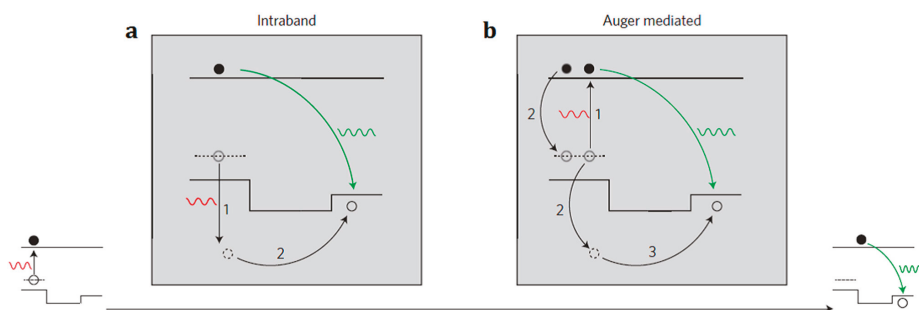


**Figure 5.** Mechanism of the upconversion in quantum nanostructures: (a) Direct intraband hole absorption mechanism of upconversion; (b) Auger-mediated upconversion (adapted with permission from [30]; Copyright Nature Publishing Group, 2013).

### 3. PV Applications

The solar cell, which directly converts solar energy into electricity, is one of the most attractive solutions to the growing energy demands, due to the omnipresence and abundance of solar energy. Light harvesting is the first but also the most important step, which determines how much sun irradiation can be absorbed. The standard solar irradiation spectrum (AM 1.5) covers the wavelength region from UV to IR (300–2500 nm). However, most single-junction PV devices are unable to absorb light quanta in the long wavelength range, typically NIR and IR, creating the performance-limiting issue of transmission loss. Upconversion materials are in play to circumvent this issue by spectral conversion, which has been applied to a wide range of solar cells. These PV devices include c-Si, amorphous Si thin-film, GaAs and dye sensitized solar cells (DSSCs). Two typical configurations have been exploited for applications in PV cells, as portrayed in Figure 6, to upconvert sub-bandgap light into above-bandgap luminescence. Structure One involves the use of a reflection layer to increase the optical path of NIR or IR light within the upconverting layer for an increase of the upconversion luminescence output, while Structure Two does not use any reflection layer, typically employed by DSSCs.

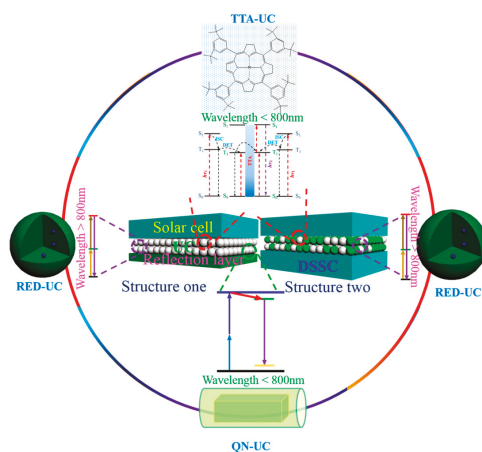


**Figure 6.** A schematic illustration of the usage of three typical upconversion materials in solar cells using two configurations. (Rare-earth upconversion, RED-UC; Upconversion in quantum nanostructure, QN-UC; Triplet-triplet annihilation upconversion, TTA-UC).

### 3.1. c-Si Solar Cells

Crystalline silicon (c-Si) photovoltaic cells are used in the largest quantity of all types of solar cells on the market, representing about 90% of the world total PV cell production in 2008. The recorded maximum conversion efficiency of crystalline silicon solar has reached 25% [84], close to the Shockley–Queisser limit (~30%). However, as mentioned before, the bandgap of crystalline silicon (~1.12 eV) limits it to absorb light less than 1100 nm, producing a transmission loss as high as 20%. On the other hand, c-Si solar cells work with the highest quantum efficiency in the spectral region of 800–1100 nm. Development of upconversion materials with absorption below 1100 nm, and the upconverted emission in the range of ~800–1100 nm are highly attractive for improvement of the efficiency of a c-Si PV cell. Yb<sup>3+</sup>-sensitized or Nd<sup>3+</sup>-sensitized RED UC materials are beyond consideration for use in c-Si PV cells, as they provide absorption at ~980 nm and ~800 nm where the semiconductor silicon has existing high spectral responses.

Single Er<sup>3+</sup>-doped RED UC materials are attractive for c-Si solar cells, as they display absorption at 145–1580 nm with sub-bandgap energy of silicon, and emit strong luminescence at ~980 nm, ~540 nm, and 650 nm that can be very useful for silicon to produce excitons. In 2005, Shalav *et al.* [63] exploited the use of NaYF<sub>4</sub>:20% Er<sup>3+</sup> microcrystals as an upconverter in bifacial c-Si solar cells. In their geometric arrangement of implementation of upconversion, microsized NaYF<sub>4</sub>:20% Er<sup>3+</sup> phosphors were dispersed into an acrylic adhesive medium with matched refractive index, and then this mixture was deposited as a thick film on the rear of a bifacial c-Si solar cell. An impressive increase of external quantum efficiency of 2.5% was accomplished under excitation at 1523 nm. Fischer *et al.* [47] also investigated the potential use of microsized or bulk NaYF<sub>4</sub>:20% Er<sup>3+</sup> materials (~3 μm) to improve the conversion performance of c-Si solar cells. The upconversion efficiency of NaYF<sub>4</sub>:20% Er<sup>3+</sup> microcrystals was quantified to be 5.1% when irradiated with 1523 nm laser with a power density of 1880 W/m<sup>2</sup>. Shalav *et al.* showed that a c-Si solar cell device can have an external quantum efficiency of 0.34% under sub-bandgap irradiation at 1522 nm with a power density of 1090 W/m<sup>2</sup>.

Alongside Er<sup>3+</sup> ions, the Ho<sup>3+</sup> ions provide a possibility to harvest sub-bandgap energy of silicon at a new wavelength range (1150–1230 nm). The centroids of upconverted luminescence of Ho<sup>3+</sup> ions are at ~910 nm (corresponding to the <sup>5</sup>I<sub>5</sub> → <sup>5</sup>I<sub>8</sub> transition) in the NIR range, and at ~650 nm (corresponding to the <sup>5</sup>F<sub>5</sub> → <sup>5</sup>I<sub>8</sub> transition) in the visible range. Both radiations have energy above the bandgap of silicon. It should be noted that the intensity of sun radiation at 1170 nm is approximately twice than that at 1520 nm, potentially delivering more effective improvement of solar cell efficiency. Lahoz *et al.* [85] first reported on the use of single Ho<sup>3+</sup> ion doped upconverting glass ceramics in a c-Si solar cell. They successfully demonstrated that the c-Si solar cell responds to light irradiation at ~1170 nm due to the upconverted visible emission (650 nm) and NIR emission (910 nm) in the glass ceramics. In another work of theirs, Ho<sup>3+</sup>-Yb<sup>3+</sup> codoped upconversion materials were investigated to improve the conversion efficiency of a c-Si solar cell [86]. They found that the Ho<sup>3+</sup>-Yb<sup>3+</sup> codoped upconverter produced much stronger NIR emission intensity than that of the single Ho<sup>3+</sup>-doped counterpart. This is because the excited Ho<sup>3+</sup> ions (at the <sup>5</sup>I<sub>5</sub> state) can sensitize Yb<sup>3+</sup> ions (at the ground state <sup>2</sup>F<sub>7/2</sub> state), making both Ho<sup>3+</sup> and Yb<sup>3+</sup> luminescence. This, in turn, result in an improved NIR response of Si solar cells in comparison to the one using single Ho<sup>3+</sup>-doped glass ceramics. Moreover, Lahoz and co-workers [86] validated the combined use of single-Er<sup>3+</sup> doped RED UC material and single Ho<sup>3+</sup> doped oxyfluoride RED UC material to encompass broader sunlight harvesting in the NIR range (Figure 7). This concept was demonstrated by placing the Er<sup>3+</sup> doped RED UC layer to the back of the Ho<sup>3+</sup> doped RED UC layer, which is then attached to the back of a c-Si solar cell. To enhance NIR light harvesting, a mirror was placed at the bottom of the cell to reflect the unabsorbed sub-bandgap sunlight back to the upconverting layers. From a material development point of view, Chen *et al.* [87] prepared a core-shell-shell structure of NaGdF<sub>4</sub>:Er<sup>3+</sup>@NaGdF<sub>4</sub>:Ho<sup>3+</sup>@NaGdF<sub>4</sub> nanocrystals, in which the Er<sup>3+</sup> and the Ho<sup>3+</sup> ions were separately doped into the core and the first shell layer (Figure 8). Intense UC emissions from both Er<sup>3+</sup> and Ho<sup>3+</sup> were shown in the same core-shell-shell nanoparticle. The intensities of luminescence bands from both ions are all much

stronger than that from  $\text{Er}^{3+}/\text{Ho}^{3+}$ -codoped nanocrystals due to a spatial isolation of  $\text{Er}^{3+}$  and  $\text{Ho}^{3+}$  ions, which can avoid the detrimental cross relaxation between these ions. However, because of high doping concentration of  $\text{Er}^{3+}$  and  $\text{Ho}^{3+}$ , adverse relaxations could still induce quenching beyond the interfaces, even though the dopants were in different layers. To circumvent this, a multi-layer core/shell design of  $\text{NaYF}_4:10\%\text{Er}^{3+}@NaYF_4@NaYF_4:10\% Ho^{3+}@NaYF_4@NaYF_4:1\% Tm^{3+}@NaYF_4$  nanoparticles were reported by us [88], in which the inert  $\text{NaYF}_4$  layers in between upconverting domains were utilized to efficiently suppress the detrimental cross-relaxation processes between different types of lanthanide ions, yielding about two times more efficient upconversion photoluminescence than the counterpart  $\text{NaYF}_4:10\% Er^{3+}@NaYF_4:10\% Ho^{3+}@NaYF_4:1\% Tm^{3+}@NaYF_4$  without the inert  $\text{NaYF}_4$  layers. Moreover, these core/multishell nanoparticles can be excited at  $\sim 1120\text{--}1190\text{ nm}$  (due to  $\text{Ho}^{3+}$ ),  $\sim 1190\text{--}1260\text{ nm}$  (due to  $\text{Tm}^{3+}$ ), and  $\sim 1450\text{--}1580\text{ nm}$  (due to  $\text{Er}^{3+}$ ), collectively covering a broad spectral range of  $\sim 270\text{ nm}$  in the infrared range that can be very useful for infrared photosensitization of c-Si solar cells.

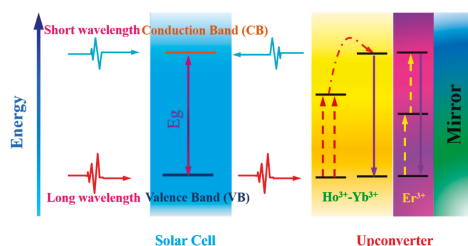


**Figure 7.** An operating mechanism for a c-Si solar cell with two upconverters, one co-doped with  $\text{Ho}^{3+}\text{--Yb}^{3+}$  and the other one single doped with  $\text{Er}^{3+}$ . Photons with short wavelength can be absorbed directly by the solar cell. The transmitted sub-bandgap light can be upconverted into high-energy photons, which would be absorbed by c-Si. The mirror behind the upconverter increases the probability of absorption of sub-bandgap light in the upconverter layer.

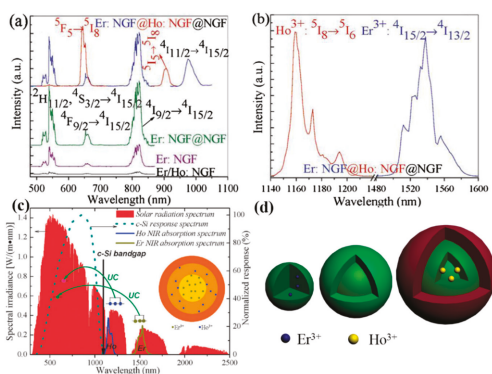


**Figure 8.** (a) Upconversion emission spectra of the core  $\text{NaGdF}_4:\text{Er}^{3+}/\text{Ho}^{3+}$  nanocrystals, the core  $\text{NaGdF}_4:\text{Er}^{3+}$  nanocrystals, the core/shell  $\text{NaGdF}_4:\text{Er}^{3+}@NaGdF_4$  nanocrystals, and the  $\text{NaGdF}_4:\text{Er}^{3+}@NaGdF_4:\text{Ho}^{3+}@NaGdF_4$  core/shell/shell nanocrystals; (b) Upconversion excitation spectrum of the  $\text{NaGdF}_4:\text{Er}^{3+}@NaGdF_4:\text{Ho}^{3+}@NaGdF_4$  core/shell/shell nanocrystals; (c) A schematic illustration of the upconversion luminescence of  $\text{NaGdF}_4:\text{Er}^{3+}@NaGdF_4:\text{Ho}^{3+}@NaGdF_4$  nanocrystals versus the bandgap of c-Si solar cell, and the spectrum of AM 1.5 sun irradiation; (d) A schematic of illustration of different nanostructures: the  $\text{NaGdF}_4:\text{Er}^{3+}$  core, the  $\text{NaGdF}_4:\text{Er}^{3+}@NaGdF_4$  core/shell, and the  $\text{NaGdF}_4:\text{Er}^{3+}@NaGdF_4:\text{Ho}^{3+}@NaGdF_4$  core/shell/shell (adapted with permission from [87]; Copyright Royal Society of Chemistry, 2012).



In addition, Alexander Dobrovolsky and co-workers [89] designed a system based on GaNP nanowires that can harvest IR light through a two-step two-photon absorption process and emits visible light. Though it is claimed to be suitable for application in third-generation Si-based solar cells, no demonstrations have yet been shown.

### 3.2. Amorphous Silicon Solar Cells

Amorphous Si solar cells have been considered as a promising substitute of c-Si cells due to their low cost, easy preparation, and excellent chemical stability. The band-gap of amorphous Si is larger than that of c-Si at about 1.75 eV, which confines it to absorb NIR light shorter than 700 nm. This means that upconverting materials with absorption above 700 nm should be appealing for uses in amorphous Si solar cells to circumvent the transmission loss.

Table 2 lists a range of investigated and selected single/co-doped RED UC materials in the literature that can be utilized towards this purpose. Zhang *et al.* [90] investigated the use of NaYF<sub>4</sub>:18% Yb<sup>3+</sup>, 2% Er<sup>3+</sup> nanocrystals as upconverter in an amorphous Si solar cell. This kind of upconverter shows visible emissions at around 655 nm (red), 525 nm and 540 nm (green) after absorbing light at 980 nm. They showed that the short circuit density can be increased by 6.25% (from 16 to 17 mA·cm<sup>-2</sup>) due to the contribution of these upconverters. In analogy, De Wild *et al.* [91,92] utilized β-NaYF<sub>4</sub>:Yb<sup>3+</sup>/Er<sup>3+</sup> as upconverter to enhance the power conversion efficiency of an amorphous Si solar cell. The upconverter layer with a thickness of 200–300 μm was deposited at the rear of the amorphous Si solar cell after mixing with polymethylmethacrylate. The maximum photocurrent was increased from 2.1 to 6.2 μA, along with a manifestation of an external quantum efficiency of 0.02% at 980 nm. Yb<sup>3+</sup>/Er<sup>3+</sup>-codoped TeO<sub>2</sub>-PbF<sub>2</sub> oxyfluoride tellurite glass [93] as well as Gd<sub>2</sub>(MoO<sub>4</sub>)<sub>3</sub>:Er<sup>3+</sup>/Yb<sup>3+</sup> UC materials [94] have also been investigated in a similar way by applying them at the back of amorphous silicon cells. The broader NIR light harvesting ability, due to the effect of host matrix, was supposed to yield a significant improvement in the solar efficiency. Unfortunately, there was only a tiny improvement obtained when co-excited by AM 1.5 and 980 nm laser radiation. The underlying mechanism remains unclear, and deserves further investigations.

**Table 2.** Typical dopant ions, the main emissions, and the corresponding energy transitions for upconversion nanocrystals reported in the literature.

Dopant Ion	Host Material	Excitation (nm)	Emission (nm)	Reference
Er <sup>3+</sup>	NaYF <sub>4</sub>	1523	550, 660, 800, 980	[63]
Er <sup>3+</sup>	YF <sub>3</sub>	1490	410, 530, 550, 660, 810, 980	[95]
Er <sup>3+</sup>	CaF <sub>2</sub>	1510	410, 550, 660, 980	[96]
Er <sup>3+</sup>	Y <sub>2</sub> O <sub>3</sub>	1538	562, 659, 801, 987	[97]
Er <sup>3+</sup>	Fluoride glasses	1538	550, 660, 820, 980	[98]
Er <sup>3+</sup>	BaCl <sub>2</sub>	1535	410, 550, 660, 980	[99]
Ho <sup>3+</sup>	Glass ceramics containing PbF <sub>2</sub> nanocrystals	1170	650, 910	[85]

In addition, Er<sup>3+</sup> doped β-NaYF<sub>4</sub> powders were also applied to amorphous Si solar cells by Chen and co-workers [100]. This solar cell displayed a current of 0.3 μA and 0.01 μA when irradiated with a laser at 980 nm (power density of 60 mW/cm<sup>2</sup>) and at 1560 nm (power density of 80 mW/cm<sup>2</sup>), respectively. An enhanced current of 0.54 μA in solar cells was observed when irradiated with 980 nm (60 mW/cm<sup>2</sup>) and 1560 nm (100 mW/cm<sup>2</sup>) simultaneously. This was associated with a broadened NIR response due to simultaneous absorption at both ~980 nm and ~1560 nm. UC materials with broad band NIR absorption are more effective to circumvent transmission losses. In this way, TTA upconversion is in play which exploits the strong and broad absorption of dye molecules. Recently, a TTA-upconverter was investigated in hydrogenated amorphous silicon (a-Si:H) solar cells, producing a high efficiency of 10.1% with an absorption threshold of 700 nm [84]. Cheng and co-workers carried out a great deal of research work on optimizing the design of amorphous silicon solar cells combined with TTA-UC materials [101–107]. For example, an amorphous silicon solar cell was shown to achieve an obvious increase of current of 2.40 × 10<sup>-3</sup> mA/cm<sup>2</sup>, on equipping with a hybrid-emitter TTA

system (namely, a filled cuvette with Ag-coated glass beads) as a back-reflecting medium. The use of TTA-UC to increase the light harvest efficiency of amorphous Si solar cells is still underway.

### 3.3. GaAs Solar Cells

Gibart *et al.* in 1995 firstly reported an application of RED UC material on a GaAs solar cell, demonstrating that it is useful to enhance the solar cell efficiency by improving the harvest of unavailable IR light [108]. In their subsequent experiment [108], a substrate-free GaAs solar cell (a band-gap of 1.43 eV) was coupled to a 100  $\mu\text{m}$  thick vitroceraic upconverting materials which contained  $\text{Yb}^{3+}$  and  $\text{Er}^{3+}$  ions. The efficiency of the GaAs solar cell was increased quadratically with the power of excitation due to the nonlinear nature of the upconversion process. A power conversion efficiency as high as 2.5% was achieved under 891 nm (1.391 eV) illumination with an irradiance of 25.6  $\text{W}/\text{cm}^2$ . In a similar way, Lin *et al.* [109] adhered a 300  $\mu\text{m}$  thick UC phosphor layer of  $\text{Y}_{5.86}\text{W}_2\text{O}_{15}:0.05\text{Yb}^{3+}, 0.09\text{Er}^{3+}$  to the rear of a GaAs solar cell. The maximum output power of  $0.339 \times 10^{-6}$  W was obtained with a 973 nm laser irradiation at 145.65  $\text{W}/\text{cm}^2$ . These results clearly indicate that GaAs solar cells can work effectively under sub-bandgap light irradiance. However, the involved light irradiances are much higher than that of sun radiance ( $10^{-2}$ – $10^{-1}$   $\text{W}/\text{cm}^2$ ). Development of efficient UC materials under low irradiance is required.

### 3.4. Dye-Sensitized Solar Cells

Dye-sensitized solar cells (DSSCs) are third-generation PV cells, which have brought revolutionary innovation to PV technology since the first report by Grätzel in 1991 [110]. Owing to their low cost, simple fabrication methodology, environmental friendliness, as well as flexible structure, DSSCs have been considered as the most promising alternative for Si-based solar cells [111]. However, due to the limited absorption range of investigated dyes, the improvement of the conversion efficiency of a DSSC is always challenging [112–115]. The band-gap of typically used dyes in DSSC, such as N3, N719, and N749, *etc.*, is usually higher than 1.8 eV. This means that they are only able to absorb photons with wavelengths shorter than 700 nm, leading to unharvesting of approximately 52% of the solar energy in the IR range (from 700 to 2500 nm) [116–118]. Efforts to develop panchromatic sensitizers for DSSCs have been hampered by poor electron injection efficiency and competing charge recombination when the absorption spectrum of the sensitizer is extended to the IR region, adversely affecting the efficiency. Moreover, the photostability of an IR absorbing dye is known to be very poor [119,120]. Photon upconversion provides an alternative approach by converting unavailable IR photons into high-energy photons that can be absorbed by the sensitizing dyes with a typical structure as presented in Figure 9.

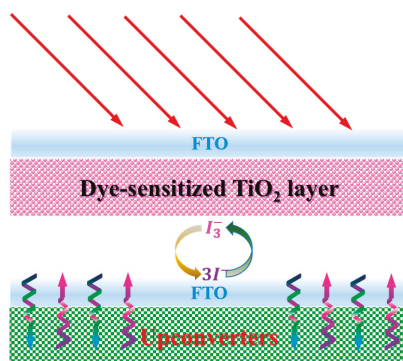
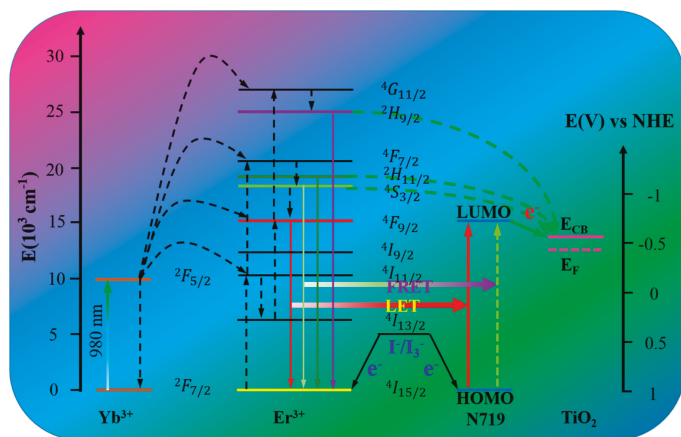


Figure 9. A typical schematic configuration of a DSSC equipped with upconverters.

The first DSSC device, based on rare-earth-doped UC materials, was presented by Demopoulos *et al.*, in which  $\text{LaF}_3:\text{Yb}^{3+}/\text{Er}^{3+}\text{-TiO}_2$  nanocomposites were used to form a multilayer electrode structure [121]. As a proof of concept demonstration, the response of DSSC at NIR light ( $\sim 980$  nm) was shown. Later, they deposited a layer of microsized  $\beta\text{-NaYF}_4:\text{Yb}^{3+}/\text{Er}^{3+}$  particles on the rear side of a counter electrode [122], which was able to provide both light reflection and NIR light harvesting without apparent charge recombination at interfaces. An improvement of NIR response was accomplished. In parallel, Yuan *et al.* [123] in 2012 proposed and validated the use of colloidal  $\beta\text{-NaYF}_4:2\% \text{Er}^{3+}/20\% \text{Yb}^{3+}$  nanoparticles in a DSSC. As the size is less than 20 nm, they are allowed to diffuse in the mesoporous  $\text{TiO}_2$  layer of the DSSC, enabling them to efficiently interact with sensitization dyes. The advantage of this approach is that these nanoparticles can be utilized in the way of using sensitizing dyes without modifications of device preparation procedure. Following that, Yang and co-workers attached  $\text{YF}_3:\text{Yb}^{3+}/\text{Er}^{3+}$  particles to the surface of the porous  $\text{TiO}_2$  thin film, the power conversion efficiency was increased from 5.18% (blank DSSC without RED UC materials) to 6.76% [124].

Researchers also placed a lot of effort in the application of RED-UC structures in photoanode layers. Wang *et al.* [125] achieved an efficiency increase of 23% when doping  $\text{YOF}:\text{Yb}^{3+}/\text{Er}^{3+}$  particles into the  $\text{TiO}_2$  photoanode layer. Zhang *et al.* exploited the use of  $\text{NaYF}_4:\text{Er}^{3+}/\text{Yb}^{3+}\text{-TiO}_2$  core-shell composite as a photoanode. The conversion efficiency was enhanced by a factor of 1.23 [126]. To avoid electron recombination losses, Zhao *et al.* separated the upconversion and  $\text{TiO}_2$  layers by growing the middle  $\text{SiO}_2$  layer between them, achieving an improvement of 29.4% in efficiency [127]. In another way, Demopoulos *et al.* [128] investigated the utilization of  $\beta\text{-NaYF}_4:\text{Yb}^{3+}/\text{Er}^{3+}\text{-TiO}_2$  submicro particles as both a light harvesting and an IR energy relay layer. An optimization of the layer of the DSSC structure resulted in a 16% relative increase of power conversion efficiency. On the other hand, there are a number of studies using a range of RED UC materials doped with  $\text{Yb}^{3+}\text{-Er}^{3+}$  [68,129,130],  $\text{Yb}^{3+}\text{-Tm}^{3+}$  [29],  $\text{Er}^{3+}$  [131], for improving the NIR response of DSSCs, and the following illustration (Figure 10) presents the energy transfer mechanisms in a DSSC equipped with a upconverter copodoped with  $\text{Yb}^{3+}$  and  $\text{Er}^{3+}$ .



**Figure 10.** A cartoon illustration of energy transfer mechanisms in upconversion nanoparticles (UCNPs)-Doped DSSCs. This figure shows the absorption and conversion of near infrared (NIR) photons into visible light of higher energy via upconversion; the electron transfer from UCNPs to the conduction band of  $\text{TiO}_2$ , as well as the electron transfer from  $\text{I}^-/\text{I}_3^-$  to the ground state of UCNPs. FRET and LET are fluorescence resonance energy transfer and luminescence-mediated energy transfer, respectively. HOMO and LUMO are highest occupied molecular orbital and lowest unoccupied molecular orbital, respectively.

Narrow absorption and high excitation threshold of RED-UC are two main limits for efficiency improvement in DSSCs. To mitigate this, Bai and co-workers [132] enhanced light harvesting by 14% due to the usage of  $\text{CeO}_2:\text{Er}^{3+}/\text{Yb}^{3+}$  nanofibers that exploited host effect to broaden the light absorption ability. Chen *et al.* [133] provided a method to broaden the NIR absorption of upconversion nanoparticles by utilization of a hexagonal core-shell structure of  $\beta\text{-NaYbF}_4:2\% \text{Er}^{3+}@ \text{NaYF}_4:30\% \text{Nd}^{3+}$ . This allows simultaneous use of the absorption of  $\text{Nd}^{3+}$  (~800 nm),  $\text{Yb}^{3+}$  (~980 nm), and possibly  $\text{Er}^{3+}$  (~1550 nm) ions for light harvesting, while the core/shell structure enables a spatial isolation of  $\text{Nd}^{3+}$  from  $\text{Yb}^{3+}$  and  $\text{Er}^{3+}$  ions to avoid detrimental cross relaxations to entail a high upconversion efficiency. Zhao *et al.* [134] achieved an efficiency of 8.32% (with a noticeable enhancement of 14.78%) by putting core-shell-structured  $\beta\text{-NaYF}_4:\text{Yb}^{3+}/\text{Er}^{3+}@ \text{SiO}_2@ \text{Au}$  nanocomposites on top of a mesoporous  $\text{TiO}_2$  layer. Yang's group [124,135,136] also did a lot research on enhancing the performance of DSSCs using different lanthanide ion doped nanoparticles. For example, the design of  $\text{Ho}^{3+}\text{-Yb}^{3+}\text{-F}^-$  tri-doped  $\text{TiO}_2$  nanoparticles enabled a 37% improvement in the power conversion efficiency. Despite recent achievements, improvement of DSSCs efficiency is still limited by the upconversion efficiency as well as the narrow and low absorption ability of RED-UC. Overcoming these two problems would lead to an epidemic use of RED-UC in DSSCs.

### 3.5. Other Types of Solar Cells

Apart from the solar cells discussed above, organic solar cells are considered to be one of the most promising alternatives for Si-based solar cells, due to their advantages of being flexible, low-cost, light-weight, of simple fabrication and large-scale production for the PV industry [137–141]. However, limited by the spectral mismatch of the absorption of organic molecules with sun irradiation, the improvement in efficiency remains a daunting task. Bulk heterojunction-based PV cells with a large bandgap of organic molecules are only able to absorb visible sunlight. Currently, some organic solar cells have been designed to harvest 800–900 nm sunlight by using low-band-gap polymer materials such as PCPDTBT (poly-[N-9'-heptadecanyl-2,7-carbazole-alt-5,5(4',7'-di-2-thienyl-2',1',3'-benzothiadiazole)] and its derivatives [18,142–144]. The poly (3-hexylthiophene) (P3HT) and the fullerene derivative [6,6]-phenyl-C61-butyric acid methyl ester (PCBM) have been exploited to increase the optical response of organic solar cells to 650–700 nm [145].

Upconversion materials have been dedicated to further extend the NIR spectral response. Wang and co-workers utilized  $\text{LaF}_3:\text{Yb}^{3+}/\text{Er}^{3+}$  phosphors to improve the NIR response of P3HT:PCBM organic solar cells. An upconverted photocurrent density of  $\sim 16.5 \mu\text{A}/\text{cm}^2$  was obtained under an excitation density of  $25 \text{ mW}/\text{cm}^2$  at 975 nm [146]. In another work of theirs, they demonstrated that the UC material ( $\text{MoO}_3:\text{Yb}^{3+}/\text{Er}^{3+}$ ), incorporated into P3HT:PCBM organic solar cells, contributed about 1% to the improvement of short-circuit current under one-sun (AM 1.5) illumination [147]. Wu *et al.* [148] in 2012 added  $\text{NaYF}_4:\text{Yb}^{3+}, \text{Er}^{3+}$  nanoparticles on the rear of a P3HT:PCBM organic solar cell, the short-circuit current was enhanced by  $0.5 \mu\text{A}$  when illuminated by a 980 nm light.

To utilize the NIR solar spectrum more efficiently, Adikaari *et al.* [149] reported an application of  $\text{Y}_2\text{BaZnO}_5:\text{Yb}^{3+}, \text{Ho}^{3+}$  UC particles in PCDTBT:PCBM organic solar cells. Two different layout designs are presented in Figure 11. The PCDTBT:PCBM active layer absorbs photons of wavelength shorter than 700 nm, while  $\text{Y}_2\text{BaZnO}_5:\text{Yb}^{3+}/\text{Ho}^{3+}$  shows an intense absorption in the NIR region of 870–1030 nm due to the  ${}^2\text{F}_{7/2} \rightarrow {}^2\text{F}_{5/2}$  ( $\text{Yb}^{3+}$ ) transition. Moreover, the UC emission peak at 545 nm from  $\text{Ho}^{3+}$ , corresponding to the  ${}^5\text{S}_2/{}^5\text{F}_4 \rightarrow {}^5\text{I}_8$  transition, matches well with the absorption band of PCDTBT:PCBM active layer. Illuminated by a 986 nm laser with an excitation density of  $\sim 390 \text{ mW}/\text{cm}^2$ , a maximum photocurrent density of  $16 \mu\text{A}/\text{cm}^2$  and a conversion of 0.45% were obtained, showing the ability to expand the response into the NIR range. Guo *et al.* [150] used a similar method to improve the performance of both NIR harvesting and light scattering of inverted polymer BHI solar cells through mixing  $\text{NaYF}_4:\text{Yb}^{3+}/\text{Er}^{3+}$  with PCDTBT:PCBM.

Instead of using UC materials as upconverters, the porphyrin-based TTA-sensitizers have also been utilized to efficiently increase the NIR response of solar cells [151]. Schulze's group carried out a comprehensive study to explore the application of TTA-UC in organic solar cells [104,106], among which the photocurrent was increased up to 0.2% under a moderate concentration of 19 suns [105]. In this system, a TTA-UC unit was conjugated to the inverted organic cell, to avoid parasitic optical losses [102].

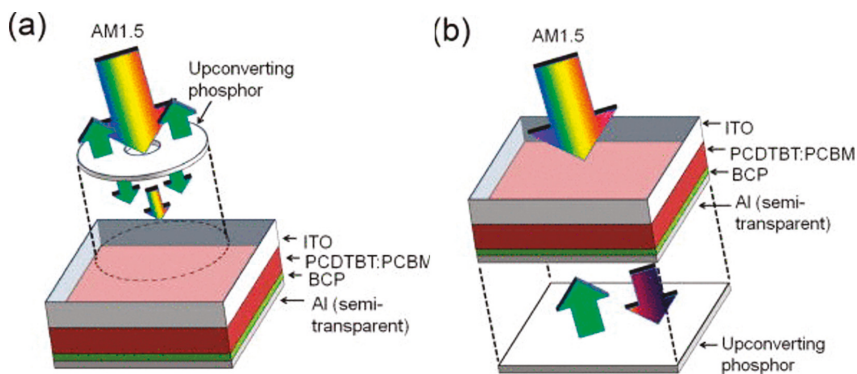


**Figure 11.** Schematic design of an organic PV device with upconversion phosphors placed (a) in front of or (b) behind the device (adapted with permission from [149]; Copyright AIP Publishing, 2012).

#### 4. Conclusions

In this review, we have summarized photon upconversion materials including rare-earth-doped upconversion materials, triplet-triplet annihilation upconversion materials, and quantum nanostructure upconversion materials as spectral modifiers for various types of photovoltaic solar cells to circumvent their major energy loss mechanism of transmission loss. The ability to convert the transmitted sub-band-gap photons into above-band-gap light where solar cells typically have high quantum efficiency, enables the Shockley-Queisser limit of single junction PV devices to be broken. The inorganic rare-earth-doped upconversion materials are able to work above 800 nm, while the organic triplet-triplet annihilation upconversion dye pairs typically work below 700 nm. Moreover, quantum nanostructures emerge as a new type of upconversion materials, where the size- and shape-induced quantum effects can be exploited to upconvert at the required wavelength ranges. Indeed, the use of these upconversion materials has improved the performance of c-Si, amorphous Si, GaAs, DSSCs as well as other PV devices with varying bandgaps. Despite recent progress, the increase of efficiency remains less than 2%, far below the theoretical prediction of ~10% as in the case of c-Si PV cells when irradiated with unconcentrated sun light [17]. This discrepancy is ascribed to several problems of current photon upconversion materials. (i) The established energy conversion efficiency of long wavelength rare-earth-doped upconversion materials is less than 3% [152], thus limiting the contribution of spectral conversion of absorbed photons for improvement of PV efficiency. To improve the upconversion efficiency, various approaches can be utilized such as non-luminescent impurity doping, using photonic crystals to tailor the excitation field [153], architecture of a core-shell structure to suppress surface-related quenching mechanisms, utilization of metallic structures for surface plasmon enhanced upconversion [154], *etc.*; (ii) The low and narrow absorption of rare earth ions results in harvesting of only a small fraction of sunlight for rare earth upconversion. Design of hierarchical nanostructures to incorporate a range of rare earth ions, without introducing deleterious cross relaxations, collectively can produce intense broad band upconversion [61,155]. Alternatively, external sensitizers that have strong and broad absorption, such as organic dyes [156], quantum dots [157], and transition metal ions [158] can be utilized to sensitize rare earth ions to entail upconversion; (iii)

Photon upconversion is a nonlinear optical process, defining the strong dependence of upconversion luminescence on light irradiance. Most photon upconversion materials thus have limited luminescent upconverting efficiency in the range of sun irradiance ( $\sim 1000 \text{ W/m}^2$ ). Triplet-triplet annihilation upconversion (TTA UC) has impressive efficacy under sun irradiation, favorable for uses in solar cells but with wide band-gap [101,159]. This is because the involved absorption is typically less than 700 nm [27,29,101,159–162]. Development of TTA UC with wavelengths in the IR range is appealing [102]; (iv) The upconversion in quantum nanostructures has been demonstrated at a visible wavelength, but not shown in the broad spectral range, in particular, the IR range under sunlight irradiance. This limits its uses in PV devices. Future works to overcome this problem are attractive. In all, development of upconversion materials with broad-band, strong, and tunable absorption as well as high upconverting efficiency is required, which will significantly boost solar cell efficiency by upconversion of transmitted sub-band-gap photons.

**Acknowledgments:** This work was supported in part by the National Science Foundation of China (No. 51102066), the National Science Fund for Distinguished Young Scholars (No. 51325201), the International Cooperation Project in the Ministry of Science and Technology (No. 2014DFA50740), the Program for Basic Research Excellent Talents in Harbin Institute of Technology, China (BRETIII 2012018), and the Fundamental Research Funds for the Central Universities, China (AUGA 5710052614).

**Conflicts of Interest:** The authors declare no conflict of interest.

## References

1. Kalyanasundaram, K.; Gratzel, M. Themed issue: Nanomaterials for energy conversion and storage. *J. Mater. Chem.* **2012**, *22*, 24190–24194. [CrossRef]
2. Nozik, J.; Miller, J. Introduction to solar photon conversion. *Chem. Rev.* **2010**, *110*, 6443–6445. [CrossRef] [PubMed]
3. Luna-Rubio, R.; Trejo-Peria, M.; Vargas-Vázquez, D.; Ríos-Moreno, G.J. Optimal sizing of renewable hybrids energy systems: A review of methodologies. *Sol. Energy* **2012**, *86*, 1077–1088. [CrossRef]
4. Muller-Furstenberger, G.; Wagner, M. Exploring the environmental Kuznets hypothesis: Theoretical and environmental problem. *Ecol. Econ.* **2007**, *62*, 648–660. [CrossRef]
5. Simmons, M.R. Twilight in the Desert. In *The Coming Saudi Oil Shock and the World Economy*; John Wiley & Sons: Hoboken, NJ, USA, 2005.
6. Olah, G.O.; Goepert, A.; Prakash, G.K.S. *Beyond Oil and Gas: The Methanol Economy*; Wiley-VCH: Weinheim, Germany, 2006.
7. Scholes, G.D.; Fleming, G.R.; Olaya-Castro, A.; van Grondelle, R. Lessons from nature about solar light harvesting. *Nat. Chem.* **2011**, *3*, 763–774. [CrossRef] [PubMed]
8. Lewis, N.S. Toward cost-effective solar energy use. *Science* **2007**, *315*, 798–801. [CrossRef] [PubMed]
9. Águas, H.; Ram, S.K.; Araújo, A.; Gaspar, D.; Vicente, A.; Filonovich, S.A.; Fortunato, E.; Martins, R.; Ferreira, I. Silicon thin film solar cells on commercial tiles. *Energy Environ. Sci.* **2011**, *4*, 4620–4632. [CrossRef]
10. Grätzel, M. Photovoltaic and photoelectrochemical conversion of solar energy. *Philos. Trans. R. Soc. A* **2007**, *365*, 993–1005. [CrossRef] [PubMed]
11. Lewis, N.S.; Nocera, D.G. Powering the planet: Chemical challenges in solar energy utilization. *Proc. Natl. Acad. Sci. USA* **2006**, *103*, 15729–15735. [CrossRef] [PubMed]
12. Morton, O. Solar energy: A new day dawning? Silicon Valley Sunrise. *Nature* **2006**, *443*, 19–22. [CrossRef] [PubMed]
13. Van der Ende, B.M.; Aarts, L.; Andries, M. Lanthanide ions as spectral converters for solar cells. *Phys. Chem. Chem. Phys.* **2009**, *11*, 11081–11095. [CrossRef] [PubMed]
14. Saga, T. Advances in crystalline silicon solar cell technology for industrial mass production. *NPG Asia Mater.* **2010**, *2*, 96–102. [CrossRef]
15. Chen, G.Y.; Seo, J.; Yang, C.H.; Prasad, P.N. Nanochemistry and nanomaterials for photovoltaics. *Chem. Soc. Rev.* **2013**, *42*, 8304–8338. [CrossRef] [PubMed]
16. Shockley, W.; Queisser, H.J. Detailed Balance Limit of Efficiency of p-n Junction Solar Cells. *J. Appl. Phys.* **1961**, *32*, 510–519. [CrossRef]



17. Trupke, T.; Shalav, A.; Richards, B.S.; Würfel, P.; Green, M.A. Efficiency enhancement of solar cells by luminescent up-conversion of sunlight. *Sol. Energy Mater. Sol. Cells* **2006**, *90*, 3327–3338. [CrossRef]
18. Zhou, J.; Liu, Q.; Feng, W.; Sun, Y.; Li, F. Upconversion Luminescent Materials: Advances and Applications. *Chem. Rev.* **2015**, *115*, 395–465. [CrossRef] [PubMed]
19. Haase, M.; Schäfer, H. Upconverting nanoparticles. *Angew. Chem. Int. Ed.* **2011**, *50*, 5808–5829.
20. Sun, L.D.; Wang, Y.F.; Yan, C.H. Paradigms and challenges for bioapplication of rare earth upconversion luminescent nanoparticles: Small size and tunable emission/excitation spectra. *Acc. Chem. Res.* **2014**, *47*, 1001–1009. [CrossRef] [PubMed]
21. Zhou, J.; Liu, Z.; Li, F.Y. Upconversion nanophosphors for small-animal imaging. *Chem. Soc. Rev.* **2012**, *41*, 1323–1349. [CrossRef] [PubMed]
22. Gorris, H.H.; Wolfbeis, O.S. Photon-upconverting nanoparticles for optical encoding and multiplexing of cells, biomolecules, and microspheres. *Angew. Chem. Int. Ed.* **2013**, *52*, 3584–3600.
23. Liu, Q.; Feng, W.; Li, F. Water-soluble lanthanide upconversion nanophosphors: Synthesis and bioimaging applications *in vivo*. *Chem. Rev.* **2014**, *273*, 100–110. [CrossRef]
24. Feng, W.; Han, C.M.; Li, F.Y. Upconversion-Nanophosphor-Based Functional Nanocomposites. *Adv. Mater.* **2013**, *25*, 5287–5303. [CrossRef] [PubMed]
25. Wang, F.; Banerjee, D.; Liu, Y.S.; Chen, X.Y.; Liu, X.G. Upconversion Nanoparticles in Biological Labeling, Imaging and Therapy. *Analyst* **2010**, *135*, 1839–1854. [CrossRef] [PubMed]
26. Wang, F.; Liu, X.G. Recent advances in the chemistry of lanthanide-doped upconversion nanocrystals. *Chem. Soc. Rev.* **2009**, *38*, 976–989. [CrossRef] [PubMed]
27. Zhao, J.Z.; Ji, S.M.; Guo, H.M. Triplet-triplet annihilation based upconversion: From triplet sensitizers and triplet acceptors to upconversion quantum yields. *RSC Adv.* **2011**, *1*, 937–950. [CrossRef]
28. Soo, H.L.; Mathieu, A.A.; Roberto, V.; Christoph, W.; Yoan, C.S. Light upconversion by triplet–triplet annihilation in diphenylanthracene-based copolymers. *Polym. Chem.* **2014**, *5*, 6898–6904.
29. Singh-Rachford, T.N.; Castellano, F.N. Photon upconversion based on sensitized triplet-triplet annihilation. *Coord. Chem. Rev.* **2010**, *254*, 2560–2573. [CrossRef]
30. Deutsch, Z.; Neeman, L.; Oron, D. Luminescence upconversion in colloidal double quantum dots. *Nat. Nanotechnol.* **2013**, *8*, 649–653. [PubMed]
31. Deutsch, Z.; Schwartz, O.; Tenne, R.; Popovitz-Biro, R.; Oron, D. Two-color antibunching from band-gap engineered colloidal semiconductor nanocrystals. *Nano Lett.* **2012**, *12*, 2948–2952. [CrossRef] [PubMed]
32. Xing, G.; Liao, Y.; Wu, X.; Chakraborty, S.; Liu, X.; Yeow, E.K.L.; Chan, Y.; Sum, T.C. Ultralow-threshold two-photon pumped amplified spontaneous emission and lasing from seeded CdSe/CdS nanorod heterostructures. *ACS Nano* **2012**, *6*, 10835–10844. [CrossRef] [PubMed]
33. Bunzli, J.C.G. Benefiting from the Unique Properties of Lanthanide Ions. *Acc. Chem. Res.* **2006**, *39*, 53–61. [CrossRef] [PubMed]
34. Bunzli, J.C.G. Lanthanide luminescence for biomedical analyses and imaging. *Chem. Rev.* **2010**, *110*, 2729–2755. [CrossRef] [PubMed]
35. Carlos, L.D.; Ferreira, R.A.S.; Bermudez, V.D.; Julian-Lopez, B.; Escibano, P. Progress on lanthanide-based organic-inorganic hybrid phosphors. *Chem. Soc. Rev.* **2011**, *40*, 536–549. [PubMed]
36. Kar, A.; Patra, A. Impacts of core-shell structures on properties of lanthanide-based nanocrystals: Crystal phase, lattice strain, downconversion, upconversion and energy transfe. *Nanoscale* **2012**, *4*, 3608–3619. [CrossRef] [PubMed]
37. Goesmann, H.; Feldmann, C. Nanoparticulate Functional Materials. *Angew. Chem. Int. Ed.* **2010**, *49*, 1362–1395. [CrossRef] [PubMed]
38. Ohwaki, J.; Wang, Y. Efficient 1.5mm to visible upconversion in Er<sup>3+</sup>-doped halide phosphors. *Jpn. J. Appl. Phys.* **1994**, *33*, 334–337. [CrossRef]
39. Auzel, F.; Pecile, D.; Morin, D. Rare earth doped vitroceraamics: New, efficient, blue and green emitting materials for infrared upconversion. *J. Electrochem. Soc.* **1975**, *122*. [CrossRef]
40. Menyuk, N.; Dwight, K.; Pierce, J.W. NaYF<sub>4</sub>:Yb,Er—An efficient upconversion phosphor. *Appl. Phys. Lett.* **1972**, *21*, 159–161. [CrossRef]
41. Suyver, J.F.; Grimm, J.; Krämer, K.W.; Güdel, H.U. Highly Efficient Near-Infrared to Visible Up-Conversion Process in NaYF<sub>4</sub>:Er<sup>3+</sup>,Yb<sup>3+</sup>. *J. Lumin.* **2005**, *114*, 53–59. [CrossRef]



42. Krämer, K.W.; Biner, D.; Frei, G.; Güdel, H.U.; Hehlen, M.P.; Lüthi, S.T. Hexagonalsodium yttrium fluoride based green and blue emitting upconversion phosphors. *Chem. Mater.* **2004**, *16*, 1244–1251. [CrossRef]
43. Wang, L.; Li, X.; Li, Z.; Chu, W.; Li, R.; Lin, K.; Qian, H.; Wang, Y.; Wu, C.; Li, J.; *et al.* A New Cubic Phase for a NaYF<sub>4</sub> Host Matrix Offering High Upconversion Luminescence Efficiency. *Adv. Mater.* **2015**, *27*. [CrossRef]
44. Chen, G.Y.; Ohulchanskyy, T.Y.; Kachynski, A.; Agren, H.; Prasad, P.N. Intense Visible and Near-Infrared Upconversion Photoluminescence in Colloidal LiYF<sub>4</sub>:Er<sup>3+</sup> Nanocrystals under Excitation at 1490 nm. *ACS Nano* **2011**, *5*, 4981–4986. [CrossRef] [PubMed]
45. Kumar, G.A.; Pokhrel, M.; Sardar, D.K. Intense visible and near infrared upconversion in M<sub>2</sub>O<sub>2</sub>S:Er (M = Y, Gd, La) phosphor under 1550 nm excitation. *Mater. Lett.* **2012**, *68*, 395–398. [CrossRef]
46. Zheng, K.Z.; Zhao, D.; Zhang, D.S.; Liu, N.; Qin, W.P. Ultraviolet upconversion fluorescence of Er<sup>3+</sup> induced by 1560 nm laser excitation. *Opt. Lett.* **2010**, *35*, 2442–2444. [CrossRef] [PubMed]
47. Fischer, S.; Goldschmidt, J.C.; Loper, P.; Bauer, G.H.; Bruggemann, R.; Kramer, K.; Biner, D.; Hermle, M.; Glunz, S.W. Enhancement of silicon solar cell efficiency by upconversion: Optical and electrical characterization. *J. Appl. Phys.* **2010**, *108*, 044912. [CrossRef]
48. Li, C.; Lin, J. Rare earth fluoride nano-/microcrystals: Synthesis, surface modification and application. *J. Mater. Chem.* **2010**, *20*, 6831–6847. [CrossRef]
49. Chen, G.Y.; Zhang, Y.G.; Somesfalean, G.; Zhang, Z.G.; Sun, Q.; Wang, F.P. Two-color upconversion in rare-earth-ion-doped ZrO<sub>2</sub> nanocrystals. *Appl. Phys. Lett.* **2006**, *89*, 163105. [CrossRef]
50. Chen, G.Y.; Somesfalean, G.; Liu, Y.; Zhang, Z.G.; Sun, Q.; Wang, F.P. Upconversion mechanism for two-color emission in rare-earth-ion-doped ZrO<sub>2</sub> nanocrystals. *Phys. Rev. B* **2007**, *75*, 195204. [CrossRef]
51. Boyer, J.C.; Johnson, N.J.J.; van Veggel, F.C.J.M. Upconverting Lanthanide-Doped NaYF<sub>4</sub>-PMMA Polymer Composites Prepared by in Situ Polymerization. *Chem. Mater.* **2009**, *21*, 2010–2012.
52. Boyer, J.C.; Cuccia, L.A.; Capobianco, J.A. Synthesis of Colloidal Upconverting NaYF<sub>4</sub>:Er<sup>3+</sup>/Yb<sup>3+</sup> and Tm<sup>3+</sup>/Yb<sup>3+</sup> Monodisperse Nanocrystals. *Nano Lett.* **2007**, *7*, 847–852. [CrossRef] [PubMed]
53. Heer, S.; Kompe, K.; Gudel, H.U.; Haase, M. Highly Efficient Multicolour Upconversion Emission in Transparent Colloids of Lanthanide-Doped NaYF<sub>4</sub> Nanocrystals. *Adv. Mater.* **2004**, *16*, 2102–2105. [CrossRef]
54. Chen, D.; Zhou, Y.; Wan, Z.; Huang, P.; Yu, H.; Lu, H.; Ji, Z. Enhanced upconversion luminescence in phase-separation-controlled crystallization glass ceramics containing Yb/Er(Tm):NaLuF<sub>4</sub> nanocrystals. *J. Eur. Ceram. Soc.* **2015**, *35*, 2129–2137. [CrossRef]
55. Cheng, E.; Yin, W.; Bai, S.; Qiao, R.; Zhong, Y.; Li, Z. Synthesis of vis/NIR-driven hybrid photocatalysts by electrostatic assembly of NaYF<sub>4</sub>:Yb, Tm nanocrystals on g-C<sub>3</sub>N<sub>4</sub> nanosheets. *Mater. Lett.* **2015**, *146*, 87–90. [CrossRef]
56. Chen, G.Y.; Shen, J.; Ohulchanskyy, T.Y.; Patel, N.J.; Kutikov, A.; Li, Z.P.; Song, J.; Pandey, R.K.; Agren, H.; Prasad, P.N.; *et al.* (α-NaYF<sub>4</sub>:Tm<sup>3+</sup>)/CaF<sub>2</sub> Core/Shell Nanoparticles with Efficient Near-Infrared to Near-Infrared Upconversion for High-Contrast Deep Tissue Bioimaging. *ACS Nano* **2012**, *6*, 8280–8287. [CrossRef] [PubMed]
57. Li, Q.; Lin, J.; Wu, J.; Lan, Z.; Wang, Y.; Peng, F.; Huang, M. Enhancing photovoltaic performance of dye-sensitized solar cell by rare-earth doped oxide of Lu<sub>2</sub>O<sub>3</sub>:(Tm<sup>3+</sup>, Yb<sup>3+</sup>). *Electrochim. Acta* **2011**, *56*, 4980–4984. [CrossRef]
58. Chen, G.Y.; Ohulchanskyy, T.Y.; Kumar, R.; Agren, H.; Prasad, P.N. Ultrasmall Monodisperse NaYF<sub>4</sub>:Yb<sup>3+</sup>/Tm<sup>3+</sup> Nanocrystals with Enhanced Near-Infrared to Near-Infrared Upconversion Photoluminescence. *ACS Nano* **2010**, *4*, 3163–3168. [CrossRef] [PubMed]
59. Ramakrishna, P.V.; Pammi, S.V.N.; Samatha, K. UV-visible upconversion studies of Nd<sup>3+</sup> ions in lead tellurite glass. *Solid State Commun.* **2013**, *155*, 21–24. [CrossRef]
60. Shang, Y.; Hao, S.; Liu, J.; Tan, M.; Wang, N.; Yang, C.; Chen, G. Synthesis of Upconversion β-NaYF<sub>4</sub>:Nd<sup>3+</sup>/Yb<sup>3+</sup>/Er<sup>3+</sup> Particles with Enhanced Luminescent Intensity through Control of Morphology and Phase. *Nanomaterials* **2015**, *5*, 218–232. [CrossRef]
61. Wang, Y.-F.; Liu, G.-Y.; Sun, L.-D.; Xiao, J.-W.; Zhou, J.-C.; Yan, C.-H. Nd<sup>3+</sup>-Sensitized Upconversion Nanophosphors: Efficient *in Vivo* Bioimaging Probes with Minimized Heating Effect. *ACS Nano* **2013**, *7*, 7200–7206. [CrossRef] [PubMed]
62. Li, X.; Wang, R.; Zhang, F.; Zhou, L.; Shen, D.; Yao, C.; Zhao, D. Nd<sup>3+</sup> Sensitized Up/Down Converting Dual-Mode Nanomaterials for Efficient *in-vitro* and *in-vivo* Bioimaging Excited at 800 nm. *Sci. Rep.* **2013**, *3*. [CrossRef]

63. Shalav, A.; Richards, B.S.; Trupke, T. Application of NaYF<sub>4</sub>:Er<sup>3+</sup> up-converting phosphors for enhanced near-infrared silicon solar cell response. *Appl. Phys. Lett.* **2005**, *86*, 013505. [CrossRef]
64. Tian, G.; Zheng, X.; Zhang, X.; Yin, W.; Yu, J.; Wang, D.; Zhang, Z.; Yang, X.; Gu, Z.; Zhao, Y. TPGS-stabilized NaYbF<sub>4</sub>:Er upconversion nanoparticles for dual-modal fluorescent/CT imaging and anticancer drug delivery to overcome multi-drug resistance. *Biomaterials* **2015**, *40*, 107–116. [CrossRef] [PubMed]
65. Chen, G.Y.; Qiu, H.L.; Fan, R.W.; Hao, S.W.; Tan, S.; Yang, C.H.; Han, G. Lanthanide-doped ultrasmall yttrium fluoride nanoparticles with enhanced multicolor upconversion photoluminescence. *J. Mater. Chem.* **2012**, *22*, 20190. [CrossRef]
66. Jung, T.; Jo, H.L.; Nam, S.H.; Yoo, B.; Cho, Y.; Kim, J.; Kim, H.M.; Hyeon, T.; Suh, Y.D.; Lee, H.; *et al.* The preferred upconversion pathway for the red emission of lanthanide-doped upconverting nanoparticles, NaYF<sub>4</sub>:Yb<sup>3+</sup>,Er<sup>3+</sup>. *Phys. Chem. Chem. Phys.* **2015**, *17*, 13201. [CrossRef] [PubMed]
67. Tian, D.; Gao, D.; Chongb, B.; Liu, X. Upconversion improvement by the reduction of Na<sup>+</sup>-vacancies in Mn<sup>2+</sup> doped hexagonal NaYbF<sub>4</sub>:Er<sup>3+</sup> nanoparticles. *Dalton Trans.* **2015**, *44*, 4133. [CrossRef] [PubMed]
68. Khan, A.F.; Yadav, R.; Mukhopadhyaya, P.K.; Singh, S.; Dwivedi, C.; Dutta, V.; Chawla, S. Core-shell nanophosphor with enhanced NIR–visible upconversion as spectrum modifier for enhancement of solar cell efficiency. *J. Nanopart. Res.* **2011**, *13*, 6837–6846. [CrossRef]
69. Chen, Y.; Liu, B.; Deng, X.; Huang, S.; Hou, Z.; Li, C.; Lin, J. Multifunctional Nd<sup>3+</sup>-sensitized upconversion nanomaterials for synchronous tumor diagnosis and treatment. *Nanoscale* **2015**, *7*, 8574. [CrossRef] [PubMed]
70. Zhang, S.; Wang, J.; Xu, W.; Chen, B.; Yu, W.; Xu, L.; Song, H. Fluorescence Resonance energy transfer between NaYF<sub>4</sub>:Yb,Tm upconversion nanoparticles and gold nanorods: Near-infrared responsive biosensor for streptavidin. *J. Lumin.* **2014**, *147*, 278–283. [CrossRef]
71. Luu, Q.; Hor, A.; Fisher, J.; Anderson, R.B.; Liu, S.; Luk, T.; Paudel, H.P.; Baroughi, M.F.; May, P.S.; Smith, S. Two-Color Surface Plasmon Polariton Enhanced Upconversion in NaYF<sub>4</sub>:Yb:Tm Nanoparticles on Au Nanopillar Arrays. *J. Phys. Chem. C* **2014**, *118*, 3251–3257. [CrossRef]
72. Lin, H.; Xu, D.; Teng, D.; Yang, S.; Zhang, Y. Simultaneous size and luminescence control of NaYF<sub>4</sub>:Yb<sup>3+</sup>/RE<sup>3+</sup> (RE = Tm, Ho) microcrystals via Li<sup>+</sup> doping. *Opt. Mater.* **2015**, *45*, 229–234. [CrossRef]
73. Amemori, S.; Yanai, N.; Kimizuka, N. Metallonaphthalocyanines as triplet sensitizers for near-infrared photon upconversion beyond 850 nm. *Phys. Chem. Chem. Phys.* **2015**, *17*, 22557–22560. [CrossRef] [PubMed]
74. Huang, Z.; Li, X.; Mahboub, M.; Hanson, K.M.; Nichols, V.M.; Le, H.; Tang, M.L.; Bardeen, C.J. Hybrid Molecule—Nanocrystal Photon Upconversion across the Visible and Near-Infrared. *Nano Lett.* **2015**, *15*, 5552–5557. [CrossRef] [PubMed]
75. Monguzzi, A.; Braga, D.; Gandini, M.; Holmberg, V.C.; Kim, D.K.; Sahu, A.; Norris, D.J.; Meinardi, A.F. Broadband Up-Conversion at Subsolar Irradiance: Triplet-Triplet Annihilation Boosted by Fluorescent Semiconductor Nanocrystals. *Nano Lett.* **2014**, *14*, 6644–6650. [CrossRef]
76. Monguzzi, A.; Borisov, S.; Pedrini, J.; Klimant, I.; Salvalaggio, M.; Biagini, P.; Melchiorre, F.; Lelii, C.; Meinardi, F. Efficient Broadband Triplet-Triplet Annihilation-Assisted Photon Upconversion at Subsolar Irradiance in Fully Organic Systems. *Adv. Funct. Mater.* **2015**, *25*. [CrossRef]
77. Mahato, P.; Monguzzi, A.; Yanai, N.; Yamada, T.; Kimizuka, N. Fast and long-range triplet exciton diffusion in metal-organic frameworks for photon upconversion at ultralow excitation power. *Nat. Mater.* **2015**, *14*, 924–930. [CrossRef] [PubMed]
78. Duan, P.; Yanai, N.; Kimizuka, N. Photon Upconverting Liquids: Matrix-Free Molecular Upconversion Systems Functioning in Air. *J. Am. Chem. Soc.* **2013**, *135*, 19056–19059. [CrossRef] [PubMed]
79. Duan, P.; Yanai, N.; Nagatomi, H.; Kimizuka, N. Photon Upconversion in Supramolecular Gel Matrixes: Spontaneous Accumulation of Light-Harvesting Donor—Acceptor Arrays in Nanofibers and Acquired Air Stability. *J. Am. Chem. Soc.* **2015**, *137*, 1887–1894. [CrossRef] [PubMed]
80. Ogawa, T.; Yanai, N.; Monguzzi, A.; Kimizuka, N. Highly Efficient Photon Upconversion in Self-Assembled Light-Harvesting Molecular Systems. *Sci. Rep.* **2015**, *5*. [CrossRef] [PubMed]
81. Hisamitsu, S.; Yanai, N.; Kimizuka, N. Photon-Upconverting Ionic Liquids: Effective Triplet Energy Migration in Contiguous Ionic Chromophore Arrays. *Angew. Chem. Int. Ed.* **2015**, *54*, 1–6. [CrossRef] [PubMed]
82. Vadrucchi, R.; Weder, C.; Simon, Y.C. Low-power photon upconversion in organic glasses. *J. Mater. Chem. C* **2014**, *2*, 2837–2841. [CrossRef]
83. Vadrucchi, R.; Weder, C.; Simon, Y.C. Organogels for low-power light upconversion. *Mater. Horiz.* **2015**, *2*, 120–124. [CrossRef]

84. Green, M.A.; Emery, K.; Hishikawa, Y.; Warta, W.; Dunlop, E.D. Solar cell efficiency tables. *Prog. Photovolt.* **2014**, *22*, 701–710. [CrossRef]
85. Lahoz, F. Ho<sup>3+</sup>-doped nanophase glass ceramics for efficiency enhancement in silicon solar cells. *Opt. Lett.* **2008**, *33*, 2982–2984. [CrossRef] [PubMed]
86. Lahoz, F.; Perez-Rodriguez, C.; Hernandez, S.E.; Martin, I.R.; Lavin, V.; Rodriguez-Mendoza, U.R. Upconversion mechanisms in rare-earth doped glasses to improve the efficiency of silicon solar cells. *Sol. Energy Mater. Sol. Cells* **2011**, *95*, 1671–1677. [CrossRef]
87. Chen, D.; Lei, L.; Yang, A.; Wang, Z.; Wang, Y. Ultra-broadband near-infrared excitable upconversion core/shell nanocrystals. *Chem. Commun.* **2012**, *48*, 5898–5900. [CrossRef] [PubMed]
88. Shao, W.; Chen, G.; Ohulchanskyy, T.Y.; Kuzmin, A.; Damasco, J.; Qiu, H.; Yang, C.; Hans, Å.; Prasad, P.N. Lanthanide-Doped Fluoride Core/Multishell Nanoparticles for Broad-Band Upconversion of Infrared Light. *Adv. Opt. Mater.* **2015**, *3*, 575–582. [CrossRef]
89. Dobrovolsky, A.; Sukritanon, S.; Kuang, Y.; Tu, C.W.; Chen, W.M.; Buyanova, I.A. Energy Upconversion in GaP/GaN Core/Shell Nanowires for Enhanced Near-Infrared Light Harvesting. *Small* **2014**, *10*, 4403–4406. [PubMed]
90. Zhang, X.D.; Jin, X.; Wang, D.F.; Xiong, S.Z.; Geng, X.H.; Zhao, Y. Synthesis of NaYF<sub>4</sub>:Yb, Er nanocrystals and its application in silicon thin film solar cells. *Phys. Status Solidi C* **2010**, *7*, 1128–1131.
91. De Wild, J.; Meijerink, A.; Rath, J.K.; van Sark, W.G.J.H.M.; Schropp, R.E.I. Towards upconversion for amorphous silicon solar cells. *Sol. Energy Mater. Sol. Cells* **2010**, *94*, 1919–1922. [CrossRef]
92. De Wild, J.; Rath, J.K.; Meijerink, A.; van Sark, W.G.J.H.M.; Schropp, R.E.I. Enhanced near-infrared response of a-Si:H solar cells with β-NaYF<sub>4</sub>:Yb<sup>3+</sup> (18%), Er<sup>3+</sup> (2%) upconversion phosphors. *Sol. Energy Mater. Sol. Cells* **2010**, *94*, 2395–2398. [CrossRef]
93. Yang, F.; Liu, C.; Wei, D.; Chen, Y.; Lu, J.; Yang, S. Er<sup>3+</sup>-Yb<sup>3+</sup> co-doped TeO<sub>2</sub>-PbF<sub>2</sub> oxyhalide tellurite glasses for amorphous silicon solar cells. *Opt. Mater.* **2014**, *36*, 1040–1043.
94. Kumar, P.; Gupta, B.K. New insight into rare-earth doped gadolinium molybdate nanophosphor assisted broad spectral converters from UV to NIR for silicon solar cells. *RSC Adv.* **2015**, *5*, 24729–24736. [CrossRef]
95. Kik, P.; Polman, A. Cooperative upconversion as the gain-limiting factor in Er doped miniature Al<sub>2</sub>O<sub>3</sub> optical waveguide amplifiers. *J. Appl. Phys.* **2003**, *93*, 5008–5012. [CrossRef]
96. Pollack, S.; Chang, D. Ion-pair upconversion pumped laser emission in Er<sup>3+</sup> ions in YAG, YLF, SrF<sub>2</sub>, and CaF<sub>2</sub> crystals. *J. Appl. Phys.* **1988**, *64*, 2885–2893. [CrossRef]
97. Wang, X.F.; Yan, X.H.; Kan, C.X. Controlled synthesis and optical characterization of multifunctional ordered Y<sub>2</sub>O<sub>3</sub>:Er<sup>3+</sup> porous pyramid arrays. *J. Mater. Chem.* **2011**, *21*, 4251–4256. [CrossRef]
98. Ivanova, S.; Pelle, F. Strong 1.53 μm to NIR-VIS-UV upconversion in Er-doped fluoride glass for high-efficiency solar cells. *J. Opt. Soc. Am. B* **2009**, *26*, 1930–1938. [CrossRef]
99. Ohwaki, J.; Wang, Y. New efficient upconversion phosphor BaCl<sub>2</sub>:Er under 1.5 mm excitation. *Electron. Lett.* **1993**, *29*, 351–352. [CrossRef]
100. Chen, Y.; He, W.; Jiao, Y.; Wang, H.; Hao, X.; Lu, J.; Yang, S.E. β-NaYF<sub>4</sub>:Er<sup>3+</sup> (10%) microprisms for the enhancement of a-Si:H solar cell near-infrared responses. *J. Lumin.* **2012**, *132*, 2247–2250. [CrossRef]
101. Cheng, Y.Y.; Fückel, B.; MacQueen, R.W.; Khoury, T.; Clady, R.G.; Schulze, T.F.; Ekins-Daukes, N.J.; Crossley, M.J.; Stannowski, B.; Lips, K.; *et al.* Improving the light-harvesting of amorphous silicon solar cells with photochemical upconversion. *Energy Environ. Sci.* **2012**, *5*, 6953–6959. [CrossRef]
102. Schulze, T.F.; Schmidt, T.W. Photochemical upconversion: Present status and prospects for its application to solar energy conversion. *Energy Environ. Sci.* **2015**, *8*, 103–125. [CrossRef]
103. Nattestad, A.; Cheng, Y.Y.; MacQueen, R.W.; Schulze, T.F.; Thompson, F.W.; Mozer, A.J.; Fückel, B.; Khoury, T.; Crossley, M.J.; Lips, K.; *et al.* Dye-Sensitized Solar Cell with Integrated Triplet–Triplet Annihilation Upconversion System. *J. Phys. Chem. Lett.* **2013**, *4*, 2073–2078. [CrossRef] [PubMed]
104. Schulze, T.F.; Cheng, Y.Y.; Fückel, B.; MacQueen, R.W.; Danos, A.; Davis, N.J.L.K.; Tayebjee, M.J.Y.; Khoury, T.; Clady, R.G.C.R.; Ekins-Daukes, N.J.; *et al.* Photochemical Upconversion Enhanced Solar Cells: Effect of a Back Reflector. *Aust. J. Chem.* **2012**, *65*, 480–485. [CrossRef]
105. Schulze, T.F.; Czolk, J.; Cheng, Y.; Fückel, B.; MacQueen, R.W.; Khoury, T.; Crossley, M.J.; Stannowski, B.; Lips, K.; Lemmer, U.; *et al.* Efficiency Enhancement of Organic and Thin-Film Silicon Solar Cells with Photochemical Upconversion. *J. Phys. Chem. C* **2012**, *116*, 22794–22801. [CrossRef]

106. Schulze, T.F.; Cheng, Y.Y.; Khoury, T.; Crossley, M.J.; Stannowski, B.; Lips, K.; Schmidt, T.W. Micro-optical design of photochemical upconverters for thin-film solar cells. *J. Photonics Energy* **2013**, *3*, 034598. [CrossRef]
107. George, B.M.; Behrends, J.; Schnegg, A.; Schulze, T.F.; Fehr, M.; Korte, L.; Rech, B.; Lips, K.; Rohrmüller, M.; Rauls, E.; *et al.* Atomic Structure of Interface States in Silicon Heterojunction Solar Cells. *Phys. Rev. Lett.* **2013**, *110*, 136803. [CrossRef] [PubMed]
108. Gibart, P.; Auzeil, F.; Guillaume, J.-C.; Zahraman, K. Below band gap IR response of substrate-free GaAs solar cells using two-photon upconversion. *Jpn. J. Appl. Phys.* **1996**, *351*, 4401–4402. [CrossRef]
109. Lin, H.Y.; Chen, H.N.; Wu, T.H.; Wu, C.S.; Su, Y.K.; Chu, S.Y. Investigation of Green Up-Conversion Behavior in  $Y_6W_2O_{15}:Yb^{3+},Er^{3+}$  Phosphor and Its Verification in 973 nm Laser-Driven GaAs Solar Cell. *J. Am. Ceram. Soc.* **2012**, *95*, 3172–3179. [CrossRef]
110. O'Regan, B.; Grätzel, M. A low-cost, high-efficiency solar cell based on dye-sensitized. *Nature* **1991**, *353*, 737–740. [CrossRef]
111. Grätzel, M. Photoelectrochemical cells. *Nature* **2001**, *414*, 338–344. [CrossRef] [PubMed]
112. Bisquert, J. Dilemmas of Dye-Sensitized Solar Cell. *Chem. Phys. Chem.* **2011**, *12*, 1633–1636. [CrossRef] [PubMed]
113. Basham, J.I.; Mor, G.K.; Grimes, C.A. Förster Resonance Energy Transfer in Dye-Sensitized Solar Cells. *ACS Nano* **2010**, *4*, 1253–1258. [CrossRef] [PubMed]
114. Chen, C.-Y.; Wang, M.; Li, J.-Y.; Pootrakulchote, N.; Alibabaei, L.; Ngoc-le, C.-H.; Decoppet, J.-D.; Tsai, J.-H.; Graetzel, C.; Wu, C.G.; *et al.* Highly Efficient Light-Harvesting Ruthenium Sensitizer for Thin-Film Dye-Sensitized Solar Cells. *ACS Nano* **2009**, *3*, 3103–3109. [CrossRef] [PubMed]
115. Huang, X.Y.; Wang, J.X.; Yu, D.C.; Ye, S.; Zhang, Q.Y.; Sun, X.W. Spectral conversion for solar cell efficiency enhancement using  $YVO_4:Bi^{3+}, Ln^{3+}$  ( $Ln = Dy, Er, Ho, Eu, Sm, \text{ and } Yb$ ) phosphors. *J. Appl. Phys.* **2011**, *109*, 113526. [CrossRef]
116. Bünzli, J.C.G.; Eliseeva, S.V. Lanthanide NIR luminescence for telecommunications, bioanalyses and solar energy conversion. *J. Rare Earths* **2010**, *28*, 824–842. [CrossRef]
117. Hafez, H.; Saif, M.; Abdel-Mottaleb, M.S.A. Down-converting lanthanide doped  $TiO_2$  photoelectrodes for efficiency enhancement of dye-sensitized solar cells. *J. Power Sources* **2011**, *196*, 5792–5796. [CrossRef]
118. Levinson, R.; Berdahl, P.; Akbari, H. Solar spectral optical properties of pigments—Part I: Model for deriving scattering and absorption coefficients from transmittance and reflectance measurements. *Sol. Energy Mater. Sol. C* **2005**, *89*, 319–349. [CrossRef]
119. Hara, K.; Sato, T.; Katoh, R.; Furube, A.; Ohga, Y.; Shinpo, A.; Suga, S.; Sayama, K.; Sugihara, H.; Arakawa, H. Molecular Design of Coumarin Dyes for Efficient Dye-Sensitized Solar Cells. *J. Phys. Chem. B* **2003**, *107*, 597–606. [CrossRef]
120. Campbell, W.M.; Burrell, A.K.; Officer, D.L.; Jolley, K.W. Porphyrins as light harvesters in the dye-sensitized  $TiO_2$  solar cell. *Coord. Chem. Rev.* **2004**, *248*, 1363–1379. [CrossRef]
121. Shan, G.-B.; Demopoulos, G.P. Near-Infrared Sunlight Harvesting in Dye-Sensitized Solar Cells via the Insertion of an Upconverter- $TiO_2$  Nanocomposite Layer. *Adv. Mater.* **2010**, *22*, 4373–4377. [CrossRef] [PubMed]
122. Shan, G.B.; Assaaoudi, H.; Demopoulos, G.P. Enhanced Performance of Dye-Sensitized Solar Cells by Utilization of an External, Bifunctional Layer Consisting of Uniform  $\beta-NaYF_4:Er^{3+}/Yb^{3+}$  Nanoplatelets. *ACS Appl. Mater. Interfaces* **2011**, *3*, 3239–3243. [CrossRef] [PubMed]
123. Yuan, C.Z.; Chen, G.Y.; Prasad, P.N.; Ohulchanskyy, T.Y.; Ning, Z.J.; Tian, H.; Sund, L.C.; Agren, H. Use of colloidal upconversion nanocrystals for energy relay solar cell light harvesting in the near-infrared region. *J. Mater. Chem.* **2012**, *22*, 16709–16713. [CrossRef]
124. Li, L.; Yang, Y.; Fan, R.; Jiang, Y.; Wei, L.; Shi, Y.; Yu, J.; Chen, S.; Wang, P.; Yang, B.; *et al.* A simple modification of near-infrared photon-to-electron response with fluorescence resonance energy transfer for dye-sensitized solar cells. *J. Power Sources* **2014**, *264*, 254–261. [CrossRef]
125. Wang, J.; Lin, J.; Wu, J.; Huang, M.; Lan, Z.; Chen, Y.; Tang, S.; Fan, L.; Huang, Y. Application of  $Yb^{3+}, Er^{3+}$ -doped yttrium oxyfluoride nanocrystals in dye-sensitized solar cells. *Electrochim. Acta* **2012**, *70*, 131–135. [CrossRef]
126. Zhang, J.; Shen, H.; Guo, W.; Wang, S.; Zhu, C.; Xue, F.; Hou, J.; Su, H.; Yuan, Z. An upconversion  $NaYF_4:Yb^{3+},Er^{3+}/TiO_2$  core-shell nanoparticle photoelectrode for improved efficiencies of dye-sensitized solar cells. *J. Power Sources* **2013**, *226*, 47–53. [CrossRef]

127. Liang, L.L.; Liu, Y.M.; Zhao, X.Z. Double-shell beta-NaYF<sub>4</sub>:Yb<sup>3+</sup>,Er<sup>3+</sup>/SiO<sub>2</sub>/TiO<sub>2</sub> submicroplates as a scattering and upconverting layer for efficient dye-sensitized solar cells. *Chem. Commun.* **2013**, *49*, 3958–3960.
128. Dyck, N.C.; Demopoulos, G.P. Integration of upconverting β-NaYF<sub>4</sub>:Yb<sup>3+</sup>,Er<sup>3+</sup>@TiO<sub>2</sub> composites as light harvesting layers in dye-sensitized solar cells. *RSC Adv.* **2014**, *4*, 52694–52701. [CrossRef]
129. Wu, J.H.; Wang, J.L.; Lin, J.M.; Lan, Z.; Tang, Q.W.; Huang, M.L.; Huang, Y.F.; Fan, L.Q.; Li, Q.B.; Tang, Z.Y. Enhancement of the Photovoltaic Performance of Dye-Sensitized Solar Cells by Doping Y<sub>0.78</sub>Yb<sub>0.20</sub>Er<sub>0.02</sub>F<sub>3</sub> in the Photoanode. *Adv. Energy Mater.* **2012**, *2*, 78–81. [CrossRef]
130. Liu, M.; Lu, Y.; Xie, Z.B.; Chow, G.M. Enhancing near-infrared solar cell response using upconverting transparentceramics. *Sol. Energy Mater. Sol. Cells* **2011**, *95*, 800–803. [CrossRef]
131. Wang, J.; Wu, J.; Lin, J.; Huang, M.; Huang, Y.; Lan, Z.; Xiao, Y.; Yue, G.; Yin, S.; Sato, T. Application of Y<sub>2</sub>O<sub>3</sub>:Er<sup>3+</sup> Nanorods in Dye-Sensitized Solar Cells. *ChemSusChem* **2012**, *5*, 1307–1312. [CrossRef] [PubMed]
132. Bai, J.; Zhao, R.; Han, G.; Li, Z.; Diao, G. Synthesis of 1D upconversion CeO<sub>2</sub>:Er,Yb nanofibers via electrospinning and their performance in dye-sensitized solar cells. *RSC Adv.* **2015**, *5*, 43328–43333. [CrossRef]
133. Yuan, C.; Chen, G.; Li, L.; Damasco, J.A.; Ning, Z.; Xing, H.; Zhang, T.; Sun, L.; Zeng, H.; Cartwright, A.N.; *et al.* Simultaneous Multiple Wavelength Upconversion in a Core-Shell Nanoparticle for Enhanced Near Infrared Light Harvesting in a Dye-Sensitized Solar Cell. *ACS Appl. Mater. Interfaces* **2014**, *6*, 18018–18025. [CrossRef] [PubMed]
134. Zhao, P.; Zhu, Y.; Yang, X.; Jiang, X.; Shen, J.; Li, C. Plasmon-enhanced efficient dye-sensitized solar cells using core-shell-structured β-NaYF<sub>4</sub>:Yb,Er@SiO<sub>2</sub>@Au nanocomposites. *J. Mater. Chem. A* **2014**, *2*, 16523–16530. [CrossRef]
135. Li, L.; Yang, Y.; Fan, R.; Chen, S.; Wang, P.; Yang, B.; Cao, W. Conductive Upconversion Er, Yb-FTO Nanoparticle Coating To Replace Pt as a Low-Cost and High-Performance Counter Electrode for Dye-Sensitized Solar Cells. *ACS Appl. Mater. Interfaces* **2014**, *6*, 8223–8229. [CrossRef] [PubMed]
136. Yu, J.; Yang, Y.; Fan, R.; Liu, D.; Wei, L.; Chen, S.; Li, L.; Yang, B.; Cao, W. Enhanced Near-Infrared to Visible Upconversion Nanoparticles of Ho<sup>3+</sup>-Yb<sup>3+</sup>-F Tri-Doped TiO<sub>2</sub> and Its Application in Dye-Sensitized Solar Cells with 37% Improvement in Power Conversion Efficiency. *Inorg. Chem.* **2014**, *53*, 8045–8053. [CrossRef] [PubMed]
137. Boudreault, P.L.T.; Najari, A.; Leclerc, M. Processable Low-Bandgap Polymers for Photovoltaic Applications. *Chem. Mater.* **2011**, *23*, 456–469. [CrossRef]
138. Chen, H.Y.; Hou, J.H.; Zhang, S.Q.; Liang, Y.Y.; Yang, G.W.; Yang, Y.; Yu, L.P.; Wu, Y.; Li, G. Polymer solar cells with enhanced open-circuit voltage and efficiency. *Nat. Photonics* **2009**, *3*, 649–653. [CrossRef]
139. Hains, A.W.; Liang, Z.Q.; Woodhouse, M.A.; Gregg, B.A. Molecular Semiconductors in Organic Photovoltaic Cells. *Chem. Rev.* **2010**, *110*, 6689–6735. [CrossRef] [PubMed]
140. Chen, J.W.; Cao, Y. Development of Novel Conjugated Donor Polymers for High-Efficiency Bulk-Heterojunction Photovoltaic Devices. *Acc. Chem. Res.* **2009**, *42*, 1709–1718. [CrossRef] [PubMed]
141. He, Z.; Zhong, C.; Su, S.; Xu, M.; Wu, H.; Cao, Y. Enhanced power-conversion efficiency in polymer solar cells using an inverted device structure. *Nat. Photonics* **2012**, *6*, 591–595. [CrossRef]
142. You, J.; Dou, L.; Yoshimura, K.; Kato, T.; Ohya, K.; Moriarty, T.; Emery, K.; Chen, C.-C.; Gao, J.; Li, G.; *et al.* A polymer tandem solar cell with 10.6% power conversion efficiency. *Nat. Commun.* **2013**, *4*, 1446. [CrossRef] [PubMed]
143. Grätzel, M. Recent Advances in Sensitized Mesoscopic Solar Cells. *Acc. Chem. Res.* **2009**, *42*, 1788–1798. [PubMed]
144. Yella, A.; Mai, C.-L.; Zakeeruddin, S.M.; Chang, S.-N.; Hsieh, C.-H.; Yeh, C.-Y.; Grätzel, M. Molecular Engineering of Push–Pull Porphyrin Dyes for Highly Efficient Dye-Sensitized Solar Cells: The Role of Benzene Spacers. *Angew. Chem.* **2014**, *126*, 3017–3021. [CrossRef]
145. Günes, S.; Neugebauer, H.; Sariciftci, N.S. Conjugated Polymer-Based Organic Solar Cells. *Chem. Rev.* **2007**, *107*, 1324–1338. [CrossRef] [PubMed]
146. Wang, H.Q.; Batentschuk, M.; Osvet, A.; Pinna, L.; Brabec, C.J. Rare-Earth Ion Doped Up-Conversion Materials for Photovoltaic Applications. *Adv. Mater.* **2011**, *23*, 2675–2680. [CrossRef] [PubMed]
147. Wang, H.Q.; Stubhan, T.; Osvet, A.; Litzov, I.; Brabec, C.J. Up-conversion semiconducting MoO<sub>3</sub>:Yb/Er nanocomposites as buffer layer in organic solar cells. *Sol. Energy Mater. Sol. Cells* **2012**, *105*, 196–201. [CrossRef]



148. Wu, J.L.; Chen, F.-C.; Chang, S.-H.; Tan, K.-S.; Tuan, H.-Y. Upconversion effects on the performance of near-infrared laser-driven polymer photovoltaic devices. *Org. Electron.* **2012**, *13*, 2104–2108. [CrossRef]
149. Adikaari, A.A.D.; Etchart, I.; Guering, P.H.; Berard, M.; Silva, S.R.P.; Cheetham, A.K.; Curry, R.J. Near infrared up-conversion in organic photovoltaic devices using an efficient  $\text{Yb}^{3+}:\text{Ho}^{3+}$  Co-doped  $\text{Ln}_2\text{BaZnO}_5$  ( $\text{Ln} = \text{Y, Gd}$ ) phosphor. *J. Appl. Phys.* **2012**, *111*. [CrossRef]
150. Guo, W.; Zheng, K.; Xie, W.; Sun, L.; Shen, L.; Liu, C.; He, Y.; Zhang, Z. Efficiency enhancement of inverted polymer solar cells by doping  $\text{NaYF}_4:\text{Yb}^{3+}, \text{Er}^{3+}$  nanocomposites in PCDTBT:PCBM active layer. *Sol. Energy Mater. Sol. Cells* **2014**, *124*, 126–132.
151. Yakutkin, V.; Aleshchenkov, S.; Chernov, S.; Miteva, T.; Nelles, G.; Cheprakov, A.; Balushev, S. Towards the IR Limit of the Triplet–Triplet Annihilation-Supported Up-Conversion: Tetraanthraporphyrin. *Chem. Eur. J.* **2008**, *14*, 9846–9850. [CrossRef] [PubMed]
152. Boyer, J.C.; van veggel, F.C.J.M. Absolute quantum yield measurements of colloidal  $\text{NaYF}_4:\text{Er}^{3+}, \text{Yb}^{3+}$  upconverting nanoparticles. *Nanoscale* **2010**, *2*, 1417–1419. [CrossRef] [PubMed]
153. Johnson, C.M.; Reece, P.J.; Conibeer, G.J. Slow-light-enhanced upconversion for photovoltaic applications in one-dimensional photonic crystals. *Opt. Lett.* **2011**, *36*, 3990–3992. [CrossRef] [PubMed]
154. Zhang, W.; Ding, F.; Chou, S.Y. Large Enhancement of Upconversion Luminescence of  $\text{NaYF}_4:\text{Yb}^{3+}/\text{Er}^{3+}$  Nanocrystal by 3D Plasmonic Nano-Antennas. *Adv. Mater.* **2012**, *24*, OP236–OP241. [CrossRef] [PubMed]
155. Xie, X.; Gao, N.; Deng, R.; Sun, Q.; Xu, Q.-H.; Liu, X. Mechanistic Investigation of Photon Upconversion in  $\text{Nd}^{3+}$ -Sensitized Core-Shell Nanoparticles. *J. Am. Chem. Soc.* **2013**, *135*, 12608–12611. [CrossRef] [PubMed]
156. Zou, W.; Visser, C.; Maduro, J.A.; Pshenichnikov, M.S.; Hummelen, J.C. Broadband dye-sensitized upconversion of near-infrared light. *Nat. Photonics* **2012**, *6*, 560–564. [CrossRef]
157. Pan, A.C.; del Canizo, C.; Canavos, E.; Santos, N.M.; Leitao, J.P.; Luque, A. Enhancement of up-conversion efficiency by combining rare earth-doped phosphors with PbS quantum dots. *Sol. Energy Mater. Sol. Cells* **2010**, *94*, 1923–1926.
158. Suyver, J.F.; Aebischer, A.; Biner, D.; Gerner, P.; Grimm, J.; Heer, S.; Kramer, K.W.; Reinhard, C.; Gudel, H.U. Novel materials doped with trivalent lanthanides and transition metal ions showing near-infrared to visible photon upconversion. *Opt. Mater.* **2005**, *27*, 1111–1130.
159. Simon, Y.C.; Weder, C. Low-Power Photon Upconversion through Triplet-Triplet Annihilation in Polymers. *J. Mater. Chem.* **2012**, *22*, 20817–20830. [CrossRef]
160. Singh-Rachford, T.N.; Nayak, A.; Muro-Small, M.L.; Goeb, S.; Therien, M.J.; Castellano, F.N. Supermolecular-Chromophore-Sensitized Near-Infrared-to-Visible Photon Upconversion. *J. Am. Chem. Soc.* **2010**, *132*, 14203–14211. [CrossRef] [PubMed]
161. Fückel, B.; Roberts, D.A.; Cheng, Y.Y.; Clady, R.; Piper, R.B.; Ekins-Daukes, N.J.; Crossley, M.J.; Schmidt, T.W. Singlet Oxygen Mediated Photochemical Upconversion of NIR Light. *J. Phys. Chem. Lett.* **2011**, *2*, 966–971. [CrossRef]
162. Singh-Rachford, T.N.; Castellano, F.N. Nonlinear photochemistry squared: Quartic light power dependence realized in photon upconversion. *J. Phys. Chem. A* **2009**, *113*, 9266–9269. [CrossRef] [PubMed]



© 2015 by the authors. Licensee MDPI, Basel, Switzerland. This article is an open access article distributed under the terms and conditions of the Creative Commons Attribution (CC BY) license (<http://creativecommons.org/licenses/by/4.0/>).





MDPI AG

St. Alban-Anlage 66  
4052 Basel, Switzerland  
Tel. +41 61 683 77 34  
Fax +41 61 302 89 18  
<http://www.mdpi.com>

*Nanomaterials* Editorial Office

E-mail: [nanomaterials@mdpi.com](mailto:nanomaterials@mdpi.com)

<http://www.mdpi.com/journal/nanomaterials>





MDPI AG  
St. Alban-Anlage 66  
4052 Basel  
Switzerland

Tel: +41 61 683 77 34  
Fax: +41 61 302 89 18

[www.mdpi.com](http://www.mdpi.com)



ISBN 978-3-03842-533-5